



HAL
open science

Performances of Raman and Brillouin fiber-based sensing of temperature and strain in harsh environments

Chiara Cangialosi

► **To cite this version:**

Chiara Cangialosi. Performances of Raman and Brillouin fiber-based sensing of temperature and strain in harsh environments. Optics / Photonic. Université de Lyon; Università degli studi (Palerme, Italie), 2016. English. NNT: 2016LYSES018 . tel-01825112

HAL Id: tel-01825112

<https://theses.hal.science/tel-01825112>

Submitted on 28 Jun 2018

HAL is a multi-disciplinary open access archive for the deposit and dissemination of scientific research documents, whether they are published or not. The documents may come from teaching and research institutions in France or abroad, or from public or private research centers.

L'archive ouverte pluridisciplinaire **HAL**, est destinée au dépôt et à la diffusion de documents scientifiques de niveau recherche, publiés ou non, émanant des établissements d'enseignement et de recherche français ou étrangers, des laboratoires publics ou privés.

UNIVERSITÉ JEAN MONNET DE SAINT ETIENNE (FRANCE)

and

UNIVERSITÀ DEGLI STUDI DI PALERMO (ITALIA)

Cotutelle Ph. D. Thesis

Performances of Raman and Brillouin fiber-based sensing of temperature and strain in harsh environments

Chiara CANGIALOSI

Saint Etienne May 19th 2016

SUPERVISOR

Prof. Y. Ouerdane	University of Saint-Etienne, France
Prof. M. Cannas	University of Palermo, Italy
Prof. S. Girard	University of Saint-Etienne, France

REVIEWERS

Dr. M. Brugger	CERN, Geneva, Switzerland
Dr. A. Gusarov	SCK-CEN, Mol, Belgium

EXAMINERS

Prof. F.M. Gelardi	University of Palermo, Italy
Prof. L. Mescia	Politecnico di Bari, Italy
Dr. S. Delepine-Lesoille	Andra, Chatenay-Malabry, France

INVITED

Prof. A. Boukenter	University of Saint-Etienne, France
--------------------	-------------------------------------



Acknowledgements

I would like to thank the institutions involved in my cotutelle PhD thesis: Université Jean Monnet de Saint Etienne, which funded this PhD thesis and Università degli Studi di Palermo, which welcomed me as PhD student.

I would also like to acknowledge the contribution of ANDRA (French National agency for the management of radioactive wastes) and CEA (French Alternative Energies and Atomic Energy Commission) towards the realization of this PhD thesis.

I wish to express my deepest thanks to Prof. Youcef Ouerdane, Prof. Sylvain Girard, Prof. Aziz Boukenter and Prof. Marco Cannas, all of whom supervised me during my PhD time, sharing their scientific experience, thus allowing me to constantly improve my skills, while at the same time granting me freedom and autonomy of thought. Above all else, I thank them for their unfaltering support and steadfast enthusiasm, both of which truly helped transform even the hardest times in an enjoyable learning experience. It would be my pleasure to thank Prof. S.Agnello, Dr. E. Marin, Dr. S. Lesoille and all those from the LAMP group for our collaboration and constructive discussions.

A big thank you to all the people of the Laboratoire Hubert Curien, to my colleagues of the MOPERE group, whom I shared my time with during working hours and my own free time as well. They have been like a second family during the last three years. I would like to especially thank Adriana and Ciro, for their lovely company during “evening measurement sessions” in the Lab and for their all-around support both during work times and out of it.

I would also like to take the time to thank my friends (Giuliana, Irene, Marco, Elena, Clementina, Stefi e Fra ...) for staying close and supportive during all this time.

Finally, I would like to express my heartiest thanks to my family and my little brother for their moral support and encouragement during these years, this work would have been impossible without them.

Contents

INTRODUCTION.....	1
CHAPTER 1 - BACKGROUND	5
1.1 Cigéo project	7
1.2 Monitoring at Cigéo	10
<i>Monitoring goals</i>	<i>10</i>
1.2.1 <i>Environmental conditions</i>	<i>11</i>
1.2.2 <i>Optical fiber sensor to monitor temperature and strain inside the storage cell</i>	<i>13</i>
1.2.3 Conclusion.....	15
CHAPTER 2 - DISTRIBUTED OPTICAL FIBER SENSORS (DOFS_s)	17
2.1 Introduction	17
2.2 DOFSs principles	18
2.2.1 <i>Spontaneous scattering.....</i>	<i>19</i>
2.2.2 <i>Rayleigh scattering</i>	<i>21</i>
2.2.3 <i>Brillouin scattering.....</i>	<i>22</i>
2.2.4 <i>Stimulated Brillouin Scattering (SBS).....</i>	<i>27</i>
2.2.5 <i>Raman scattering.....</i>	<i>31</i>
2.2.3 DOFSs of strain and temperature	36
2.3.2 <i>Rayleigh scattering based optical frequency domain reflectometer (OFDR)</i>	<i>36</i>
2.3.3 <i>Brillouin distributed T and strain sensor (B-DSTS)</i>	<i>37</i>
<i>Raman distributed temperature sensor (RDTS).....</i>	<i>41</i>
2.4 Conclusion.....	45
CHAPTER 3 - DOFS_s IN HARSH ENVIRONMENTS	49
3.2.1 Losses in silica-based OFs	49
3.2.2 OFDR sensor vulnerability in nuclear environment	51
3.2.3 <i>BOTDA sensor vulnerability in harsh environment.....</i>	<i>52</i>
<i>RDTS sensor vulnerability in nuclear environment</i>	<i>56</i>
<i>Choice of the sensor for the Cigéo application.....</i>	<i>64</i>
CHAPTER 4 - MATERIALS AND EXPERIMENTAL SETUPS	69

4.1	Investigated Samples	69
4.2	Experimental set-ups: distributed measurements	73
	<i>Raman set-up</i>	74
	<i>Brillouin set up</i>	76
	<i>Optical time domain reflectometer</i>	79
4.2.1	Experimental set-ups: spectroscopic analysis	80
4.2.2	<i>Optical Absorption measurement</i>	80
4.2.3	<i>Electron Spin Resonance spectroscopy</i>	82
4.3	Facility and treatments	85
4.3.2	<i>H₂ loading sessions and procedure</i>	85
4.4.1	<i>γ-rays irradiation session at high total ionizing dose (Mol)</i>	87
4.4.2	<i>γ-rays irradiation session at low dose rate (Saclay)</i>	87
4.4.3	<i>Thermal treatments</i>	89
4.4.4
CHAPTER 5 - SE-RDTS UNDER GAMMA-RAYS AND H₂ EXPOSURE		91
5.1	Introduction	91
5.2	H ₂ presence effects on RDTS response	94
5.2.1	<i>IR Spectral attenuation changes induced by H₂</i>	97
5.3	γ-rays effects on RDTS response: <i>Ex situ measurements</i>	100
5.3.1	<i>Spectral attenuation changes induced by γ-rays</i>	102
5.4	Combined γ-rays and H ₂ effects on the RDTS performance: Ex situ measurements	105
5.4.1	<i>Spectral attenuation measurements changes due to combined H₂ and γ-rays</i>	107
5.5	Discussion	108
5.6	Conclusion	118
CHAPTER 6 - RDTS RESPONSE DURING RADIATION EXPOSURES AND THERMAL TREATMENT		121
6.1	γ-rays effects on RDTS response: <i>In situ measurements</i>	122
6.2	Thermal treatment effects on RDTS response using a pre-irradiated fiber	126
6.3	Conclusion	129
CHAPTER 7 - MITIGATION OF THE RADIATION-INDUCED DEGRADATION OF THE SE-RDTS: CORRECTION TECHNIQUE		131
7.1	Introduction	131
7.2	Correction procedure	133
7.3	Online correction	139
7.4	Conclusion	143
CHAPTER 8 - BOTDA SENSING IN GAMMA-RAY AND H₂ PRESENCE: RESULTS		145

8.1	Introduction	145
8.2	RI-BFS	147
8.3	Germanium doped fibers	148
	<i>Ex-situ measurements</i>	148
	<i>In-situ measurements</i>	155
8.3.1	<i>Discussion</i>	158
8.3.2	PSC-doped fiber	159
8.3.3	<i>Ex-situ measurement</i>	159
	<i>In-situ measurements</i>	164
8.4.1	<i>Discussion</i>	168
8.4.2	8.5 Thermal treatment	170
8.4.3	8.6 Conclusion.....	171
	CHAPTER 9 - CONCLUSION AND FUTURE DEVELOPMENTS	173
	LIST OF PUBLICATIONS AND COMMUNICATIONS.....	179
	REFERENCES	183

Introduction

The optical fibers (OFs) are one of the greatest technological advances of the 20th century. Today, optical communication systems are the keystone technology used in a variety of applications, such as medical, military, telecommunication, industrial, data storage, networking etc. For the last few decades, in the scientific community, optical fibers have shown an important growth and relevance in sensing technology fields. This interest in OF sensors is motivated by their remarkable capabilities, as resistance to electromagnetic interferences, remote sensing, small dimensions, low weight, real time monitoring or multiplexing ability. In particular, the nuclear industry showed an increasing interest on the integration of distributed optical fiber sensors (DOFSs) sensing applications in nuclear power plants (NPPs).

Nowadays, the use of new-generation nuclear power plants or radioisotopes for beneficial purposes in research, industry, medicine and agriculture, etc. is growing strongly, as well as the need to managing the different radioactive wastes produced in these applications. In this context, the DOFSs have been shown to be promising diagnostic tools for monitoring of different nuclear sites. Therefore, these sensors must be designed depending on the specific application. Each project provides new challenges on the DOFSs techniques adaptation and standards, as well as the transducer implementation, ranges of measurement, calibration and environmental conditions. Therefore, the performances (resolution, operating range, response time...) of these technologies have to be evaluated and developed in order to survive to the severe environmental constraints (hydrogen release, high radiation dose and/or high temperature ...) of these facilities.

This work was carried out in collaboration with Andra, the French National agency for the management of radioactive wastes, in view of the development and design of the French deep geological repository where long-lived high level and intermediated-level activity wastes will be stored. The aim of this thesis is the evaluation of Raman and Brillouin scattering based optical fiber distributed sensor performances in preparation of their integration in this storage site. These sensing technologies will support conventional electromagnetic sensors in order to

guarantee the surveillance and the safety of the facility. For this purpose the response of these DOFSs working in the typical harsh environment of this repository (ionizing radiation and hydrogen presence...) was evaluated.

The Thesis is organized in two main Parts: The first Part is subdivided in chapters 1-3, while the second concerns chapters 4-9. The objective of Part I is to provide a background on the project and the specialized literature dealing with both the physical principles and the different technologies of the distributed optical fiber sensors. Part II is devoted to the experimental contributions developed in this works. More specifically, Chapter 4 provides a description of the studied samples, the adopted experimental techniques and the description of both setups and facilities used during the different measurements sessions (such as γ -rays source or hydrogen loading set up...). Chapters 5, 6 and 7 report the studies performed on the Raman based sensors when the fiber sensing element is submitted to γ -rays exposures and hydrogen releases. The same investigation was also performed on the Brillouin based sensors and is reported in Chapter 8. Finally, in Chapter 9 we draw the main conclusions and the perspectives for the employment of these sensors in the deep geological repository. A list of bibliographic references including the results which came from this thesis work are reported at the end of the manuscript, together with a list of communications to congresses.

PART I
BACKGROUND

Chapter 1

In this chapter we describe the context of this PhD work that was done in the framework of a contract between the Laboratoire Hubert Curien in Saint-Etienne, Andra (Agence Nationale pour la gestion des Déchets RAdioactifs) and CEA-DAM (Commissariat à l'Energie Atomique, Direction des Applications Militaires). The objectives of this work were to participate to the evaluation of fiber-based sensing techniques to design the monitoring of the radioactive wastes repository facilities that are currently under definition at ANDRA in the framework of the Cigéo project.

Background

Today, the production of radioactive wastes, its storage and handling are of great importance in order to protect people and the environment from their harmful effects. Radioactive wastes are generated in a broad range of activities involving a wide variety of radioactive materials associated with, for example, the operation of nuclear facilities, the use of sealed radioactive sources in industry, the use of human made radionuclides in hospitals and laboratories, and the decommissioning of such facilities [1]. Radioactive waste refers to radioactive substances for which no subsequent use is planned or envisaged and is classified according to its activity level and its longevity. The activity level determines the degree of protection to be provided and can be very low, low, intermediate or high. The longevity depends on the radioactive half-life¹ associated with each radionuclide it contains. Radioactive waste is said to be “short-lived” if it merely only contains radionuclides with a half-life of less than 31 years. It is said

¹Half-life is the amount of time it takes for half the atoms in a given radionuclide to decay.

to be “long-lived” if it contains a significant quantity of radionuclides with a half-life of more than 31 years.

In France, radioactive waste is classified into five categories depending on its radioactivity level and its longevity [2], [3]: very-low-level waste (VLL-W), low-and Short-Lived Intermediate-Level Waste (SL/LIL-W), Long-Lived Low-Level Waste (LL/LL-W), **Long-Lived Intermediate-Level Waste (LL/IL-W)** and **High-Level Waste (HL-W)**.

The French National Radioactive Waste Management Agency, Andra, is charged to design and implement safe solutions for the management of all types of radioactive waste in France. More than 90% of the volume of radioactive waste generated each year in France is disposed at Andra's two disposal repositories. These wastes consist in both very-low-level radioactive wastes and low- and intermediate-level short-lived radioactive wastes. Instead, concerning the high level or long-lived waste, disposal solutions are currently under study. In 2006 Andra was charged by the Planning Act n°2006-739 [4] to design and create an industrial site for deep geological disposal for LL/IL-W and HL-W, called Cigéo. The Planning also imposes for such a repository to be reversible for at least 100 years [5]. Moreover, if licensed, the facility will be commissioned in 2025. The existing or expected management solutions are notably based on the radioactive waste classification, as illustrated in Figure 1.1.

Classification of radioactive waste

		HALF-LIFE →		
		Very short-lived Half-life < 100 days	Short-lived Half-life ≤ 31 years	Long-lived Half-life > 31 years
ACTIVITY	Very low level (VLL)	<i>Stored to allow radioactive decay on the production site then disposed of adopting conventional solutions</i>	Surface disposal facility <i>(Very-low-level radioactive waste disposal facility in the Aube district)</i>	
	Low level (LL)		Surface disposal facility <i>(Low-and intermediate-level waste disposal facility in the Aube district)</i>	Shallow disposal facility <i>(studied in accordance with the Act of 28 June 2006)</i>
	Intermediate level (IL)			
	High level (HL)		Reversible deep geological disposal facility <i>(studied in accordance with the Act of 28 June 2006)</i>	

Figure 1.1. Classification of radioactive waste and their management [6].

HL-W and LL/IL-W are produced mainly by the nuclear power industry and its associated research activities as well as, to a lesser extent, national defense operations. In particular:

LL/IL-W consists of residues arising from spent nuclear fuel used to generate electricity or propel submarines and ships of the French Navy, compound apart from fuel that have resided in nuclear reactor and technological waste resulting from maintenance of nuclear facility, laboratory, dismantling, etc. Some LL/IL-W can emit low amounts of radioactive gases (^3H , ^{14}C and ^{85}Kr), generate hydrogen or other gasses through radiolysis.

HL-W corresponds mainly to highly radioactive residues arising from spent fuel reprocessing operations (fuels used to generate electricity and, to a very minor extent, fuels related to national defense activities). They contain various short- and long-lived radionuclides (half-life up to $3 \cdot 10^5$ years) and due to the presence of certain fission products and actinides high-level waste generates heat. Moreover, molecular hydrogen is generated in the repository cell due to the anoxic corrosion of metallic materials (see section 1.2.2).

1.1 Cigéo project

Cigéo (Centre Industriel de Stockage GEOlogique) will consist in surface installations for controlling and conditioning waste packages, as well as underground installations for waste-disposal purposes and connecting infrastructures between surface and underground [6]. The envisioned site is displayed in Figure 1.2. Design is ongoing on, thus figures are orders of magnitudes. They are subjected to evolution.

The *surface installations* (A) will be spread over two sites:

- One site (A1) located directly above the underground installations. It will have a footprint of the order of 20 hectares and it regroups the required industrial workshops for the construction of the repository, administrative buildings etc.
- The other (A2) located a few kilometers away will mostly include the nuclear installations where radioactive waste packages will be controlled and conditioned in containers, if required, before being transferred to the underground installations.

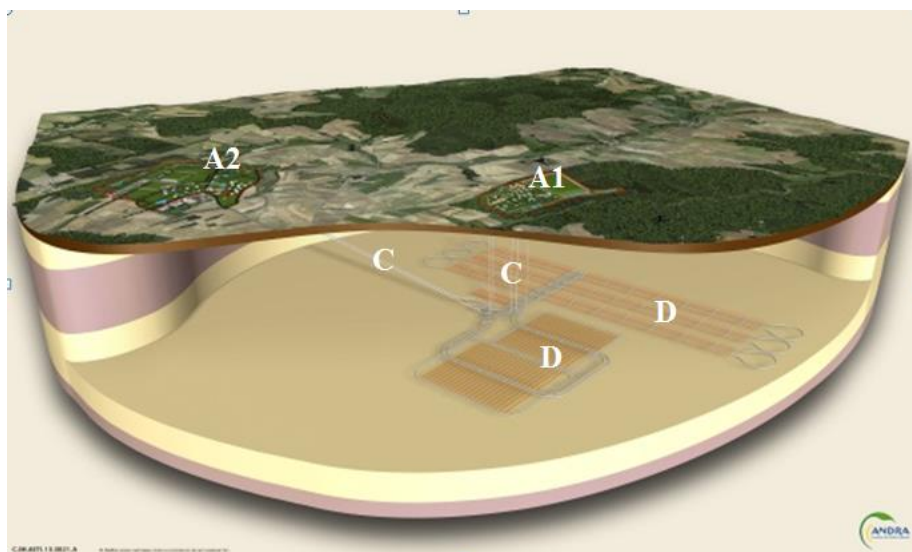


Figure 1.2. General layout of Cigéo facilities [2].

The *connecting infrastructures* (C) will ensure transfers between surface and underground installations, notably for conveying staff, transferring disposal containers and worksite machinery, as well as ventilating underground installations.

The *underground installations* (D) will store the radioactive wastes and will consist of specific disposal areas for the different waste categories (HL-W and LL/IL-W), as well as connecting drifts and technical installations. The installations, located at a depth of about 500 m, will be progressively added as the operation progresses until they reach a total maximum area of about 15 km², after about 100 years.

In order to prevent the dispersion of radioactive elements into the environment, the geological environment of the site has been conveniently selected: an impermeable clay layer constitutes a natural barrier to isolate the waste and protect the environment in case of accidental releases of radioactive elements towards the extern. Indeed, the **remarkable properties of the clay, such as retention capability, low permeability and homogeneity of the formation delay and mitigate the migration of the radioactive substances contained in the HL-W or LL/IL-W.**

Package of radioactive wastes:

An adapted disposal concept has been designed for each waste category. Upon their arrival at the underground facility, **HL-W packages** will be conditioned one by one in steel containers

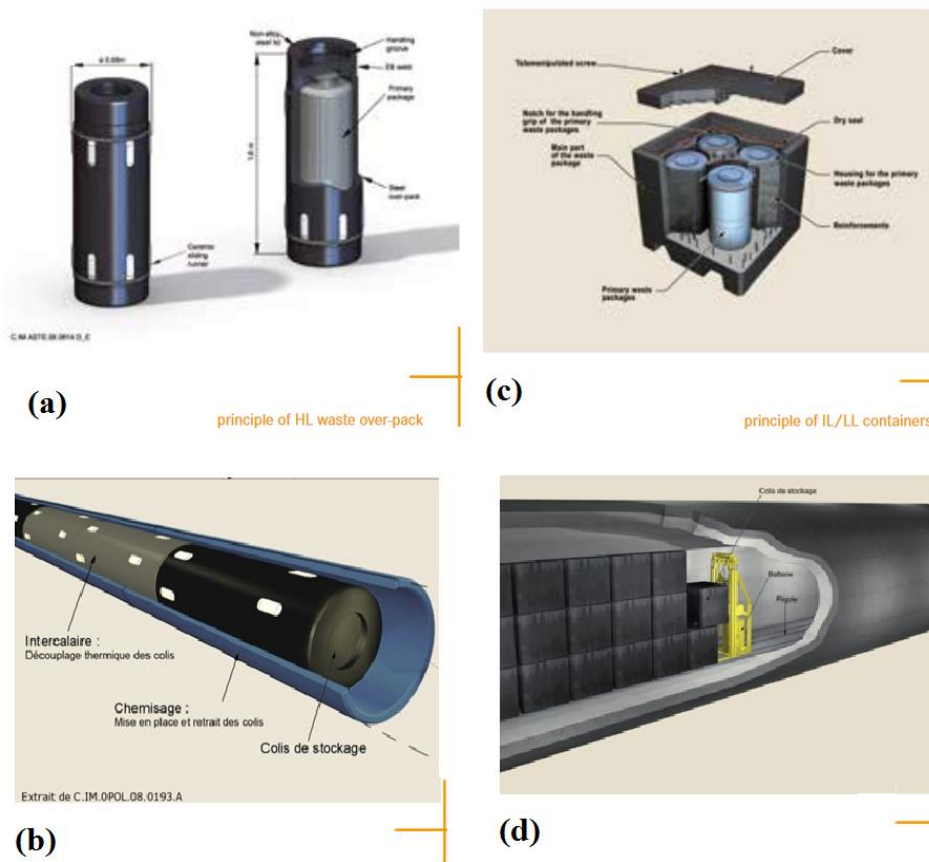


Figure 1.3. Disposal concept for high-level wastes (a) and (b) and intermediate level long live wastes (c) and (d) [2].

shown in Figure 1.3 a, which in turn will be deposited into transport overpack in order to ensure the radiological protection of the staff, and finally laid down one behind the other in **tunnel-like disposal cells measuring a few hundred meters** [2], illustrated in Figure 1.3 b. Instead, the **LL/IL-W packages** will be deposited in the concrete containers shown in Figure 1.3 c, which in turn will be inserted into transport overpacks. In the repository, they will be juxtaposed and stacked **in dedicated disposal cells presently designed as 400-600 m long tunnels**, shown in Figure 1.3 d.

1.2 Monitoring at Cigéo

Monitoring goals

1.2.1 Long-term safety is the driving objective for Cigéo: to protect the present and future generations from waste-associated risks. The French Safety Guide [7] recommends that Andra develops a monitoring program to be implemented at repository construction and conducted until closure, and possibly after closure, with the aim to confirming prior expectations and enhancing knowledge of relevant processes. To achieve these objectives and thus verify the basis for long term safety, an overall monitoring strategy including waste package characterization prior to emplacement and “observation and surveillance” of disposal structures and infrastructures (galleries, shafts/ramps...) is being developed by Andra as part of the Cigéo project. The data acquired in this monitoring process should thus provide information to aid repository operation both to updating the safety analyses, during operation and after closure, and to supporting future decisions that need to be taken during the reversible management of the disposal process. More specifically, the observation of the phenomenological evolutions consists of three parts [8]:

- *In-situ* investigations (monitoring) aim at verifying, confirming and further enhancing prior knowledge in order to support the periodic re-evaluation of the long-term safety of Cigéo and reversibility conditions. It will happen verifying the compatibility of in situ measurements performed on first decades of storage life with the results of prediction.
- Large-scale monitoring of the structures and environmental conditions evolution required for a reversible management of the disposal process or a possible withdrawal of packages. The design of the structures are based on envelop assumptions and degraded scenarios, therefore the monitoring must help reducing margins, to optimize the structure design.
- Monitoring also contributes to operational safety.

The monitoring equipment must be able to provide information on Thermal-Hydraulic-Mechanical-Chemical-Radiological (THMCR) phenomena surrounding the disposal cell. A high level of confidence in signal reliability and longevity of monitoring equipment are

required. At the disposal cell scale, the monitoring devices and installed equipment must further resist the severe environmental conditions existing in a repository described in section 1.2.2. Moreover, the sensing devices placed in the storage cell will be inaccessible from the introduction of the first radioactive waste package which limits instrument maintenance (except by robotic devices).

Environmental conditions

1.2.2 At the repository cell scale, the monitoring devices and installed equipment must further resist to the severe environmental conditions existing in a repository, which may include high temperatures, high pressures, humidity and/or submersion, chemically aggressive

Table 1.1 Disposal cells environmental conditions

Constraint type	Expected environmental conditions
Radiation	*DC-HL-W: Dose rate changing in the range $1 \div 10$ Gy/h up to TID 0.8-10 MGy (100 years). *DC-LL/IL-W: TID $2.4 \div 3$ Gy after 10 years.
Temperature	DC-HL-W: $T_{\max} = 90^{\circ}\text{C}$. DC-LL/IL-W: $T_{\max} = 70^{\circ}\text{C}$.
Pressure	DC-HL-W < 1 Bar DC-LL/IL-W > 1 Bar
Humidity	DC-HL-W: 40 % DC-LL/IL-W: [40% - 60%] during 50 years
Gas release	H ₂ presence

*TID means total ionizing dose.

DC-HL-W indicates the Disposal Cell for High Level activity radioactive Waste.

DC-LL/IL-W indicates the Disposal Cell for Long-Lived Intermediate-Level activity radioactive Waste.

environments, and levels of radiation that may degrade electrical and optical cable performance and accelerate sensor degradation, as some of the sensors will be placed in the

immediate vicinity of waste packages. The expected environment conditions in the repository cell are reported in Table 1.1

Therefore, inside the repository cells the temperature ranges between 25 °C and 90 °C and both dose rate and H₂ production mechanism depend on the waste category. In particular, for LL/IL-W a dose rate of 1 Gy/h is estimated leading to TID up to 0.8 MGy in 100 years; instead, for HL-W a dose rates up to 10 Gy/h are expected, reaching maximum TID of 8 MGy in one century. Concerning the H₂ release, the main mechanism of production in the HL-W disposal cell is the anoxic corrosion of the metallic surface in presence of water. Indeed, because of the expected scenario, within months from the closure, the HL-W cells will quickly be drowned in the water from the host rock and both the over pack and the liner inside the cell may corrode. However, the hydrogen release is weak and ranges between 50 and 150 mol/year (the main reaction is: $3Fe + 4H_2O \leftrightarrow Fe_3O_4 + 4H_2$). Instead, in the case of LL/IL-W disposal cells the H₂ production (~ 0.5 mol/hour release for each radioactive waste package [9]) arises by radiolysis of the organic material contained in some of LL/IL-W and to a lesser extent by the radiolysis of the water exposure to the radiation. Moreover, when ventilation stops with cell closure, concentrations would slowly yet regularly increase. Its maximum levels could approach 100% hydrogen content in the atmosphere in few months.

Finally, also the evolution of the temperature inside the storage cell was simulated and a thermal gradient is expected. The thermal field will be anisotropic. The example of thermal gradients in clay stone is illustrated in Figure 1.4. At the scale of a single storage cell, the maximum temperature will be reached few years after waste emplacement [10].

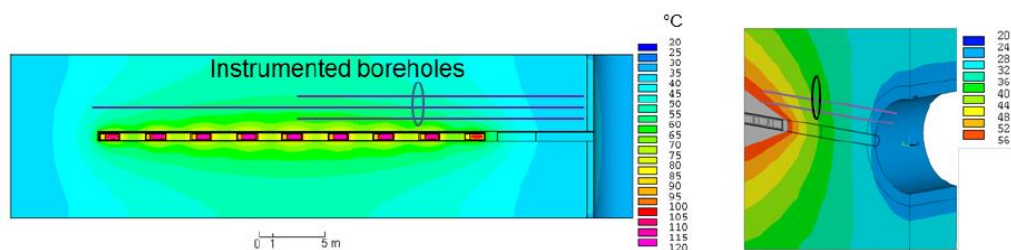


Figure 1.4. Thermal simulation around a HL-W cell when the temperature is at its maximum (horizontal and vertical cross-section) [10].

Furthermore, along the disposal cell, longitudinal heterogeneities are expected, illustrated in Figure 1.5. A "sawtooth" effect is observable and it is due to the spaces left between the

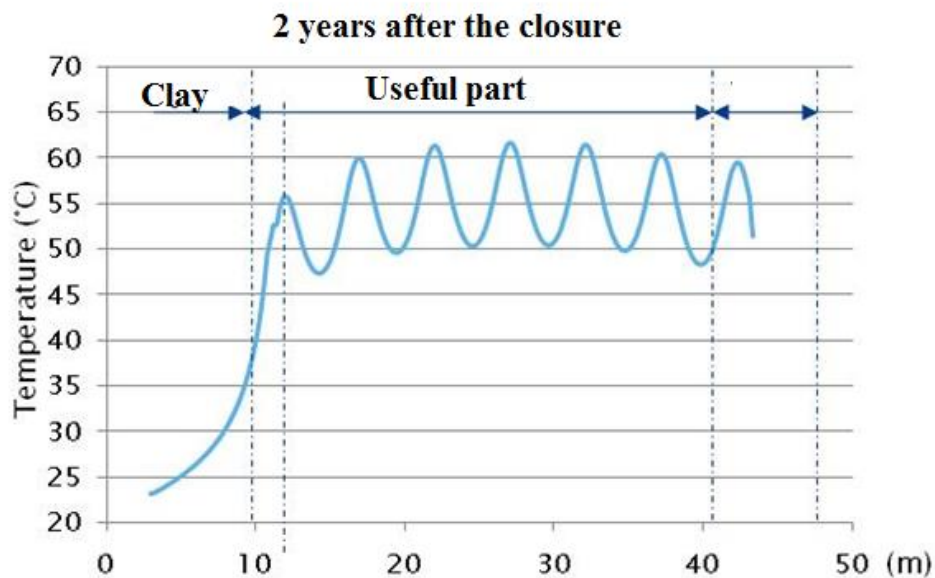


Figure 1.5. Thermal simulation along 40 m long HL-W cell after two years from the closure. The “sawtooth” effect is observable. Adapted by [8].

waste packages to limit the thermal load and to satisfy the safety criteria of 90 °C in the surrounding clay rock. The step of this phenomenon is about 2 m. The temperature oscillation amplitude is expected to be ~20 °C during the first year after the closure and ~5 °C after 100 years [8].

1.2.3

Optical fiber sensor to monitor temperature and strain inside the storage cell

In order to monitor the temperature and the strain along the storage cell distributed optical fiber sensor (DOFSs) were selected. Indeed, as discussed in the next chapter, they are able to provide continuous spatial distributed temperature or strain measurements over distance exceeding several km. For these reasons, they provide information calibration to traditional punctual sensor technology, whose measure is localized. Moreover, these systems are small,

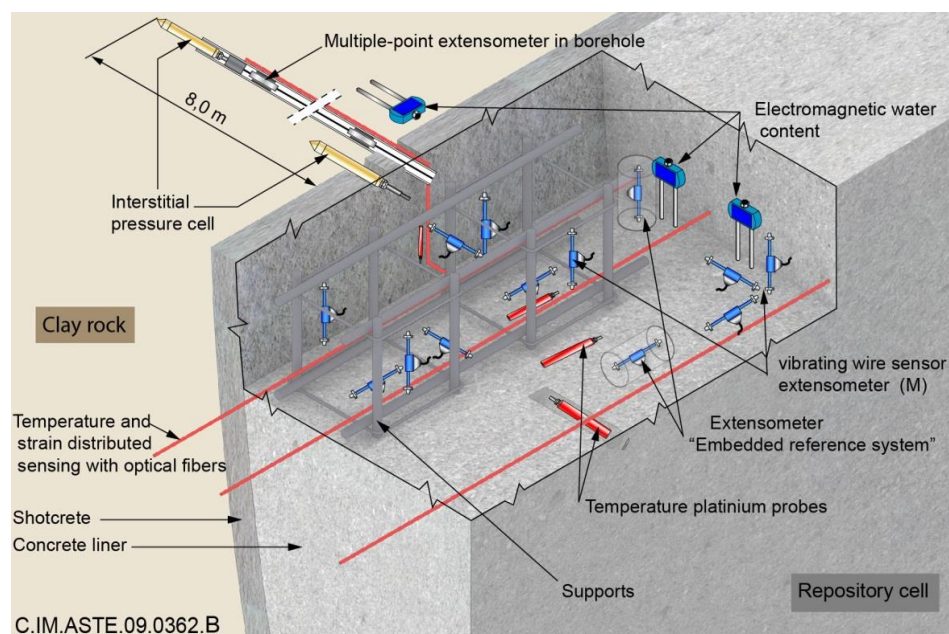


Figure 1.6. Example for concrete instrumentation to provide THM characterizations which will be implemented in the access gallery liners.

easy to handle and can be robust² for decades performing remote sensing, which enables maintenance of optoelectronic instruments into instrumentation zones of more easy access.

Therefore, DOFs are planned in the overall monitoring system in order to have a time and spatial cartography of the strain and temperature inside the storage cell. As shown in Figure 1.6 [10], thermal monitoring is ensured with platinum probes (Pt100 or similar) placed near the Raman distributed optical fiber sensors. A reference element is inserted into the sensing line (i.e. along the tunnel). Punctual temperature sensors are numerous because gradients are expected along the tunnels. Moreover, mechanical monitoring will be performed with vibrating wire extensometers located on 3 axes and optical fibers based on Brillouin scattering. Figure 1.6 illustrates an example of this general approach for Thermal-Hydraulic-Mechanical (THM) and which will be implemented in the HL-W repository cell concrete liners and in several access gallery liners.

In the IL-W repository cells, on top of temperature sensing, strain optical fibers are envisioned at the surface of the metallic liner. They will contribute to evaluate whether clay

² They withstand very large stresses during liner pushing operations

mechanical load is homogeneous over the liner, whether thermal expansion of metallic components is not restricted by unexpected frictions on the rock.

The optimal performances required by the Cigéo application are a spatial resolution of about 1 m, temperature accuracy of 1°C and strain accuracy of 20 $\mu\epsilon$. Moreover, the minimum sensing distance to be monitored is 100 m (HL-W tunnel length).

1.3 Conclusion

The process of selecting appropriate deep final repositories for high level (HL) and long-lived and intermediated-level (LL/IL) activity radioactive wastes requires careful evaluation and control of the potential risks. It also must guarantee long-term safety of the site. In this context the monitoring of the underground installation is mandatory. The ability to provide distributed temperature and strain measurements over long distances made the fiber-based sensors a particularly interesting monitoring technology for the disposal cells containing radioactive wastes. However, the environmental constraints of the future disposal sites impose to develop sensors sufficiently resistant to these harsh conditions such as a high level of radiation, high temperature and an important concentration of hydrogen in the air. The aim of this PhD Thesis's work is to evaluate and to improve the performances (resolution, operating range, response time...) of DOFs in order to be able to survive to the harsh environmental constraints. In particular, our work is focused on the γ -ray and molecular hydrogen presence effects on the Brillouin- and Raman-scattering based optical fiber sensors.

Chapter 2

Distributed Optical Fiber Sensors (DOFSs)

In this chapter we present a comparative overview of the DOFS technologies, focusing our discussion on the sensors exploiting the fiber Raman and Brillouin signatures. First, we briefly summarize the theoretical approach allowing to obtain the basic equations describing the operation principles of these two DOFSs types. Later, we provide a review about the optical and radiation performances of these sensors.

2.1 Introduction

In the last decades, several architectures for DOFSs have been proposed and further optimized with significant improvements in their performances, as highlighted in many review papers [11]- [12]. The use of single-mode or multi-mode optical fibers (OFs) as the sensing element is due to their exclusive characteristics, not shared by other conventional sensor techniques. DOFSs allow the monitoring of several physical quantities such as temperature, strain, pressure, magnetic field, chemical concentration with a high spatial resolution (typically better than one meter) all along kilometer long fibers [13]. Furthermore, the DOFSs have the peculiarity to be able to monitor simultaneously both spatial and temporal evolutions of a physical quantity. They benefit from the remarkable properties of the OFs: small size, light weight and resistance to electromagnetic interference, as well as no need of electrical power supply at the sensing point and the ability to be easily multiplexed. Nowadays, the DOFSs performances are considered as suitable for many application fields

such as temperature and strain monitoring in infrastructures that require large areas of coverage with high level of accuracy. For example, by Brillouin scattering based DOFS, for long distances of hundred kilometers, it is possible to achieve strain resolution of few micrometers over one meter (micro-strain) and temperature resolution better than 1°C [14], [15]. Some interesting applications of DOFSs are reported in [15] and demonstrate the attractiveness of these techniques. First, in civil infrastructures DOFSs are used as parts of fire alarm systems to monitor the temperature along railway tunnels or electric power system... Second, the DOFSs are currently implemented to monitor the strain evolution for large civil and nuclear structures and vehicles such as bridges, railways, buildings, aircraft... Last example concerns the pipelines monitoring in the oil and gas industry, requiring DOFSs to perform real-time monitoring and early warning systems for leakage detection occurring along liquid and gas pipes.

2.2 DOFSs principles

DOFS technology is able to monitor environmental parameters that act on the fiber structural properties by exploiting its scattering process signature, and recording this signal with a proper interrogation system. Three different scattering processes can occur in a silica-based OF and can be exploited to design DOFSs: Rayleigh, Raman and Brillouin scatterings [16]. In this section we summarize the theoretical derivation of these three phenomena and the relation between their scattered signatures and the temperature or the strain [17].

The light scattering occurs as a consequence of localized or propagative motion of atoms or molecules (vibrations) or of fluctuations in the structural properties of a material medium, i.e. it is linked to the presence of permanent or transient inhomogeneity in the propagation medium. The scattering in optical fibers arise from microscopic and macroscopic density variation, composition or structure of the material in which light is propagating. The disordered distribution of atoms and molecules in amorphous silica and the presence of additional dopants induce localized density changes (therefore refractive index variations) modifying temporally and/or spatially the structural properties and then the optical properties of the OF. We consider two types of scattering describing the interaction between the light and fiber molecules. First one is the *elastic scattering* where the light is diffused by the

molecule without being shifted in frequency. This category deals with Rayleigh scattering. Second one is the *linear inelastic scattering*, it occurs when the light interacts with two different types of phonons: the propagative phonons (or pressure density fluctuation) and the non-propagative or localized phonons ones corresponding to the molecular vibrations (molecular density fluctuation). In the first case we have the Brillouin scattering, while the second case corresponds to the Raman scattering. The frequency of the localized phonons is higher with respect to that of the acoustic ones. Indeed, for the Raman scattering the shift frequency is >10 THz and for the Brillouin scattering it is around 10 GHz. In silicate glasses, among Rayleigh, Raman and Brillouin scatterings, the amplitude of the Rayleigh scattering is the strongest one; Brillouin and Raman amplitudes are ~ 20 dB and ~ 30 dB weaker, respectively. A typical spectrum of the light scattering is shown in Figure 2.1, in which the three types of diffusion features are displayed. By definition, the components of the scattered light that are shifted to lower frequencies are indicated as Stokes components, and those shifted to higher frequencies are identified as anti-Stokes ones.

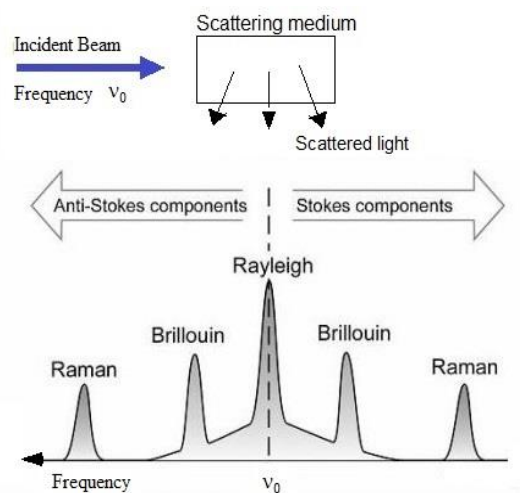


Figure 2.1. Typical spontaneous scattering spectrum from solid state matter.

2.2.1

Spontaneous scattering

The wave equation describing the light propagation as an electromagnetic wave is [18]:

$$\nabla^2 \bar{E} - \frac{1}{c^2} \frac{\partial^2 \bar{E}}{\partial t^2} = \mu_0 \frac{\partial^2 \bar{P}}{\partial t^2} \quad 2.1$$

where \bar{E} is the electric field vector, n the refractive index, $c = \frac{1}{\sqrt{\mu_0 \epsilon_0}}$ the speed of light in the vacuum ($3 \cdot 10^8$ m/s), μ_0 and ϵ_0 denote the magnetic permeability and the dielectric permittivity in the free space, respectively. \bar{P} is the medium polarization field in presence of the electromagnetic wave. In linear regime, its amplitude is proportional to the external electric field: $\bar{P}_L = \epsilon_0 \chi \bar{E}$ where χ is the dielectric susceptibility.

Since the optical fiber is, at scale of interest, an inhomogeneous medium the spatial and temporal dielectric susceptibility fluctuation, $\Delta\chi$, has to be taking into account. Therefore, the relation between the electric field and the polarization is:

$$\bar{P}_L = \epsilon_0 \chi \bar{E} + \bar{P}_1 = (\epsilon_0 \chi + \Delta\epsilon) \bar{E} \quad 2.2$$

Where $\bar{P}_1 = \Delta\epsilon \bar{E}$ is a term of supplementary polarization [16] developed by the medium due to its inhomogeneity. $\Delta\epsilon$ is the dielectric tensor that includes the information on the (spatio-temporal) fluctuations leading to the spontaneous scattering. The light propagation is therefore described by the wave equation:

$$\nabla^2 \bar{E} - \frac{n^2}{c^2} \frac{\partial^2 \bar{E}}{\partial t^2} = \mu_0 \frac{\partial^2 \bar{P}_1}{\partial t^2}$$

The tensor $\Delta\epsilon$ comes from two different contributions: a scalar component $\Delta\epsilon \delta_{ij}^{(s)}$ and a tensor component $\Delta\epsilon \delta_{ij}^{(t)}$. The first contribution arises from the thermodynamic fluctuations (i.e. pressure, temperature, entropy, and density fluctuations) and is responsible for the Rayleigh and Brillouin scattering. Instead, the asymmetric part of $\Delta\epsilon \delta_{ij}^{(t)}$ is responsible for the Raman scattering. It is associated with the polarizability change of molecules in the medium in presence of an electric field [19].

Rayleigh scattering

The Rayleigh scattering occurs when the oscillating electric field of a light wave acts on the electrons, creating induced dipoles. These particle dipoles radiate at the same frequency and give rise to the Rayleigh scattering. It is the scattering of light from static density fluctuation and its diffused power is proportional to the incident power signal.

Since the scattering processes originate by the thermodynamic fluctuations, we introduce the macroscopic thermodynamic quantities: density (ρ), entropy (S), pressure (p) and temperature (T). These quantities are necessary to describe these phenomena [19], [20]. The scalar component of the dielectric fluctuations, $\Delta\epsilon\delta_{ij}^{(s)}$, that for convenience we indicate with $\Delta\epsilon$, can be expressed in terms of the thermodynamic variables as [16]:

$$\Delta\epsilon = \left(\frac{\partial\epsilon}{\partial\rho}\right)_T \Delta\rho + \left(\frac{\partial\epsilon}{\partial T}\right)_\rho \Delta T \quad 2.3$$

According to [16], the second term in equation 2.3 can be neglected, since the density fluctuation affects the dielectric constant more than the temperature fluctuation, whose contribution is less than 2%. As the propagation of the sound wave is an adiabatic process, $\Delta\rho$ is expressed in terms of pressure fluctuations at constant entropy plus the entropy fluctuations at constant pressure:

$$\Delta\rho = \left(\frac{\partial\rho}{\partial S}\right)_p \Delta S + \left(\frac{\partial\rho}{\partial p}\right)_s \Delta p \quad 2.4$$

The first term of Eq. 2.4 is the entropy and gives rise to the Rayleigh scattering. While, the second term of Eq. 2.4 describes the adiabatic density fluctuations that generate the Brillouin scattering. Therefore, in order to describe the Rayleigh scattering we take into account the diffusion equation for the entropy fluctuations:

$$\rho c_p \frac{\partial\Delta S}{\partial t} - k\nabla^2\Delta S = 0 \quad 2.5$$

Where c_p is the specific heat at constant pressure and k is the thermal conductivity. Equation 2.6 is a solution to the diffusion equation:

$$\Delta S = \Delta S_0 \exp(-Dt) \exp(-\bar{u} \cdot \bar{r}) \quad 2.6$$

where \bar{u} is the scattered wavevector and $D = \frac{k}{\rho c_p} |\bar{u}|^2$ is the damping rate of the entropy disturbance.

Therefore, assuming to be in presence of a monochromatic electromagnetic incident wave, $\bar{E}(r, t)$, substituting the solution ΔS (Eq. 2.6) into equation 2.4 we obtain the change of the dielectric constant $\Delta\epsilon$ that can be used in the perturbed equation 2.1 in order to calculate the Rayleigh scattering component. Then, solving this equation gives only one spectral component related to this effect. The line spectrum is not shifted in frequency and is only broadened by thermal dissipative process.

2.2.3 Brillouin scattering

In the Brillouin scattering process an optical pump causes excitation of molecules either from the ground state or from an excited state and their decays lead to Stokes (at longer wavelength than that of the pump) and anti-Stokes (at shorter wavelength than that of the pump) components [21]. For Brillouin scattering, the real excited states are due to bulk movements of the molecules.

Essentially, the scattering is produced by acoustic waves (acting as Bragg grating) propagating axially in the fiber (see Figure 2.2). These acoustic waves can be generated spontaneously by thermal excitation and in this case is known as **spontaneous Brillouin scattering**.

Referring to Eq. 2.4 of the previous section, we discussed that the first term is related to the isobaric density fluctuations responsible for the Rayleigh scattering, which line spectrum is not shifted in frequency and results broadened by thermal dissipative process. Instead, the second term corresponds to density fluctuations at constant entropy i.e. pressure wave or propagative wave (phonons), so the Brillouin scattering.

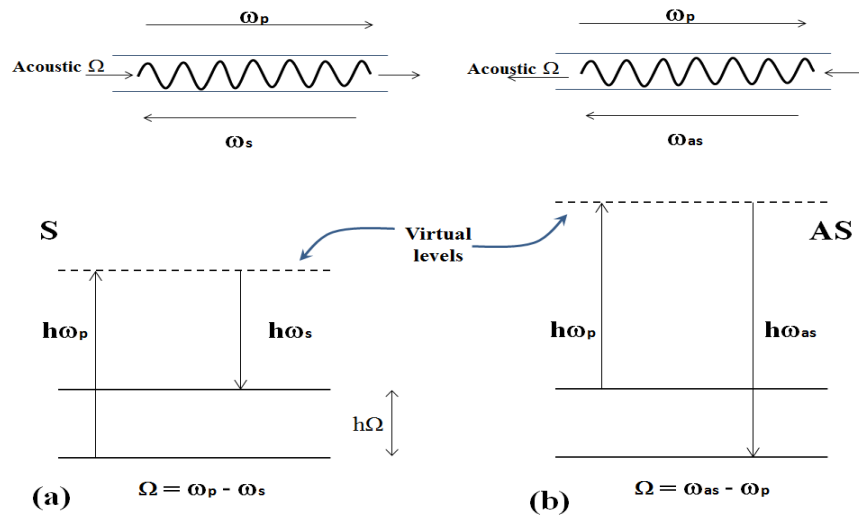


Figure 2.2. The Brillouin scattering components and mechanisms: Stokes (a) and anti-Stokes (b) signals [21].

Therefore, the Brillouin scattering can be described through the Equation 2.7 as:

$$\Delta\epsilon = \left(\frac{\partial\epsilon}{\partial\rho}\right) \left(\frac{\partial\rho}{\partial p}\right)_s \Delta p = \frac{\gamma_e}{\rho_0} \left(\frac{\partial\rho}{\partial p}\right)_s \Delta p \quad 2.7$$

where $\gamma_e = \rho_0 \left(\frac{\partial\epsilon}{\partial\rho}\right)$ is the electrostrictive constant and ρ_0 is the average density of the fiber material. The Brillouin scattering originating by Eq. 2.7 is shifted in frequency by a quantity proportional to the phonons number or sound wave speed, v_a . Two lines are observed (Stokes and anti-Stokes) because the scattering arises from waves propagating both in forward and backward directions at the same speed. Also in this case the lines are broadened by dissipative process.

From an acoustic point of view, a silica-based optical fiber can be considered as an isotropic homogenous fluid, viscous and compressible. Since the silica is compressible, pressure variation can occur. These variations result in pressure waves or acoustic waves. At the thermal equilibrium, the thermal phonons are the main source of pressure variation. This leads to small changes of the permittivity and therefore to local variation of the material density.

Propagation of the acoustic waves

In an optical fiber the scattering can occur from both the cladding and the core. If the acoustic and the optical mode do not significantly overlap, and this is the case of step index SMF, the Brillouin scattered light originating from the cladding is weak and so negligible. For a fixed propagation direction, there are three types of oscillation modes: those of longitudinal waves and those of the shear waves propagating in two different transversal directions. The light scattering has a certain angular distribution, but the OF geometry selects only two preferential directions, forward and backward, and therefore only the longitudinal acoustic oscillations are relevant in the Brillouin scattering. The acoustic wave is a pressure wave inducing local and periodic density variation, for this reason it can be represented by local variations $\Delta\rho(z,t)$ of the OF average density, ρ_0 :

$$\rho(z, t) = \rho_0 + \Delta\rho(z, t) \quad 2.8$$

where $\Delta\rho$ is expressed by the periodical function:

$$\Delta\rho(z, t) = \frac{1}{2} A(z, t) \cdot \exp[j(\Omega t - \bar{q}\bar{r})] + c. c. \quad 2.9$$

c.c. is the conjugate complex, Ω the angular frequency and \bar{q} the wave vector.

In presence of a monochromatic electromagnetic wave, $\bar{E}(r, t)$, propagating in the OF, the coupling of these optical and acoustic waves must be considered. Then, using Eq. 2.7 the electric polarization of Eq. 2.2 becomes:

$$\bar{P}_1(\bar{r}, t) = \Delta\epsilon\bar{E}(\bar{r}, t) = \frac{\gamma_e}{\rho_0} \Delta\rho(z, t)\bar{E}(\bar{r}, t) \quad 2.10$$

where the electromagnetic field is:

$$\bar{E}(\bar{r}, t) = \frac{1}{2} B(z, t) \cdot \exp[j(\omega t - \bar{k}\bar{r})] + c. c. \quad 2.11$$

\bar{k} is the wave vector of the incident light. The Eq. 2.10 can therefore be made explicit using the equations 2.9 and 2.11:

$$\bar{P}_1(\bar{r}, t) = B \frac{\gamma_e}{4\rho_0} \{ABe^{j[(\omega+\Omega)t - (\bar{k}+\bar{q})\bar{r}]} + A^*Be^{j[(\omega-\Omega)t - (\bar{k}+\bar{q})\bar{r}]}\} + c. c \quad 2.12$$

Finally, by inserting this equation in the Eq. 2.1 we derive the **wave equation describing the spontaneous Brillouin scattering**:

$$\nabla^2 \bar{E} - \frac{n^2}{c^2} \frac{\partial^2 \bar{E}}{\partial t^2} = \frac{\mu_0 \gamma_e}{4\rho_0} [(\omega + \Omega)^2 ABe^{j[(\omega+\Omega)t - (\bar{k}+\bar{q})\bar{r}]} + (\omega - \Omega)^2 A^*Be^{j[(\omega-\Omega)t - (\bar{k}+\bar{q})\bar{r}]}] + c. c. \quad 2.13$$

where \bar{E} is the Brillouin scattered wave field.

Ergo, because of the polarization of the medium in presence of acoustic waves, two new spectral components, downshifted (Stokes) and upshifted (anti-Stokes) are observed in the frequency domain. For the Stokes wave, we obtain the following angular frequency and momentum relationships:

$$\begin{aligned} \omega_s &= (\omega - \Omega) \\ \bar{k}_s &= (\bar{k} - \bar{q}) \end{aligned} \quad 2.14$$

And for the anti-Stokes wave:

$$\begin{aligned} \omega_{as} &= (\omega + \Omega) \\ \bar{k}_{as} &= (\bar{k} + \bar{q}) \end{aligned} \quad 2.15$$

The two relations in Eq. 2.14 and 2.15 are the energy and momentum conservations.

It is known that the dispersion relation between the wave vector and the angular frequency of a light wave is expressed by the refractive index [16]:

$$k = n(\omega) \frac{\omega}{c}, \quad k_s = n(\omega_s) \frac{\omega_s}{c}, \quad 2.16$$

whereas the dispersion for acoustic waves is $q = \Omega/v_a$.

The acoustic frequency is much smaller than the optical frequencies $\Omega \ll \omega, \omega_s$. Then, assuming the acoustic wave propagation in the positive direction +z of the optical axes and considering that \bar{k}_s and \bar{k} propagate in opposite directions, the momentum conservation of the anti-Stokes component imposes [14]:

$$\begin{aligned}
n(\omega_{as}) \frac{\omega_{as}}{c} &= -n(\omega) \frac{\omega}{c} + \frac{\Omega}{v_a} = n(\omega + \Omega) \frac{\omega + \Omega}{c} \\
&\cong n(\omega) \frac{\omega}{c} + \frac{\Omega}{c} \frac{d[n(\omega)\omega]}{d\omega} \cong n(\omega) \frac{\omega}{c} + \frac{\Omega}{c} n_g(\omega)
\end{aligned} \tag{2.17}$$

where $n_g(\omega) \cong \frac{d[n(\omega)\omega]}{d\omega}$ is the group refractive index. Let solve for the Brillouin frequency Ω :

$$\begin{aligned}
\Omega &\cong \frac{2n(\omega)\omega}{c/v_a - n_g(\omega)} \approx 2n(\omega) \frac{v_a}{c} + 2n(\omega)n_g(\omega)\omega \left(\frac{v_a}{c}\right)^2 \\
&= \frac{4\pi}{\lambda} n(\omega)v_a \left(1 + n_g(\omega) \frac{v_a}{c}\right)
\end{aligned} \tag{2.18}$$

We observe that to the first order of $\frac{v_a}{c}$, the Brillouin frequency for the anti-Stokes component is proportional to the acoustic speed and to the local phase refractive index, whereas it is inversely proportional to the incident wavelength λ . However, at the first order the Brillouin frequency shift for the Stokes and anti-Stokes component remains the same in absolute value, while the directions of propagation of the acoustic waves related to the two processes lead to Stokes down-shift $\nu_s = \nu - \nu_B$ and anti-Stokes up-shift $\nu_{as} = \nu + \nu_B$.

Fiber sensors based on Brillouin scattering do not take into account the second order effect and use the fact that the Brillouin frequency is proportional to the material's local thermodynamic properties such as sound velocity and phase refractive index (see the following Eq. 2.19), two quantities which in turn depend on local temperature and strain.

$$\nu_B = \frac{2}{\lambda} n v_a \tag{2.19}$$

To summarize:

In the *spontaneous regime* the Brillouin scattering is a linear phenomenon since the intensity of the incident light has no effect on this optical signature of the material. It is attributed to the presence of inhomogeneities in the medium and so to density fluctuation caused by propagative phonons.

Stimulated Brillouin Scattering (SBS)

As discussed in section 2.2, the efficiency of the spontaneous Brillouin scattering is very small if compared to the one of the Rayleigh scattering. If the fluctuations in the medium are stimulated by the presence of another electromagnetic wave the spontaneous scattering is reinforced. When this happens the resulting scattering process is called *stimulated* [15]. It is a nonlinear phenomenon since the high-power light can drive the generation of propagative phonons and is capable of modifying the optical properties of the material medium. The stimulated scattering process is observed when the light intensity reaches a range between 10^6 and 10^9 Wcm^{-2} [15].

The main origin of the Stimulated Brillouin Scattering (SBS) is a physical phenomenon called **electrostriction**, which is the tendency of materials to be compressed in presence of an electric field. Indeed, in presence of an inhomogeneous electric field, the dipole moment (\vec{p}) of each molecule in the material undergoes a translation force $\vec{F} = \nabla(\vec{p} \cdot \vec{E})$ and therefore an internal pressure, called electrostrictive pressure p_{st} and given by $p_{st} = -\frac{1}{2}\gamma_e\langle|\vec{E}|^2\rangle$, where γ_e is the electrostrictive constant. Since p_{st} is negative, in the zones of intense electric field the total pressure is reduced. This results in the natural transfer of the molecules inducing fluctuations in the material density [20]. Therefore, at a particular high level of the power pump (incident light), the source of phonons is no longer only the thermal noise, but there is also the electrostriction process caused by the incident light itself.

The stimulated process can originate by two different ways. If the back-scattered Stokes wave (called signal wave) is enhanced starting by the spontaneous scattering, we have a Brillouin generator. Instead, if the back-propagating signal wave is external injected into the fiber, we have a Brillouin amplifier. Consequently, in addition to the pump signal, a continuous wave (CW), the so-called probe signal, is used to investigate the Brillouin frequency profile [22]. The stimulation of the Brillouin scattering process occurs when the frequency difference between the pump and the CW signal corresponds to the Brillouin shift. The interaction leads to a larger scattering efficiency, resulting in an energy transfer from the pulse to the probe signal with its amplification [15], [22]. Both spontaneous and stimulated Brillouin scattering processes are schematically illustrated in Figure 2.3 [23].

It is worth to highlight that while in the spontaneous Brillouin scattering the backscattered power signals of the two components, Stokes and anti-Stokes, are small but comparable, in stimulated regime the Stokes component becomes dominant, overcoming even the Rayleigh power signal. Indeed, from a quantum point of view: in the case of the Stokes process, a pump photon is annihilated to generate a Stokes photon and a propagative phonon, increasing quickly their number, and hence intensifying the Stokes process already present in the OF.

On the other hand, concerning the anti-Stokes process, a pump photon and a propagative phonon are annihilated to produce an anti-Stokes photon, thus decreasing the phonons number which leads to the disappearance of the acoustic wave and the decrease of the anti-Stokes process efficiency [22].

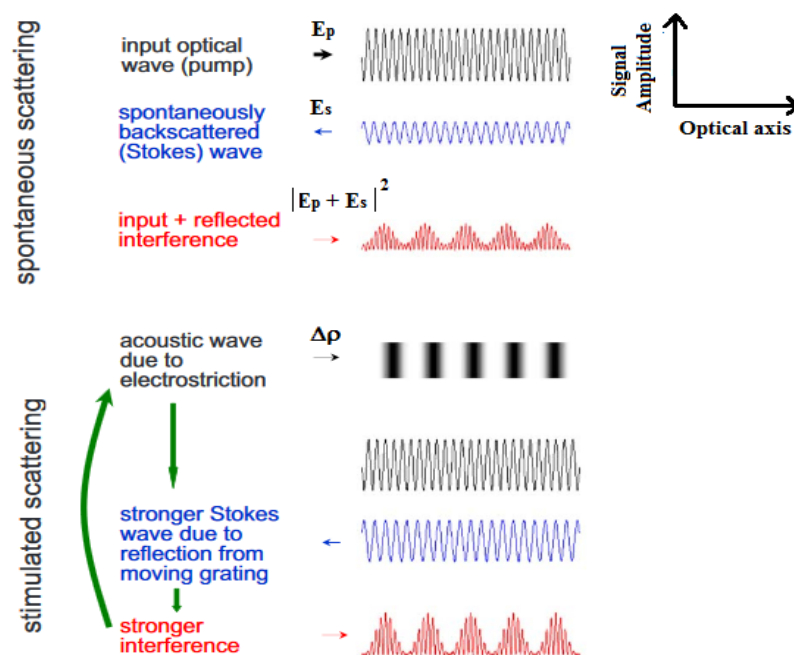


Figure 2.3. Spontaneous (top) and stimulated (bottom) Brillouin scatterings. The Stokes wave (blue), spontaneously backscattered from acoustic wave, interferes with the pump wave (black). The interference pattern is shown in red. The amplitude of the acoustic wave is proportional to the optical intensity. The acoustic wave generated as a result of electrostriction further stimulates back-scattering, which in turn enhances the interference between the pump and the Stokes waves and reinforces the acoustic wave. Figure rearranged from [23].

Therefore, Stokes scattering creates phonons, while anti-Stokes scattering annihilates phonons. In SBS the energy exchange of the photon with medium is made from the higher frequencies to lower ones; thus stimulated Brillouin scattering is never an anti-Stokes process.

Brief theoretical description of the SBS

The stimulated Brillouin interaction in single mode fibers can be described by the coupled-
2.2.4.1
wave transient equations for the pump, $\bar{E}_p(z, t)$ and Stokes $\bar{E}_s(z, t)$ waves with the field amplitudes ($\bar{E}_p + \bar{E}_s$) interacting with the acoustic wave $\Delta\rho(z, t)$ (at time t and position z along the fiber) [16]:

$$\nabla^2 \bar{E}_p - \frac{n^2}{c^2} \frac{\partial^2 \bar{E}_p}{\partial t^2} = \mu_0 \frac{\partial^2 \bar{P}_p^{NL}}{\partial t^2} \quad 2.20$$

$$\nabla^2 \bar{E}_s - \frac{n^2}{c^2} \frac{\partial^2 \bar{E}_s}{\partial t^2} = \mu_0 \frac{\partial^2 \bar{P}_s^{NL}}{\partial t^2} \quad 2.21$$

$$\frac{\partial^2 \Delta\rho}{\partial t^2} - 2\Gamma_B \frac{\partial \Delta\rho}{\partial t} - v_a^2 \nabla^2 \Delta\rho = -\nabla \cdot \bar{f} \quad 2.22$$

where $\Gamma_B = \Gamma_1 + i \Gamma_2$ is the damping constant of the acoustic wave, Γ_1 is the damping time of the phonon field $\Gamma_1 = 1/2\tau_{ph}$ with $\tau_{ph} \sim 10ns$ for silica fiber, and Γ_2 is the detuning angular frequency. \bar{f} is the electrostrictive force per unit volume, $\bar{f} = -\nabla p_{st} = -\frac{1}{2}\gamma_e \nabla \langle |\bar{E}|^2 \rangle$.

Solving the set of equations 2.20 to 2.22 in steady-state approximation we obtain the intensity equation describing the SBS interaction between two counter propagating laser beams (pump and signal waves) [16]:

$$\frac{dI_p}{dz} = -g_B(\nu) I_p I_s - \alpha I_p \quad 2.23 \text{ a}$$

$$\frac{dI_s}{dz} = -g_B(\nu) I_p I_s + \alpha I_s \quad 2.23 \text{ b}$$

Where α is the fiber attenuation coefficient (see section 3.1) and the Brillouin gain spectrum (BGS) is given by:

$$g_B(\nu) = g_0 \frac{(\Delta\nu_B/2)^2}{(\nu - \nu_B)^2 + (\Delta\nu_B/2)^2} \quad 2.24$$

where $\Delta\nu_B$ indicates the natural linewidth of the Brillouin gain, $g_0 = \frac{2\pi n^7 p_{12}^2}{c_0 \lambda_p^2 \rho_0 v_a \Delta\nu_B}$ is the center frequency gain coefficient (p_{12} is the elasto-optic coefficient) [22]. The Full Width Half Maximum (FWHM), measured in Hertz, is given by $\Delta\nu_B = 1/2\pi\tau_{ph}$.

Brillouin gain spectrum shape

2.2.4.2 The steady-state approximation is valid for pulses larger than the phonon lifetime, ~ 10 ns, which is equivalent to a spatial resolution > 1 m. In particular, for long probe pulses > 50 ns, the recorded spectra correspond to a Lorentzian profile of the Brillouin gain (Eq. 2.24) [24], [25]. Although, shorter (nanosecond) probe pulses increase the spatial resolution, they lead to the broadening of the Brillouin spectrum (at 10 ns the effective BGS width is 2 times the natural Brillouin linewidth [26]) and then reduces the strain or temperature measurement accuracy. The broadening is induced by the wide spectrum of the pulse, so the effective BGS experienced by the signal wave is given by the convolution between the original BGS, $g_B(\nu)$, and the spectrum of the pump pulse $f(\nu)$ [27]. As the line-shapes gradually change, the spectra are fitted to the pseudo-Voigt profile, with contributions of Lorentzian and Gaussian distributions. However, it was found that reducing the pulse duration to values smaller than the acoustic relaxation time entails a sudden decrease of the spectral width. This decrease is due to the combination of a reduction of the gain for very short pulses and the presence of an acoustic wave before the pulse passage.

The intensity, and therefore the influence, of this steady acoustic wave results inversely proportional to the extinction ratio of the electro-optic modulator (EOM) used to generate the pulses. For a given extinction ratio, the Brillouin gain (or loss) curve first broadens as the pulse duration is reduced. But shortening of the pulses is accompanied by a gain decrease, the acoustic wave created by the pulses can become of the same order of magnitude than the steady acoustic wave that is present before the pulse's arrival. Eventually, the recorded Brillouin spectrum reproduces the same features as the steady-state interaction, i.e., a Lorentzian profile [24]. The BGS spectrum, its signal and width have been deeply studied in [24], [25], [27], their evolutions as a function of the pulse duration and width are illustrated in Figure 2.4.

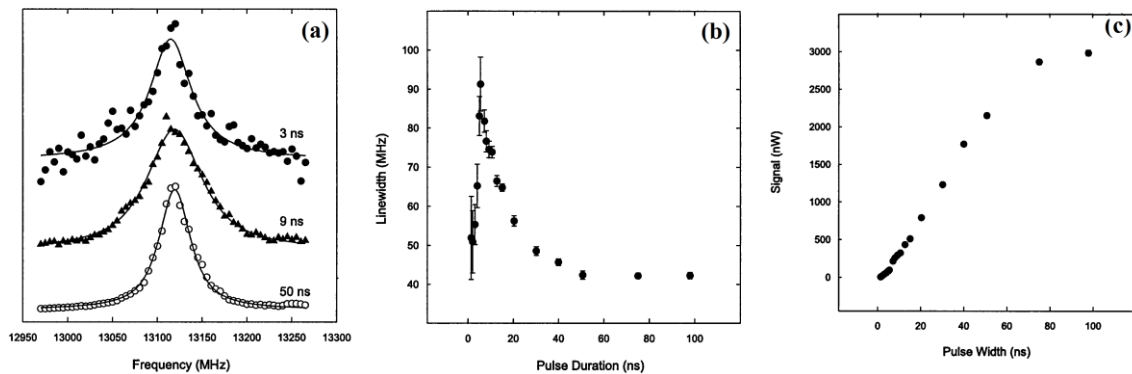


Figure 2.4. BGS for pulse durations of 50, 9 and 3 ns (a). Brillouin linewidth as a function of pulse duration (b). Peak Brillouin gain as a function of pulse duration (c) [25]. Estimated extinction ratio of ~30 dB [24].

Raman scattering

2.2.5

Raman scattering originates from the interaction of light with the localized vibrational modes of the molecules constituting the matrix-material. In the first step, a photon of energy $\hbar\omega_0$ excites the system from a vibronic state α to a virtual state f ; in the second step, the excited molecule emits a photon of energy $\hbar\omega$ and is de-excited from the virtual state f to a final vibronic state b . If the final state b of the system is the same as the initial state α , the resulting photon has the same frequency as the incident radiation (Rayleigh scattering); on the contrary if the final state b differs from the initial state, the scattering is inelastic and the Raman scattering occurs. In the spontaneous scattering, for each molecular vibration, the scattered wave contains energies different from those of the excitation source ($\hbar\omega_0$), Stokes ($\hbar\omega_s$) and anti-Stokes ($\hbar\omega_{as}$) lines. These processes are schematically shown in Figure 2.5, where the Stokes and anti-Stokes radiations are, for example, originating from the processes: ground vibronic state (of energy (E1) \Rightarrow virtual state (E3) \Rightarrow first excited vibronic state (E2) and first excited vibronic state (E2) \Rightarrow virtual state (E4) \Rightarrow ground vibronic state (E1), respectively. The anti-Stokes lines are less intense than the Stokes lines since usually the ground vibronic state is more populated than states with higher energy, as a natural consequence of the Bose-Einstein distribution.

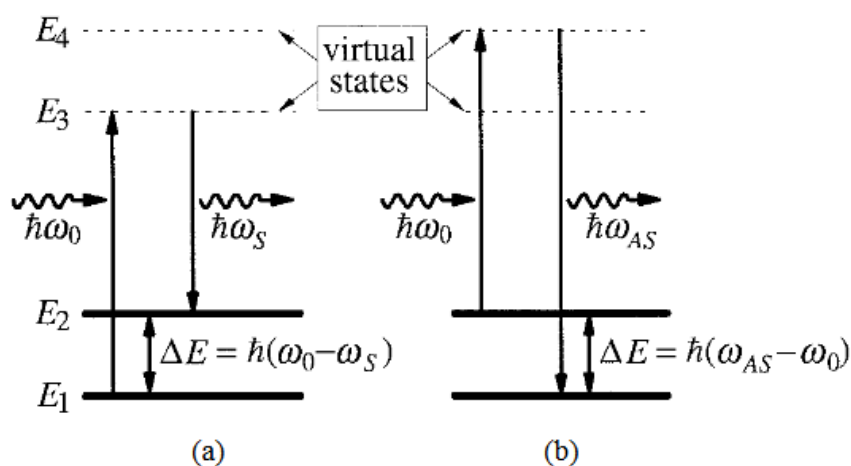


Figure 2.5. Energy levels scheme in which the Raman Stokes and anti-Stokes transitions are depicted.

2.2.5.1 Brief Raman scattering theoretical description

In this section the origin of the Raman scattering process is explained by using a classical approach [28], [29], [30]. If a molecule is located in an electric field \vec{E} , a dipole moment, \vec{p}_{ind} , is induced in the molecule since the forces ($\vec{F} = q\vec{E}$, where q is the charge) acting on nuclei and electrons are directed in opposite directions. The induced dipole is approximately proportional to the force by the factor α , commonly called polarizability: $\vec{p}_{ind} = \alpha\vec{E}$. The polarizability represents the facility with which the electron cloud around a molecule can be distorted. If the molecule is in an electromagnetic field whose electric field oscillates at the frequency ω_0 , the induced dipole momentum of the molecule results:

$$\vec{p}_{ind} = \alpha E_0 \cos(\omega_0 t) \quad 2.25$$

where E_0 is the electric field amplitude value.

If the polarizability is constant, \vec{p}_{ind} should oscillate at the same frequency ω_0 of the electric field. Nevertheless, the molecules oscillate at the frequencies associated with their normal vibrational modes impacting the dipole momentum through, for example, the polarizability. In order to simplify the calculation, we treat the case of a diatomic molecule that is

characterized by only the stretching vibration mode. We noted ω_m the angular frequency of this vibration mode and Q the normal coordinate, therefore the time evolution of Q can be written as follow:

$$Q(z, t) = Q_0 \cos(\omega_m t + \phi) \quad 2.26$$

where Q_0 is the amplitude value of the normal coordinate and ϕ is the phase. For vibration of small amplitude the polarizability of a single molecule can be approximated by the expansion up to first order in Q around $Q = 0$:

$$\alpha \sim \alpha_0 + \left(\frac{\partial \alpha}{\partial Q} \right)_{Q=0} Q \quad 2.27$$

Where α_0 and $\partial \alpha / \partial Q$ are the polarizability and the rate of change of α with respect to the change of Q valued around the equilibrium position $Q = 0$. Therefore, the electric dipole moment induced in a molecule can be calculated by the equations 2.25, 2.26, 2.27 [28], [29]:

$$\begin{aligned} \bar{p}_{ind} &= \alpha_0 E_0 \cos(\omega_0 t) + \left(\frac{\partial \alpha}{\partial Q} \right)_{Q=0} Q_0 E_0 \cos(\omega_m t + \phi) \cos(\omega_0 t) = \\ &= \alpha_0 E_0 \cos(\omega_0 t) + \frac{Q_0 E_0}{2} \left(\frac{\partial \alpha}{\partial Q} \right)_{Q=0} \{ \cos[(\omega_0 - \omega_m)t + \phi] + \\ &+ \cos[(\omega_0 + \omega_m)t + \phi] \} \end{aligned} \quad 2.28$$

Therefore, beside the Rayleigh scattered wave characterized by the angular frequency ω_0 , the dipole moment radiates electromagnetic waves at frequencies $(\omega_0 - \omega_m)$ and $(\omega_0 + \omega_m)$, corresponding to the Stokes and anti-Stokes Raman components, respectively. The Raman scattering is due to a molecular vibration which can change the polarizability. Ergo, the polarizability changes during the vibration are *necessary and sufficient* in order to have the Raman scattering and the selection rule for a Raman-active vibration is expressed as:

$$\left(\frac{\partial \alpha}{\partial Q} \right)_{Q=0} \neq 0 \quad 2.29$$

Raman scattering in Multimode Fiber

From the electrodynamic theory it is known that for a single molecule, the power per unit of solid angle Ω radiated from an oscillating electric dipole moment is proportional to the square of the dipole moment \bar{p}_j and to ω_j^4 [31]:

$$\frac{dP_{j,mol}}{d\Omega} = \frac{n\omega_j^4}{32\pi\epsilon_0c^3} |\bar{p}_j|^2 \sin^2(\theta) \quad 2.30$$

where θ is the angle between the direction of \bar{p}_j and the direction along which the light is emitted, n is the refractive index of the material and ϵ_0 the dielectric constant in the vacuum. \bar{p}_j is the oscillating dipole moment of a molecular dipole, which emits the Stokes wave of angular frequency ω_j , where the index j can indicate the Stokes (S), anti-Stokes (AS) or Rayleigh (R) components.

An important parameter characterizing the Raman scattering is the cross section which expresses the Raman scattering efficiency and is defined as the ratio between the scattered power and the incident pump power. It is given by:

$$\sigma \propto \omega_j^4 \frac{n_0}{n_j} \left(\frac{\partial \alpha}{\partial Q} \right)_{Q=0}^2 Q_0^2 \quad 2.31$$

where n_0 and n_j are the refractive indexes at the pump and scattered wavelengths. The cross section depends not only on frequency as ω^4 , but also by $\frac{\partial \alpha}{\partial Q}$. This underlines the central importance of the condition of a non-zero polarizability change along the normal coordinate. Moreover, it is worth highlighting that the Raman cross section depends on the different mode distributions of the molecule inside the fiber and therefore on the fiber structure, i.e. step index, graded index, MMF or SMF [31].

Let us assume that the wave propagation in a MMF can be described by classic geometric optics. From equation 2.30 the total Stokes and anti-Stokes powers backscattered from the molecules contained in a volume Adz of the fiber are acquired and expressed as:

$$\text{Stokes} \quad dP_S = \mathcal{P}_S \Gamma_S P_0 dz \quad 2.32 \text{ a}$$

$$\text{anti-Stokes} \quad dP_{as} = \mathcal{P}_{as} \Gamma_{as} P_0 dz \quad 2.32 b$$

with $P_0 = AI_0$ is the power of the incident light at the considered location in the fiber. Γ_S and Γ_{as} are the Stokes and anti-Stokes Raman capture coefficients depending on the respective differential Raman cross-sections and by the fiber type employed such as SMF, SI-MMF and GI-MMF [31]. \mathcal{P}_S and \mathcal{P}_{as} are given by the Bose-Einstein probability distribution of phonons:

$$\text{Stokes} \quad \mathcal{P}_S = \frac{1}{1 - \exp\left(-\frac{h\Delta\nu_R}{k_B T}\right)} \quad 2.33 a$$

$$\text{Anti-Stokes} \quad \mathcal{P}_{as} = \frac{\exp\left(-\frac{h\Delta\nu_R}{k_B T}\right)}{1 - \exp\left(-\frac{h\Delta\nu_R}{k_B T}\right)} \quad 2.33 b$$

where k_B is the Boltzmann's constant, h is the plank constant, T the absolute temperature and $\Delta\nu_R$ is the Raman shift, i.e. the frequency of the created or annihilated phonon in the Raman scattering. The frequency shift generated by SiO_2 and GeO_2 molecules of the fiber is quite similar. The Raman spectrum shows a maximum intensity for the vitreous silica around $\Delta\nu_R^{\text{SiO}_2} \cong 13.2 \text{ THz}$ (i.e. 440 cm^{-1}) and for the vitreous germania around $\Delta\nu_R^{\text{GeO}_2} \cong 12.6 \text{ THz}$ (i.e. 420 cm^{-1}) [32].

Since the backscattered signal is dominated by the exponential dependence of the optical transmission through the fiber, characteristic for the three light waves, pump, Stokes and anti-Stokes, the powers of the S and AS signals measured in a point z of the fiber can be expressed by [33], [34]:

$$P_S(z, T) = C_S \exp\left(-\int_0^z (\alpha_0(z') + \alpha_S(z')) dz'\right) * \frac{1}{1 - \exp\left(-\frac{h\Delta\nu_R}{k_B T}\right)} \quad 2.34 a$$

$$P_{aS}(z, T) = C_{aS} \exp \left(- \int_0^z (\alpha_0(z') + \alpha_{aS}(z')) dz' \right) * \frac{\exp \left(- \frac{h\Delta\nu_R}{k_B T(z)} \right)}{1 - \exp \left(- \frac{h\Delta\nu_R}{k_B T} \right)} \quad 2.34 \text{ b}$$

where the attenuation coefficient $\alpha_j(z)$ (subscript 0, S and AS) includes all local fiber losses, such as absorption, splices, connectors and bending losses and the constant parameter C_S and C_{aS} account for the incident pump power, P_0 , and the respective S and AS Raman cross sections depending on the transmission characteristic of the optical receiver.

2.3 DOFSs of strain and temperature

In this section we shall use some of the previously described relationships to compare the potentials of the various physical effects by which pressure, strain and temperature may be measured with DOFSs. At the end of this section Table 2.1 reports the best claimed performances of commercial Rayleigh, Brillouin and Raman scattering based sensors here described.

2.3.1 Rayleigh scattering based optical frequency domain reflectometer (OFDR)

The most advantageous Rayleigh-based distributed temperature and strain sensor, in terms of spatial resolution (millimeter scale) is the one working in the coherent optical frequency domain scheme: the OFDR (Optical Frequency Domain Reflectometry). Although Rayleigh scattering itself is independent of temperature and strain as shown in section 2.2.2, temperature, strain and pressure changes induce variations of the refractive index that can be measured by OFDR. The principle of this technique is based on swept-wavelength interferometry (SWI): light from a tunable laser source (TLS) is split between a static reference and measurement arms of an interferometer and recombined at an optical detector. Interference fringes are generated as the laser frequency is tuned. Those fringes are detected and related to the optical amplitude and phase response of the fiber under test (FUT). The interference fringes, occurring in the spectral domain of the FUT and the Fourier transform is performed to obtain the Rayleigh signature as a function of the fiber length [35]. Therefore,

the strain or temperature sensor using the OFDR approach is based on the response of Rayleigh scattering signature of the FUT in both unperturbed (reference) and perturbed states. The scatter profiles from the two data sets are then cross correlated along the perturbed portion of the single mode fiber (SMF) to obtain the spectral shift in this part of the fiber due to a temperature or strain change [36]. The found spectral shift is then a measurement of the relative change in optical fiber obtained from applied perturbation and it does not give an absolute value of the perturbation. Indeed, the strain and temperature dependence of the Rayleigh spectral shift is described by:

$$\frac{\Delta\lambda_0}{\lambda_0} = -\frac{\Delta\nu_0}{\nu_0} = C'_T\Delta T + C'_\varepsilon\varepsilon \quad 2.35$$

where λ_0 and ν_0 are the incident optical wavelength and frequency respectively and C_T and C_ε are thermal and strain reduced coefficients and are characteristics of the optical fiber type, mainly of its core composition. [35].

2.3.2 Brillouin distributed T and strain sensor (B-DSTS)

As discussed in section 2.2.3, the Brillouin spectrum is peaking at a frequency shifted from the pump by a quantity equal to $\nu_B = \frac{2}{\lambda}n\nu_a$ (Eq. 2.19). So, the Brillouin frequency shift (BFS) depends on the acoustic speed and any change of this velocity will be observed as a spectral shift of the resonance. In the theory of elasticity the acoustic wave speed is related to the medium density, ρ , through the relation:

$$\nu_a = \sqrt{\left.\frac{\partial p}{\partial \rho}\right|_s} = \sqrt{\frac{K}{\rho}} \quad 2.36$$

where $K = 1/\mathcal{X}$ is the bulk modulus and \mathcal{X} the material compressibility. The density of the material is temperature dependent as results of the thermal expansion. Moreover, any deformation experienced by the fiber will also impact ρ . The first work dealing directly with strain sensing based on Brillouin scattering was carried out in 1989 [37]. The BFS was found

to linearly depend on the applied strain. In the same year, the BFS was also found to be linearly dependent on temperature [38].

Consequently, the evolution of BFS follows the equation 2.38:

$$v_B(T, \varepsilon) - v_{B_0}(T_0, \varepsilon = 0) = C_\varepsilon \varepsilon + C_T \Delta T \quad 2.37$$

where C_ε is the strain coefficient in units of MHz/ $\mu\varepsilon$, C_T is the thermal coefficient in units of MHz/ $^\circ\text{C}$, ΔT is the temperature variation, ε is the applied strain and v_{B_0} is the Brillouin frequency response measured at room temperature T_0 (reference temperature) without strain. These coefficients depend on the optical fiber type, mainly on its core composition, and also on the pump wavelength, fiber elaboration parameters such as coating and drawing conditions. Typical values of these coefficients for Telecom-grade germanosilicate SMFs such as SMF28 are $C_\varepsilon=0.056$ MHz/ $\mu\varepsilon$ and $C_T=1.26$ MHz/ $^\circ\text{C}$ [17]. Hence, the sensor requires a preliminary temperature and strain characterization of its sensing fiber to determinate the two coefficients. An example of such calibration curves for a standard single mode fiber is shown in Figure 2.6 [15].

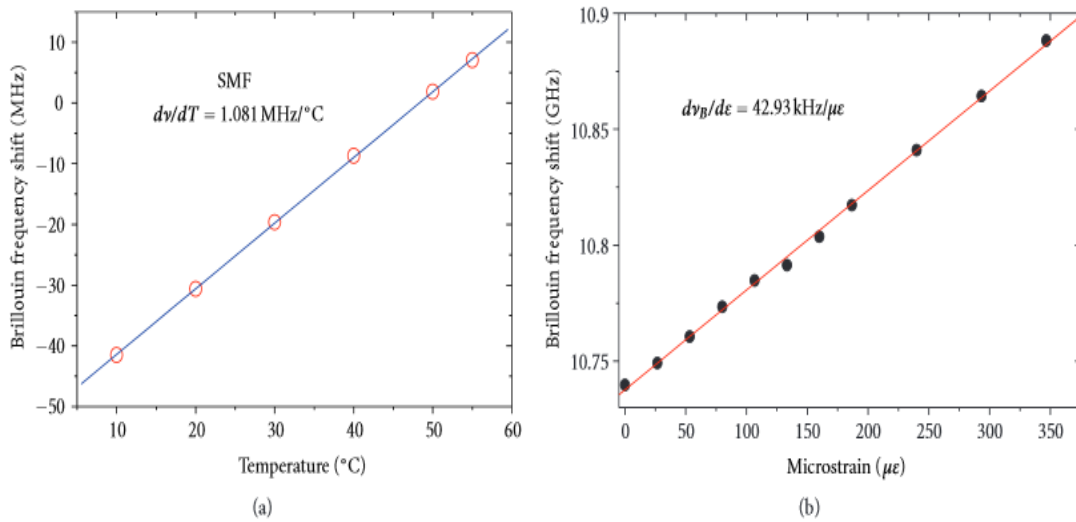


Figure 2.6 Experimental data of BFS dependence on the temperature (a) and strain (b) [15].

The Brillouin shift process can be accurately localized along the OF, by time domain or frequency correlation technique, among others. Hence, the Brillouin scattering of light in optical fiber can be used as a basis to realize accurate DSTSs working in different domains.

Common fully distributed optical fiber sensing techniques are based on optical time domain reflectometer (OTDR) [39]. The Brillouin optical time domain reflectometer (BOTDR) and the Brillouin optical time domain analyzer (BOTDA) are in this category.

The BOTDR is based on the spontaneous Brillouin scattering. A pulse light generates the backscattering wave which is measured with a coherent receiver by mixing the scattering signal with that from a local oscillator. The shift is then determined by scanning, step by step, the frequency and recording the signal as a function of the time. Then, the frequency spectrum of the backscattered signal can be reconstructed at each position by recording at each time the amplitude as a function of the frequency. A spatial resolution of 1 m over 10 km range was obtained with this system [19], [40], [41]. However, because of the weakness of the Brillouin spontaneous backscattered power (its efficiency is approximately 20 dB weaker than that of Rayleigh scattering [26], [27]), the fiber attenuation can negatively affect the quality of the measurement, strongly reducing the possible sensing range. Therefore, this sensor is not suitable for applications in which the fiber transmission can be degraded by the severe environment conditions, such as that of our application.

The BOTDA is the technique used in this PhD thesis work. It is based on the stimulated Brillouin scattering using two counter propagating signals: a pulse optical wave and a probe wave (CW). The working principle was explained in section 2.2.4: the two waves are injected into the optical fiber and when the frequency difference between the pulsed and the continuous light is tuned to the Brillouin frequency of the fiber, the CW is continuously amplified and recorded as a function of the time, like with the OTDR. The scheme of a typical BOTDA system is reported in section 4.2.2 of Chapter 4. Differently from the BOTDR, the gathered signal using this technique is strong, even higher than the Rayleigh backscattering power; e.g. for continuous light power of around 0.1 mW the Brillouin backscattered signal can be a hundred times higher than the Rayleigh one [26]. Moreover, better spatial resolution of centimeter can be reached (see Table 2.1).

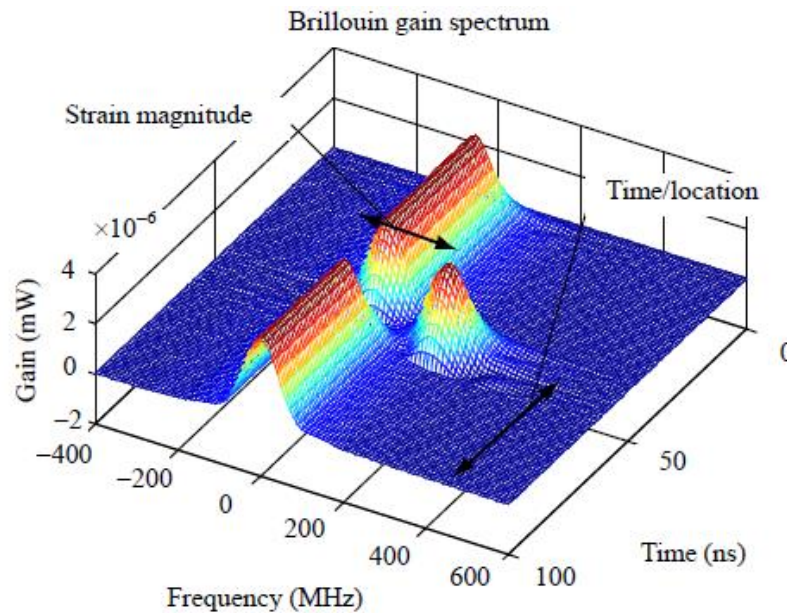


Figure 2.7. Brillouin gain spectrum obtained by a BOTDA sensor [131].

The measurement time required by typical BOTDA devices is on the order of minutes and depends on the total distance range. This could be a drawback for this technique in some applications such as the health monitoring structures, requiring long fiber length. An example of the Brillouin gain spectrum of the BOTDA is reported Figure 2.7.

Another distributed optical fiber sensing technique used to acquire the Brillouin scattering signal is working on the optical frequency domain. The Brillouin optical frequency domain analyzer (BOFDA) fits this category. The BOFDA is a technique based on the measurement of a complex base-band transfer function (BBTF) by the ratio of the Fourier transform of the two counter-propagating pump and probe waves (CW) along the fiber length [42]. The probe CW is modulated in intensity with a sinusoidal signal over a range of frequencies, whereas the pump wave is modulated in intensity. This induced signal has an alternating component (AC component/part) due to the interaction with the counter-propagating probe wave. By measuring the changes in the AC pump wave component the Brillouin frequency shift profile is determined via the complex BBTF. Once the BBTF is determined, applying the inverse Fourier transform to the function, the temporal pulse response is obtained. Thus the temperature or strain can be determined from the Brillouin profile along the fiber converting the pulse response to a spatial response by using the

relationship $t=2nz/c$, where c is the vacuum light speed, n the fiber refractive index and z indicates the position along the fiber [42]. Nowadays, great effort has been given with this technology to improve its spatial resolution, indeed 3 cm has been demonstrated on 9 m sensing length and with a resolution for the Brillouin frequency of 1.8 MHz [17]. However, although this technique offers the possibility of narrow-band operation and hence improvements in the signal-to-noise ratio (SNR), the measurement time using BOFDA technique exceeds those of BOTDA, since it requires many measurements at different frequencies to obtain the transfer function with an acceptable spatial resolution [19]. For this reason, the BOFDA architecture was not selected for our study.

Raman distributed temperature sensor (RDTS)

2.3.3

The Raman distributed temperature sensor (RDTS) operates as a transducer converting temperature changes into optical power intensity variations. Through the flight time of the probe pulse the interrogator derives the location along the multimode fiber using an optical time domain reflectometry principle (see Chapter 4). A high power probe laser launches a pulsed optical signal in the optical fiber, at 1064 nm in our case. Only a small fraction of the probing power is transferred to frequencies downshifted (Stokes) or upshifted (anti-Stokes) and is spontaneously Raman backscattered to the fiber input (the Raman intensity is typically 30 dB lower than the Rayleigh one) [43]. Because of its small scattering efficiency the RDTS usually uses MMFs as the sensing element, as they have higher scattering cross section (and then Γ_j) than SMF ones.

As highlighted by equations 2.34 (a) and 2.34 (b), the Stokes and anti-Stokes temperature-dependencies differ. The RDTS system usually evaluates the temperature by calculating the ratio between the two backscattered Raman components, anti-Stokes (AS) and Stokes (S), detected at one end of the fiber.

The normalization of the AS intensity by the Stokes one is calculated by the following equation:

$$R(T, z) = \frac{P_{aS}}{P_S} = C_R \exp\left(-\int_0^z (\alpha_{aS}(z') - \alpha_S(z')) dz'\right) * \exp\left(-\frac{h\Delta\nu_R}{k_B T}\right) \quad 2.38$$

where $C_R = \frac{c_{aS}}{c_S} \propto \left(\frac{\lambda_S}{\lambda_{aS}}\right)^4$. Although the ratio $R(z)$ of the two backscattered Raman components results independent on the incident power pump P_0 , it depends on the differential attenuation, $\Delta\alpha = (\alpha_{aS} - \alpha_S)$, between the anti-Stokes and Stokes waves owing to their wavelength difference which ranges from 100 nm to 200 nm and depends on the wavelength of pump light source [34].

Commonly, commercial RDTS devices make the assumption that $\Delta\alpha$ is uniform along the length of the fiber, i.e. $\alpha_{aS}(z') \approx \alpha_S(z')$, and/or constant with time and therefore can be characterized as a function of the distance [43]. Consequently, the equation 2.38 results independent from this differential attenuation:

$$R(T, z) = C_R \exp\left(-\frac{h\Delta\nu_R}{k_B T(z)}\right) \quad 2.39$$

where the term C_R accounts for the differences in effective detector sensitivities with respect to Stokes and anti-Stokes, which can vary in time. Time change in $C(t)$ may be caused by thermal sensitivity of the detector as well as thermal variation in the alignment of the optical system [44]. Since its value is unknown and can differ from fiber to fiber, in order to obtain an accurate temperature evaluation along the fiber a calibration of the sensor is mandatory. Assuming C_R constant, if $R_0(T_0, z)$ is the reference ratio obtained by a measurement performed at a known temperature T_0 , through $R(T, z)/R_0(T_0, z)$ it is possible to estimate the temperature from:

$$T(z) = \left[\frac{1}{T_0(z)} - \frac{k_B}{h\Delta\nu_R} \ln\left(\frac{R(T, z)}{R_0(T_0, z)}\right) \right]^{-1} \quad 2.40$$

However, this assumption is inappropriate when the fiber is implemented inside an environment where its transmission is likely to be degraded. In such cases, the $\Delta\alpha$ evolves with time and/or can be not uniform along the fiber length. As a consequence the $R(T, z)$

measured at $z=0$ is differs from the one detected at a given point z of the fiber where one wants to monitor the temperature [44]. This leads the device to badly evaluate temperature. Experimental evidence of such error source will be shown in the next chapters, where we will discuss our experimental results obtained in conditions for which the fiber losses are significantly changed by environmental constraints.

During the past years, some correction methods have been proposed in order to overcome this error source [44], [45], [46], [47]. The most common way employs the **dual-ended configuration** (DE-RDTS) which allows for the automatic correction of the measurement by separating temperature modulations from fiber attenuation effects. An illustration of the DE-principle is reported in Figure 2.8. In this configuration both ends of the sensing fiber need to be connected to the RDTS system to compensate for the differential attenuation [43], [44], [47]. In such loop arrangement the laser source switches between the two RDTS channels of the system sending alternatively pump pulses into the fiber from both ends. In case of non-uniform $\Delta\alpha$ along the fiber under test, if the geometric mean of the two ratios measured in the forward (starting at $z=0$) and backward (starting at $z=L$) directions is taken, then the optical loss effects can be corrected.

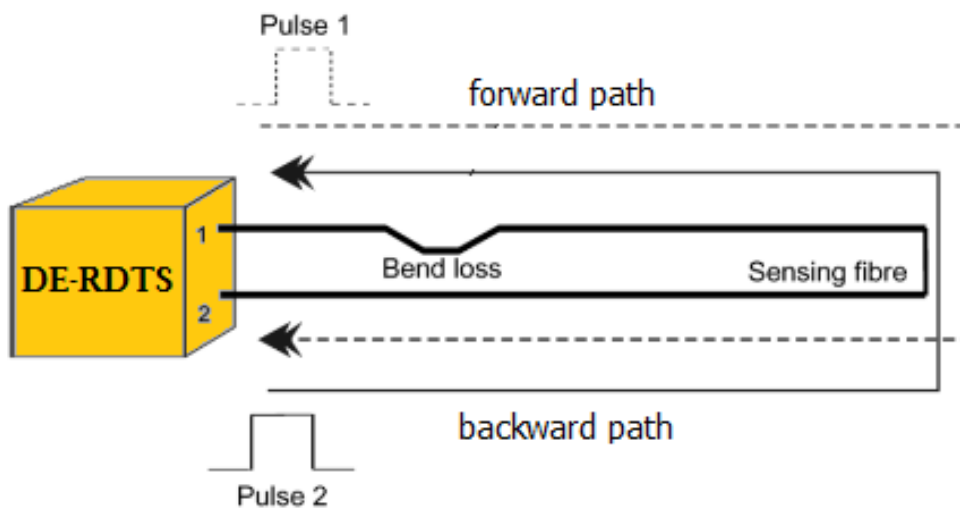


Figure 2.8. Double-ended detection scheme for a Raman Distributed Temperature System [47].

The Stokes and anti-Stokes power traces measured in the forward directions are expressed by:

$$P_S^{for}(z, T) = C_S^{for} \exp\left(-\int_0^z (\alpha_0(z') + \alpha_S(z')) dz'\right) * \frac{1}{1 - \exp\left(-\frac{h\Delta\nu_R}{k_B T}\right)} \quad 2.41 \text{ a}$$

$$P_{aS}^{for}(z, T) = C_{aS}^{for} \exp\left(-\int_0^z (\alpha_0(z') + \alpha_{aS}(z')) dz'\right) * \frac{\exp\left(-\frac{h\Delta\nu_R}{k_B T}\right)}{1 - \exp\left(-\frac{h\Delta\nu_R}{k_B T}\right)} \quad 2.41 \text{ b}$$

where the constant parameters C_{aS}^{for} and C_S^{for} take into account the incident pump power, the respective AS and S Raman cross sections and the transmission characteristic of the optical receiver used for the forward direction.

Likewise the Stokes and anti-Stokes power traces detected in the backward directions are:

$$P_S^{back}(z, T) = C_S^{back} \exp\left(-\int_L^{L-z} (\alpha_0(z') + \alpha_S(z')) dz'\right) * \frac{1}{1 - \exp\left(-\frac{h\Delta\nu_R}{k_B T}\right)} \quad 2.42 \text{ a}$$

$$P_{aS}^{back}(z, T) = C_{aS}^{back} \exp\left(-\int_L^{L-z} (\alpha_0(z') + \alpha_{aS}(z')) dz'\right) * \frac{\exp\left(-\frac{h\Delta\nu_R}{k_B T}\right)}{1 - \exp\left(-\frac{h\Delta\nu_R}{k_B T}\right)} \quad 2.42 \text{ b}$$

where the constant parameters C_{aS}^{back} and C_S^{back} take into account the incident pump power, the respective AS and S Raman cross sections and the transmission characteristic of the optical receiver used for the backward direction.

If we assume that the temperature of a small section, Δz , of the OF does not evolve between the two measurements in the forward and backward directions (*a typical minimum acquisition time value is 30 s per measure*), then through the anti-Stokes over Stokes ratio (using equations 2.41 a and 2.42 a) we can calculate the temperature, $T(z)$, in both directions, see Eq. 2.43 in order to remove the issue related to the differential attenuation, $\Delta\alpha$, over Δz [44]:

$$T^{for}(z) = \frac{\gamma}{\ln R^{for}(z) - \ln C_R^{for} + \int_0^L \Delta\alpha(z') dz'} \quad 2.43 \text{ a}$$

$$T^{back}(z) = \frac{\gamma}{\ln R^{back}(z) - \ln C_R^{back} + \int_L^{L-z} \Delta\alpha(z') dz'} \quad 2.43 \text{ b}$$

Imposing $T(z) = T(L - z)$ after some calculation, we obtain:

$$\begin{aligned} & \int_z^{z+\Delta z} \Delta\alpha(z') dz' = \\ & = \frac{\ln R^{for}(z + \Delta z) - \ln R^{for}(z) + \ln R^{back}(z) - \ln R^{back}(z + \Delta z)}{2} \end{aligned} \quad 2.44$$

By stepping along all fiber length with steps of Δz , which are usually set equal to the spatial measurement interval, the value of $\int_z^{z+\Delta z} \Delta\alpha(z') dz'$ is acquired for each interval Δz . Then, if we sum these values starting a $z=0$, we have an evaluation of $\int_0^z \Delta\alpha(z') dz'$ for every z . This technique requires also an initial calibration at a well-known temperature.

It is important to underline that this estimation can be obtained from a time-average over the entire period during which the differential attenuation was assumed to be constant. On the other hand the DE calibration technique must be implemented. One possible solution is recalculating $\Delta\alpha$ over time intervals on which the values may be taken constant. Another option consists in re-computing $\Delta\alpha$ for each measurement, although this tends to increase the noise in the temperature data measurement [44].

2.4 Conclusion

As explained in the first chapter, the temperature and strain monitoring of the future geological repository for nuclear wastes plays a key role in assessing the long-term safety of the project. This requires an evaluation of different classes of DOFSs, considering the different environmental conditions which can degrade the sensor response. In the previous section, the main DOFSs have been presented and their best claimed performances and characteristics are reported in Table 2.1. Raman sensing authorizes temperature measurements only whereas both Rayleigh and Brillouin scattering based sensors provide

simultaneous strain and temperature measurements. Indeed, the frequency shift is sensitive to these two parameters as expressed by equation 2.35 and equation 2.37 obtained for the OFDR and BOTDA systems, respectively. Hence, using only one of these techniques one cannot discriminate between temperature and strain contributions to the frequency shift. A solution to differentiate between these two effects and therefore providing separate spatially-resolved strain and temperature values is to combine the two different classes of sensors [48], [49].

Table 2.1 Performance chart for commercial DOFS.

	BOTDA [50]	RDTS [51]	OFDR [52]
Fiber Type	SMF	MMF	SMF
Measurable quantity	Strain and Temperature	Temperature	Strain and Temperature
Typical Spatial resolution	10 cm, (up to 50 m)	1 m	10 μm over 30 m 20 μm over 70 m
Sensing range	100 km round-trip (physical distance 50 km)	30 km	30 m or 70 m
Temperature accuracy	0.1 C	0.01 C	0.1 $^{\circ}\text{C}$
Strain accuracy	2 $\mu\epsilon$	---	1 $\mu\epsilon$
Measurement time	From 1 s to 10 minutes based up the requirements of the application	10 s	5 s at highest resolution
Measurement Base - Calibration	Frequency based, after setup, no calibration required	Intensity based, Require Calibrations (Relative measurement)	Frequency based, Require Calibrations (Relative measurement)
Detection scheme	Direct	Direct	Coherent

*Measurement time depends on: precision of measurement, variation of strain and temperature to be quantified, spatial resolution, and length of considered fiber.

The parameters spatial resolution; sensing range and the accuracy are defined in section 4.1

Although the BOTDA and OFDR systems show similar performances, among the three distributed sensors, BOTDA device shows the best performance in terms of the sensing length. Since the maximum sensing range of the OFDR is of about 70 m, this sensor does not fulfill the requirement of the Cigéo application, where the minimum distance to be monitored exceeds 100 m (tunnel of HL-W). Moreover, another advantage of the Brillouin sensor with

respect to the Rayleigh sensor is that it measures the absolute frequency variation rather than the phase change. Indeed, the OFDR can only acquire relative changes from a reference trace. It uses a cross-correlation function to localize the temperature or strain variations between two events; it means that large temperature or strain gradients will not be detected as the temperature or strain induced wavelength shift can be larger than the wavelength peak itself [17].

Therefore, in order to discriminate strain and temperature contributions, the BOTDA and the RDTS devices have been chosen as possible candidates for the monitoring and the surveillance of the ANDRA deep geological repository. Of course, the evaluation of their efficiencies and the improvement of these two sensors in severe mixed environment (γ -ray and H_2 presence) are mandatory before consideration of their implementation in Cigéo. In the next sections we will report the previous studies from literature conducted on the performances of these sensors when they are exposed to γ -rays or in presence of hydrogen.

Chapter 3

DOFSs in harsh environments

In this chapter we provide a general background on the radiation and hydrogen presence effects on the DOFS's response, in order to better contextualize our work with respect to the literature.

3.1 Losses in silica-based OFs

It is known that one of the most important parameters characterizing the OF performances is the attenuation (see 2.23 a and 2.34 a) which is a measure of the decrease of the signal light power over the length of the light-carrying medium. It is usually measured in dB/m or dB/km and is defined by the following equation:

$$a = -\frac{10}{L} \times \log_{10} \left(\frac{P_T}{P_0} \right) \quad 3.1$$

where L is the fiber length and can be expressed in meters or kilometers, P_T is the transmitted power from the fiber after the distance L and P_0 is the initial input power. As shown in Figure 3.1, the OF attenuation is wavelength-dependent.

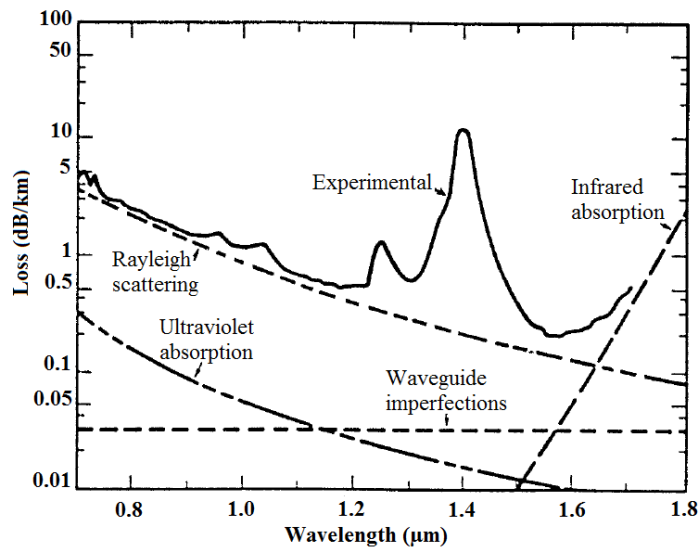


Figure 3.1. Typical attenuation spectrum of a silica based optical fiber [135].

Several phenomena contribute to the reduction of the light intensity along the propagation axis:

- Rayleigh scattering discussed in section 2.2.2 that depends on the wavelength as $1/\lambda^4$.
- The infrared absorption tail, which arises from the absorption of light related to vibrations of atoms.
- The ultraviolet (UV) tail, which arises from absorption of light associated with electronic transitions in the UV spectral domain.
- The absorption of light by point defects, such as the OH groups that absorb light at 2.73, 1.38 and 0.95 μm .
- Scattering due to the waveguide imperfections and bending losses.

In the study of the sensor performances in harsh environment, the attenuation plays a key role since the fiber transmission can be strongly degraded by radiations or hydrogen leading to errors in sensor measurement results or even the complete loss of the signal.

Radiation and hydrogen induced attenuation

Light transmission in optical fibers exposed to radiations is significantly influenced by the creation of point defects in silica network and the appearance of the corresponding absorption bands (see Figure 3.2). The nature of radiation-induced defects depends mainly on glass composition [53], but also on other parameters like glass elaboration process and history or residual stress [54]. Each defect has specific absorption properties, growth and recovery

kinetics. Figure 3.2 shows the normalized Radiation-Induced Attenuation (RIA) spectra for three fibers characterized by different compositions: pure-silica core, Ge-doped and P-doped fibers. It shows the poor radiation-resistance of P-doped fibers [54] compared to Ge-doped and undoped silica fibers over the whole spectral range. Moreover, for the three OFs, RIA curves result from three main contributions: a strong absorption band in the UV range with a tail that extends to the infrared, absorption bands located in the Visible range (more important in the P-doped sample) and an IR-contribution that increases toward the higher wavelengths. The RIA depends on several extrinsic factors such as irradiation conditions (dose-rate, temperature, total dose) and operating conditions (spectral domain, injected power).

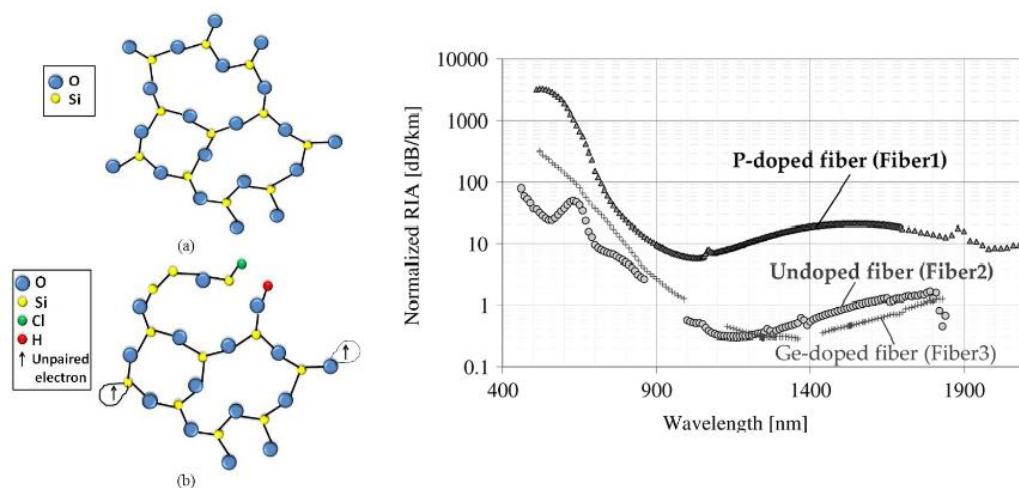


Figure 3.2. On the left: ideal pure-silica glass structure (a) Defective pure-silica glass structure (b) [53]. On the right: normalized RIA spectra for the P-doped, fiber (after 5 Gy), the Ge-doped fiber, and the undoped fiber (after 100 Gy) [92].

3.2 OFDR sensor vulnerability in nuclear environment

This PhD work is focused on Raman and Brillouin scattering based sensors. However, concerning the radiation effect on the OFDR systems, only few works are present in literature: the first study was done by *Sang et al.* who investigated the Rayleigh sensor performances under a mixed environment consisting of a neutron flux of $1.2 \cdot 10^{13} n cm^{-2} s^{-1}$ and a dose rate of 1 MGy/h. The study demonstrates a good sensor

response, at least during the 13 hours run duration [55]. Successive investigations performed under γ -rays (~ 700 Gy/h dose rate up to 110 kGy [56]) and X-rays (10 keV exposure up to 1 MGy [57]) prove that OFDR technique is almost unaffected by radiation up to the explored doses. Moreover, *ex-situ* (after radiation exposure) investigations [36] up to high dose level of 10 MGy show again this sensor unaffected by γ -radiation (changes below 5%). These results are very promising for the future integration of Rayleigh based sensors in nuclear facilities.

BOTDA sensor vulnerability in harsh environment

3.2.1

State of the art: To our knowledge only three studies investigating the vulnerability of the BOTDA systems in presence of radiation or hydrogen have been published.

Vulnerability in radiation environment

The first study of the effects of ionizing irradiation on the Brillouin performances was realized in 2006 through the pioneering work of *Alasia et al.* [58]. The authors use a BOTDA sensor with an operating wavelength of 1550 nm. The Ge-doped samples were 50 m long and γ -irradiated at the same dose rate of 27 kGy/h for different durations up to a total ionizing dose (TID) of ~ 10 MGy. The test was performed after irradiation (*ex-situ*) of the fibers. Spectral RIA measurements performed on the samples are reported and show increasing attenuation with increasing TID at 1550 nm. A RIA value of 170 dB/km is observed at the highest investigated dose, ~ 10 MGy, i.e. ~ 8.5 dB over 50 m fiber length. However, despite the significant RIA level, the BOTDA operates unbiased and the radiation-induced attenuation only affects the signal-to-noise ratio. The BOTDA tests were carried out under the same conditions and constant room temperature (RT) of ~ 22 °C and their results are reported in Figure 3.3. A clear dependence of the Brillouin scattering on the ionizing radiation dose is observed, indeed frequency peak and linewidth of the Brillouin spectrum increase nonlinearly as a function of the TID. In the worst case, 10 MGy, a frequency shift of 5 MHz, corresponding to a temperature error of ~ 5 °C, is observed. The authors attributed the observed radiation induced Brillouin frequency shift (RI-BFS) to silica compaction phenomenon i.e. the change in the silica density, which leads a change in the acoustic velocity and hence in the v_B (as expressed by equations 2.19 and 2.36).

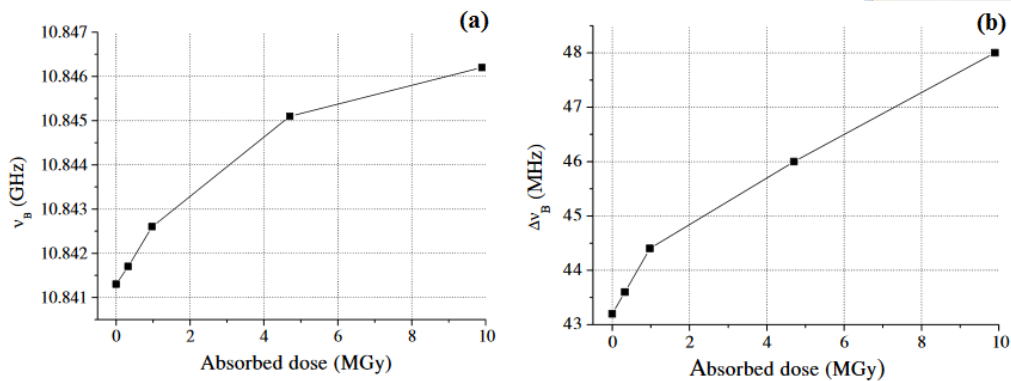


Figure 3.3. Brillouin frequency ν_B (a) and FWHM linewidth $\Delta\nu_B$ measured as a function of the TID (b). Test performed at constant RT ($\sim 22^\circ\text{C}$) [58].

The second work was done by *Phéron et al.* in our laboratory [59], [60]. If on one hand this work integrates the results of *Alasia et al.* providing a study of the radiation influence on the BOTDA response as a function of the fiber composition, on the other hand supplies a first important evaluation of the sensor performances for its integration in Cigéo. The tests are carried out on one pure silica core and two Ge-doped fibers, labeled SiO₂/F, SM28 (4 wt.% of Ge) and HGe (28 wt.% of Ge), respectively. Two different types of investigation are conducted: *ex-situ* and *in-situ*. The *ex-situ* tests are done at controlled RT ($\sim 22^\circ\text{C}$) some weeks or months after the end of the γ -rays exposure. The experimental conditions are close to those of *Alasia et al.*'s study [58]: 4 samples for each fiber γ -irradiated at a dose rate of ~ 28 kGy/h to reach up to 10 MGy (SiO₂) TID. Instead, the *in-situ* tests are executed during the γ -ray exposure in two different irradiation sessions, characterized by two different dose rates, 10 Gy/h and 1 kGy/h, and monitored during several days at room temperature (around 25°C). Moreover, all tests were supported by RIA measurements acquired at the BOTDA operating wavelength of 1550 nm.

In the *ex-situ* session [59], [60], the authors confirm the observations of *Alasia et al.* [58], showing a BFS induced by the radiation. Furthermore, the shift results depending on both fiber composition and germanium concentration are shown in Figure 3.4. The measurements reveal a good radiation resistance of the pure-silica-core fiber showing limited values of RIA (~ 50 dB/km at 10°MGy) and of radiation induced BFS (~ 2 MHz), corresponding to a temperature error below 2°C for this fiber and at the highest investigated TID.

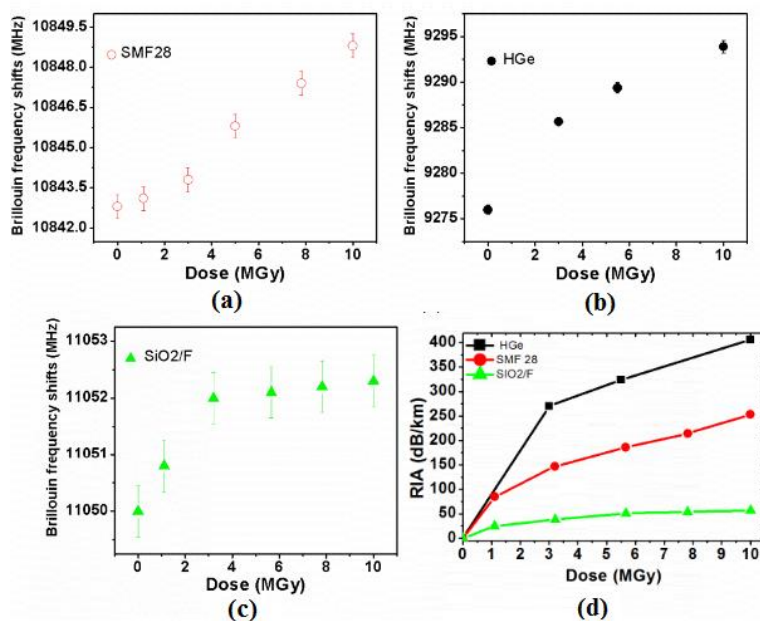


Figure 3.4. BFS with the TID for the SMF28 (a) the HGe-doped (b) and pure-silica core (c) fibers. RIA dose dependence at 1550 nm for the three tested samples (d) [59].

For all fibers, linear dependences of the BFS with strain and temperature were also maintained for the irradiated samples. Furthermore, no change of the fiber strain and temperature coefficients as a function of the TID was observed. An example of the obtained results is shown in Figure 3.5.

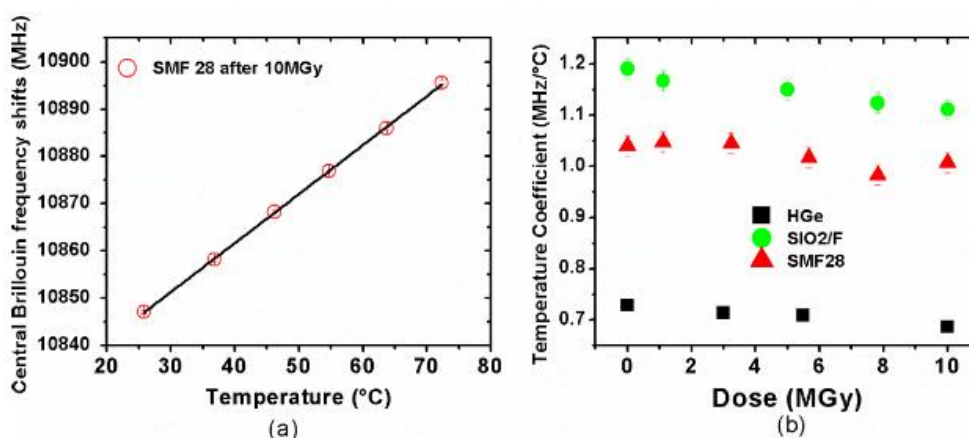


Figure 3.5. BFS dependence on temperature for the 10 MGy irradiated SMF28 (a). Evolution of the temperature coefficients (C_T) as a function of TID for the three fiber types [59].

During the *in situ* tests [60] the device response under γ -rays was investigated when different levels of external stress are applied to the sensing fiber coil reaching value up to 150 g. The experiment was carried out at 1 kGy/h dose rate up to two different TID: 400 Gy for the SMF28 and 90 kGy for the SiO₂/F fiber. The results corrected for the temperature variations ($20^{\circ}\text{C} < T < 30^{\circ}\text{C}$) are reported in Figure 3.6 for the SiO₂/F fiber.

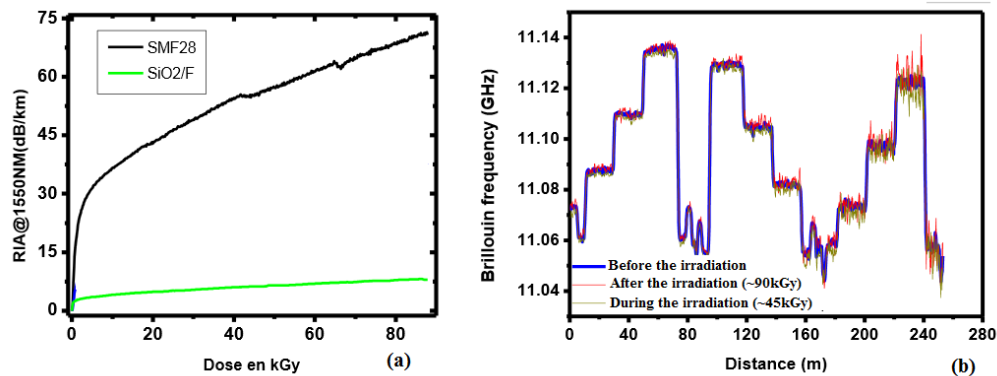


Figure 3.6. RIA dose dependence (a) observed for the SMF28 (black line) and pure-silica-core (green line) fibers. Brillouin frequency as a function of the length observed for the pure-silica-core fiber having parts differently stressed. The non-irradiated fiber (blue line) and that ones detected after ~45 h (green line) and ~90 h (red line) are compared. The tests were performed at a dose rate of 1 kGy/h.

For both fibers no significant change of the Brillouin frequency due to the γ -ray exposure at tested dose rate and TIDs is observed. Nevertheless, the SMF28 fiber exhibits an important decrease (60%) of the Brillouin spectrum amplitude after a TID of 511 kGy. For the pure-silica-core fiber, the observed shift of about 0.5 MHz is within the instrumental accuracy. Similarly, the strain coefficient exhibits no significant variation during the irradiation run. Moreover, Phéron performed tests using the pure-silica-core fiber during 341 h under γ -rays at a dose rate of 1.5 kGy/h to reach a high TID level of ~4 MGy. All measurements were corrected for the temperature fluctuations between 35°C and 55°C . Also in this case, although a SNR decrease was observed during the test no important change of the Brillouin frequency, of the strain coefficient and even of the amplitude (only 5% from 5 kGy to 4 MGy) have been detected. The authors concluded that the performances of the BOTDA system using the pure-silica-core fiber as sensing element seem promising for its integration in Cigéo environment.

Issues related to hydrogen presence

Only one work [61] in literature concerns with the BOTDA response under operation in a hydrogen-rich environment. The authors used a BOTDA operating at 1550 nm employing two Ge-doped fibers (G652) one coated with acrylate and the other surrounded by a carbon layer. For both fibers they monitored the evolution of the H₂ loading (25 °C and 150 bars) inside the fiber core from 0 % to ~95 % (saturation level) of molecular hydrogen content. Absorption measurement reveals hydrogen presence (its characteristic band at 1245 nm was observed) in the acrylate coated fiber and attenuation values increasing up to 0.075 dB/m at the saturation level. Instead, no transmission variation is noticed for the carbon coated fiber, confirming the well-known characteristic of this coating to be hermetic to molecular hydrogen diffusion. Concerning the sensor response, a linear shift as a function of the H₂ concentration to saturation level is measured for the acrylate coated sample. The results are shown in Figure 3.7.

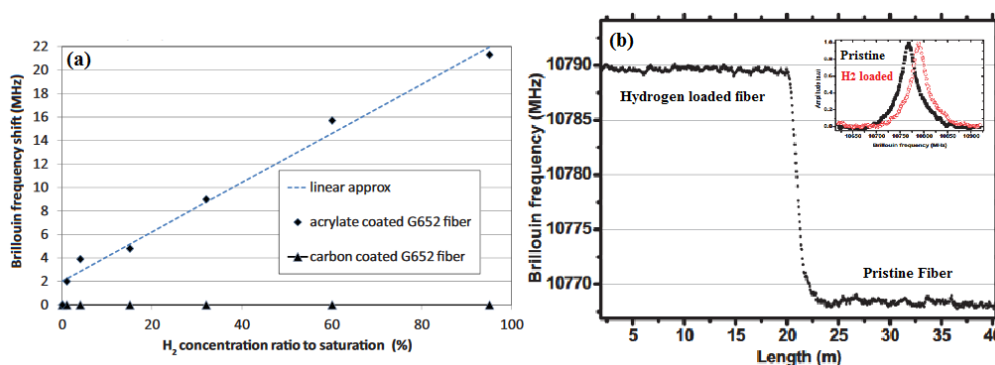


Figure 3.7. BFS as a function of the molecular hydrogen concentration to saturation level observed in the acrylate (circles) and carbon (triangles) coated fiber (a). Brillouin frequency detected as a function of the measurement line (H₂ loaded + Pristine Fiber) distance when the fiber is saturate of hydrogen (b). The inset in (b) shows the shift in the Brillouin spectrum due to the H₂ loading.

Concluding, the authors propose this BOTDA system using the G652 acrylate fiber suitable as distributed hydrogen sensor.

RDTs sensor vulnerability in nuclear environment

The first studies of the radiation influence on Raman scattering based sensor (in open ended configuration) response were done in the 1996 by *Jensen et al.* [45], [62]. Their works were focused on the radiation exposure effects on the absorption spectra in the IR-domain for an

undoped fiber, highlighting the time evolution of the RIA at the pump, Stoke and anti-Stokes wavelengths characteristics of their two Raman sensors: one working at $\lambda_0=854$ nm ($\lambda_S=886$ nm and $\lambda_{aS}=824$ nm) and the other at $\lambda_0=1047$ nm ($\lambda_S=1095$ nm and $\lambda_{aS}=1003$ nm). The irradiations were conducted with a ^{60}Co -source with dose rates ranging from $\sim 10^{-2}$ Gy/h to $\sim 10^4$ Gy/h. The fiber absorption spectra were monitored at 20 °C during γ -rays exposures at a dose rate of 1.9 kGy(SiO_2)/h and the related pump, Stoke and anti-Stokes attenuations time-evolution at two different temperatures, 20°C and 300°C, are reported in Figure 3.8 [45], [62].

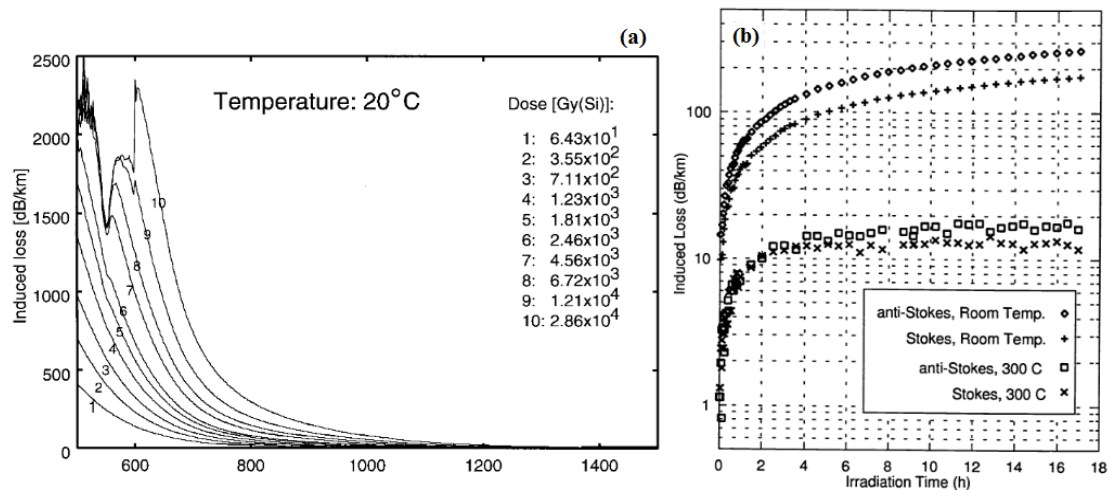


Figure 3.8. In (a): γ -ray induced attenuation spectra in polyimide-coated, pure-silica core fiber acquired at a dose rate of 1.9 kGy(SiO_2)/h and RT (~ 20 °C) [62], [45]. In (b): kinetic growth curves obtained at 20 °C and 300 °C by γ -rays at $\lambda_S=886$ nm and $\lambda_{aS}=824$ nm. Dose rate ~ 1.9 kGy/h [45].

The authors observed significant variations in the IR-attenuation spectra during the γ -rays exposure detected both at RT (~ 20 °C) and at 300 °C (not shown), concluding that the RIA is reduced, but not removed, by high-temperature over the spectral region 700-1500 nm. Concerning the Raman sensor, through temperature measurements (not shown in the papers), the authors reported two different phenomena impacting the device response: i) the RIA and ii) the “*relative radiation induced absorption*” (that we identify as differential RIA, ΔRIA). In fact, on the one hand the RIA level increases with the dose (and dose rate) and causes the SNR decrease during the irradiation. On the other hand the difference between the attenuation detected at both the Stokes and anti-Stokes wavelengths (see Figure 3.8 b) leads to a temperature error increasing along the sensing fiber. Therefore, the differential RIA impacts

the sensor response contributing to increase $\Delta\alpha$, in equation 2.38, making it not negligible anymore. Moreover, Figure 3.8 b shows the tendency of the anti-Stokes and Stokes components attenuations to saturate at higher doses and the resulting ΔRIA to be larger at the lowest temperature (20°C). Finally, *Jensen et al.* reported advantages in terms of attenuation and ΔRIA to use laser probe working at higher wavelength which is associated with smaller temperature errors. However, in [45] they concluded that although the SE-RDTS is not suitable in nuclear environment, even at relatively low dose rate of 10 Gy/h [62], using a laser pump at 854 nm with 20 m long fiber, the radiation influence on the sensor performances is low enough to perform measurement at dose rate of ~ 1.8 Gy/h, that is a typical upper level at nuclear power plant coolant loops. The temperature error was estimated to be of about 2 °C [45].

Later works [63], [64], [47] confirmed the strong impact of the ΔRIA on the RDTS performances and proposed diverse solutions to correct the related error:

1. Method with thermocouple (TC) data [63], [64]. It is applicable when both the temperature and radiation-induced loss distribution are almost uniform along the fiber length, such as in the case of the primary loop area of nuclear power plants. The conceptual set-up of this calibration method is reported in Figure 3.9 a. This technique uses the real temperature measured by both two TC and Raman technique at the two fiber ends and also at a given point along the fiber.
2. Method with loop arrangement [62], [63], [64]. It was proposed for nuclear environments with an unknown ionizing field distribution. The conceptual set-up of this calibration method is reported in Figure 3.9 b. It consists of making a loop with the sensing fiber in order to have two parts set as close as possible so that the temperature and the radiation conditions can be assumed to be the same. By comparing the measured results for points A and D, the effect of radiation-induced losses between A and D can be calculated. Also, from the results for points B and C, the effect between B and C can be known. From the above two effects, we can obtain the radiation-induced loss between point A and B, which should be the same as that between points C and D. From the correct temperature at point A (T_0) and the radiation-induced effect in A–B, the correct temperature for point B (T_1) can be calculated [64].

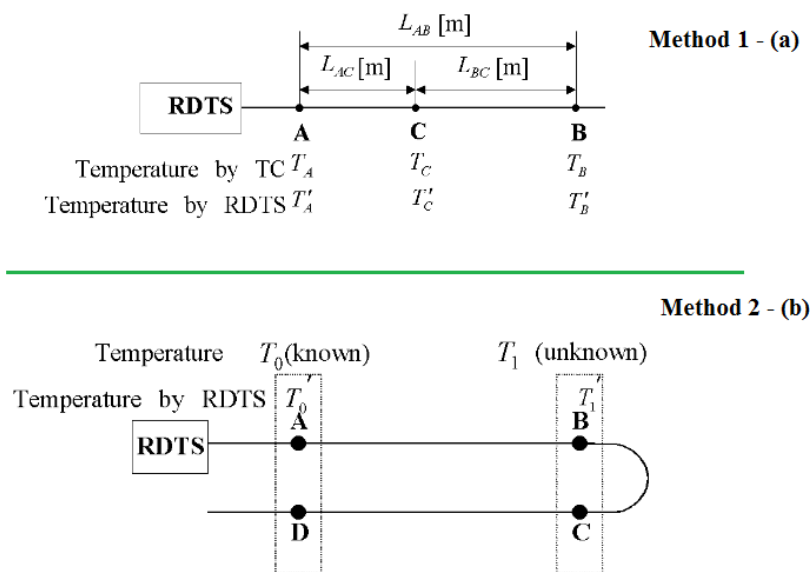


Figure 3.9. Conceptual set-ups for the calibration method using two TCs (a) and using a loop arrangement (b) [64].

3. Method with dual ended configuration [47], [43]. This method was extensively explained in section 2.3.3 of Chapter 2

Since the study done by Kimura [64] is an extension of the Takada's one [63], we present both papers as a single work. The authors investigated the RDTs responses under γ -ray exposures (fast reactor) at about ~ 60 Gy/h dose rate, using 120 m long pure-silica core OH-doped fiber as sensing element. The sensor is a commercial RDTs operating at 1047 nm and the measurements were continued through three operating cycles at the same dose rate for 9000 h. Thermocouples were placed at three different point along the fiber. Firstly, they show, in Figure 3.10 a, the negative effect of the ΔRIA on the temperature measurement along the fiber, making a comparison between the temperature detected by the RDTs and that monitored with the TCs, before and during the γ -rays exposure. Figure 3.10 b reports the time

dependence of the RDTS temperature error at the beginning and at the end of the fiber.

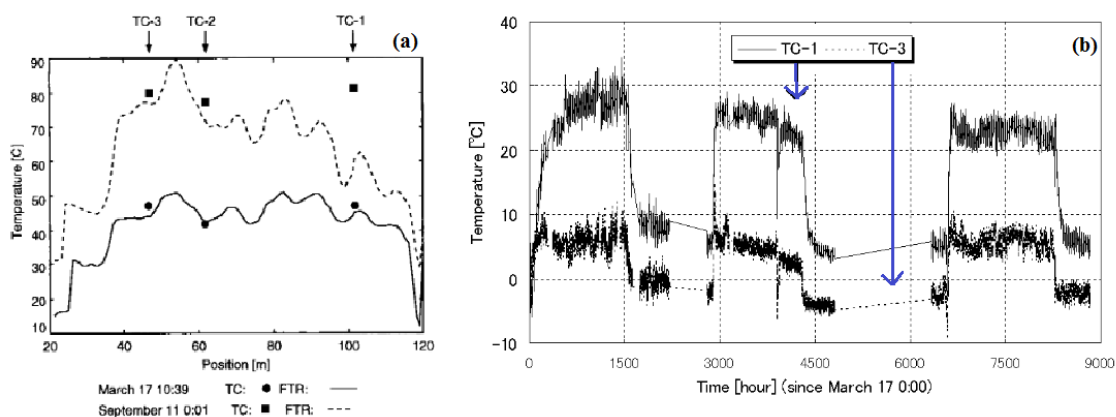


Figure 3.10. In (a): comparison between the T measurements acquired with the thermocouples and with the RDTS. Tests performed before (solid line) and after (dashed line) irradiation are shown [63]. In (b): time dependence of the temperature errors observed on the RDTS measurements [64].

The errors were larger at the fiber end reaching the value of 30 °C and decrease, tending to the saturation, as a function of the exposure time. This saturation was explained by the competition between the generation and the recovery of color centers.

In a second step, the authors operated the correction methods, 1 and 2. Since the dose rate in the primary loop area of their fast reactor can be assumed almost constant as well as the temperature, they applied the first correction technique. The result in Figure 3.11 a shows that the correction method with two thermocouples works fairly well, giving only 2.5 °C of T error at the TC-2 position compared to the 8 °C detected without correction. Moreover, studying the irradiation time dependence of the temperature error in this case (not reported) an average value of 2.5 °C is calculated for the whole irradiation run. In conclusion, the authors applied the second method and showed, in Figure 3.11 b, the comparison between the two different correction techniques, concluding that both calibrations are exploitable during radiation exposures at ~60 Gy/h dose rate and ~0.26 MGy. However, in accidental conditions the assumption of uniform radiation along the fiber cannot be used.

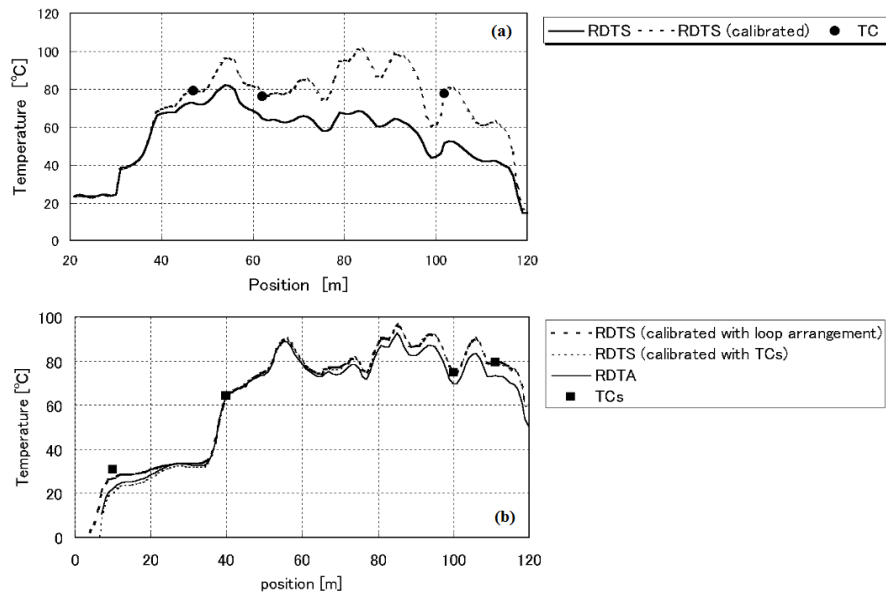


Figure 3.11. RDTS temperature measurements performed during the γ -rays exposure without (solid line in a) and with (dashed line in a) the correction using two thermocouples (a). Comparison between the two calibration methods: using two thermocouples and with loop arrangement (b).

Finally, the most recent works use the dual ended configuration methods to correct the measurements. *Fernandez et al.* [47], tested two graded index MMFs as sensing elements: one, coated with carbon and polyimide, optimized to operate in harsh environment, while the other one was a standard fiber surrounded by an acrylate layer. For both fibers, spools of 26 m length were located inside the water in three different positions 1, 2 and 3 characterized by three different dose rates (80, 360 and 760 Gy/h, respectively), which remain constant during the γ -radiation runs. The irradiation session was carried out up to a total dose of 326.8 kGy. The samples were inside an oven providing a stable temperature gradient. The experimental setup and the temperature profile detected with the RDTS system before the irradiation are displayed in Figure 3.12. Moreover, the authors provide spectral measurements in the region from 700 to 1700 nm and showed the RIA evolution during the irradiation for the three different zones. As expected, the RIA levels change with the dose showing different evolutions in the three zones. However, the maximum measured total attenuation value (7.5 dB on around 90 m for the acrylate fiber) can be compensated by their device, which has a dynamic range of about 17 dB permitting sensor use at MGy dose levels. Finally, they showed that although the Δ RIA varies in the time and along the fiber length, the DE-RDTS read-out remains constant, within an accuracy of $\pm 1^\circ\text{C}$, as displayed in Figure 3.13. They

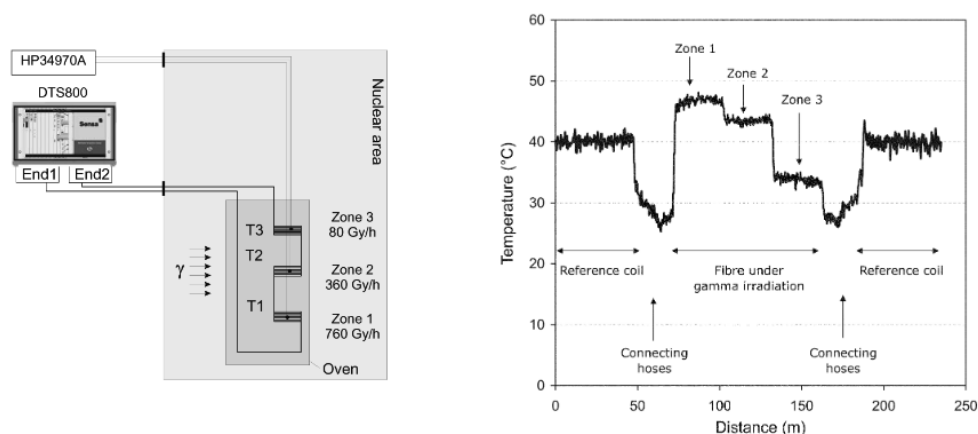


Figure 3.12. Experimental setup (on the left) and related temperature profile obtained before the irradiation with the RDTS system (on the right). The reference coil is located inside the detection unit itself [47].

concluded that DE-RDTS system can still operate despite the radiation induced power losses up to 300 kGy and that the radiation tolerance of the DE-system must be assessed up to higher doses.

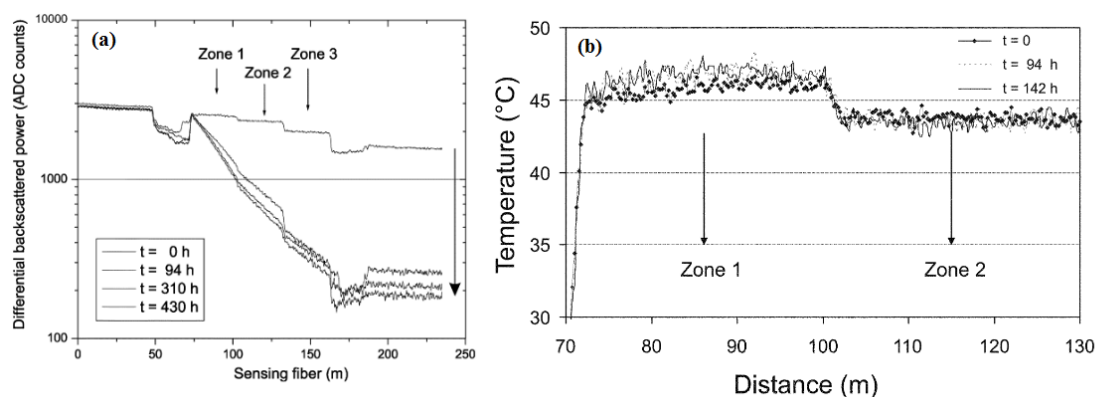


Figure 3.13. Differential attenuation ($\alpha_{aS}-\alpha_S$) detected in the polyamide coated fiber by the SE-RDTS prior to signal during the radiation run (a). Temperature profile detected in the acrylate coated fiber by the DE-RDTS system during the radiation run (b) [47].

In 2015 *Toccafondo et al.* [43], [65] investigated for the first time the performances of the DE-RDTS system in a mixed field radiation environment, including not only photons, but also protons, neutrons, muons and other particles (generated by a 24 GeV/c beam focused on a copper target). The sensor operating at 1064 nm uses a MMF graded index Ge-doped fiber, defined as radiation tolerant sensing element and its response was monitored for 24 h; the highest total accumulated equivalent dose was of 1.25 kGy at about 50 and 180 m along the

fiber exposed length. Their experimental setup is shown in Figure 3.14: the distances along the fiber's path from the rack to which the RDTS is connected are indicated. In particular, the point in which the OF passes near to the target is shown at a distance of either 50 m or 180 m from the RDTS depending on the direction of light propagation in the fiber.

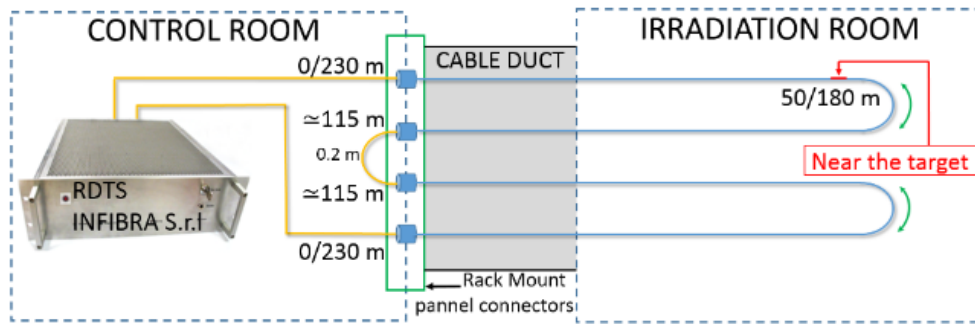


Figure 3.14. Experimental set-up for RDTS temperature measurement in a mixed radiation field [43].

In order to prove that the Δ RIA change during the measurements, the authors showed dissimilar RDTS Stokes and anti-Stokes signals as a function of the distance detected before and after 24 h of irradiation. Also the time evolution of RIA spectral measurements performed on the fiber γ -irradiated at a constant dose rate of 0.23 Gy/s up to total dose of 1.25 kGy are reported (see Figure 3.15 a) and clearly show that the Stokes and anti-Stokes power components will be differently affected by the radiation.

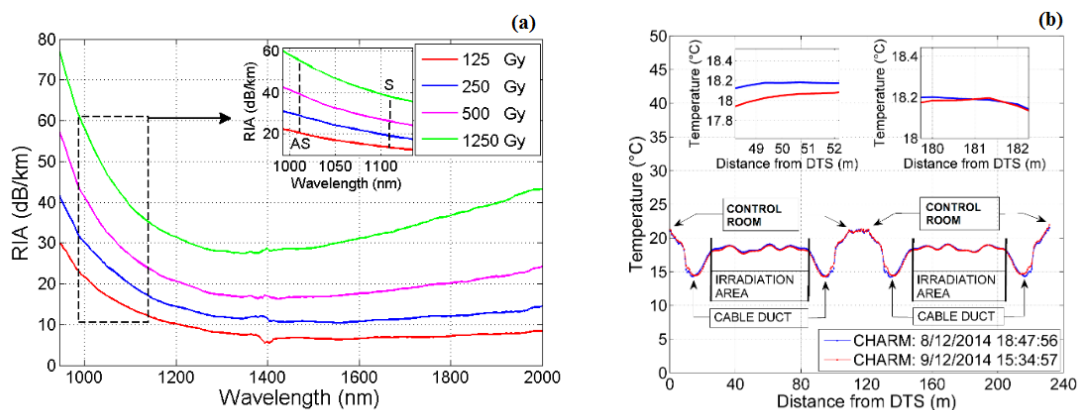


Figure 3.15. Evolution of the RIA spectrum during γ -rays exposure at constant dose rate of 0.23 Gy/s up to total dose of 1.25 kGy (a). Temperature profiles along the OF before and at the end of the irradiation run (b) [65].

Finally, the temperature profile measured with the DE-RDTS is reported in Figure 3.15 b. No significant temperature errors are observed. Indeed, the two fiber sections corresponding to the positions along the OF exposed to higher radiation levels (ranged from 600 Gy to 1250 Gy), zoomed in the insets, show no important temperature variations during the whole measurement test, as expected, since the irradiation area is meant to be kept at constant and uniform temperature. In conclusion, the authors demonstrated the efficiency of the DE-RDTS in mixed field radiation environment.

Choice of the sensor for the Cigéo application

3.2.3

The choice of our sensor for health monitoring of the envisaged French deep geological repository is strongly influenced by the environment conditions in which the DOFs are employed. In Chapter 2 (section 3.2.3), the Rayleigh sensor was not evaluated as promising candidate due its too short sensing range ($< 70^{\circ}\text{m}$; value in 2013 date of the PhD start) not suitable for the application requiring optical fiber of minimum 100 m length. Thus Brillouin and Raman scattering based-DOFSs have been selected. Associating Raman sensors with Brillouin ones it is possible to obtain spatially-resolved cartographies of discriminated temperature and strain values using a two fibers cable. However, the evolution of their performances must be evaluated under γ -rays and hydrogen. This is the main objective of this PhD thesis work.

From literature, two macroscopic phenomena are shown to affect the BOTDA performances:

- i) The RIA degrades the optical sensor performances by limiting its sensing range.
- ii) The BFS caused by variations of the Brillouin scattering properties modifying the central Brillouin frequency or its dependence on temperature and strain leads to errors in temperature or strain measurements.

However, if the sensing fiber is suitably chosen to reduce these radiation effects this sensor fulfills the Cigéo requirements.

From literature, the RDTS performances were found to be strongly affected by radiations through two phenomena:

- i) The RIA also degrades the sensor performances by limiting its sensing range, as for the BOTDA sensor.
- ii) The Δ RIA between Stokes and Anti Stokes signals leads to errors in the temperature measurement; error that increases with the sensing fiber length.

In order to overcome these issues, different solutions employing the RDTS system in loop arrangements were proposed. Nevertheless the loop arrangement is not suitable for our application. Indeed, this configuration requires a sensing fiber length $\times 2$ times the length of the storage tunnel. At the Cigéo targeted MGy doses the RIA limits the sensing distance range too much and this factor $\times 2$ becomes important avoiding an easy use of the loop arrangement systems even with the so-called radiation hard or radiation tolerant optical fibers. As an example, we take into account a 2×100 m long sensing fiber linked to an acquisition system with an optical budget of 8 dB operating at the wavelength of 1064 nm. At a low TID of ~ 1 kGy, the signal will be attenuated at the fiber end by 10 dB for a commercial Ge-doped fiber (~ 50 dB/km at 1064 nm, see Figure 3.15), which means that the measures will be not exploitable for fiber length > 160 m.

Therefore, the integration of the standard RDTS in extreme applications requires improvements of the single-ended technique, if possible.

PART II
EXPERIMENTS AND RESULTS

Chapter 4

Materials and experimental setups

This chapter is concerned with the description of the materials, instruments, and setups used to perform the experiments described and discussed in this manuscript.

4.1 Investigated Samples

In this section we provide a description of the optical fiber (OF) samples studied in this PhD thesis and we introduce the scope of their investigation.

The silica glass based OF samples present in this work have been selected to be representative of the current commercial fibers and to allow evaluating the next OF sensors generation that could be employed in future nuclear facilities and radioactive wastes repository. As discussed in Chapter 2, the two investigation units work with different type of optical fibers. That based on Brillouin scattering utilizes single-mode fibers (SMFs) like sensing component, whereas the Raman distributed temperature device operates with multi-mode fibers (MMFs). Moreover, previous studies [45], [47], [58], [59] have shown that radiation impacts the Brillouin and the Raman scattering by decreasing the fiber linear transmission efficiency through the radiation-induced attenuation (RIA). RIA then affects the sensing distance range. Since the extent of this attenuation phenomenon depends on many factors, such as dopant types, cladding co-dopants, and coatings, the fibers were selected in order to evaluate the sensor radiation response as a function of these features. Fibers with

pure-silica core (PSC), cores doped with fluorine (F), germanium (Ge) and Phosphorous (P) at various concentration levels have been studied. The evaluation of dopants concentration along the fiber diameter has been achieved by employing energy dispersive X-ray (EDX) spectroscopy. In our case, a spatial resolution of $<1 \mu\text{m}$ was required. For this aim, we used a scanning electronic microscope (SEM) JEOL JSM 7100f [66] equipped with an EDX detector of OXFORD Aztec 2.0 SP1 type [67] at Materials Research Laboratory, University of Nova Gorica, Slovenia.

In addition, to estimate the γ -ray response of our sensors, our studies are also devoted to gauge their performances in presence of molecular hydrogen released from nuclear waste. In hydrogen-rich environment the employment of fibers with standard coating can cause significant problems. Indeed, the hydrogen molecules can quickly diffuse into the fiber core leading to significant increase in optical loss [68], [69]. For this reason, the use of fibers with a hermetic coating is evaluated. It is known [69] that the most successful solution is the carbon-coated optical fiber made by depositing thin carbon layers ($\sim 50 \text{ nm}$) on the surface of the cladding material during the fiber-drawing process [69] surrounded by a single-layer polyimide coating. A representative schematic view of a poly-carbon coated optical fiber is illustrated in Figure 4.1.

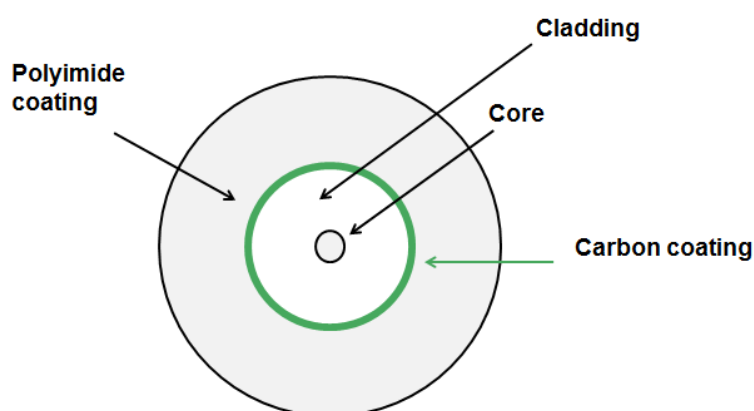


Figure 4.1. Schematic representation of an optical fiber with a hermetic carbon coating and an external polyimide material.

Moreover, some fibers are covered with polyimide external coating which resist to temperatures up to $300 \text{ }^\circ\text{C}$.

It is important to underline that, in this work, we indicate as “pristine” the not treated OF sample, i.e. not γ -irradiated and/or H₂ loaded.

The best claimed fiber performances reported in this section are provided by their manufacturer data sheets.

Multimode fiber

Six different types of standard multimode fibers are studied:

- P-MMF is a graded multi-mode fiber, phosphorous and germanium doped in the core (0.5 wt.% and 15 wt.%, respectively). It is surrounded by a carbon and polyimide coating.
- Ge-MMF is a commercial graded index multi-mode fiber, doped with Germanium in the core (15 wt.%). It is widely used in telecom markets requiring high-speed networks.

Both P-MMF and Ge-MMF are widely used in the telecom and sensor markets.

- PSC-MMF_1 is a step-index multi-mode fiber having a pure silica core and a F-doped silica cladding, operating in the range from 400 to 2400 nm and showing high transmission efficiency. It surrounded by an acrylate coating.
- PSC-MMF_2 is a step index multi-mode fiber with a pure silica core and a cladding in F-doped silica, surrounded by a polyimide coating. It is manufactured to have extreme resistance to hydrogen in the Raman band from 1014 to 1114 nm in DTS applications.
- F-MMF_1 is a graded index multimode fiber fluorine doped in the cladding (5 wt.%), optimized for use in highly radioactive environment. It is coated with a dual layer UV Acrylate.
- F_MMF_2 is graded index multimode fiber fluorine doped in the cladding, optimized for use in highly irradiative environment. It is coated with a dual layer UV cured resin.

Table 4.1 reports the most important MMFs characteristics as given by manufacturers.

Table 4.1 Characteristics of the tested MM-Fibers

Fiber	ϕ_{core} (μm)	$\phi_{\text{clad.}}$ (μm)	ϕ_{coat} (μm)	Coating type
P-MMF	50	125	155	Polyimide and Carbon
Ge-MMF	50	125	242	Dual layer UV Acrylate
PSC-MMF_1	50	125	250	Acrylate
PSC-MMF_2	50	125	155	Polyimide
F-MMF_1	50	125	242	Dual layer UV Acrylate
F-MMF_2	50	125	245	UV cured resin

Single mode fiber

Six different types of standard single mode fibers are studied:

- Ge-SMF_50g, Ge-SMF_110g and Ge-SMF_270g are three step index single-mode fibers characterized by high concentration of Ge-dopant in the core, 10.7 wt.% and with a small core diameter of 5.2 μm . These characteristics make the fibers highly photosensitive and adapted to the photo-inscription of Bragg gratings. They are manufactured starting from the same preform, but varying the drawing tensions (DrT): 50g, 110g and 270g, respectively. All fibers are coated with standard dual layers acrylate.
- PSC-SMF_1 is a step index single-mode fiber with a pure silica core and a cladding in F-doped silica (1.8 wt.%), surrounded by a polyimide coating.
- PSC-SMF_2 is a step index single-mode fiber with a pure silica core and a cladding in F-doped silica (1.8 wt.%) surrounded by a polyimide and carbon coating. This hermetically coated fiber is done to operate at high temperatures.
- PSC-SMF_3 is a standard SMF with a pure silica core and a cladding in F-doped silica (1.5 wt.%). It is characterized by lowest losses than any terrestrial-grade single mode fiber.

Table 4.2 reports the most important SMFs characteristics as given by manufacturers.

Table 4.2 Characteristics of tested SM-Fibers

Fiber	ϕ_{core} (μm)	$\phi_{\text{clad.}}$ (μm)	ϕ_{coat} (μm)	α @1550 nm (dB/km)	Coating type
Ge-SMF_50g	5.2	175	243	0.28	Acrylate
Ge-SMF_110g	5.2	175	243	0.35	Acrylate
Ge-SMF_270g	5.2	175	243	0.55	Acrylate
PSC-SMF_1	8.5	124.2	146.9	2.20	Polyimide
PSC-SMF_2	8.4	125	155	0.50	Polyimide and Carbon
PSC-SMF_3	8.2	125	242	0.17	Acrylate

ϕ indicate the diameter and α the fiber attenuation

4.2 Experimental set-ups: distributed measurements

As it was previously mentioned in Chapter 2, distributed sensor technologies have shown several advantages for the temperature and strain monitoring of nuclear facility [36], [45], [47], [59], [62], [63], [64], in comparison to the traditional sensor technology, whose measurements are limited to the probing of local effects. Two types of distributed sensors are under test in this thesis: the Raman Distributed Temperature Sensor (RDTS) in single ended configuration and the Brillouin Distributed Strain and Temperature Sensor (B-DSTS) using an optical sensing technology based on Brillouin Optical Time-Domain Analysis (BOTDA). The scheme of these experimental set-ups is explained in the next two sections. Meanwhile, it is important to clarify the meaning of some important parameters commonly used to characterize the distributed fiber sensors, such as spatial resolution, distance range and optical budget [70], [19], [15]. The minimum change in the measurement, meaningfully detectable by the measurement system, is the *resolution*. The *spatial resolution* for an optical fiber is the smallest length of fiber over which any possible change in the variation of the measurand can be detectable by the measurement system (it can also be defined as minimum distance between two step transitions of the measurand). The minimum change in the measurement, meaningfully detectable by the measurement system, is the *resolution*. The *spatial resolution*

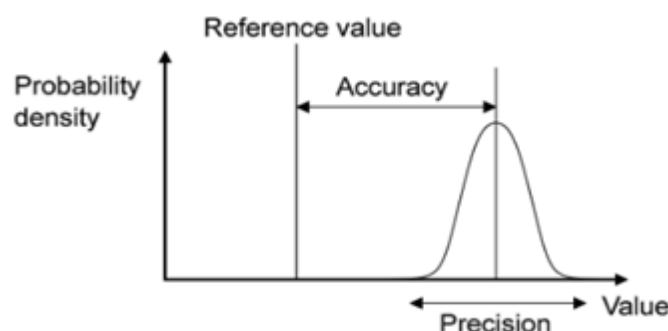


Figure 4.2. Illustration of the definition of accuracy and of the precision [70].

for an optical fiber is the smallest length of fiber over which any possible change in the variation of the measurand can be detectable by the measurement system (it can also be defined as minimum distance between two step transitions of the measurand). The *distance range* is the fiber length over which the measurement can be performed within the stated uncertainty and spatial resolution. The *optical budget* is the difference between the transmitter power level of the source and the receiver sensitivity (in dB). Consequently, the system is not useful when the power loss in the link exceeds the optical budget value. The *accuracy* represents the difference between the measured result and the ideal value and is affected by both bias and precision. The *precision* describes how repeatable a measurement result is (see Figure 4.2). It is expressed by the estimated standard deviation of a specified series of measurements. Sometimes, precision is expressed as a multiple of the estimated standard deviation, e.g. 2σ (meaning that about 95% of the observations fall within 2 standard deviations).

During all tests the temperature were monitored through thermocouples using the Picolog Technology TC-08 able to provide up to 10 measurements per second and temperature resolution of 0.025 °C [71].

Raman set-up

The device employed in this thesis is an optical time domain reflectometer (OTDR) based DTS-SR Sentinel provided by Sensornet company [51], which uses a Nd:YAG laser operating at the probe wavelength of 1064 nm. It works using the Stokes signal to normalize the anti-Stokes trace. The best instrument claimed performances are 0.01 °C of accuracy for

distances < 5 km, 0.5 m of sampling resolution, 10 s of minimum measurement time and spatial resolution of 1 m. A typical optical budgeted value for our instrument is ~ 5 dB. Moreover, our system is linked to an 8 channels multiplexer provided as well by Sensornet using multimode optical fibers through standard E2000 connectors.

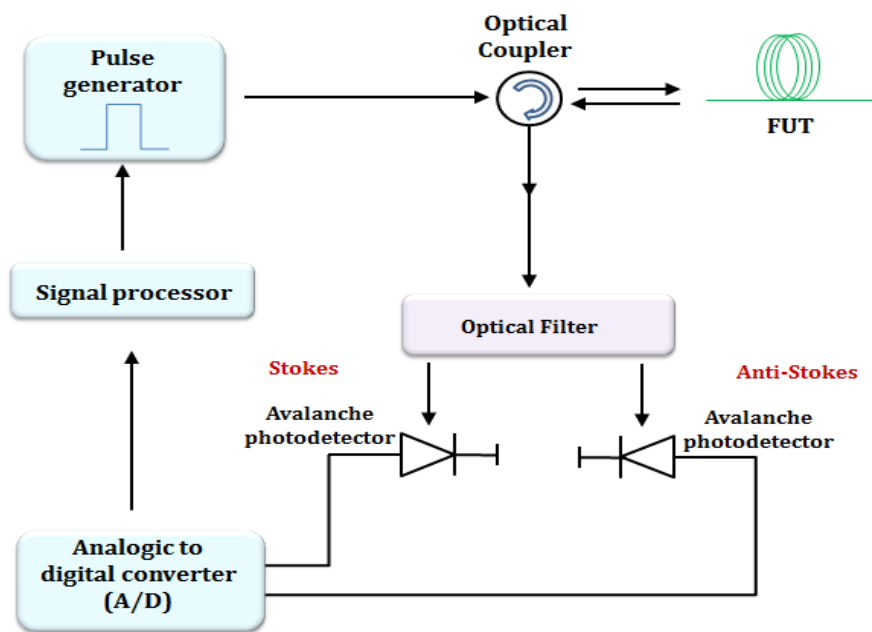


Figure 4.3 Scheme of a typical OTDR-based RDTs temperature sensor. FUT: Fiber Under Test.

The schematic configuration of a typical OTDR based RDTs system [72] is presented in Figure 4.3. It operates having access to only one fiber end and includes a pulsed probe laser, an optical circulator to separate forward path from the backward one, one optical narrow band pass filter which selects the anti-Stokes and the Stokes signals. Each receiver branch is made up of an avalanche photodiode (APD) and an analog-to-digital converter, which is connected to a processor for data logging. Since the Raman scattering is a rather weak signal (its intensity is typically 30 dB lower than the Rayleigh one [65]), the APD is usually coupled with a high-gain electrical amplification stage.

This instrument offers the possibility to compensate the differential attenuation, $\Delta\alpha$, performing an initial calibration. This calibration is only applicable in a limited number of operations for which $\Delta\alpha$ is constant along the fiber length. As previously reported (section

1.2.2), in Cigéo the radiation might be not uniform and changing in the course of time. For this reason we choose to not use this procedure.

It is important to underline that, if not specified, all RDTs measurements are made in single-ended configuration, at normal pressure, controlled RT conditions, a spatial averaging of 1.02 m and acquisition time of 60 s.

Brillouin set up

4.2.2

In the previous chapter we discussed the two different main classes of Brillouin scattering based sensors: spontaneous Brillouin sensors and stimulated Brillouin sensors.

The Brillouin set-up used in this work is a commercially BOTDA device provided by OZ Optics company [50], operating at the wavelength of 1550 nm and employing SMFs.

A BOTDA is a system that uses frequency shifts due to Brillouin scattering of light at different sample points. The block diagram of our device is depicted in Figure 4.4.

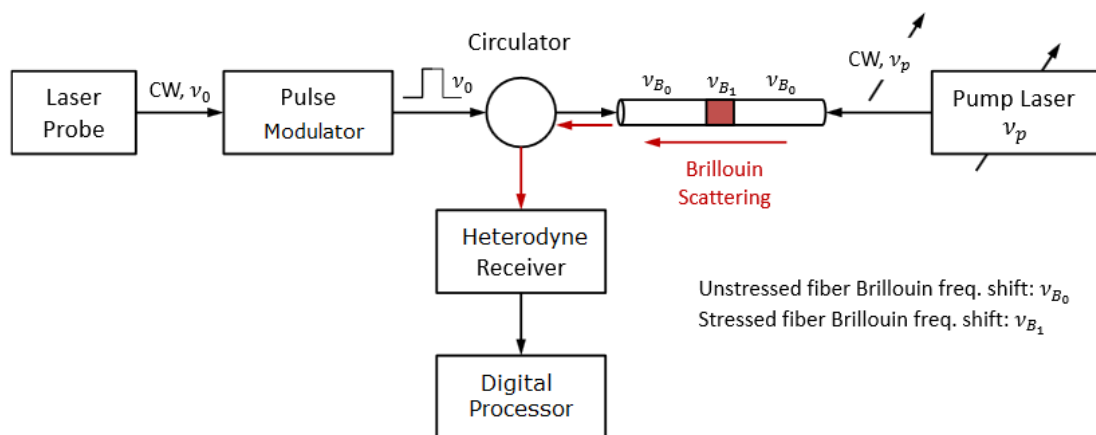


Figure 4.4. Scheme of the BOTDA system provided by OZ optics company [50], [73].

Both ends of the FUT are required with this system: one for the injection of the probe laser pulse and the second for the continuous-wave (CW) pump signal. The use of two counter-propagating waves (CW and probe pulse) leads to enhance the Brillouin scattering process. Indeed, the probe beam exhibits Brillouin amplification at the expense of the CW beam. The power drop in the CW beam is measured while the frequency difference between two lasers

is scanned, giving the Brillouin loss spectrum of the sensing fiber [73]. Hence, the shift detected in the Brillouin spectrum is used to evaluate the temperature and/or strain variation of the sensing fiber-zone according to the equation 2.37 of Chapter 2.

In standard conditions, the instrument claimed performances are: spatial resolution ≥ 0.1 m, adjustable up to 50 m with increment of 0.5 m, spatial step ≥ 0.05 m, sensing range ≤ 50 km, strain accuracy of $\pm 2 \mu\epsilon$ and temperature accuracy of 0.1 °C. A typical optical budgeted value for our instrument is ~ 10 dB. Moreover, our set-up is provided with 12 channels optical switch from JDSU [74].

The Brillouin central frequency (ν_B) assigned to each measurement was evaluated through an arithmetic average of the ν_B along the fiber length, the experimental signals were fitted with a pseudo-Voight profile at each point of the sensing SMF. The related error is therefore the standard deviation. Moreover, if not specified, all BOTDA tests were acquired using 0.64 MHz frequency step, 10 ns pulse with 20 cm spatial step.

4.2.2.1 **Procedure: Temperature and strain characterization**

In order to perform temperature and strain characterization of the BOTDA sensors and to evaluate the radiation effects on the performance of this technology, different set-up configurations are employed.

The study of the Brillouin frequency shift as a function of the total ionizing dose (TID) on the fiber requires tests performed on samples at the same strain and temperature conditions to avoid the shift due to these parameters (discussed in section 8.2 of Chapter 8). For this reason, the BFS dose dependency measurements have been done on ~ 100 m long samples free-coiled (i.e. without applied strain) with 8 cm diameter and inside an oven maintained at the constant temperature.

As discussed in Chapter 2 (equation 2.37), the linear dependence of the Brillouin frequency shift (BFS) on both the temperature and strain, does not permit the complete discrimination between these two parameters when applied simultaneously. In order to obtain the two coefficients; C_T and C_ϵ , two different kinds of measurements must be carried out. Figure 4.5 shows the arrangement set-up used to perform the temperature characterization of each sensing fiber.

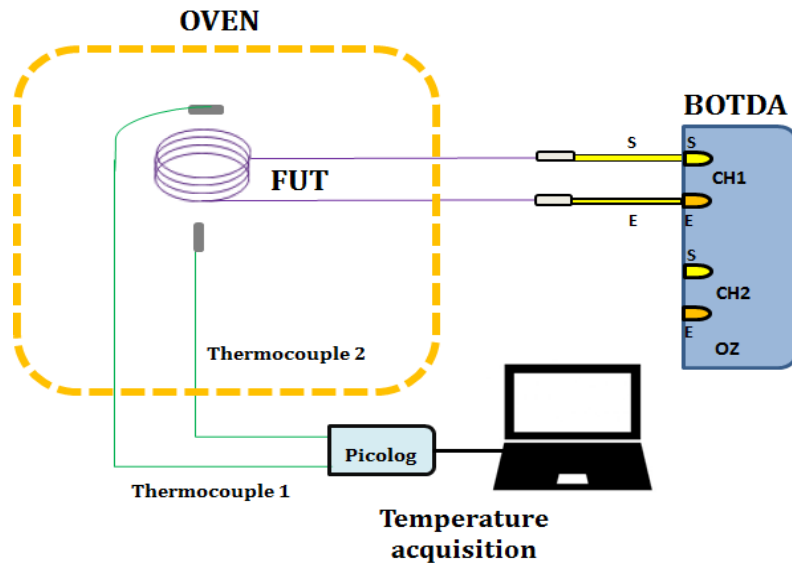


Figure 4.5 Set-up configuration used to perform temperature characterization. The fiber under test is designed as FUT.

For this investigation, a twenty meter long fiber was "free-coiled" with a diameter of ~20 cm with no solicitation applied, the sample was kept at a constant temperature inside an electrical furnace. For all thermal tests performed on the different samples, except the PSC-SMF_2, the temperature was increased from 30°C to 80°C with a step of 10°C or 20°C. In the case of the PSC-SMF_2, with a polyimide coating, the investigated temperature range was between 20 °C and 300 °C. The furnace temperature was monitored with two thermocouples located in close proximity to the sample.

The BFS temperature coefficient C_T is determined as the slope of the BFS evolution with temperature.

The strain coefficient is acquired by the experimental set-up illustrated in Figure 4.6. With this arrangement, 8 m long of pristine or irradiated sample passing through 5 pulleys is maintained stretched between two attachment points (indicated in figure as fixed and mobile plates). The axial strain is induced by stretching the optical fiber with a mechanical translation of 1 mm per displacement (mobile plate) and is given by: $\varepsilon = \frac{\Delta L}{L}$, where L is the length of stretched fiber (~8 m). The BFS strain coefficient C_ε is therefore extracted from the slope of the BFS changes as a function of the applied strain. During all tests the ambient

temperature (ranging between 22°C and 23°C) is under control via two thermocouples to allow the temperature correction on the strain measurement.

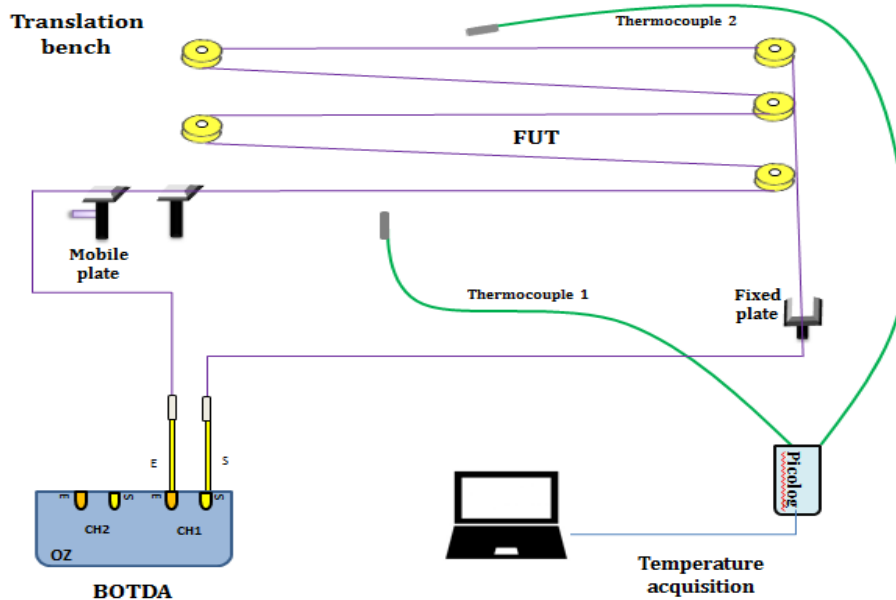


Figure 4.6. Translation set-up used to performed strain characterization. FUT indicate the fiber under test.

4.2.3 Optical time domain reflectometer

To evaluate the impact of the induced losses on the device performances, the BOTDA tests are supported by attenuation measurements performed with an OTDR working at 1550 nm. This technology has been developed in 1976 by Barnosky and Jensen [39] and is used to measure optical fiber attenuation characteristics on the overall fiber length. It allows both the evaluation of fiber losses due to connectors, splices and others sources and the determination of their exact location along the fiber link.

The equipment used in this work is a commercially OTDR from EXFO company [75]. The set-up of a generic optical reflectometer, shown in Figure 4.7, is relatively simple and basically includes a source of optical pulses, a photo-receiver, proper optical circuitry (such as couplers or circulators) to separate forward path from the backward one, and adapted electronics to process and store the recorded data [13]. Its working principle consists in launching a single short laser pulse into the fiber under test (FUT) to measure the roundtrip

time propagation and the amplitude of the reflected impulse (Rayleigh scattering). The device calculates the flight time of the pulse that is converted into distance. This task is carried out and repeated-averaged several times, at the end, a signal processing is performed to calculate the attenuation.

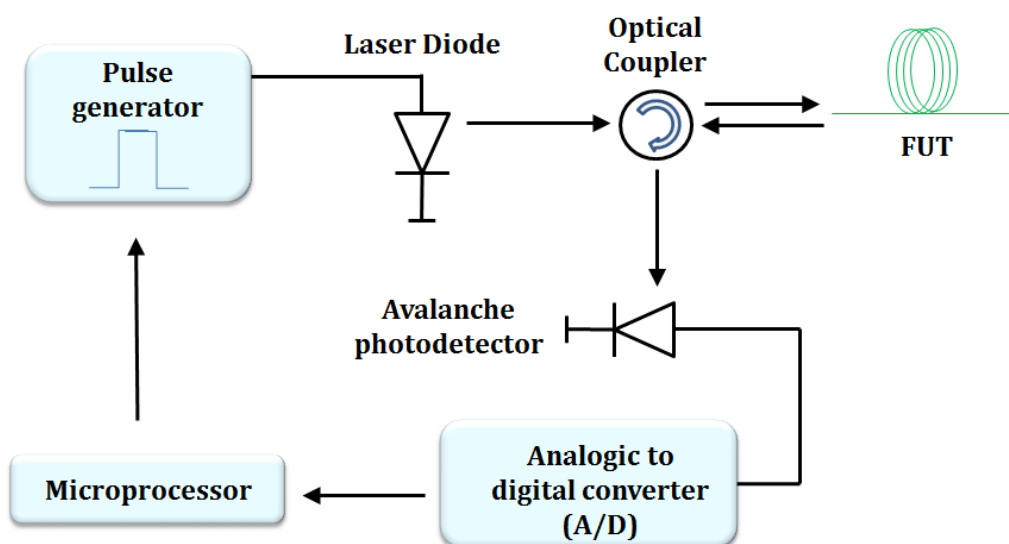


Figure 4.7. Blocks scheme of the OTDR. FUT designates the fiber under test.

All OTDR measurements in this thesis are performed using 10 ns pulse width and an acquisition time of 45 s. The induced attenuation (IA), at 1550 nm, is derived as the difference between the irradiated and/or hydrogenated attenuation and that acquired in the pristine sample.

4.3 Experimental set-ups: spectroscopic analysis

In this section we describe the experimental set-ups employed to investigate the optical properties of our OFs and the most relevant terms considered for carrying out the

4.3.1 measurements.

Optical Absorption measurement

To estimate the modifications in the OF transmission due to the harsh environment (γ -ray and/or hydrogen presences and T changes) representative of the Cigéo site (see Chapter 1),

optical absorption (OA) measurements were conducted from time to time in the spectral domain of interest. The IR range between 750 and 1700 nm, was explored by using an halogen lamp coupled to an Optical Spectrum Analyzer AQ6370C from Yokogawa. While, the UV-Visible range, between 200 and 750 nm, was studied with a deuterium light source coupled to a spectrometer QE65000 from Ocean Optics.

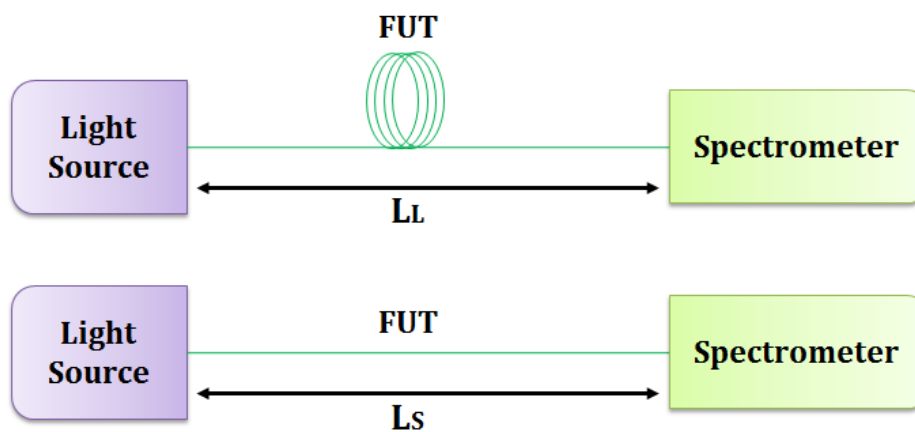


Figure 4.8. Experimental configuration of the *cut-back* technique used to acquire OA spectra of the fiber under test (FUT).

Both *ex-situ* and *in-situ* attenuation measurements were conducted during this study.

The *ex-situ* tests are performed at controlled RT some weeks or months after the γ -irradiation and/or hydrogenation. It means that the induced changes in the OF transmission can be considered as permanent at RT conditions. These measurements are based on the well-known cut-back technique [54], [76], which schematic diagram is illustrated in Figure 4.8.

It consists in measuring the OF transmission spectrum for two different lengths L_L (long) and L_S (short) respectively. L_S is obtained by cutting a fiber length ΔL , without changing injection conditions. The absorption spectrum, $a(\lambda)$, is therefore derived by applying the following equation [54]:

$$a(\lambda) = -\frac{10}{\Delta L} \times \log_{10} \left(\frac{I_{L_L}(\lambda)}{I_{L_S}(\lambda)} \right) \quad (\text{dBm}^{-1})^3 \quad 4.1$$

*The absorption coefficient, α , in cm^{-1} has been converted in dB/m by multiply for $2.303 \cdot 10^{-3}$.

where I indicates the intensities acquired with the long and short samples and ΔL is expressed in meter. While, the *in-situ* tests are conducted to monitor the infrared OA evolutions during the H_2 desorption and during the thermal treatment of one pre-irradiated sample (see section 4.4). In this case, the FUT (H_2 loaded or treated at $80^\circ C$) is linked to the white light source and to the IR spectrometer and the time evolution of the induced losses, $a(\lambda, t)$, (during the hydrogen desorption at RT or the thermal treatment at $80^\circ C$) is calculated relatively to the initial transmitted spectrum, $I(\lambda, t_0)$, as shown in equation 4.2:

$$a(\lambda, t) = -\frac{10}{L} \times \log_{10} \left(\frac{I(\lambda, t)}{I(\lambda, t_0)} \right) \quad (dBm^{-1}) \quad 4.2$$

where L is the fiber length expressed in meter. The continuous measurements are recorded every two minutes.

4.3.2 Electron Spin Resonance spectroscopy

The Electron Spin Resonance (ESR), also referred to Electron Paramagnetic Resonance (EPR) is the resonant absorption of electromagnetic radiation by an electronic spin system coupled to a static magnetic field, which takes place when the radiation frequency matches one of the characteristic transition frequencies of the system [77]. A standard ESR system investigates the resonance condition by exposing the sample to a fixed frequency ω_0 (in the microwave range) and varying the static magnetic field.

The ESR method can yield meaningful structural and dynamic information of systems characterized by an electronic magnetic dipole moment $\mu \neq 0$, as for example atoms and molecules with an odd number of electrons or partially filled shell, paramagnetic point defects, transition metal and rare earths ions. The main information obtained for the structure of all defects in the a-SiO₂ (amorphous silica) has been explained through ESR measurements on the models of paramagnetic defects.

When an atom or molecule with an unpaired electron is placed in a magnetic field, the spin of the unpaired electron can become aligned either in the same direction (spin up) or in the opposite direction (spin down) of the applied field. These two possible electron alignments correspond to different energy levels (i.e. are no longer degenerate) and are directly

proportional to the applied magnetic field strength [78]. This is the Zeeman effect which is explained through the levels diagram in Figure 4.9.

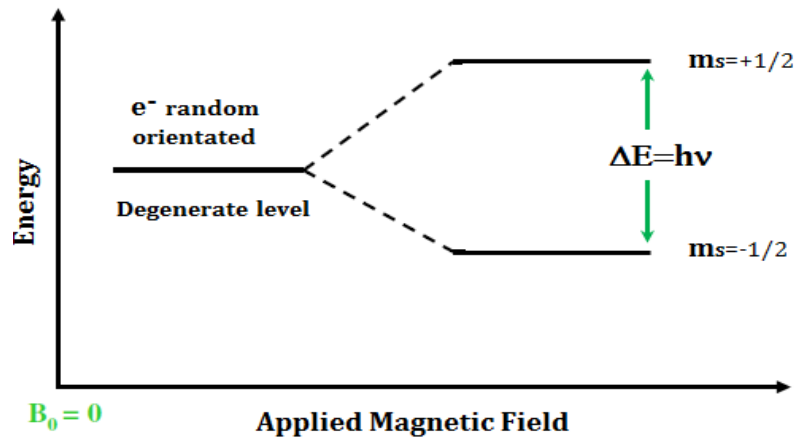


Figure 4.9. Zeeman effect on the ground state level of a system with $\bar{S} = 1/2$. \mathbf{B} indicates the magnetic field.

The corresponding measurements are performed with a Bruker EMX micro-Bay spectrometer working at 9.8 GHz (X-band) whose block scheme is reported in Figure 4.10 [79].

The sample to be investigated is located at the center of a resonant cavity, whose internal dimensions are comparable to the microwave wavelength. The microwave normal mode of the cavity, TE_{102} , resonating at about 9.8 GHz, is such that the magnetic field is maximum and the microwave electric field is minimum.

The microwave radiation (i.e. the oscillating magnetic field \mathbf{H}_1), is generated by a Gunn diode. During the measurement its frequency is controlled and modified by the Automatic Frequency Control (AFC) to keep the microwave radiation tuned to the frequency of the resonance cavity, filled by the sample under study. The power transmitted to the cavity, P_i , through a waveguide can be attenuated with respect to the maximum power generated by the microwave source (200 mW); it is measured in decibel units of attenuation using following equation:

$$Att(dB) = -10 \cdot \log_{10} \frac{P_i}{200mW} \quad 4.3$$

Moreover, the cavity is placed between the magnetic expansions of an electromagnet which generates a uniform static magnetic field \vec{H}_0 , perpendicular to the microwave field and varied during the measurement around the resonance value, responsible of the Zeeman splitting.

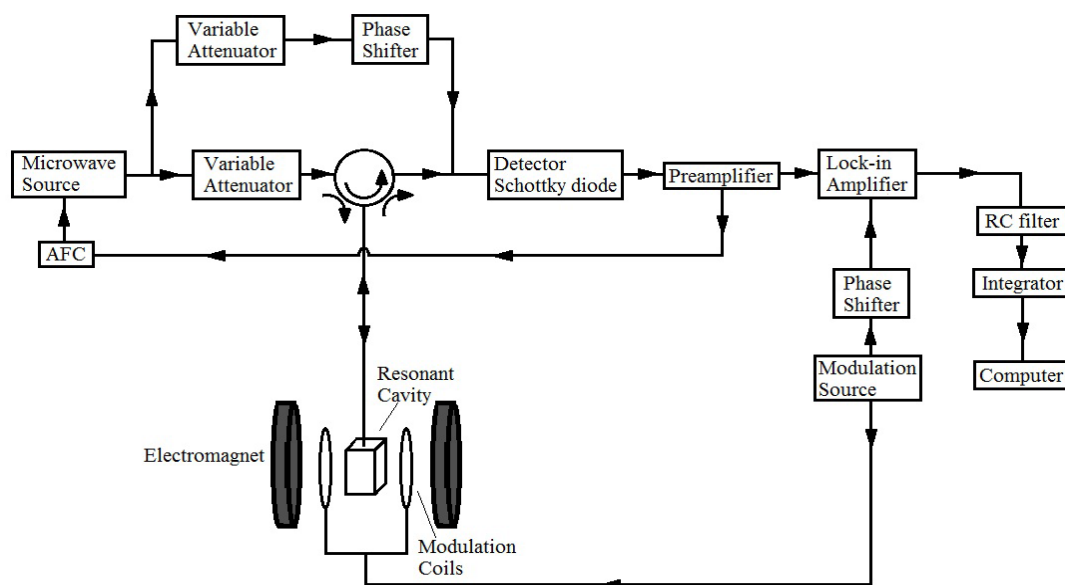


Figure 4.10. Block scheme of the ESR reflection spectrometer [79].

In order to enhance the signal to noise ratio of the ESR spectrometer, a third magnetic field \vec{H}_m , oscillating at $\omega_m = 2\pi 100$ kHz and called modulation field, is superimposed parallel to \vec{H}_0 allowing the use a lock-in detection system for the reflected microwave power. Then, the reflected microwave radiation is passed through two further steps: i) a filtering step (RC filter) required to improve the signal to noise ratio and ii) an integrating step (analog-to-digital converter) converting the current signal in digital ESR data.

For quantitative measurements, in order to avoid distortion and to obtained optimal quality of the ESR signal, the instrumental parameter of the incident microwave power, modulation field amplitude and integration range, are opportunely selected to satisfy specific conditions and more details can be found in [80], [81].

The ESR spectra are recorded using the *first-harmonic mode* (FH-ESR) [81], [30], It reveals the component of the signal oscillating at the frequency ω_m and in phase with the modulation magnetic field. The related ESR spectrum is a curve proportional to the first derivative of the

absorption line shape. The corresponding double integral, is proportional to the centers number present in the sample under study. Then, the concentration of the paramagnetic defects is usually estimated by comparison with a reference irradiated silica bulk samples whose spins concentration is known (i.e. the E'(Si) centers concentration is known through absorption measurements). The accuracy of the absolute concentration measurements obtained by ESR is estimated as 20%.

4.4 Facility and treatments

This section illustrates the different irradiation or hydrogen fiber-loading sessions conducted in this thesis work. Indeed, the evaluation of the distributed sensors performances requires taking into account the different constraints of Cigéo environment, such as γ -ray and H₂ release. From this viewpoint, two types of experiments are conducted: *ex-situ* and *in-situ*. The *ex-situ* measurements are performed some months after the treatments, i.e. γ -irradiation and/or hydrogen loading, at controlled temperature. Instead, the *in-situ* tests are conducted in the course of several days investigating the devices responses during γ -ray exposure or the H₂ desorption from the fiber core.

4.4.1

H₂ loading sessions and procedure

Two different sessions of H₂ loading treatment were performed on some FUT.

Session 1: H₂ loading at 80°C

The first H₂ loading session was conducted at the iXBlue SAS in Lannion (France) [82]. During this session, 100 m length of some SMFs and MMFs, coiled in 8 cm diameter loops were treated in H₂ atmosphere. In order to load molecular hydrogen in the OFs, they were soaked in hydrogen at 80 °C and 202 bars for 62 hours using a typical high-pressure reactor, whose schematic representation is showed in Figure 4.11. These loading conditions are sufficient to ensure the saturation of a typical fiber with mobile H₂ species. Afterwards the fibers are then removed from the H₂ tank and the samples were left at ambient atmosphere conditions allowing hydrogen to desorb naturally outside the fibers [83].

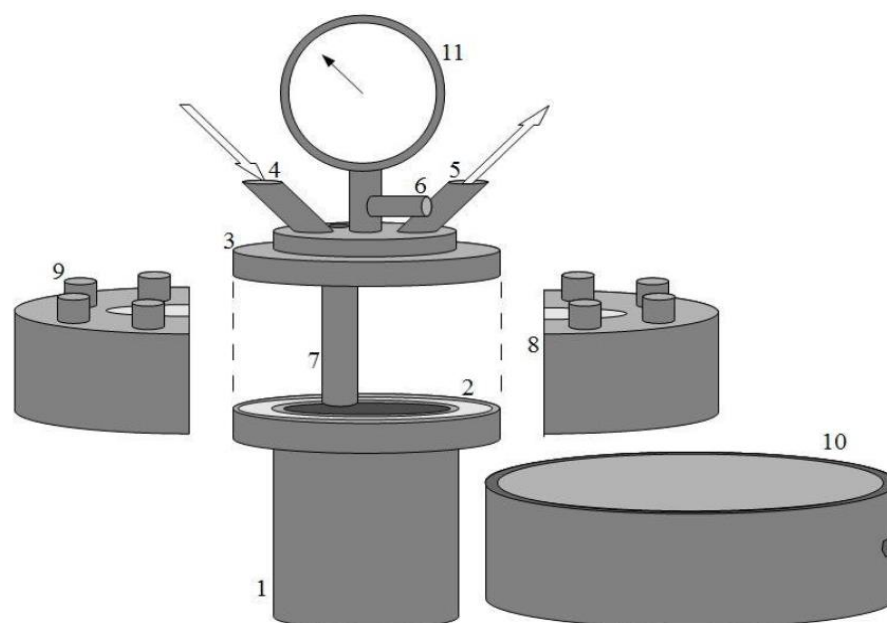


Figure 4.11. Schematic representation of a typical reactor employed for the H₂ loading treatments. 1 is the vessel, 2 is a gasket, 3 is the cover of the vessel, 4 and 5 are the input and output valves for the gases, 6 is a pressure transducer, 7 is the well in which a thermocouple is placed, 8 and 9 are two steel half-rings for closing, 10 is a safety steel ring, 11 is a analogical pressure gauge [132].

During session 1 both RDTS and BOTDA measurements were performed at RT ($22 \div 26^\circ \text{C}$) to monitor the sensors responses as a function of the H₂ concentration level inside the OF for several days. In this case, the RDTS measurements were performed with 300 s of acquisition time. Instead, the BOTDA response evolution was conducted at on pristine and H₂ loaded sample, spliced in series on the same measurement line. Frequency step of 1.28 MHz, pulse width of 10 ns and 20 cm spatial step were used. The attenuation measurements were also performed on the same samples at 1550 nm.

Session 2: H₂ loading at RT

This H₂ loading session was conducted as well at LabHC of Saint Etienne (France). To achieve the H₂ saturation in the investigated samples, the loading was executed for 474 h (~20 days) at RT and 140 bars. The hydrogen induced attenuation spectra evolution was recorded during the H₂ outgassing at RT ($20 \div 24^\circ \text{C}$).

γ -rays irradiation session at high total ionizing dose (Mol)

4.4.2 The γ -rays irradiations were performed with a ^{60}Co source (1.25 MeV photons) at BRIGITTE facility in SCK•CEN (Mol, Belgium) [84]. The dose-rate changes between 10 and 30 kGy(SiO_2)/h and the irradiation temperature can reach $\sim 50^\circ\text{C}$. During the runs, samples were located at different distances far from the ^{60}Co source, so the investigated TID ranges from 1 up to 10 MGy(SiO_2).

Regarding the H_2 -loaded fibers, we investigated two different kinds of samples: those loaded just before the γ -irradiation session (to maintain the highest possible molecular hydrogen level inside the fiber) and those loaded two months before the irradiation and left at RT allowing the mobile molecular hydrogen species to out-diffuse.

The corresponding OFs were characterized during the *ex-situ* tests session.

4.4.3 γ -rays irradiation session at low dose rate (Saclay)

The *in-situ* γ -rays irradiation tests were performed using the IRMA ^{60}Co source facility [85] of the IRSN⁴ (Paris-Saclay, France). This facility has a panoramic ^{60}Co irradiation cell available using four, independent, cylindrical sealed sources (11 mm in diameter and 452 mm in length). Its internal volume of 24 m^3 permits to accommodate a wide variety of geometric configurations for exposures to gamma radiation and give us the possibility to investigate both RDTS / BOTDA responses using as sensing elements OFs exposed to the same dose rate. The dose-rate and temperature values depend on the sample location relative to the source and also on the aimed total dose.

The measurements were performed at irradiation-room temperature (iRT) with a dose rate of 1 kGy(SiO_2)/h to reach TID of $\sim 160\text{ kGy}(\text{SiO}_2)$. The temperature was monitored and recorded by two thermocouples located inside the irradiation room during and after the irradiation run. Its amplitude ranges from 23°C to 26°C . The set-up configuration of our experiment is shown in Figure 4.12. Four different MMF samples were under test as sensing elements for the RDTS device: Ge-MMF, PSC-MMF_2, F-MMF_1 and a 10 MGy pre-

⁴ Radioprotection and nuclear safety institute

irradiated F-MMF_1. All samples were 100 m long coiled in 8 cm diameter. Moreover, the acquisition time was set to 120 s for one measure every 14 min in each sample.

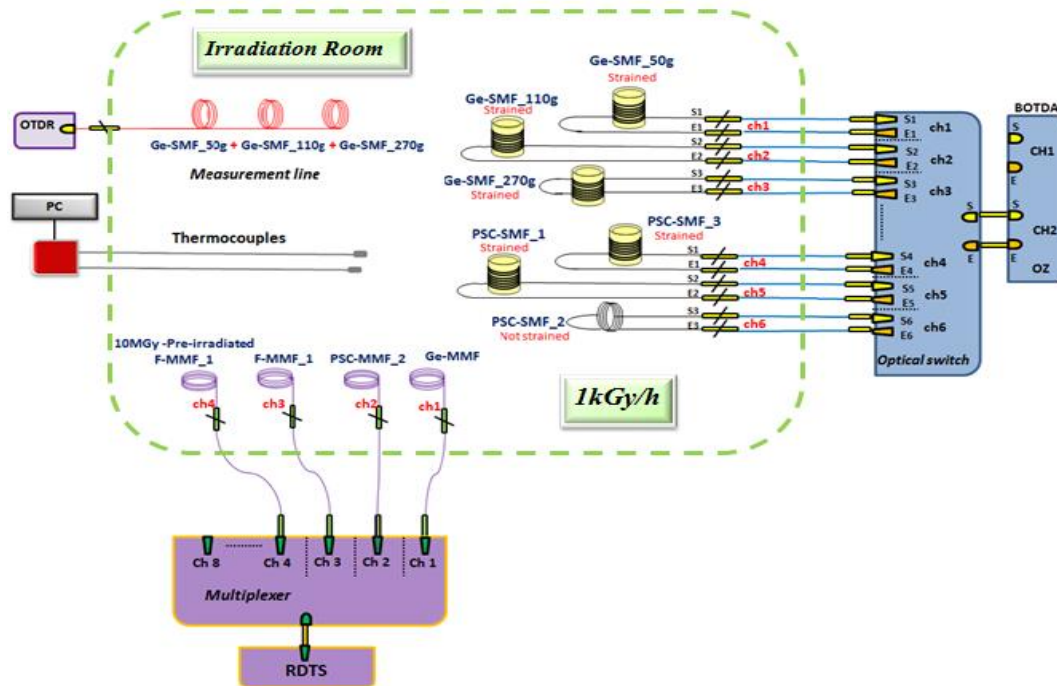


Figure 4.12. Set-ups configuration of our experiment. BOTDA, RDTs and OTDR devices linked to the investigated OFs are shown. The green dashed rectangle indicates the irradiation room. The samples' locations were chosen to achieve the same dose rate of 1 kGy(SiO₂)/h.

Concerning the BOTDA tests, the 6 different SMFs were studied as sensing elements. For all samples, except PSC-SMF_2 (100 m long "free-coiled" in 8 cm diameter), the device response is evaluated when different levels of external stress are applied along the fiber coil. Each of these samples was looped around a quartz cylinder⁵ of 10 cm diameter:

- The Ge-SMF_50g, Ge-SMF_110g, Ge-SMF_270g and PSC-SMF_3 are 70 m long with 4 different applied strain levels along the sensing line, 20 g, 131 g, 240 g, and 349 g.
- The PSC-SMF_1 is 115 m long with 7 applied stress steps of 20 g, 38g, 73g, 101g, 131g, 159, 184 g.

Each sample was analyzed every 8 hours as the BOTDA time response is long.

⁵ The quartz cylinder as a small thermal expansion coefficient similar to that one of a standard OFs.

Finally, in order to evaluate the radiation impact on the device performances, the OTDR measurements on Ge-SMF_50g, Ge-SMF_110g, and Ge-SMF_270g were performed at the operation wavelength of our BOTDA: 1550 nm.

It is important to indicate that due to a technical problem the irradiation stopped 42 h after the irradiation start and re-launched few hours afterwards. Because of this problem the first detected measurement by the RDTS is that one at 42 kGy cumulated dose.

Thermal treatments

4.4.4

The thermal treatments were carried out on PSC-MMF_1 and PSC-SMF_1 pre-irradiated samples and in the same configuration used for the BOTDA temperature characterization discussed in section 4.2.2.1 (see Figure 4.5). During all treatments the samples were kept at constant temperature of 80 °C for different days, this temperature was reached with a heating fast ramp of ~6 °C/min. The response of both RDTS and BOTDA using a pre-irradiated fiber as sensing element were monitored, during 7 and 55 days, respectively. In particular, the 10 MGy irradiated PSC-SMF_1 was characterized using the BOTDA while the 6 MGy irradiated PSC-MMF_1 was analyzed with the RDTS equipment. This RDTS test is supported by attenuation spectra evolution in the IR spectral range recorded on the 10 MGy PSC-MMF_1.

Chapter 5

SE-RDTS under gamma-rays and H₂ exposure

This is the first of the 5 chapters in which we report and discuss our experimental results about γ -rays and H₂ loading influences on the SE-RDTS performances at MGy dose levels. The obtained results allow us to characterize the radiation and hydrogen tolerance of SE-RDTS using different classes of optical fibers as the sensing element.

5.1 Introduction

As formerly discussed in Chapter 2 our SE-RDTS relies on optical intensities and is sensitive to the fiber attenuation at the Nd:YAG laser pump wavelength ($\lambda=1064$ nm) used to excite the Stokes (S) and anti-Stokes (AS) lines at 1014 nm and 1114 nm, respectively. In particular, if the measurement is not compensated for the differential attenuation ($\Delta\alpha$) between the S and AS intensities, an incorrect temperature evaluation is provided by the system. An example of a typical temperature measurement performed with our SE-RDTS system (without any calibration) on a 4 km long commercial fiber (F-MMF_1) at laboratory ambient conditions (RT and no radiations) is shown in Figure 5.1. Despite the constant and uniform temperature along the whole sample length, we observed an error on the measured temperature; its amplitude increases with the fiber distance (up to 10 °C after 4 km). In fact, such a discrepancy is due to the previously-discussed differential attenuation, $\Delta\alpha$, whose impact becomes more and more important when the sensing distance increases. If during the

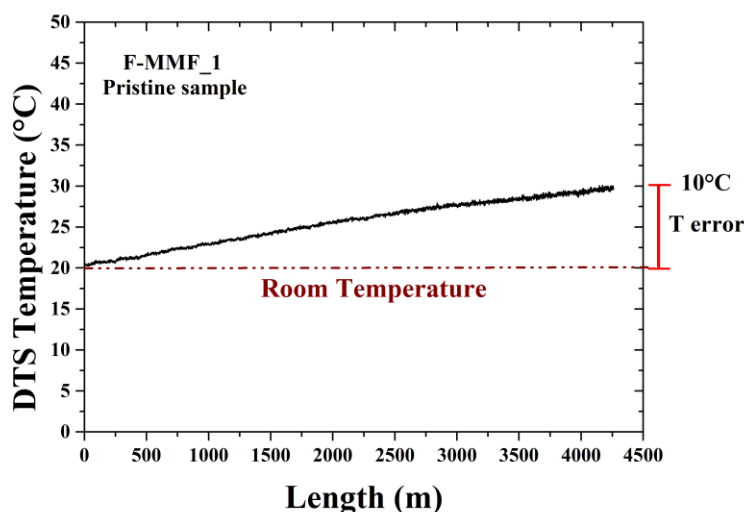


Figure 5.1. Raman Distributed Temperature measurements using the commercial F-MMF_1 fiber as sensing element. Test performed at RT ($\sim 20^\circ\text{C}$) and without any RDTS calibration.

temperature measurements $\Delta\alpha$ remains constant in time and is uniform along the fiber, a simple starting calibration permits to overcome this error source. In the framework of the present PhD thesis work, the Cigéo application requires to use the RDTS systems inside an environment in which the γ -ray dose rates and the H_2 release can evolve with time and with position and then highly degrade the optical fiber by causing non-homogeneous $\Delta\alpha$ along the sensing line.

Radiation tolerance of the Raman spectrum at MGy dose

Confocal micro-Raman *ex-situ* (after the γ -radiation exposure) measurements⁶, performed on a 2 cm fiber length of F-MMF_1, were executed to compare the S and AS signal intensities observed in the pristine and 10 MGy γ -irradiated F-MMF_1 samples. The spectrum is reported in Figure 5.2: it shows the typical Raman features of the fiber core related to the amorphous silica structure. The intense band at 440 cm^{-1} is assigned to the symmetric stretching mode of the bridging oxygen (Si-O-Si) in the large rings (number of Si atoms >4)

⁶ Raman spectra were executed with a LabRAM HR-Evolution spectrometer from Horiba Jobin Yvon [133] an integrated multiline confocal microRaman system at the CHAB laboratory of Palermo (Microscopy and Bioimaging Lab, PONA3_00273, University of Palermo) enabling Stokes and anti-Stokes signal detection with excitation laser at 532 nm.

of SiO₄ tetrahedra [86]. The frequency of the 440 cm⁻¹ band is 13.2 THz, coinciding with that one used by our RDTS device. The sharp shoulders near 480 cm⁻¹ (D₁-bands) and the peak at ~ 600 cm⁻¹ (D₂-band) are associated with the same mode of the characteristic four- and three-membered rings of SiO₄ tetrahedra, respectively [87]. We note that these confocal microscope measurements reveal no change in the Raman AS and S relative intensities of the two 2 cm samples, pristine and 10 MGy γ -irradiated. This is not really surprising since at such a dose level, the Raman spectra are robust to small changes in the fiber structure [88]; in fact, it is known that large neutron fluencies ($>10^{17}$ n/cm²) are required to induce significant modifications of Raman spectra [89].

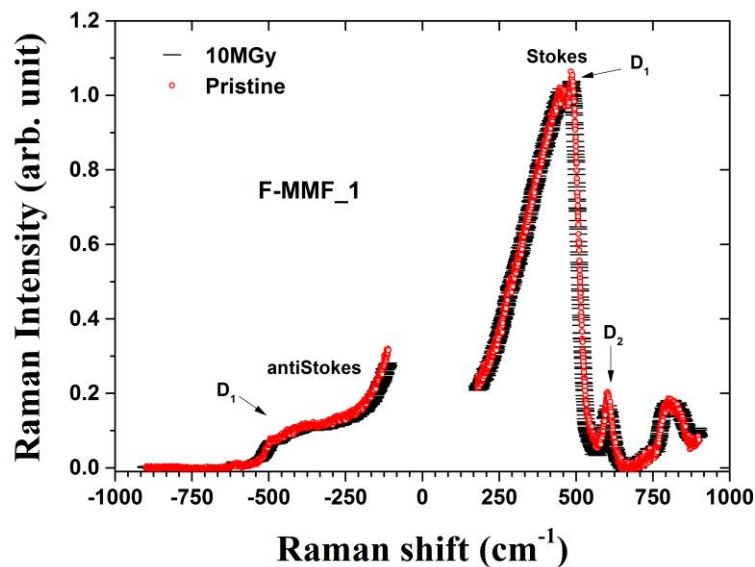


Figure 5.2. Raman spectra in the cores of pristine (red dots) and 10 MGy irradiated (black dash) samples of fiber F-MMF₁. The measurements were performed at room temperature (~20°C).

Despite the robustness of the Raman scattering phenomenon against γ -rays (up to 10 MGy TID⁷), such conditions strongly affect the fiber infrared transmission [90], [91], [92], as well as the H₂ presence [68]. Both radiation and hydrogenation induced attenuation (RIA or HIA, respectively) can influence the SE-RDTS temperature monitoring when the sensing range exceeds tenths of meters. The experiments presented in this chapter aim to evaluate the importance of these attenuation phenomena on the device performances. In order to highlight

⁷ Total ionizing dose

the strong connection between the RDTS response and the evolution of the spectral attenuation with γ -ray exposure and/or H_2 loading, the RDTS temperature measurements are supported by attenuation measurements in the IR, that is the spectral range of our interest, $1014nm \div 1114nm$ ($\lambda_{as} \div \lambda_s$).

5.2 H_2 presence effects on RDTS response

The experiments concerning the influence of the hydrogen presence inside the sensing fiber on the RDTS performances were carried out on 4 types of multimode fibers: PSC-MMF_1, PSC-MMF_2, F-MMF_2 and P-MMF, their characteristics being reported in section 4.1. The evolution of RDTS temperature error as a function of the H_2 concentration was investigated depending on fiber dopant. The coated optical fibers were soaked in hydrogen at 80 °C and 202 bars for 62 hours, conditions sufficient to ensure the saturation of a typical multimode fiber with mobile H_2 species (H_2 -loading session 1, see section 4.4.1). The fibers are then removed from the H_2 tank and the effect of the natural hydrogen desorption on the RDTS response is followed leaving the treated samples at RT [83].

Figure 5.3 shows the influences of the H_2 -loading of PSC-MMF_1, PSC-MMF_2, F-MMF_2 and P-MMF (a, b, c, d, respectively) on the temperature calculated by the RDTS at room temperature. In order to highlight the evolution of RDTS response as a function of the H_2 content into the fiber, the temperature is reported for several days during the H_2 outgassing. Similar results are obtained for PSC-MMF_1, PSC-MMF_2, F-MMF_2 (Figure 5.3 a, b, c, respectively): it appears not possible to measure the temperature with RDTS sensors when the sensing fiber contains molecular hydrogen, even at low concentrations ($\geq 10^{19} - 10^{20}$ H_2 molecules/cm³). Indeed, we observe a nonlinear growth of the temperature error along the fiber distance up to ~ 800 °C, corresponding to the RDTS limit. For each of these fibers (PSC-MMF_1, PSC-MMF_2, F-MMF_2), the amplitude of the temperature error at a given fiber location decreases with the H_2 concentration inside the fiber.

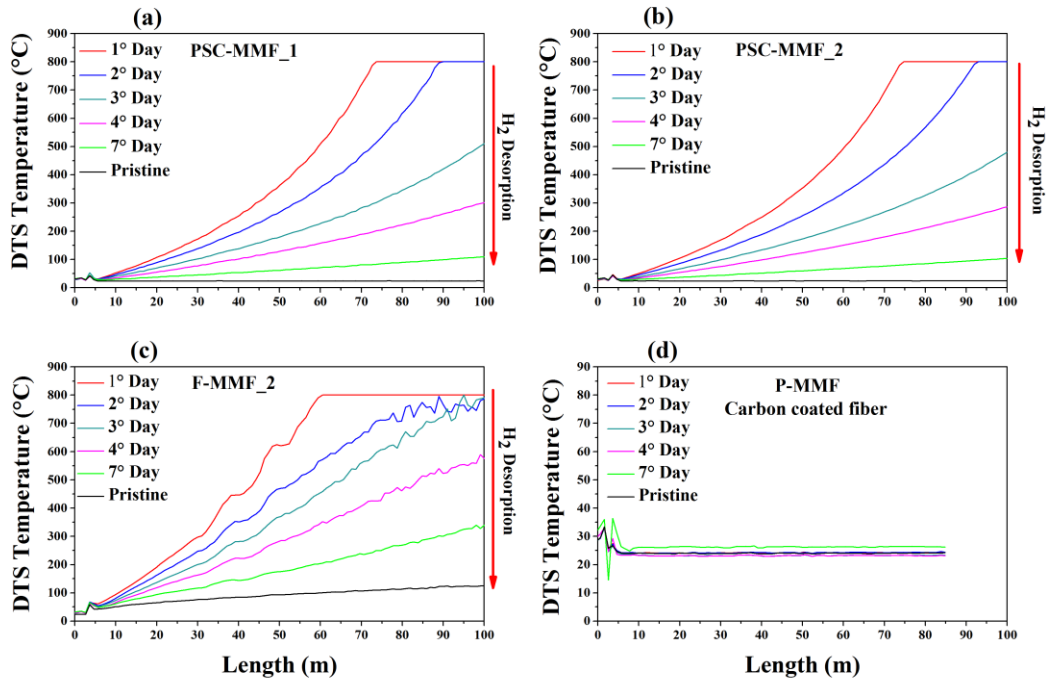


Figure 5.3 Distributed Temperature measurements calculated by the RDTS instrument on PSC-MMF_1 (a), PSC-MMF_2 (b), F-MMF_2 (c) and P-MMF (d). Results of pristine and H₂-loaded samples monitored during different days are shown. All measurements are performed at room temperature during 7 days.

It should be noted that the pristine fluorine doped F-MMF_2 shows a nonlinear temperature increase with the fiber length up to 110 °C at the distance of 100 m. Therefore, it appears not suitable as sensing element for our RDTS systems due to this specific behavior that was not observed in any other sample (see Figure 5.4). Finally, worth of attention is the result observed for the fiber P-MMF, shown in Figure 5.3 d. Indeed, to overcome the strong modifications in the propagation losses due to the H₂ presence, we selected a carbon coated fiber (see section 4.1), which ought to prevent the hydrogen diffusion inside the fiber in our loading conditions (80°C, 202 bars). In Figure 5.3 d, displaying the temperature calculated by RDTS device at the same times than for the other fibers, no H₂-related temperature error is observed. Therefore, this special coating is particularly suitable for Raman sensing in hydrogen presence, at least when temperature and pressure remain sufficiently limited to ensure that the thin carbon layer of few nanometers remains not permeable to hydrogen.

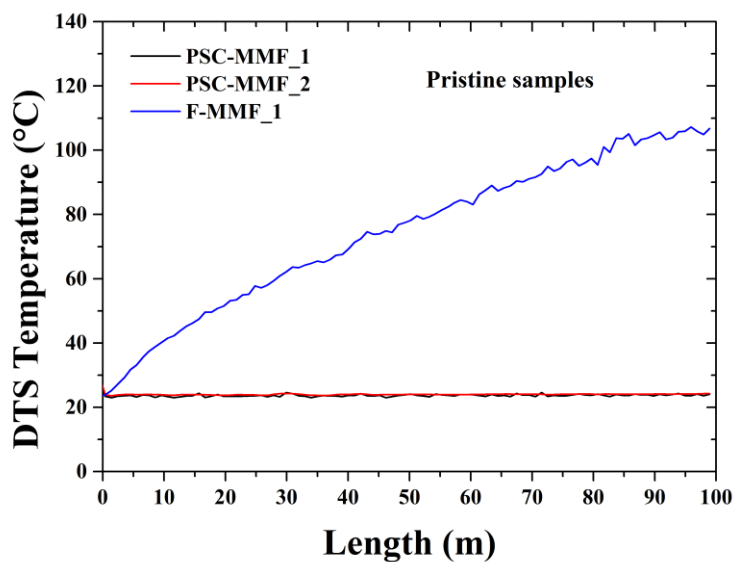


Figure 5.4 Comparison of distributed temperature measurements performed at room temperature on pristine sample of PSC-MMF_1 (black line), PSC-MMF_2 (red line) and F-MMF_2 (blue line).

Figure 5.5 illustrates the comparison between a hydrogen diffusion resistant (H-DR) fiber coated with carbon, P-MMF, and the PSC-MMF_1 surrounded by a standard acrylate coating.

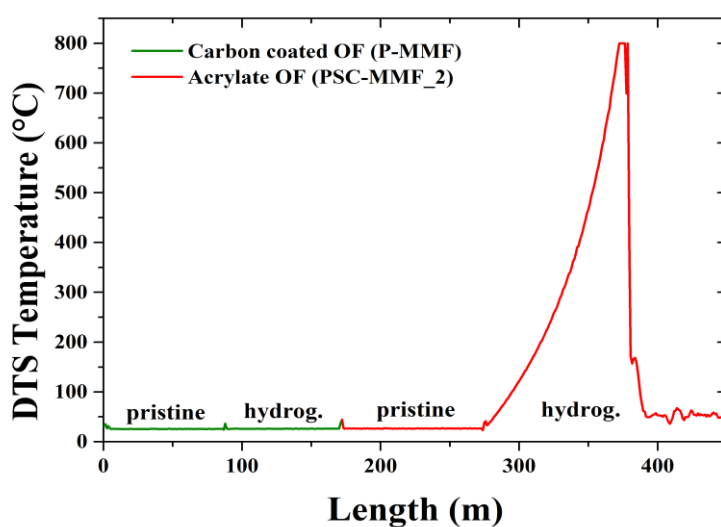


Figure 5.5. Distributed Temperature measurements calculated by the instrument on H₂-diffusion resistant (H-DR) P-MMF and on standard optical fiber PSC_MMF_1 (pristine or loaded with H₂).

Four samples have been connected in series: first, the pristine P-MMF, second the H₂-loaded P-MMF, third the pristine PSC-MMF_1 and at the end the H₂-loaded PSC-MMF_1. Whereas the H₂-loading of the PSC-MMF_1 induces the maximal temperature error of ~800 °C calculated by the RDTS at a distance of 100 m length, the H-DR fiber P-MMF treated in the same conditions still provides a correct estimation of temperature.

IR Spectral attenuation changes induced by H₂

5.2.1

As previously argued the false temperature reading increase with distances is caused by the differential hydrogen induced attenuation, ΔHIA ($\alpha_{AS} - \alpha_S$), between the S and AS signals that is due to the absorption bands associated with the H₂-presence. Transmission measurements on H₂-loaded silica optical fibers are present in literature and show, near the spectral range 1014nm ÷ 1114nm, the existence of absorption peaks (at 1083 nm, 1132 nm and 1245 nm) identified as overtones of the fundamental vibration at 2410 nm for the molecular hydrogen and combined silica-lattice vibrations [68], [93], [94]. The strengths of the H₂-induced absorption bands allow us to estimate the initial hydrogen content in our low-OH fibers using the first overtone amplitude at 1245 nm. Moreover, the overtones absorption linked to H₂ is reversible [94], the extra losses will disappear when H₂ will diffuse out the sample. For this reason, spectral attenuation measurements have been performed at the different H₂ levels and are shown below.

In order to achieve the H₂ saturation in the investigated samples, the loading has been executed for 474 h (~20 days) at room temperature and 140 bars (H₂ loading session 2). The attenuation spectra of PSC-MMF_1, PSC-MMF_2, F-MMF_2, were monitored at room temperature during the first two weeks following the end of the hydrogen loading. As similar spectral behaviors were observed for these 3 fibers, we reported in Figure 5.6 only the results of the pure-silica core, PSC-MMF_2 (Figure 5.6 a); and the fluorine doped, F-MMF_2 (Figure 5.6 b). The spectra present the typical first overtone (Q₂) absorption band at 1245 nm of H₂ species. As reported by Stone [8], at this wavelength, 5.6×10^{20} H₂ molecules/cm⁻³ induce an additional optical loss of 7.5 dB/m. In the present case, on the basis of HIA measured at 1245 nm (1.3 dB/m), we can estimated the initial H₂ concentration at the saturation to be of the order of $\sim 10^{20}$ molecules/cm⁻³.

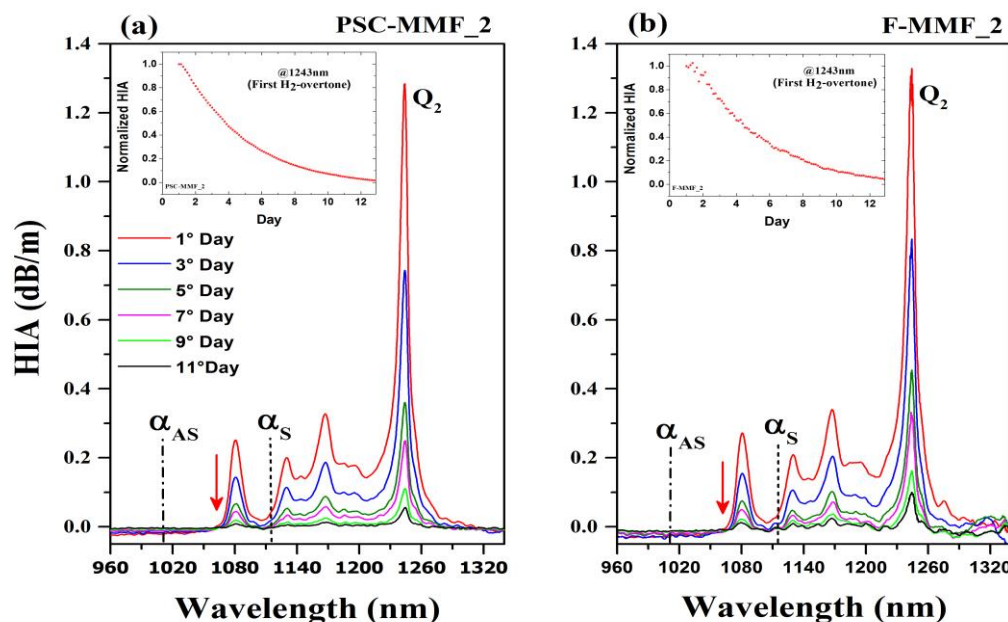


Figure 5.6. Attenuation spectra evolution in samples PSC-MMF_2 (a) and F-MMF_2 (b) saturated with H_2 and during H_2 desorption for 12 days at RT. The insert shows the normalized hydrogen induced attenuation (HIA) evolution as function of desorption time. The red arrow indicates the pump wavelength, λ_0 , and the vertical lines mark the wavelength positions of Raman anti-Stokes, I_{AS} , and Stokes, I_S signals (at 1014 nm and 1114 nm, respectively).

Figure 5.6 and Figure 5.7 provide a clear evidence for noticeable differences between the HIA values at the anti-Stokes and at Stokes wavelengths, resulting in a significant ΔHIA that will directly affect the RDTS performance causing an error on its temperature monitoring.

This effect is larger when large amount of H_2 species is present in the fiber core. Figure 5.8 shows, for PSC-MMF_2 (a), F-MMF_2 (b), PSC-MMF_1 (c), both the desorption kinetics of H_2 through the temporal evolution of HIA related to the H_2 overtone peak, Q_2 , at 1245 nm and the kinetics of the temperature error affecting the RDTS measurements. This comparison highlights the direct relationship between this microscopic effect and the macroscopic degradation of the sensor. Nevertheless, the kinetics of the temperature error slightly differs from that observed for the HIA; it is explained by to the different H_2 loading conditions leading to different initial saturation conditions [95], [96].

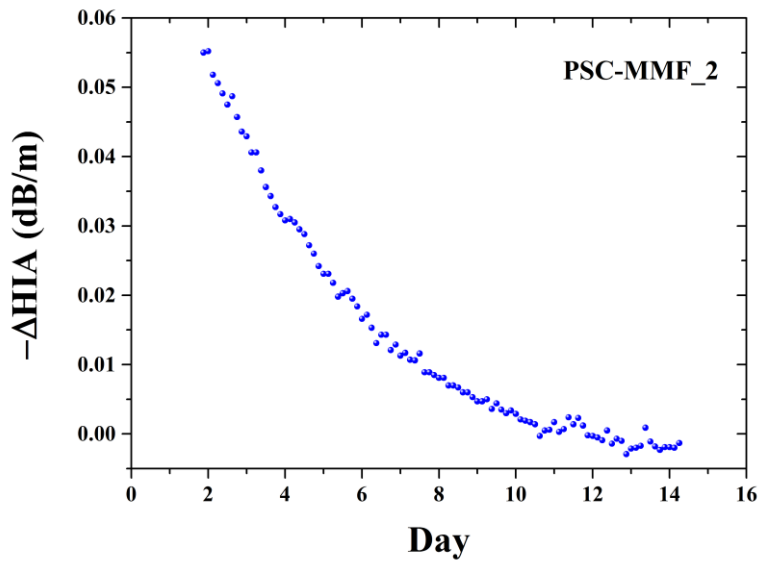


Figure 5.7. Differential hydrogen induced attenuation, ΔHIA ($\alpha_{\text{AS}}-\alpha_{\text{S}}$), evolution obtained by HIA spectra of PSC-MMF_2.

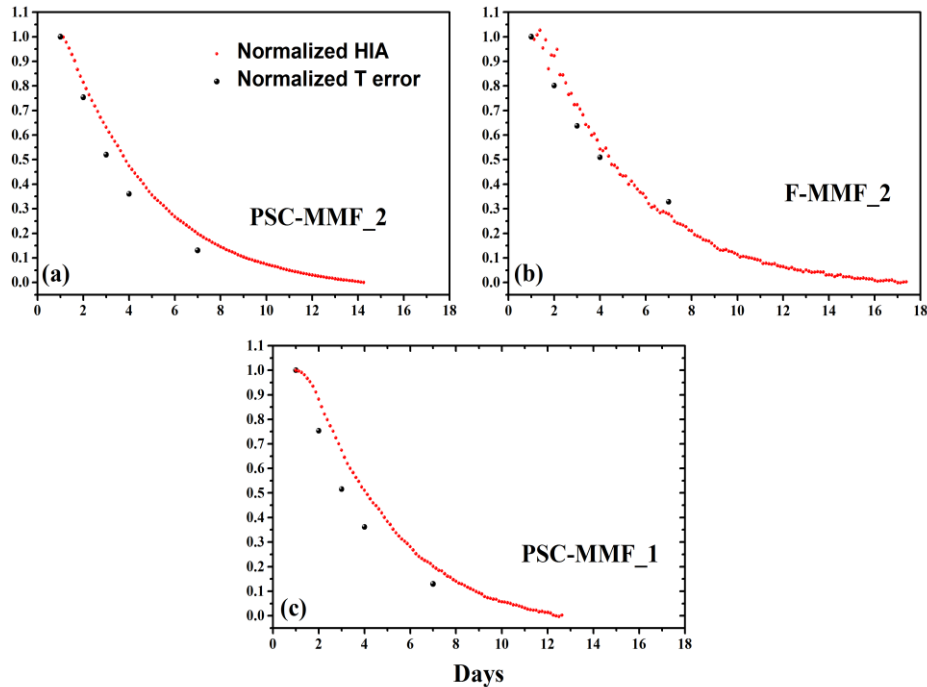


Figure 5.8. Comparison between the time kinetics of normalized T error time evolution and the H_2 -induced normalized attenuation at ~ 1243 nm (Q_2) during H_2 desorption for PSC-MMF_2 (a), PSC-MMF_1 (b), F-MMF_2 (c) fibers is reported. In both case the hydrogen outgassing is monitored at RT.

5.3 γ -rays effects on RDTs response: *Ex situ* measurements

This section reviews our study on the *ex-situ* RDTs performance when the sensing fibers designed with various dopants and irradiated at the MGy dose levels are used. Such tests were carried out on 6 types of sensing MMF, whose characteristics are reported in section 4.1. The RDTs performances are investigated as a function of the TID (up to 10 MGy) and as a function of the fiber type.

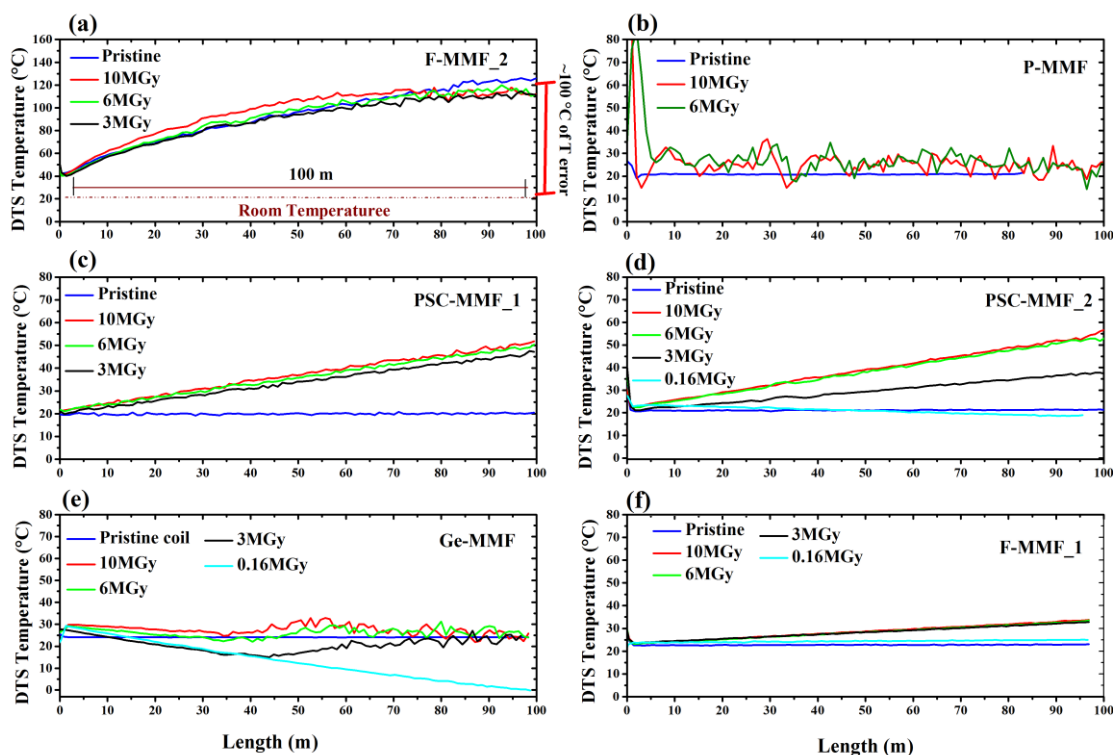


Figure 5.9. RT (~ 22 °C). Distributed Temperature measurements detected by the RDTs instrument on F-MMF_2 (a), P-MMF (b), PSC_MMF_1 (c), PSC-MMF_2 (d), Ge-MMF (e), F-MMF_1 (f). Results of pristine and γ -irradiated samples at 0.16, 3, 6, 10 MGy (sky blue, black, green and red line, respectively) are shown.

Figure 5.9 illustrates the Raman temperature measurements performed at RT (~ 22 °C) on samples of F-MMF_2, P-MMF, PSC_MMF_1, PSC-MMF_2, Ge-MMF, F-MMF_1 (a, b, c, d, e, f, respectively) pristine and pre-irradiated at different TIDs. Gamma irradiation of the sensing fiber leads the RDTs device to evaluate wrong temperatures; the error depends on the sensing distance. For the reported results, these false measurements can be compared to the

temperature that is correctly monitored by RDTS system using the pristine samples. An exception should be noted for the F-MMF_2 that is radiation resistant but gives false results even with the pristine sample (Figure 5.9 a). As previously stated, this commercial fiber is not suitable as sensing element for our RDTS system.

Figure 5.9 b shows the γ -ray influence on the RDTS temperature evaluation using the hydrogen diffusion resistant P-MMF. The optical incident or backscattered signals are completely absorbed along the 100 m fiber length at 10 MGy and 6 MGy. Therefore, the use of this commercial P-doped fiber, despite its tolerance to H₂ presence, is forbidden for our applications.

For the PCS-MMF_2, Ge-MMF and F-MMF_1 fibers, studied in details in the forthcoming paragraphs, the RDTS response is also investigated at a lower TID value of 0.16 MGy. This sample was irradiated during the IRMA irradiation session (see section 4.4.3).

Figure 5.9 c and d illustrate the Raman temperature measurements performed at RT on pristine and γ -ray irradiated PCS-MMF_1 and PCS-MMF_2, respectively. Gamma irradiation of the sensing fiber affects the sensor response: a false large linear increase of the calculated temperature assessed by the RDTS with the fiber distance is observed. In detail, a temperature of ~ 50 °C (i.e. ~ 30 °C of T error) is detected at a distance of 100 m. Using the PSC-MMF_2 sample irradiated at the low TID of 0.16 MGy, RDTS shows an opposite behavior detecting a temperature slightly decreasing along the sensing fiber. Therefore, temperature error increases both with the distance and with the total ionizing dose. As reported in literature (see Chapter 3) this negative impact is caused by the RIA.

Figure 5.9 e reports the RDTS response when pristine or γ -ray samples of Ge-MMF fiber are used. In this case, we observe a correct temperature evaluation with the pristine sample and a more complex response of the sensor with the irradiated samples. Indeed, all cases with irradiated samples show that temperature decreases linearly with the distance up to 40 m, at longer distance, the Raman signal is lost. Decreasing values of the temperature error with distance differs from the observed response of the other fibers, for which the temperature error increases with the fiber distance at high TID (3, 6, 10 MGy).

Finally, Figure 5.9 f presents the irradiation effects on the RDTS measurements when the radiation resistant F-MMF_1 is used as sensing element. We need to give special attention to

this commercial fiber as it exhibits for high TID value a limited increase of temperature error of ~ 10 °C (with respect to the pristine sample) at a 100 m distance. The temperature error increases more weakly with the distance than for the other tested fibers and the radiation related error tends to saturate in the investigated dose range (3 MGy \div 10 MGy). Furthermore, no important γ -ray-influence on the RDTS measurement is observable in the 0.16 MGy irradiated sample. It means that the RDTS measure is not permanently impacted by γ -rays at doses below 0.16 MGy.

Therefore, the comparison between the radiation resistant F-MMF_1 (Figure 5.9 f) and the standard PSC-MMF_1 or PSC-MMF_2 (Figure 5.9 c and Figure 5.9 d, respectively) highlights that, at the larger TID (10 MGy), the error on DTS temperature evaluation can be reduced using this radiation resistant fiber (~ 10 °C on 100 m fiber length).

5.3.1 Spectral attenuation changes induced by γ -rays

We first focus our attention on the attenuation spectra of the pristine and γ -irradiated (3 MGy) of F-MMF_2 samples, reported in Figure 5.10. Both pristine and irradiated F-MMF_2 samples present the same attenuation spectra, confirming the resistance to radiations of this commercial fiber. This fiber presents the huge absorption bands associated with the OH overtones in the IR domain that disturb the RDTS system by causing a differential attenuation between Stokes and anti-Stokes lines. This differential attenuation results in the false nonlinear increase of RDTS calculated temperature with the sensing fiber distance, as observed in Figure 5.4 and Figure 5.9 a.

Figure 5.11 illustrates the attenuation spectra obtained for the P-MMF, Ge-MMF, PSC-MMF_1 and PSC-MMF_2 (a, b, c, d, respectively) at RT. They show higher RIA values in irradiated samples of P-MMF compared to the three other fibers. All fibers present different RIA values at the anti-Stokes and Stokes wavelengths and at the different TIDs. As expected, the RIA level is fiber composition dependent.

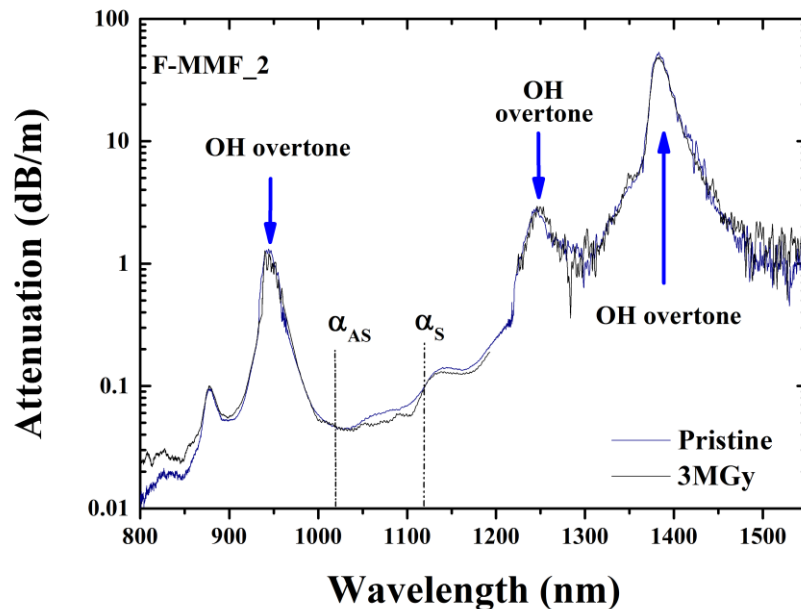


Figure 5.10. Attenuation spectra at RT of pristine and 3 MGy γ -irradiated samples of F-MMF_2. The OH overtones at 943 nm and 1384 nm, 1240 nm [134] are highlighted. Vertical lines mark the wavelength positions of Raman intensity anti-Stokes, I_{AS} , and Stokes, I_S (at 1014 nm and 1114 nm, respectively).

The poor radiation resistance of P-doped glasses, and at a lower level of Ge-doped ones compared to the pure or F-doped fibers in the IR is well known [91], [92]. Figure 5.11 a and b reveal high RIA levels in the spectral operation domain of our RDTS system, between the AS and S lines around 1064 nm. This RIA limits the available sensing distance down to ~ 40 m for the Ge-MMF (Figure 5.9 e) and forbids the use of sensors based on phosphorus-containing fibers (Figure 5.9 b). Furthermore, for the Ge-doped fiber the radiation-induced temperature error decreases linearly up to the sensing distance of 40 m whereas it increases for the other fiber types (Figure 5.9 c and d). This behavior can be explained by the differential attenuation, $\alpha_{AS} - \alpha_S$ (ΔRIA), that is positive for this Ge-doped fiber and negative for the other types. These ΔRIA values are reported in Table 5.2 of section 5.5. **Therefore, we clearly provide evidence for two different features impacting the RDTS temperature measurements: the radiation-induced attenuation (RIA) that limits the sensing distance range and the differential radiation-induced attenuation (ΔRIA) between Stokes and anti-Stokes lines that causes an error in the RDTS temperature calculation increasing with the sensing distance.**

Figure 5.11 c and d report the attenuation spectra of pristine and γ -irradiated (at 0.16 MGy, 3 MGy, 6 MGy, 10 MGy) samples of PSC-MMF_1 and PSC-MMF_2, respectively. These fibers have the same RIA spectral dependence, induced losses being minimum around 1000 nm. In our spectral region of interest, the RIA at high TID values (3, 6, 10 MGy) is of the same order of magnitude (~ 0.05 dB/m) for both fibers and the Δ RIA appears negative.

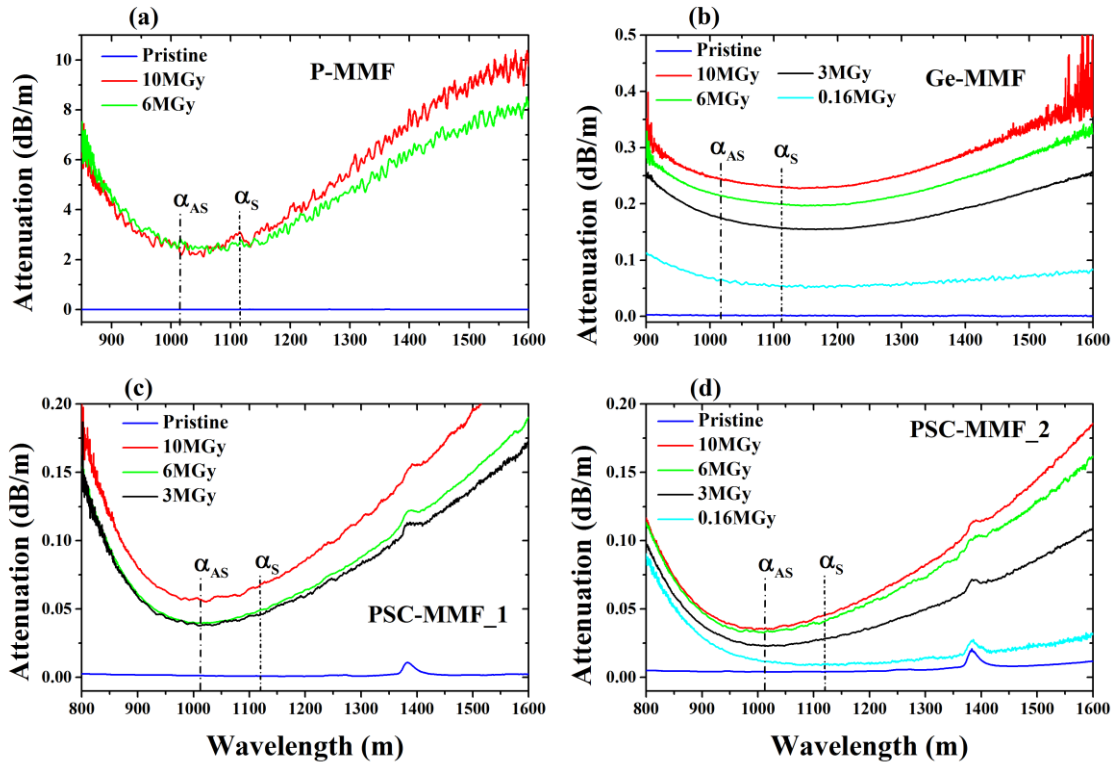


Figure 5.11. Attenuation spectra at RT of pristine and γ -irradiated samples at 0.16, 3, 6, 10 MGy of P-MMF (a), Ge-MMF (b), PSC-MMF_1 (c), PSC-MMF_2 (d) fibers. Vertical lines mark the wavelength positions of Raman anti-Stokes, I_{AS} , and Stokes, I_S signals.

Moreover, focusing our attention on PSC-MMF_2, comparing the RDTS measurements (Figure 5.9 d) and the spectral attenuation measurements (Figure 5.11 d), we observe a temperature error increasing with the fiber distance combined with negative Δ RIA values at the high TID of 3, 6, 10 MGy (black, green and red lines in Figure 5.11 d, respectively), whereas the temperature error decreases with distance at the lowest dose of 0.16 MGy for which we measure a positive Δ RIA (sky blue line in Figure 5.11 d). These results are another

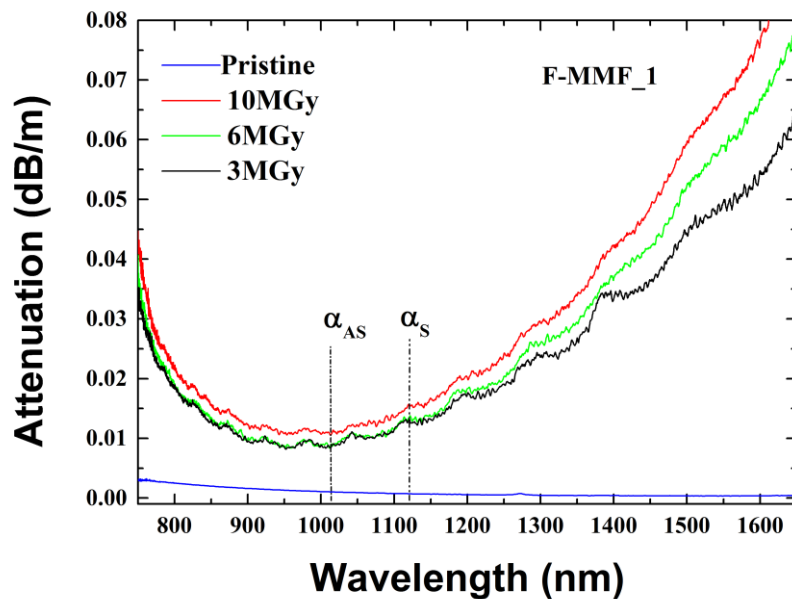


Figure 5.12. Attenuation spectra at RT of pristine (blue line) and γ -irradiated samples at 3, 6, 10 MGy (black, green and red lines, respectively) of F-MMF_1. The vertical lines mark the wavelength positions of Raman intensity anti-Stokes, I_{AS} , and Stokes, I_S signals.

nice confirmation that the increasing temperature error detected along the sensing fibers originates by the different signal attenuations at the anti-Stokes and Stokes wavelengths.

Figure 5.12 shows the attenuation spectra measured on the radiation resistant F-MMF_1 before and after irradiation at different TIDs. For this fiber, the linear trend of the temperature error with the fiber distance is still observed at TID of 3, 6 and 10°MGy. By contrast with the pure-silica-core fibers, PSC-MMF_1 and PSC-MMF_2 (Figure 5.11 c and d), the radiation resistant F-MMF_1 has lower values of RIA and smaller Δ RIA between the two Stokes and anti-Stokes signals. This leads to a better RDTS response, as observed in Figure 5.9 f.

5.4 Combined γ -rays and H₂ effects on the RDTS performance: Ex situ measurements

In the previous 5.2 and 5.3 sections, the evaluation of the vulnerability of RDTS performances as a function of the extreme conditions of Cigéo (H₂ and γ -rays presence) was done for several fiber types. The Raman response is strongly impacted by the dose and by the

hydrogen presence into the sensing fiber core. Both HIA and RIA influence the relative intensities of Stokes and anti-Stokes components used by the RDTS system to monitor temperature thus leading to both large errors in the evaluation of this parameter and errors increasing with the sensing distance.

This section aims to study the RDTS temperature evaluation performed during *ex-situ measurements* in which the device response is investigated as a function of combined γ -rays radiation and hydrogen loading effects. These tests were carried out on the two sensing MMF possessing a pure-silica core fibers, PSC-MMF_1 and PSC-MMF_2. In particular, regarding the hydrogen influence, for each of them we considered two different situations: while one sample was H₂-loaded just before the irradiation run, the second one was also H₂-loaded and kept at RT for two months before the irradiation session. Consequently, the differences between the two samples is quiet clear as the first one will have the entire H₂ content during the irradiation, the second will have enough time to out-diffuse.

Figure 5.13 highlights the impact of γ -rays on these H₂-pretreated samples of PSC-MMF_1 and PSC-MMF_2, (Figure 5.13 a and b, respectively). It compares different samples: pristine (*the reference*), γ -irradiated at 6 MGy, γ -irradiated at 6 MGy with H₂ present during irradiation and γ -irradiated at 6 MGy two months after H₂-loading. In both fiber types we observe a meaningful negative effect of γ -rays on the RDTS measures with the sample H₂-loaded two months before the irradiation and left to desorb naturally at ambient conditions. Indeed, the error of the RDTS is larger with this fiber than with its non-treated counterpart. In this case, the temperature error at 6 MGy exceeds that one measured with the non-treated sample at 10 MGy. In details, while the temperature error detected at a 100 m distance is about 30 °C for the PSC-MMF_1 and 35 °C for the PSC-MMF_2 using the 10°MGy irradiated samples (see Figure 5.9 c and d), the ones observed in the samples γ -irradiated at 6 MGy two months after their H₂-loading gives RDTS errors of ~35 °C for the PSC-MMF_1 and ~47 °C for the PSC-MMF_2. Nevertheless, our *ex-situ* investigations show that the RDTS measurements using the sample containing H₂ during the irradiation is only slightly affected by this combined treatment two months after the end of the irradiation. However, it should be pointed out that this good response is certainly not maintained during the irradiation due to the high HIA that will counterbalance the lower RIA.

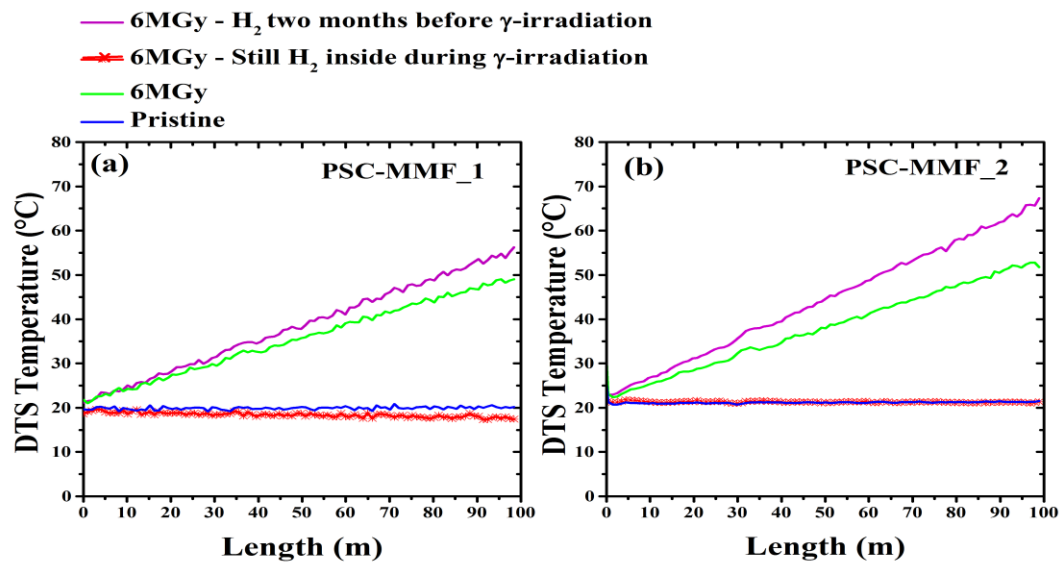


Figure 5.13. RT (~ 22 °C). Distributed Temperature measurements detected by the RDTS instrument using pristine (blue line), γ -irradiated at 6 MGy (green line), γ -irradiated at 6 MGy with H₂ inside (red line) and γ -irradiated at 6 MGy two months after H₂-loading (violet line) samples of PSC_MMF_1 (a), and PSC-MMF_2 (b). Results of all samples are shown.

5.4.1 Spectral attenuation measurements changes due to combined H₂ and γ -rays

The attenuation spectra of pristine and irradiated PSC-MMF_1 and PSC-MMF_2, samples are presented in Figure 5.14 a and b, respectively.

In both fibers, for both H₂-treated samples, high RIA values are observed with respect to the pristine one. In both samples, we note a main attenuation peak at ~ 1390 nm due to the hydroxyl groups (OH) generation inside the fibers, but only in the sample irradiated when there was still H₂ inside are observed the two higher OH overtones at ~ 940 nm and at 1245 nm [97] as in this case the OH concentration is clearly enhanced.

For both the 6 MGy irradiated and 6 MGy irradiated in the 2 months pre-treated fibers, the induced attenuation, ΔIA , observed at the AS and S wavelengths is around ~ 0.05 dB/m, whereas it remains negligible in both pristine and γ -irradiated at 6 MGy with H₂ inside the samples (see Figure 5.14). This further confirms that the RDTS response is related to the spectral dependence of the RIA around 1064 nm, whatever the origins of the differential

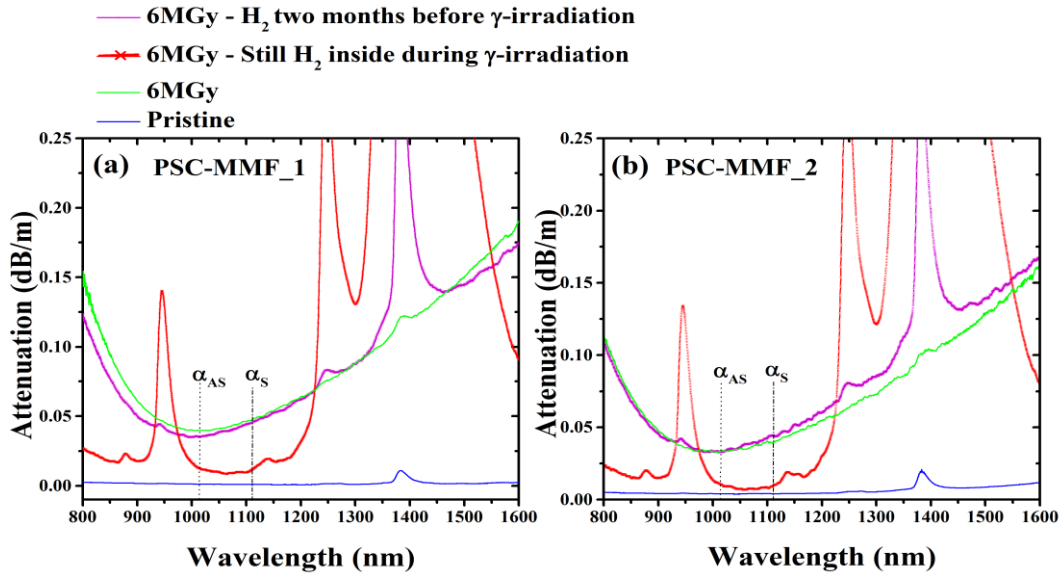


Figure 5.14. Attenuation spectra of PSC-MMF_1 (a), PSC-MMF_2 (b). Results of pristine (blue line), γ -irradiated at 6 MGy (green line), γ -irradiated at 6 MGy with H₂ inside (red line) and γ -irradiated at 6 MGy two months after H₂-loading (violet line) samples are shown. Vertical lines mark the wavelength positions of Raman intensity anti-Stokes, I_{AS} , and Stokes, I_S (at 1014nm and 1114nm, respectively). Test performed at room temperature.

attenuation. Furthermore, also in this case we note a direct correlation between Raman response and the differential RIA. Indeed, the H₂ loaded-samples two months before γ -irradiation show both remarkable error in the RDTs temperature measures, reported in Figure 5.13 and a non-negligible difference between α_{AS} and α_S : $\Delta IA \sim 10^{-2}$ dB/m.

5.5 Discussion

The Raman response is strongly influenced by γ -rays and by hydrogen diffusion into the fiber core. In our harsh environment associated with these two constraints, we must consider the following effects to select a sensor scheme suitable for our application:

1. the radiation and/or hydrogen induced attenuation (RIA and/or HIA, respectively) or combined effects at the three RDTs main wavelengths: λ_0 , λ_s , and λ_{as} ,
2. the differential induced attenuation ΔIA , (ΔRIA and/or ΔHIA) at the two Raman detected signals, Stokes and anti-Stokes.

A. Influence of defects on the induced attenuation, IA.

The exposure of the material to radiation and/or H₂ release results in the generation of defects; often it occurs by transformation or conversion of defects preexisting in the as-grown material before irradiation, and known as precursors.

The molecular hydrogen exposure of the silica optical fiber induces attenuation, HIA, in the IR-transmission range. The origin of this HIA is due to the presence of several absorption bands identified as overtones of the fundamental vibration of the molecular hydrogen, located at 2400 nm (see Figure 5.6) [68], [97], [98].

For all F-doped, pure silica doped, Ge-doped and P-doped fibers the infrared radiation induced attenuation, IR-RIA follows the same trend increasing with the dose. The RIA spectra highlight two main contributions [92]:

- absorption bands located in the visible range (especially strong for PSC- and F-doped fibers),
- an IR contribution that increases with increasing wavelengths.

However, at high TID the attenuation values of these fibers differ of magnitude orders, e.g. the RIA in the Ge-doped fiber is one order of magnitude higher than that observed in the F-doped fiber. As expected from literature [91], [92], for high TID, the RIA values in the IR domain are larger for the P-doped, followed by Ge-doped, pure-silica core and F-doped fibers.

The spectral measurements of PSC-MMF_1 (Figure 5.11 c) extended to visible range (400÷700 nm) are shown in Figure 5.15. This is a typical RIA spectrum for a PSC-MMF fiber as a function of the TID. Despite the missing part, due to the limited ranges of our detectors, it is evident that the RIA curves present a minimum around 1000 nm. Moreover, the influence of an UV-absorption tail that increases with decreasing wavelength is observed in agreement with literature [92].

In pure-silica core and F-doped fibers the RIA arises from generation of the absorption band in the visible range at ~ 620 nm that grows with the deposited dose. The origin of this band is still debated, the main doubt is its attribution to one or more point defects (such as NBOHC, POR...) [99]. However, some findings weaken the hypothesis of a multi-defect model associated with overlapping absorption bands around ~ 620 nm in favor of a “single-defect” model associated to the NBOHC band [100], [101]. In particular, a recent study executed, in F-doped fiber, by *Morana et al.* [101], concludes that the RIA band around 2 eV (~ 620 nm)

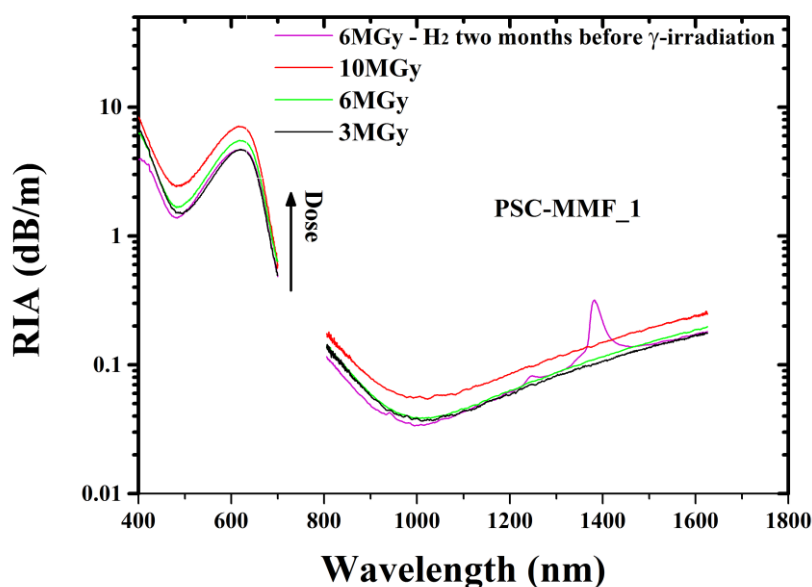


Figure 5.15. RIA spectra of PSC-MMF_1. Results of γ -irradiated at 3, 6, 10°MGy (black, green and red line, respectively) and γ -irradiated at 6 MGy two months after H₂-loading (violet line) samples are shown. Test performed at room temperature. A base-10 log scale is used for the y-axis.

has to be attributed only to the NBOHC defect. We note also that the RIA increases after irradiation in the NIR spectral domain above 1100 nm, however the nature of the defects absorbing in this region is unclear yet. A study performed at doses < 100 Gy by Regnier et al. [92] suggests that the NIR-absorption bands are related to STH species in pure silica and Ge-doped fibers. Some guiding effects also have to be considered even if their contribution should be lower in the case of MMFs compared to single-mode fibers.

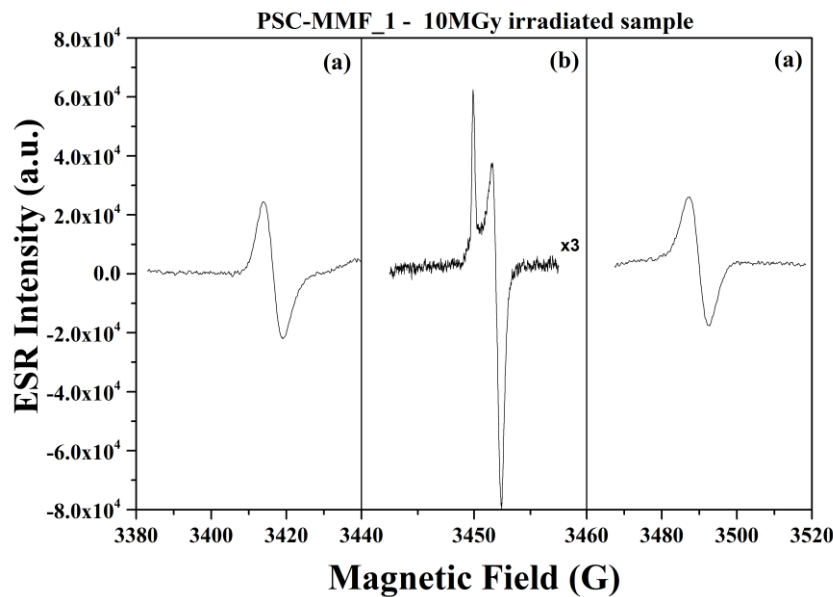


Figure 5.16. ESR spectra of the 10 MGy γ -irradiated PSC_MMF_1 recorded at RT. The signal in the panels (a) was acquired with a 4 G modulation amplitude (H_m) and a P=0.2 mW power (attenuation of 30 dB) and show the doublet of the H(I) center ($\equiv Si^\bullet - H$). The signal in the panel (b) was recorded with a 0.1 G modulation amplitude and a P= $8 \cdot 10^{-4}$ mW (att. of 54 dB) and shows the lineshape of the E' center ($\equiv Si^\bullet$).

To clarify the irradiation effects at a microscopic scale, we have performed electron spin resonance (ESR) measurements. Figure 5.16 displays typical ESR spectra recorded at RT in the 10 MGy irradiated PSC-MMF_1: the lineshape associated with the E' center is shown in panel (b), it is characterized by an axial symmetry due to its structure (a dangling Si bond, $\equiv Si^\bullet$) [102] whereas the signal related to the H(I) defect, characterized by an hyperfine splitting of 74 G, is observable in panels (a), it is a variant of the E' defect where one of the O atom is substituted by an H one ($\equiv Si^\bullet - H$) [103]. Differently from E' and H(I), the ESR signals of oxygen associated hole centers are broad and overlapping each other and, therefore, not distinguishable at RT. In order to separate their related spectra the measurements were performed at low temperature (in liquid nitrogen 77 K). Figure 5.17 reports a typical ESR spectrum of these centers acquired in the 10 MGy irradiated PSC-MMF_1. The recorded spectrum results by the overlapping of NBOHC and POR signals; it is shown in panel (a). Instead, panels (b) and (c) show the two lineshapes (reported in literature [104]) related to the NBOHC and POR, respectively, which are used for the deconvolution. We also note the NBOHC manifests itself with the absorption at 620 nm shown in Figure

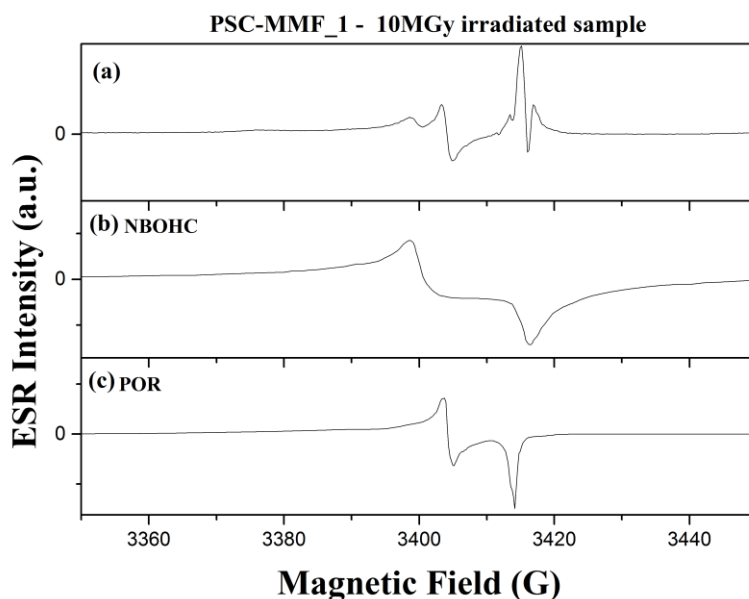


Figure 5.17. ESR spectra of the 10 MGy γ -irradiated PSC_MMF_1 recorded at LT, panel (a). The signal was acquired with a 0.6 G modulation amplitude (H_m) and a P=1 mW power (attenuation of 23 dB). Panels (b) and (c) report respectively the two lineshapes related to the NBOHC and POR [21], which are used for the deconvolution.

5.15. In addition, Figure 5.17 shows the strong component near 3410 G associated with the E' signal, which here appears distorted due to the high modulation field and power being used in the acquisition.

To show the dose-dependence of these paramagnetic centers we extract from the ESR measurements their concentration values for each PSC-MMF_1 sample. This dependence is displayed in Figure 5.18 and shows the concentration of all defects increasing with the γ -TID (3, 6, 10 MGy). Our results agree with the literature ones obtained on F-doped fibers by Morana *et al.* [76].

The effect of H₂ loading on ESR active centers is highlighted in the histogram of Figure 5.19. E' and H(I) centers shows a similar behavior: their concentration does not change if the loading was done 2 months before whereas it increases when H₂ is inside. As concerns both NBOHC and POR, the concentration reduces when H₂ is loaded two months before the γ -radiation and it is below the experiment sensitivity ($<10^{14}$ cm⁻³) when H₂ is inside. We note that these results are common to all investigated pure- and F-doped fibers. These findings can be interpreted on the basis of reaction processes of hydrogen with the paramagnetic centers. It

is well known that H₂ spontaneously reacts with NBOHC and POR [105], [106], this causes the H₂ cracking in two H atoms one of them being trapped at the defect site with the formation of OH groups ($\equiv Si - OH + H$). This process, on the one hand, explains the absence of these defects when the H₂ is inside the fiber during irradiation, on the other side, agrees with the increase of OH related bands in the IR spectra (see Figure 5.14). Vice versa, H₂ does not react spontaneously with E' center and its variant H(I), the activation energy being ~ 0.4 eV [107] in this case the reaction of H atom with S-H causes the bond breaking with production of E' centers and H₂ molecules. This agrees with the increase of these centers when H₂ is inside the fiber.

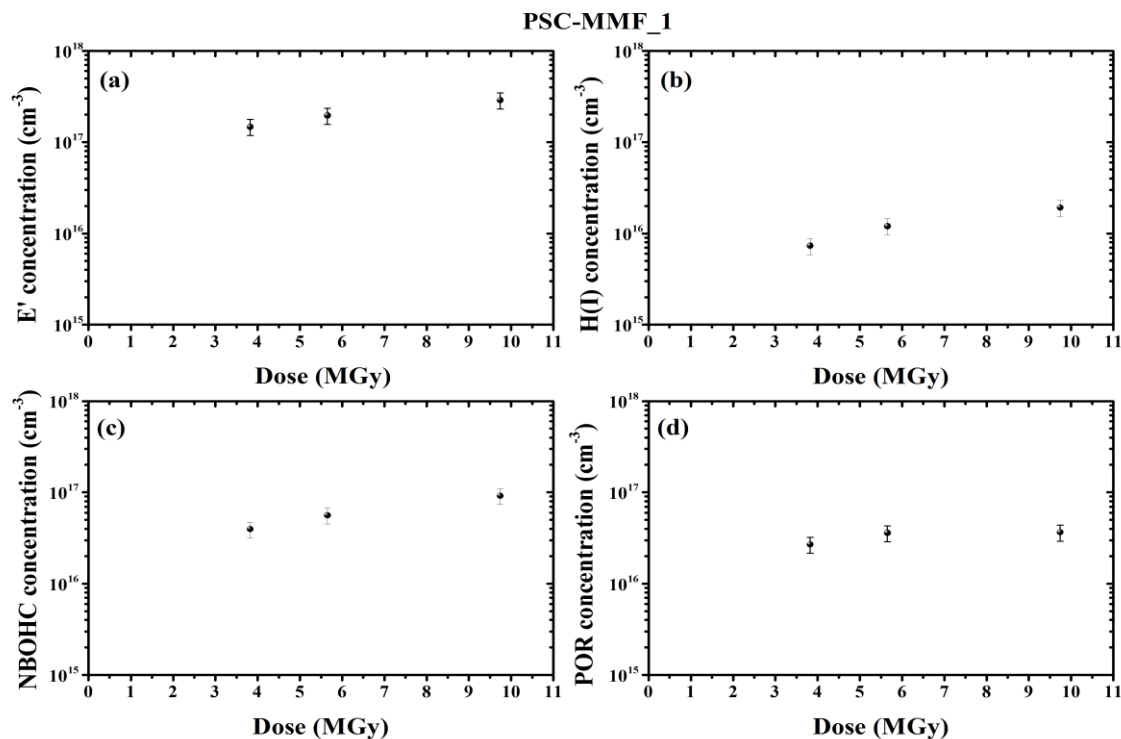


Figure 5.18. Concentration of E', H(I), NBOHC and POR centers (a, b, c and d, respectively) estimated by the *ex situ* ESR measurements of the PSC-MMF_1 fiber. The investigated TID are 3, 6 and 10 MGy. For the pristine sample, the concentration of all defects, if present, is under the experiment sensitivity ($< 10^{14}$ cm⁻³). The concentration accuracy is estimated as 20%.

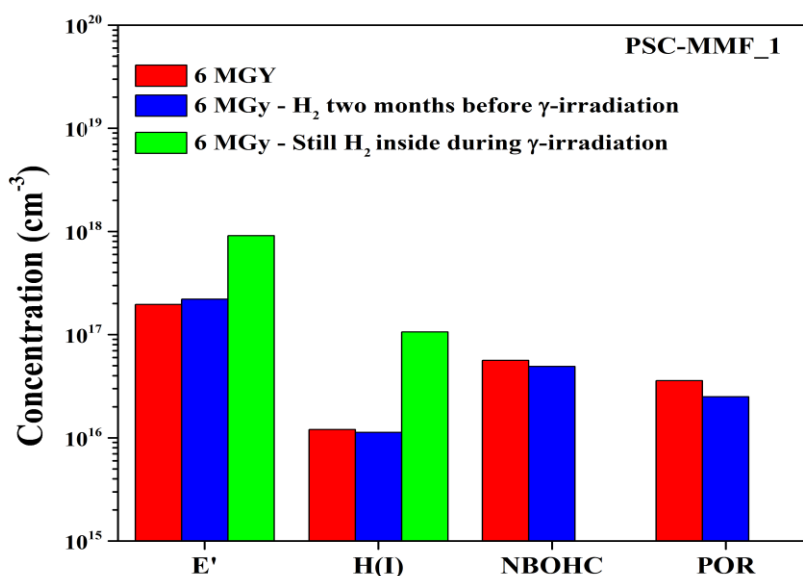


Figure 5.19. Histogram displaying the concentration of the different defects (E', H(I), NBOHC and POR) estimated on different samples of PSC-MMF_1: γ -irradiated at 6 MGy (in red), γ -irradiated at 6 MGy two months after H₂-loading (in blue) and γ -irradiated at 6 MGy with H₂ present during irradiation (in green).

As concerns the Ge-doped fibers, RIA is mainly influenced by Ge related defects rather than ones related to Si. In fact, both experimental and theoretical studies confirm that Ge-related defects are more efficiently generated than Si-related defects in pure and F-doped glasses [53], [108], [109], [110]. In the spectral domain of our interest (1014 nm \div 1114 nm), for high TID, RIA is due by two contribution: i) the tail of the absorption bands in the visible (such as that at \sim 620 nm evidenced in figure) and UV range; ii) the band extending above 1100 nm. The origin of the IR contribution, ii), remains still unclear; the proposed models of absorbing defects are the Ge-STH [92]. Similarly to PSC and F-doped fibers, the other contribution, i), is attributed in literature to the composition of different bands peaked in the UV-Visible region [76], [90], [111]. In particular Griscom [90] and Girard *et al.* [111] have associated the RIA with the growth of three absorption bands, in the UV-Visible domain, of the following defects: Ge(1), GeX, and Ge-NBOHC. A study at a microscopic scale of the irradiation

effects on a highly-Ge-doped MMF⁸, treated at the same TID investigated in this work, was done by *Morana et al.* few years ago [76].

By through ESR experiments, the authors have shown that the radiation gives rise to paramagnetic defects whose concentration increases with increasing dose. The ESR spectra of irradiated Ge-doped preform and fibers show the overlap of several signals related to different paramagnetic centers [78], [112], as SiE', GeE' ($\equiv Ge^\bullet$), Ge(1) (GeO_4^\bullet) and Ge(2), whose structure is still questioned between models consisting either in a trapped electron center or in a hole center. Both *Morana et al.* [76] and *Alessi* [113] have concluded that these defects are created during the irradiation, except for the Ge(2) that is not observed. Moreover, the doublet signal characterizing the H(II) defect, structurally identical to the H(I) center apart from the substitution of Si with Ge, is also absent.

Concerning the RIA observed in P-doped fiber, there is a general consensus that the IR-spectrum is mainly due to P1 defects that have an absorption band centered at ~1570 nm [114], [115]; the P1 is paramagnetic and its structure has been identified by ESR [112].

Finally, the induced attenuation caused by combined γ -ray and H₂ presences (RIA and HIA), show substantial changes in the NIR-spectrum with respect to both pristine and γ -irradiated fibers. The study is conducted only on the pure silica core MMFs, PSC-MMF_1 and PSC-MMF_2. Two different cases are matter of research: i) the RIA variation in H₂ pre-loaded sample, ii) the RIA change in sample loaded with H₂ two months before the γ -irradiation.

Regarding the first topic, i), Brichard et al. [116] have performed a *in situ* study on the radiation-induced absorption in hydrogenated pure-silica-core fibers irradiated with γ -rays up to ~6 MGy. By comparing the RIA spectrum of the γ -irradiated H₂-free sample with that of the γ -irradiated H₂-loaded samples, they observed a reduction of the RIA peak at 630 nm in favor of a strong increase of the OH absorption band at 1380 nm. Although, in Figure 1.13, our measurements on the γ -irradiated H₂-loaded sample of both fibers (PSC-MMF_1 and PSC-MMF_2) are limited to the IR range and only the IR-tail of the visible band is observable, the observed spectral behavior agrees with that of Brichard et al. Indeed, with

⁸ with Ge concentration of 25wt.% and geometrical properties of $\phi_{\text{core}}=50\ \mu\text{m}$, $\phi_{\text{clad}}=125^\circ\ \mu\text{m}$ and $\phi_{\text{coat}}=242^\circ\ \mu\text{m}$.

respect to the only 6 MGy γ -irradiated sample, the 6 MGy γ -irradiated H₂-loaded one shows both lower attenuation values of the IR-tail and the appearance of strong OH-band at 1380 nm. In [116], this is explained by the fact that radiation-induced OH groups arise from the action of hydrogen to convert NBOHCs and likely peroxy-linkages (indeed, under the action of γ -rays the peroxy-linkages break and form NBOHCs that are quickly converted into OH groups by the hydrogen [117]).

To the best of our knowledge, studies regarding the second topic, ii), are not present in literature. The sample H₂-loaded two months before the γ -irradiation session shows the worse Raman response and RIA level comparable with the other irradiated samples. We interpret this finding assuming that the H₂-preloading in the fiber creates functional groups, such as SiOH and SiH that increase HIA level in the IR. On the other side they are also precursors for γ -rays induced generation of NBOHC and E' centers, that are responsible for absorption bands in the visible and UV range thus resulting in an increase of RIA [19], [118]. Also in this case the nature of the defects absorbing in the IR spectral domain above 1100 nm is still

TABLE 5.1. INDUCED ATTENUATION, **IA**, AT 1064 nm, OBTAINED BY SPECTRAL ATTENUATION MEASUREMENT

FIBER	P-MMF	Ge-MMF	PSC-MMF_1	PSC-MMF_2	F-MMF_1	F-MMF_2
DOSE	dB/m	dB/m	dB/m	dB/m	dB/m	dB/m
10 MGy	2.45±0.23	(22.02±0.05)·10 ⁻²	(58.55±0.14)·10 ⁻³	(34.50±0.18)·10 ⁻³	(11.6±1.0)·10 ⁻³	(8.27±1.3)·10 ⁻³
6 MGy	2.26±0.23	(20.35±0.05)·10 ⁻²	(41.10±0.14)·10 ⁻³	(31.31±0.18)·10 ⁻³	(9.3±1.0)·10 ⁻³	--
3 MGy	--	(16.04±0.05)·10 ⁻²	(40.60±0.14)·10 ⁻³	(20.48±0.18)·10 ⁻³	(9.6±1.0)·10 ⁻³	-(10.5±1.3)·10 ⁻³
0.16 MGy	--	(5.57±0.05)·10 ⁻²	--	(5.36±0.18)·10 ⁻³	--	--
6 MGy TWO MONTHS AFTER THE H ₂ .	--	--	(38.28±0.14)·10 ⁻³	(34.27±0.18)·10 ⁻³	--	--
6 MGy WITH STILL H ₂ INSIDE	--	--	(7.58±0.14)·10 ⁻³	(3.22±0.18)·10 ⁻³	--	--

The confidence level is of the order of a two standard deviation (95%).

unknown.

The permanent induced attenuation values obtained by the spectral measurements of irradiated and/or hydrogenated samples are reported in Table 5.1.

B. Differential IA, Δ -IA, between S and AS wavelengths

The Δ -IA is strictly linked to the changes in the IR-transmission of the fibers. Indeed, it depends on how the induced attenuation (e.g. by radiation and/or hydrogenation) influences the relative intensities of anti-Stokes and Stokes components. Thanks to the spectral attenuation measurements, it is clear that the RDTS response in harsh environments is mainly affected by an increase of this differential attenuation that will cause an error in the temperature calculation. Indeed, with respect to the pristine sample both irradiated and/or hydrogenated samples are affected by important changes of their IR spectra. Then, if the differential RIA and HIA are not taken into account, the measurement error increases with the distance along the fiber faster than the RIA and will limit the sensing length to very short lengths. The $\Delta\alpha$ values acquired through spectral attenuation measurement in the diverse samples are reported in Table 5.2.

TABLE 5.2 DIFFERENTIAL ATTENUATION OF THE TESTED FIBERS OBTAINED BY SPECTRAL ATTENUATION MEASUREMENT, $\Delta\alpha_{\text{OA}}$

FIBER	Ge-MMF	PSC-MMF_1	PSC-MMF_2	F-MMF_1	F-MMF_2
DOSE	dB/m	dB/m	dB/m	dB/m	dB/m
10 MGY	$(14.8 \pm 0.5) \cdot 10^{-3}$	$-(8.83 \pm 0.14) \cdot 10^{-3}$	$-(8.90 \pm 0.18) \cdot 10^{-3}$	$-(4.7 \pm 1.0) \cdot 10^{-3}$	$-(40.16 \pm 1.3) \cdot 10^{-3}$
6 MGY	$(15.9 \pm 0.5) \cdot 10^{-3}$	$-(8.78 \pm 0.14) \cdot 10^{-3}$	$-(6.45 \pm 0.18) \cdot 10^{-3}$	$-(4.6 \pm 1.0) \cdot 10^{-3}$	--
3 MGY	$(19.3 \pm 0.5) \cdot 10^{-3}$	$-(8.03 \pm 0.14) \cdot 10^{-3}$	$-(4.86 \pm 0.18) \cdot 10^{-3}$	$-(4.5 \pm 1.0) \cdot 10^{-3}$	$-(31.0 \pm 1.3) \cdot 10^{-3}$
0.16 MGY	$(10.9 \pm 0.5) \cdot 10^{-3}$	--	$(2.25 \pm 0.18) \cdot 10^{-3}$	--	--
PRISTINE	$\leq 0.5 \cdot 10^{-3}$	$\leq 0.14 \cdot 10^{-3}$	$\leq 0.18 \cdot 10^{-3}$	$\leq 1.0 \cdot 10^{-3}$	$-(38.6 \pm 1.3) \cdot 10^{-3}$
6 MGY TWO MONTHS AFTER THE H ₂ LOADING	--	$-(11.09 \pm 0.14) \cdot 10^{-3}$	$-(10.53 \pm 0.18) \cdot 10^{-3}$	--	--
6MGY WITH STILL H ₂ INSIDE	--	$\leq 0.14 \cdot 10^{-3}$	$\leq 0.18 \cdot 10^{-3}$	--	--

In the pristine and irradiated sample with H₂ inside the measure of RIA is less than the accuracy limit. The confidence level is of the order of a two standard deviation (95%).

5.6 Conclusion

The study concerning the vulnerability of the single-ended RDTSs using different classes of sensing optical fibers exposed to different harsh constraints such as γ -rays and/or hydrogen has been presented in this chapter. Both *ex situ RDTS measurements* using fiber samples previously exposed to γ -rays or/and hydrogen and *in situ RDTS measurements* with fiber samples containing various concentrations of hydrogen (from zero to nearly fully-loaded) have been performed. We have shown that the performances of our SE-RDTS are strongly affected by RIA (and/or HIA), that limits the sensing range, and Δ RIA (and/or Δ HIA), that causes a temperature measurement error. Indeed, with additional spectroscopic measurements, we have shown that the sensor degradation is linked to the hydrogen and/or radiation induced attenuation (RIA and/or HIA) strongly influenced by fiber dopant, coating and manufacturing conditions. In more details, we observe that:

- The HIA limits the SE-RDTS sensing length and Δ HIA leads to a wrong temperature evaluation ($>750^{\circ}\text{C}$ in some H_2 -loading conditions). The amplitude of the RDTS errors is related to the hydrogen concentration into the fiber. However, it is possible to prevent this degradation mechanism by selecting fibers with appropriate coating such as carbon ones that inhibit the gas diffusion into the fiber core for a large range of operating conditions.
- The RIA limits the sensing distance of our sensor (with the best fiber we estimate a maximal distance range of 430 m at 10 MGy). In particular, P-doped and Ge-doped fibers present values of RIA too large to satisfy the Cigéo application constraints. On the other hand the differential RIA has to also be taken into account. Indeed, Δ RIA strongly affects the response of Raman sensor leading to an increase of the temperature error with the distance length (up to 30°C at a distance of 100 m for Telecom-grade optical fibers) becoming more and more impacting as the dose increases. However, the amplitude of these errors is fiber-composition dependent: we have identified a commercial radiation resistant fiber that is associated with a reduced RDTS error of $\sim 10^{\circ}\text{C}$ after a short 100 m sensing distance.

The situation is more complex when considering combined radiations and hydrogen effects as expected in the real application. We have observed a good RDTS response on the hydrogen

loaded samples during the irradiation, in which the defects generated by γ -rays have been recovered by molecular hydrogen presents in the fiber, thus improving the γ -irradiation hardness of the sensor in terms of permanent damages. However, in the case of *in situ* measurements, hydrogen induced attenuation HIA will strongly limit the interest of such loading. Moreover, the H₂-presence before the irradiation seems to negatively impact the sensor performance by enhancing the RIA differences between Stokes and anti-Stokes wavelengths.

To conclude a suitable choice of the selected fiber type for the project can however limit these two degradation mechanisms. Hydrogen issues can be bypass using specific hermetic coatings around the fibers, and the RIA and differential RIA will be reduced employing radiation resistant fiber. Nevertheless, a further study appears mandatory before integration of single-ended RDTSs in Cigéo.

Chapter 6

RDTS response during radiation exposures and thermal treatment

The main topic of this chapter is to report and discuss distributed fiber optic temperature measurements based on Raman scattering performed *in-situ* during steady state γ -irradiation at a dose rate of 1 kGy/h and up to a total ionizing dose of ~ 160 kGy.

In Chapter 5 through *ex-situ* measurements we reported the permanent radiation effects on the RDTS sensors. RDTS is influenced by the RIA phenomena leading to both large errors in the temperature measurements and a diminution of the available fiber sensing length. The amplitude of the radiation-induced temperature error strongly depends on the fiber choice and on the irradiation conditions. However, the *ex-situ* measurements are not enough to design the monitoring system of Cigéo, where radiation never stops. Therefore, for the SE-RDTS operation in the targeted Cigéo application, *in-situ* tests performed during irradiation are mandatory in order to evaluate the performance of this sensor via the responses of the studied fibers. However, since the differential RIA shows saturation (see Table 5.2) for high total ionizing doses we test the sensor using the radiation resistant fiber after a pre-irradiation at the highest investigated TID value of 10 MGy.

We also evaluate the sensor response after γ -rays exposure undergoing to a constant temperature of 80 °C as inside the waste storage cells the temperature can change between 25 °C and 90 °C.

It should be noted that our *in-situ* tests are performed at a higher dose rate (1 kGy/h) than those representative of Cigéo that remain below 10 Gy/h. Such accelerated test is mandatory to reach, in a reasonable time, 160 kGy, typical magnitude order of TID representative of some LL/IL radioactive wastes. Furthermore it should be emphasized that working at higher dose rate than expected ones at Cigéo allows overestimating the RIA that in passive optical fibers. Indeed, RIA has always being shown to increase at higher dose rate, as at a given dose, increasing the dose rate decreases the time allowed for the defects to recover during the irradiation run.

6.1 γ -rays effects on RDTS response: *In situ* measurements

This section reports our study on the *in-situ* SE-RDTS performance characterization using the previous sensing fibers designed with various dopants and continuously γ -ray irradiated at the steady state dose rate of 1 kGy/h.

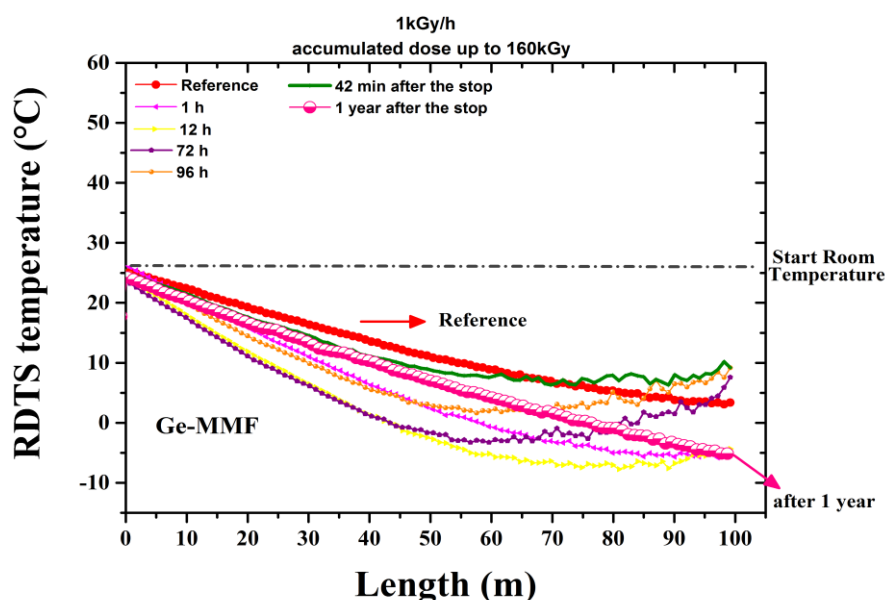


Figure 6.1. RDTS results on Ge-MMF sample. The measurements were performed both during and after the γ -irradiation at 1 kGy/h dose rate. The red line indicates our reference while the dot line designates the room temperature at the beginning of the irradiation run. An error of about 18°C is reported at a distance of 30 m and after 72 h from the start.

The device response evolution is monitored during several days of γ -rays exposure to reach ~ 160 kGy. The measurements were performed at room temperature ranging between 23°C and 26°C .

The tests were carried out on three types of sensing multimode optical fibers: Ge-MMF, PSC-MMF_2, F-MMF_1. During this irradiation session, as explained in Chapter 4 the references were considered at 42 kGy cumulated dose for all samples and the elapsed measurement time is considered with respect to the re-launched of the irradiation.

Figure 6.1 illustrates Raman distributed temperature *in-situ* measurements performed on the Ge-MMF. γ -ray effects both during (*on-line*) and after the irradiation (recovery phase) are reported. The sensing fiber estimates a wrong temperature, the amplitude of the error increases (from RT down to -10°C) with increasing fiber distance even if during the irradiation the temperature probe fluctuations remain below 3°C . However, we notice a linear decrease up to ~ 40 m followed by a deviation in the behavior of the detected temperature as a function of the fiber length along the other part of the tested sample. Such behavior is not observed on the *ex-situ* measurement performed on the same sample 1 year after this γ -irradiation run (pink curve in Figure 6.1).

Similarly to our previous investigations Chapter 5, we attribute the increasing temperature error along the fiber length to the differential radiation induced attenuation, ΔRIA , between the Stokes and anti-Stokes signals. However, it's well known that during the irradiation the RIA evolution is driven by defects generation/transformation which have a direct impact on these measurements. The post-irradiation RIA behavior is governed by the permanent defects which reflect the final structural modifications of the entire silica matrix. Consequently, it is not so surprising to obtain different RDTS responses during the irradiation run compared to the result recorded one year after.

Moreover, the fiber sensing distance in which we observe a linear behavior response is shortened with the increasing of irradiation time (i.e. with the TID). This negative influence can be due to the spectral dependence of the RIA that limits the sensing length. All in all, the previous assumptions definitely require further investigations, such as the *in-situ* RIA acquisitions during a similar irradiation run.

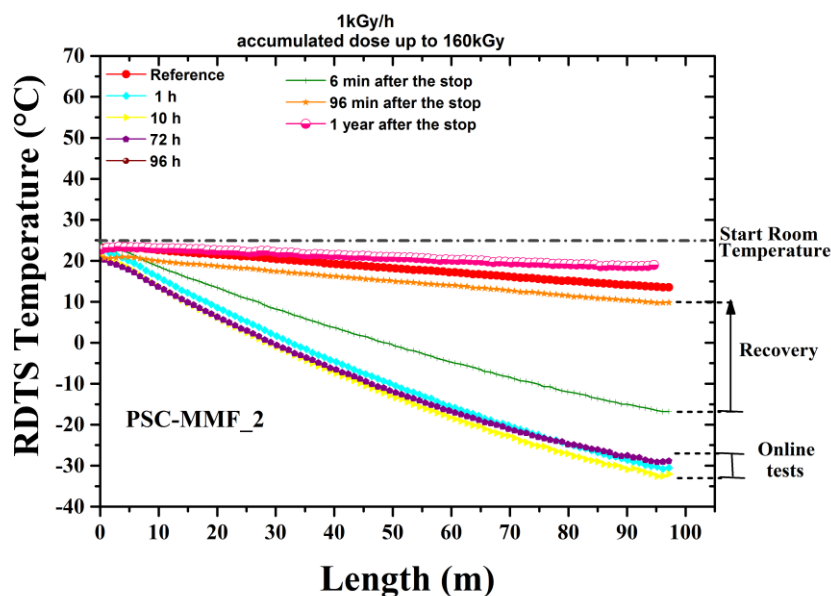


Figure 6.2. RDTs results on PSC-MMF_2 both during and after the γ -irradiation at 1 kGy/h dose rate. The red line indicates our reference while the dot line designates the room temperature at the beginning of the irradiation run. An error of about 20 °C is observed at 30 m distance, after 72 h of irradiation.

Similarly, Figure 6.2 reports the PSC-MMF_2 temperature evolution as a function of the sample checked distance as well as during the irradiation and a deviation from the usual linear temperature error is observed after ~ 50 m. Otherwise, during the post irradiation phase we notice an increase of the fiber sensing distance for which the usual linear behavior is due to the thermal annealing of defect (recovery). 96 minutes after the irradiation run stop the detected temperature becomes close to the reference one.

Therefore, Ge-doped and pure-silica-core fibers are significantly influenced by the RIA when acting as RDTs sensing elements. These measurements confirm the RIA impact and its key role in limiting the sensor performances. The spectral measurements at the 160 kGy TID of Ge-MMF and PSC-MMF_2 performed after 1 year from the γ -irradiation were already discussed in Chapter 5 (sky blue lines in Figure 5.11 b and d, respectively). The radiation impact on the fiber transmission is ten times stronger in the Ge-doped sample (~ 0.06 dB/m at λ_0) than in the pure-silica-core one (~ 0.005 dB/m at λ_0). Although the RIA impacts differently the two sensing fibers, the T error, supposed to be depending on the $\Delta\alpha$, results in the same order of magnitude for both samples. The temperature error along the sensors is

estimated with respect to the temperature value observed at the shortest fiber distance where the ΔRIA , does not affect significantly the measurement.

Figure 6.3 illustrates the steady state γ -ray effects at 1 kGy/h on the radiation resistant F-MMF_1. In particular, the Figure 6.3 a and Figure 6.3 b compare the online tests performed on two samples: *sample A* (Figure 6.3 a) pre-irradiated at dose of 42 kGy and *sample B* (Figure 6.3 b) pre-irradiated at high dose value of 10 MGy.

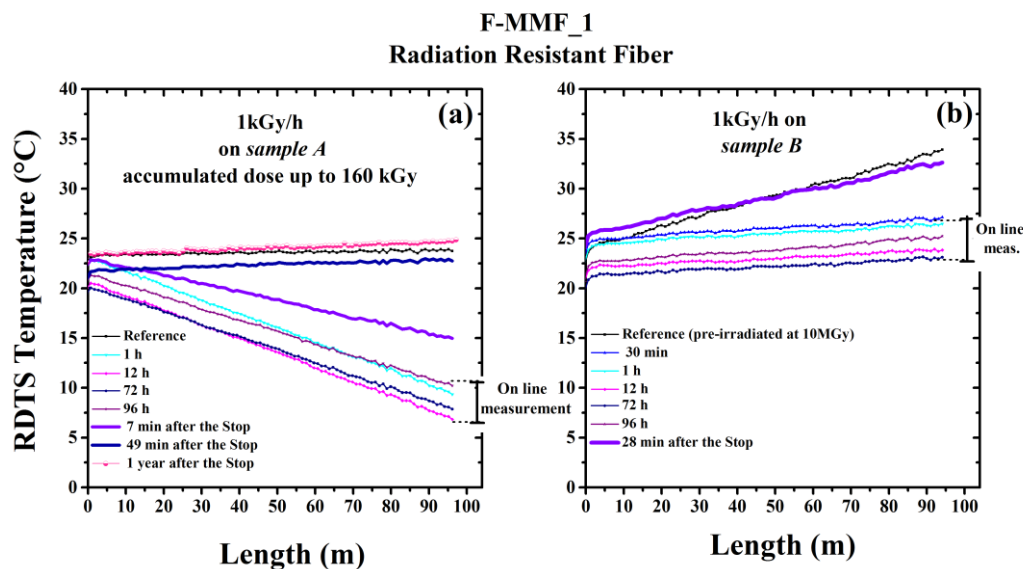


Figure 6.3. RDTS results on F-MMF_1 both during and after the γ -irradiation at 1 kGy/h. The measurements performed on the *sample A* (42 kGy pre-irradiated sample) are reported in figure (a) and on the *sample B* (10 MGy pre-irradiated sample) in figure (b). The black line is set to the reference measurement. At 30 m fiber length T error of ~ 4 °C and of ~ 0.5 °C is observed in (a) after 72 h and (b)

Concerning the *sample A*, we observe no radiation impact after 42 h, Figure 6.3 a (black line). As previously reported on the Ge-MMF and the PSC-MMF_2, also the F-MMF_1 *sample A* exhibits a false decrease of the detected temperature as a function of the distance. Nevertheless, this bad temperature estimation remains linear along the fiber and during the whole irradiation run. During the γ -rays exposure the temperature error increases with the sensing distance reaching a maximum value of 15 °C, after 100 m. Furthermore, as for PSC-MMF_2, the acquired temperature along the fiber tends to fit the reference one during the recovery and the temperature error decreases with the time during the recovery phase.

Figure 6.3 b reports *in-situ* measurements (1 kGy/h) performed on the F-MMF_1 *sample B* (pre-irradiated at 10 MGy). In this case, the reference is set to the measurements performed just before this new irradiation run and it exhibits a linear temperature increase with the fiber distance (Chapter 5). The low RIA values measured for this fiber seems acceptable for our application (indeed the fiber sensing distance over 100 m length is not reduced). Nevertheless, the Δ RIA is not negligible and leads to wrong temperature evaluation along the fiber. The measurement shows an initial error of ~ 10 °C all along 100 m although the temperature on the sample is constant (RT). When the irradiation run starts, the temperature error increases with the sensing distance and decreases with respect to the reference. Although during the irradiation the temperature provided by the sensor along the fiber is still not correct, 30 min after the beginning of the online test, the temperature error over 100 m is limited to only 2 °C. Moreover, the slope of the temperature curve remains constant during the whole irradiation run. It means that the RDTS error along the fiber does not change during the online tests. It is worth noting that, after 28 minutes from the source switching off the temperature curve gets closer to the reference one. Thus, the pre-irradiation at high TID of the sensing radiation resistant fiber could be a mitigation solution for the targeted application, such as the monitoring of radioactive structures like Cigéo underground repository. However, the measurement quality still needs to be improved.

6.2 Thermal treatment effects on RDTS response using a pre-irradiated fiber.

Since the pre-irradiation treatment of the fiber seems to be promising for the temperature monitoring in radioactive environment characterized by low TID values (up to 160°kGy), further studies based on this treatment must be conducted to check their robustness regarding the Cigéo facility. Indeed, the instrument performances and evaluations require to test the sensor in presence of γ -rays as well as temperature changing from RT up to 90°C. For this reason, we monitored, during different days the SE-RDTS response using the 6 MGy pre-irradiated PSC-MMF_1 kept at a constant temperature of 80 °C. Moreover, this study is

supported by attenuation spectral measurement performed in the IR domain on the 10 MGy pre-irradiated sample of the same fiber.

Figure 6.4 reports the evolution of temperature responses on PSC_MMF_1 sample (pre-irradiated at 6 MGy γ -dose) during ~ 7 days of thermal treatment at 80°C. As expected, during the first day, we observe a linear temperature growth with distance up to T error of about 28 °C. However, this growth and so the temperature error decreases with the time. Therefore, the temperature error increasing with the sensing distance is reduced by the thermal treatment during the week: ~ 28 °C of T error is observed at the beginning and ~ 15 °C at the end after seven days.

The 80°C was reached with a temporal slope of ~ 6 °C/min starting from 25 °C. During this ramp the T error in each point of the fiber shows a slightly progressive growth (not reported in Figure 6.4) and after several hours (>10 h) we observe the decreasing behavior discussed previously (Figure 6.4).

In order to investigate if the temperature error variation detected by the RDTS response during the thermal treatment of the pre-irradiated PSC-MMF_1 are linked to the differential attenuation, the spectral evolution (800 nm-1600 nm) of the 10 MGy irradiated PSC-MMF_1 kept at a constant temperature of 80 °C was investigated for different days. Through the spectral measurement the time evolution of the temperature induced differential attenuation (ΔTIA), $\alpha_{as}-\alpha_s$, is calculated and reported in Figure 6.5. In Figure 6.5, the ΔTIA curve decreases progressively with the time reaching a minimum after 9 hours. After that, the ΔTIA starts to increase reaching the saturation after 180 h.

Although, the RDTS measurement and the spectral measurement were performed on sample at two different TIDs (6 MGy and 10 MGy, respectively), the comparison shows a connection between the ΔTIA measurement and the RDTS temperature error performed during the thermal treatment at 80 °C. Indeed, the temperature error time diminution is accompanied by the time increase of the ΔTIA and vice versa.

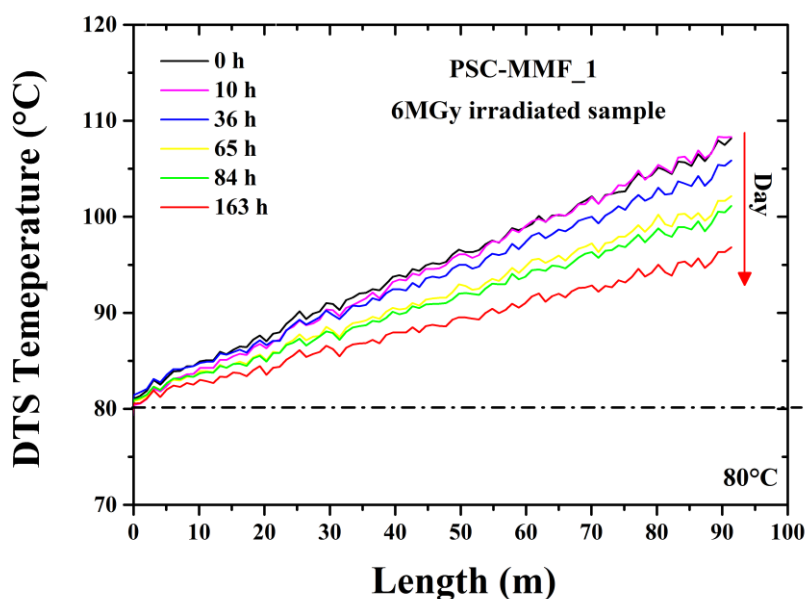


Figure 6.4. RDTS responses on 6 MGy irradiated PSC-MMF_1 sample and kept at constant temperature of 80 °C during 7 days.

Temperature “induced” attenuation, TIA

Radiation induced changes strongly depend on the operating temperature, which affects the stability of the optically active defects. This result is not surprising, indeed, few years ago, Kuhnenn *et al.* compared different optical fibers with very tight constraints, they concluded that even a few degrees difference (± 5 °C) can lead to noticeable change in the RIA [119]. Their study was performed between 24 °C and 29 °C during γ -ray exposure at the dose rate of 0.2 Gy/s and showed the temperature effect on the induced losses which depend on the fiber type. Most of the recent studies devoted to temperature effects in optical fibers have been done in the -50 °C to 100 °C range [120].

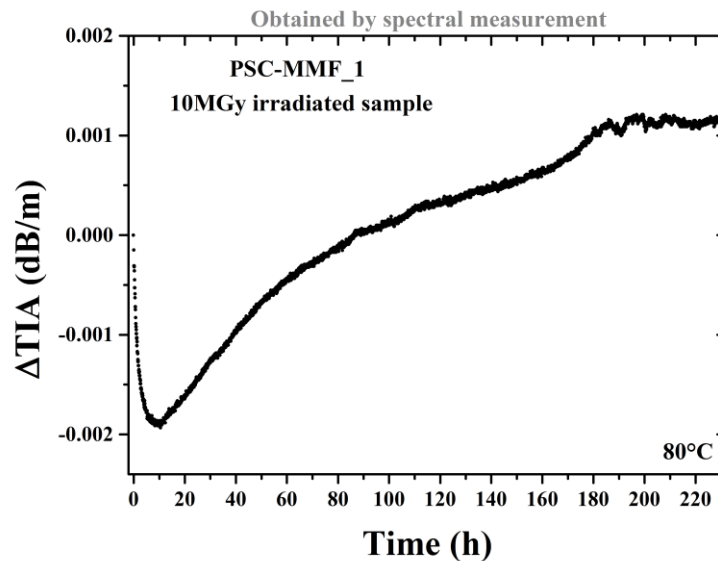


Figure 6.5. Differential temperature induced attenuation evolution induced by temperature as a function of time acquired by spectral measurement for the 10 MGy irradiated sample of PSC-MMF_1 kept at 80 °C.

6.3 Conclusion

The single-ended RDTS response is strongly influenced by ionizing radiation. Indeed, the radiation induced point defects leads to two different constraints on our sensor: the RIA and the ΔRIA , causing temperature measurement errors and signal to noise ratio degradation. The *in situ* radiation tests (at dose rate of 1 kGy/h) reveal that the sensor degradation amplitude depends on the fiber selected as the sensing optical fiber: pure-silica, Ge-doped or F-doped cores. These online results complete and agree with the experimental evidence discussed in the previous Chapter 5 where we reported the results after the irradiation at higher TID levels up to 10 MGy and therefore considering the sole part of the RIA that is stable at the RT.

Under radiation a suitable choice of the sensor is mandatory to limit the observed degradation mechanisms since the RIA will less affect the RDTS performances when radiation hardened fiber is used and the RIA value of such fiber seems acceptable for the Cigéo application.

The radiation exposure seems to affect the response of all tested optical fibers leading a false temperature evaluation along the fiber length. All fibers, even the radiation resistant MMF,

exhibit an increasing temperature error with the fiber distance. Similar to the *ex situ* measurements formerly discussed, also in this case this temperature error behavior can be attributed, for a large part, to the differential induced attenuation, ΔRIA . However, the pre-treatments at high TID of the radiation resistant fiber, i.e. the *ex situ* pre-irradiation at 10 MGy, reduce the error (≤ 2 °C along 100 m length) during the irradiation run at the uniform γ dose rate of 1 kGy/h.

Clearly, further tests aimed to measure the spectral changes induced by radiation during the γ -ray exposure could help to understand both the cause of this temperature error and the origin linear behavior deviation observed in our in situ test on Ge-doped and pure-silica-core fibers.

Finally, through the temperature treatment at 80 °C of pre-irradiated pure-silica-core samples we showed that both the sensor response and the differential attenuation of the sensing fiber follow a similar behavior. This result is a further confirmation that the observed temperature error growing with the distance originates by the differential attenuation of the fiber. Moreover, the thermal treatment leads to a decrease of this error in the course of time.

In conclusion, in radiation environment the SE-RDTS response is influenced by three different factors: the RIA, the ΔRIA and ΔTIA . The first factor limits the sensing distance of our sensor, requiring a selection of suitable fibers. Instead, the other two factors, due to the induced spectral changes on the fiber, lead to bad temperature estimation. Although using of radiation resistant sample could contain the error due to the ΔRIA at only few degrees, the ΔTIA effects is not predictable and needs further investigation.

Chapter 7

Mitigation of the radiation-induced degradation of the SE-RDTS: Correction technique

In this chapter we discuss in detail the development of an original procedure allowing for some operating conditions to reduce or correct the observed systematic error in the evaluation of the temperature by Single-Ended Raman scattering-based Distributed Temperature Sensors (SE-RDTS). As previously demonstrated, this error is induced by the ΔRIA due to γ -rays irradiation or/and hydrogen presence effects.

7.1 Introduction

In the previous chapter the degradation mechanisms of RDTS induced by H_2 and/or γ -rays have been discussed as these harsh constraints are present in the Cigéo environment. To evaluate the vulnerability of SE-RDTS in the envisaged French deep geological repository, diverse classes of sensing fibers were exposed to these harsh constraints: P-doped, Ge-doped, pure silica core and F-doped fibers with different coating types. The Raman response is strongly influenced by γ -rays and by the hydrogen presence into the fiber core. The radiation-induced degradation is mainly related to the excess of IA and to its different impacts on the Stokes and anti-Stokes signals, affecting the intensity ratio used by these RDTS system to monitor temperature evolution with time and along the sensing fiber. Indeed, we observe two

main issues: on the one hand high values of induced attenuation limit the sensing range and on the other hand the differential IA induces large errors in the temperature measurements. The differential RIA and the differential HIA lead to wrong temperature evaluation, with error exceeding 100° C for most cases. Nevertheless, we showed that by selecting an appropriate fiber, it is possible to limit its γ -rays and/or H₂ related degradation. First, the hydrogen issues can be mitigated with specific hermetic coatings around the fibers (such as carbon coated ones) and the RIA level can be considered as nearly acceptable (in the Cigéo context) using the last generation of radiation resistant F-doped optical fibers. However, with the best tested fiber and considering the more constraining TID (10°MGy) the temperature error due to differential RIA cannot be reduced below 10 °C. For this reason, we investigated additional hardening-by-system procedure to reduce the related T error.

As discussed in Chapter 3, our commercial SE-RDTS device acquires temperature measurements assuming that the differential attenuation, $\Delta\alpha$, is constant with time and/or uniform along the fiber length (Eq. 2.39). Nevertheless this assumption is no more appropriate when the fiber is subjected to constraints that degrade the optical fiber transmission such as γ -rays and molecular hydrogen release. Practical scenarios consider that both dose rate and temperature will be evolving during the facility lifetime and/or should not be uniform along the tunnel (and then along the sensing fiber).

Ergo, in order to obtain correct temperature measurements, the differential attenuation must be taken into account to compensate the measurement for $\Delta\alpha$ using the equation 7.1 obtained in section 2.3.3. Equation 2.38 can be rearranged as below:

$$T(z) = \frac{\gamma}{-\ln R + \ln C_R - \int_0^z (\alpha_{aS}(z') - \alpha_S(z')) dz'} \quad 7.1$$

where T is the absolute temperature as a function of the position z of the scattering element dz' , R is the anti-Stokes to Stokes optical power ratio, $\gamma = \frac{h\Delta\nu_R}{k_{SB}}$ (with k_B Boltzmann's constant, h Planck constant, $\Delta\nu_R$ the Raman shift) and C_R , ($\propto \frac{\lambda_S^4}{\lambda_{aS}^4}$) is a parameter supposed to be constant accounting for the incident pump power and the respective S and AS Raman cross sections depending on the transmission characteristic of the optical receiver.

Nevertheless, any compensation technique for the ΔRIA (or ΔHIA) will require to know the AS and S attenuation at each time and in each point of the fiber during the sensor measurements.

7.2 Correction procedure

The aim of this chapter is developing a correction technique to improve the performance of our instrument in a harsh environment avoiding the systematic radiation-induced error of SE-RDTS temperature measurements. The methodology of this correction will be illustrated for the PSC-MMF_1 case.

The response of our RDTS device depends on various parameters such as the type of fiber, induced differential attenuation ΔIA and also instrumental parameters. Taking into account these issues we evaluate a correction procedure to improve the performance of our instrument in extreme environment. From Eq. 7.1 we found that the temperature can be evaluated as:

$$T(z) = \frac{\gamma}{-\ln R - \Delta\alpha z + C'_R} \quad 7.2$$

where $C'_R = \ln C_R$ and the differential attenuation is supposed to be the same along the sensing fiber (this is the first hypothesis and for sure a limitation of the proposed method). In this case, in equation 7.2 the two factors, $\Delta\alpha$ and C'_R , are unknown and have to be determined.

To obtain the differential attenuation, $\Delta\alpha$

The following method is used to find the value of the differential attenuation $\Delta\alpha$ for each sample. When the temperature is constant (this is the second hypothesis of our method) along the fiber from the equation 7.2 we obtain:

$$\frac{d}{dz'} \ln[R(T, z)] = \frac{d}{dz'} \ln \frac{P_{aS}}{P_S} = -\Delta\alpha \quad 7.3$$

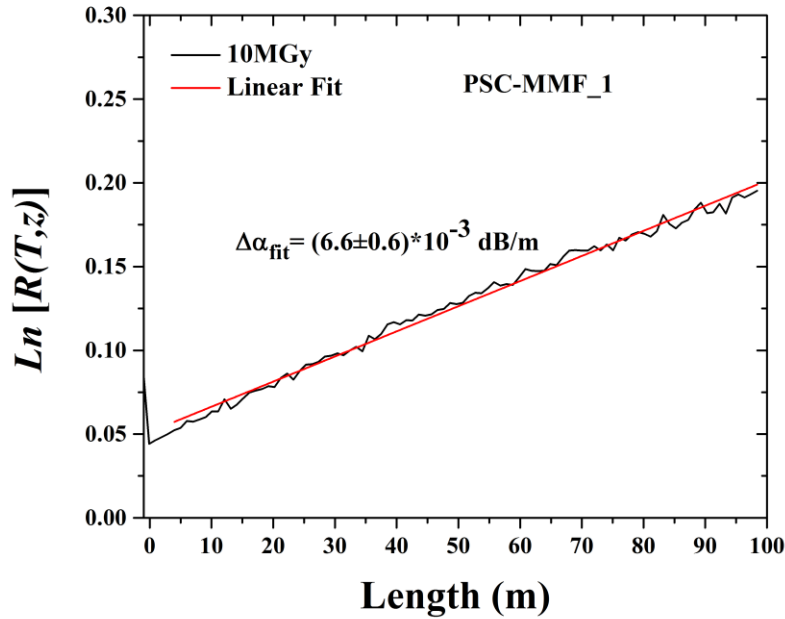


Figure 7.1. Natural logarithm of anti-Stokes over Stokes ratio as a function of the fiber length calculated for the 10 MGy irradiated PSC-MMF_1 (black line). The red line illustrates the linear fit used to reproduce the experimental data and extract the differential attenuation ($\alpha_{AS}-\alpha_S$) value.

With a linear fit of the natural logarithm of the anti-Stokes over Stokes ratio as function of the distance and using Equation 7.3, we can directly deduce $\Delta\alpha$ for each sample. For example, the linear fit done on 10 MGy irradiated sample of the PSC-MMF_1 is illustrated in Figure 7.1.

In Chapter 5 the spectral measurements performed on irradiated (and hydrogenated) as well as on pristine samples were shown in Figure 5.11 (and Figure 5.6). For the PSC-MMF_1 the ΔRIA value at 10 MGy obtained through the linear regression, $-\Delta\alpha_{FIT}$, results ~ -0.007 dB/m, close to the one $\Delta\alpha_{OA}$ estimated through spectral measurement equal to ~ -0.009 dB/m.

Figure 7.2 reports, for the same fiber and samples irradiated at different TIDs, the various differential attenuation values obtained by fitting on the anti-Stokes over Stokes ratios. We observe that $\Delta\alpha$ increases with the accumulated dose at lower dose and then saturates for higher TID values. Moreover, the sample irradiated at 6 MGy when there was still H_2 inside shows the lowest value $\Delta\alpha_{fit}$, close to the one extracted for the pristine sample. Differently,

the sample irradiated at the same 6 MGy dose but two months after the H₂-loading exhibits the highest value $\Delta\alpha_{\text{fit}}$ among all samples. These behaviors are comparable with the spectral measurements performed on the same samples and discussed in Chapter 5. Indeed, in Figure 5.13 a, the PSC-MMF_1 sample irradiated at 6 MGy when containing H₂ shows the lowest T error value comparable with the pristine one. At the opposite, the samples irradiated at the same dose but two months after the H₂-loading exhibits the highest temperature error value among all samples. Therefore, these results proof that the RDTS temperature error originates from the differential attenuation of the sensing fiber.

Table 7.1 reviews the differential attenuation values extracted from both the linear fit ($\Delta\alpha_{\text{FIT}}$) and the spectral measurements ($\Delta\alpha_{\text{OA}}$) for PSC-MMF_1, PSC-MMF_2 and F-MMF_1 in which the temperature error increases linearly with the sensing distance.

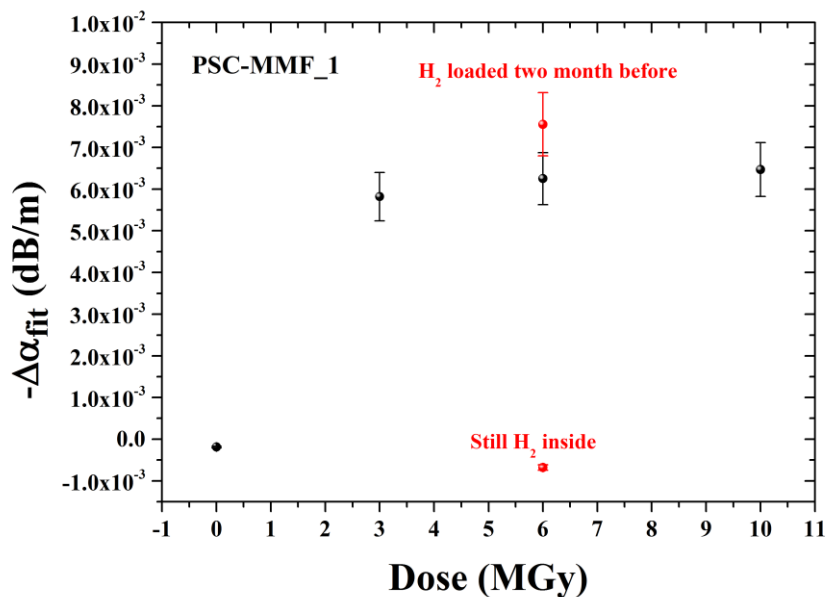


Figure 7.2. Differential attenuation, $\Delta\alpha$, evolution obtained by the linear fit of the intensity ratio as a function of TID for PSC-MMF_1. The black points indicate the $-\Delta\alpha_{\text{fit}}$ of the samples irradiated at different TIDs. Instead, the red ones are the $-\Delta\alpha_{\text{fit}}$ obtained from the samples submitted to both radiation and H₂ effects. The confidence level is of the order of two standard deviations (95%).

TABLE 7.1. DIFFERENTIAL ATTENUATION OBTAINED FROM BOTH LINEAR FIT, $\Delta\alpha_{\text{FIT}}$, AND SPECTRAL MEASUREMENTS, $\Delta\alpha_{\text{OA}}$.

FIBER	PSC-MMF_1	PSC-MMF_2	F-MMF_1
DOSE	$\Delta\alpha_{\text{OA}}$ (dB/m)	$\Delta\alpha_{\text{OA}}$ (dB/m)	$\Delta\alpha_{\text{OA}}$ (dB/m)
	$-\Delta\alpha_{\text{FIT}}$ (dB/m)	$-\Delta\alpha_{\text{FIT}}$ (dB/m)	$-\Delta\alpha_{\text{FIT}}$ (dB/m)
10 MGy	$-(8.83 \pm 0.14) \cdot 10^{-3}$	$-(8.90 \pm 0.18) \cdot 10^{-3}$	$-(4.7 \pm 1.0) \cdot 10^{-3}$
6 MGy	$-(8.78 \pm 0.14) \cdot 10^{-3}$	$-(6.45 \pm 0.18) \cdot 10^{-3}$	$-(4.6 \pm 1.0) \cdot 10^{-3}$
3 MGy	$-(8.03 \pm 0.14) \cdot 10^{-3}$	$-(4.86 \pm 0.18) \cdot 10^{-3}$	$-(4.5 \pm 1.0) \cdot 10^{-3}$
0.16 MGy	--	$(2.25 \pm 0.18) \cdot 10^{-3}$	$-(0.35 \pm 0.03) \cdot 10^{-4}$
PRISTINE	$\leq 0.14 \cdot 10^{-3}$	$\leq 0.18 \cdot 10^{-3}$	$\leq 1.0 \cdot 10^{-3}$
6 MGy TWO MONTHS AFTER THE H ₂ -LOADING	$-(11.09 \pm 0.14) \cdot 10^{-3}$	$-(10.53 \pm 0.18) \cdot 10^{-3}$	--
6 MGy WITH STILL H ₂ INSIDE	$\leq 0.14 \cdot 10^{-3}$	$\leq 0.18 \cdot 10^{-3}$	--

In both pristine and irradiated sample with H₂ inside the measure of $\Delta\alpha_{\text{OA}}$ is less than the accuracy limit. The confidence level is of the magnitude order of two standard deviations (95%).

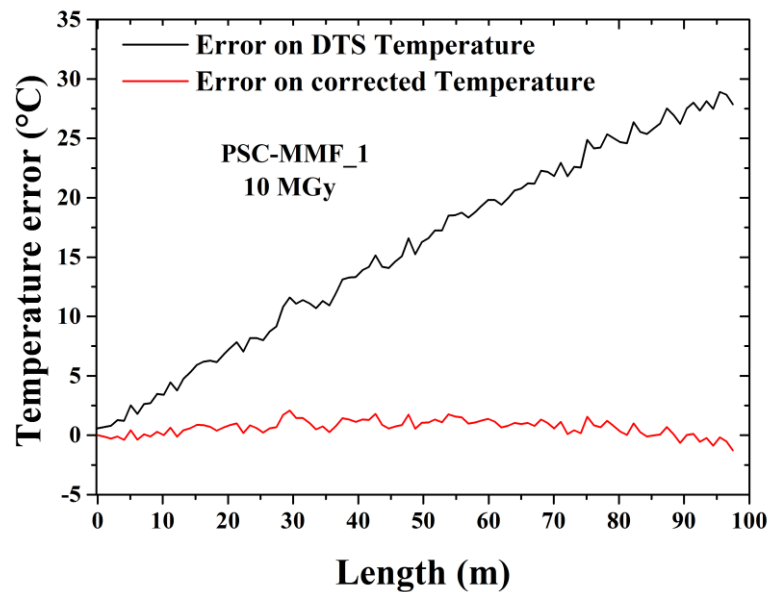


Figure 7.3. Comparison between the temperature errors of the RDTS measurements before and after the application of the correction technique when using the γ -ray irradiated at 10 MGy PSC MMF_1 as the sensing element.

To acquire the instrumental parameter, C'_R

Equation 7.2 demonstrates that the knowledge of the C'_R coefficient plays a key role in the correction of the RDTS temperature value. To determinate this parameter we have extracted, through the formula 7.2 the C'_R value for each sample of the PSC-MMF_1 in the first point of the fiber ($L=0$ m) where the signal is not still attenuated, imposing the temperature detected by an external thermocouple. Therefore, it is possible to correct the RDTS measurements using Eq. 7.3 and reconstruct the temperature distribution all over the fiber length.

For the worst case (TID of 10 MGy), we then obtain a temperature error limited to about 2°C after correction Figure 7.4 reports, for the PSC-MMF_1 γ -irradiated at 10 MGy, the temperature error calculated with respect to a reference temperature detected in the initial part of the sensing fiber, where the effect of attenuation is negligible. In the graph this temperature error is compared to the error we obtained after our procedure correction on the same data set. It's clear that this new technique improves the temperature measurements performed in harsh environment. Moreover, plotting the obtained C'_R coefficients of PSC-MMF_1 as a function of the TID (black point of Figure 7.5) we observe a linear behavior

suggesting that this coefficient probably depends on the power levels of the Raman signals and probe lasers.

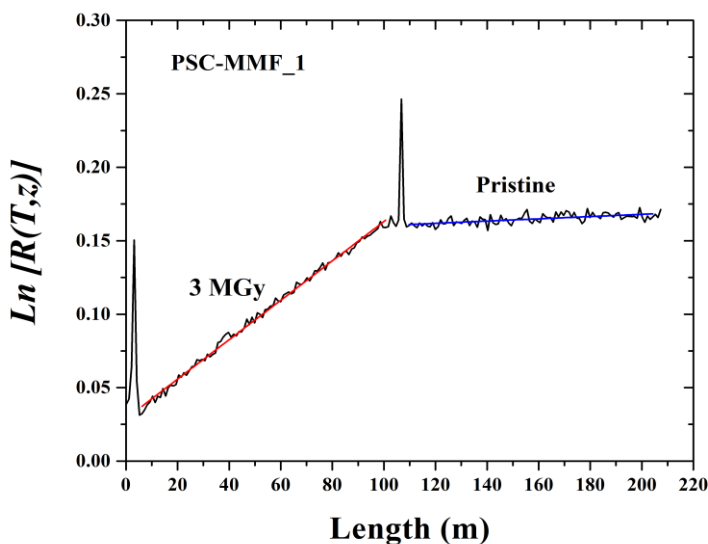


Figure 7.4. Linear fits (red and blue lines) realized on the natural logarithm of anti-Stokes over Stokes intensities ratio plotted as a function of the fiber length calculated by measurement performed in this configuration: 3 MGy + Pristine of PSC-MMF₁. Test performed at constant room temperature (~22 °C)

To support this hypothesis, we illustrate in Figure 7.4 an additional test executed on the PSC-MMF₁ performing the Raman measurement with the following measurement line: 3 MGy sample spliced with the pristine sample. Also in this case we calculate through a linear fit the C'_R factor for both samples and we plot the achieved parameters as a function of TID, as in Figure 7.5. Comparing the value of C'_R acquired for the pristine sample through the serial measurement (3 MGy + pristine configuration) and that one extracted from single measurement on the sole pristine sample, we observe different results as expected. Ergo, the coefficient, C'_R , depends on the power of the detected light. A study of this dependence will permit to know the right value of C'_R for each measurement and hence to obtain an automatic correction functions for SE-RDTS system.

This correction procedure is applicable to the *ex situ* measurements performed on all γ -irradiated and/or hydrogenated type of fibers showing a linear evolution of the temperature error versus the sensing distance, such as PSC-MMF₁, PSC-MMF₂ and F-MMF₁. It is

not applicable to fibers Ge-MMF and F-MMF_2 that do not exhibit such a linear dependence of the temperature measurement error under γ -rays or H₂-loading.

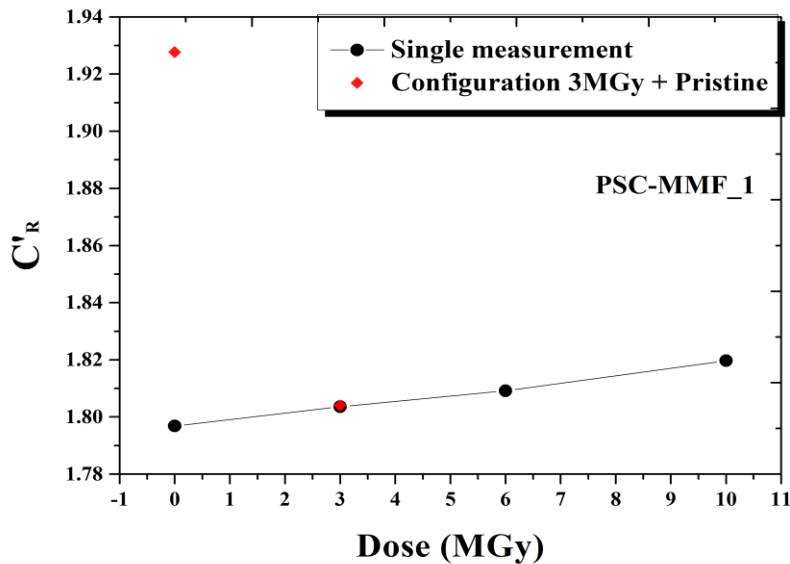


Figure 7.5. The C'_R parameter, calculated in function of the α -radiation dose for PSC-MMF_1. Black points are obtained by single samples measurement. Red points are the C'_R values acquired by measurement with configuration: 3 MGy + Pristine. Test performed at constant room temperature (~ 22 °C).

7.3 Online correction

Concerning the *in-situ* measurements of the IRMA session discussed in the previous Chapter 6, only the radiation resistant fiber, F-MMF_1, shows a linear increase of the SE-RDTS temperature error along the whole sensing distance of 100 m. Two different samples of this fiber types were tested during the IRMA run at 1 kGy/h of dose rate for ~ 4 days in order to reach a TID ~ 0.16 MGy: *i) sample A* (42 kGy pre-irradiated) in Figure 7.6 a and *sample B* (pre-irradiated at high TID value of 10 MGy) in Figure 7.6 b. Figure 7.6 reports for both F-MMF_1 samples the RDTS temperature errors measurements exposing the sensing element to γ -rays. It is calculated using the *in-situ* results discussed in Chapter 6 and estimating the error done with respect to the temperature value observed at the beginning of the sensing line that remains unaffected by the differential attenuation issue.

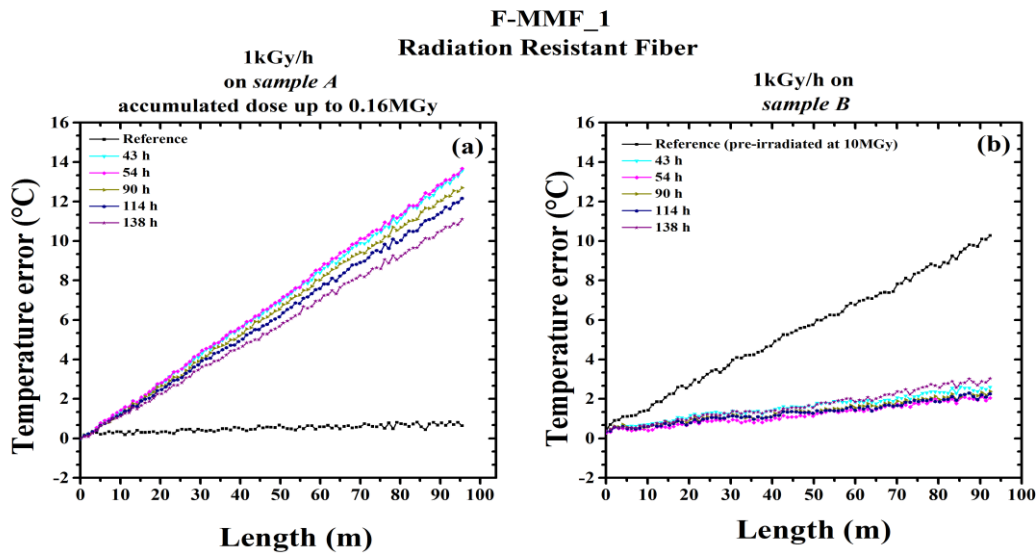


Figure 7.6. Temperature error calculated by the RDTs during *in-situ* irradiation at RT of F-MMF_1 samples, formerly discussed in Chapter 6. Results obtained during γ -irradiations at 1 kGy/h dose rate for (a) *sample A* (42 kGy pre-irradiated) and (b) *sample B* (10 MGy pre-irradiated). The black lines is set to the reference measurement.

Through our calculations on the RDTs measured ratio values, we estimate the *in-situ* differential attenuation for each measurement (as explained in the previous section for *ex-situ* tests).

Figure 7.7 reports, for the two samples, the time evolution of the differential attenuation achieved by the RDTs measurements (i.e. $-\Delta\alpha_{\text{fit}}$, as explained in the previous section) during the γ -ray exposure. When the reference is the *sample A* the differential attenuation decreases from $4.1 \times 10^{-3} \text{ dB/m}$ to $3.2 \times 10^{-3} \text{ dB/m}$ along the fiber with the evolution of the irradiation run. Instead, if we use the 10 MGy pre-irradiated sample (*sample B*), the $\Delta\alpha$ value remains constant at $-2.8 \times 10^{-4} \text{ dB/m}$ during the whole test duration. The inset in the graph shows the “transient ΔRIA ” ($i\delta\alpha$), i.e. the contribution to the differential attenuation only related to the online radiation. It has been acquired by the difference between the $\Delta\alpha$ obtained at every instant and those calculated on the reference measurement. Using the pre-irradiated sample the $i\delta\alpha$ value (about $-2 \times 10^{-4} \text{ dB/m}$) results $2\times$ times lower than those associated with the pristine sample (ranging from $4 \times 10^{-3} \text{ dB/m}$ and $3 \times 10^{-3} \text{ dB/m}$).

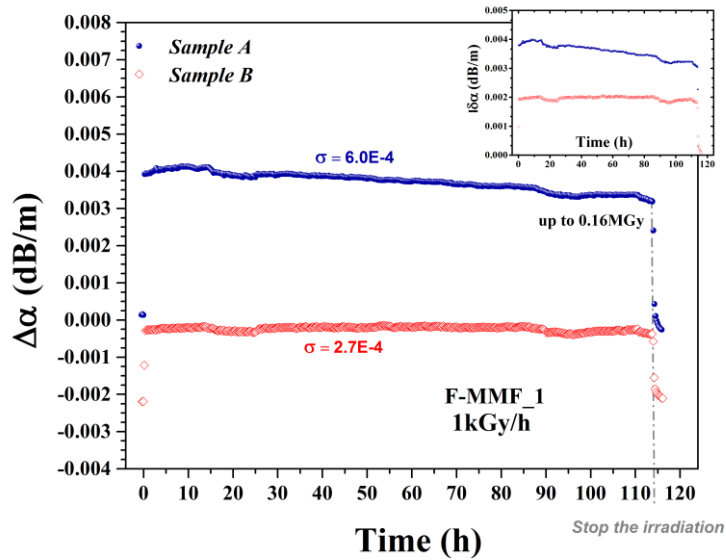


Figure 7.7. Time evolution of the differential attenuation extracted from RDTS results using the F-MMF_1 samples as the sensing element: *sample A* (blue spheres) and *sample B* (red squares). The inset shows the variation on the differential attenuation due to *in-situ* irradiation at 1 kGy(SiO₂)/h as a function of the time.

Since the γ -ray irradiation on our two samples (F-MMF_1) is homogeneous, we are here able to correct the RDTS temperature measurement as explained in section 7.2. In both cases, the temperature error after our correction remains limited to ~ 0.2 °C. It is reported as a function of the sensing length in Figure 7.8. However, although these results are promising, this procedure works only in specific environment conditions limiting its potential to favor the practical implementation of SE-RDTS in Cigéo. Namely, the case of non-uniform irradiation along the optical fiber will also have to be considered and corrected.

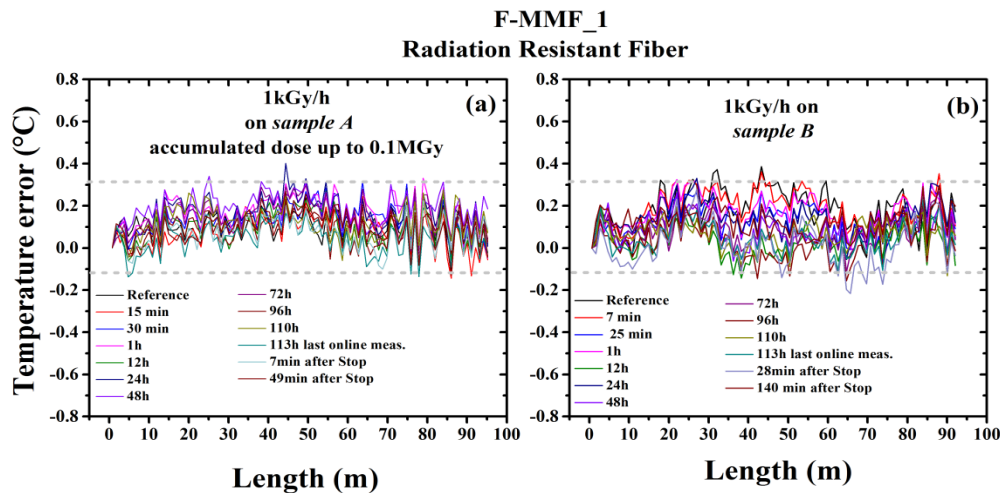


Figure 7.8. Temperature error achieved after our correction of radiation effects on F-MMF_1. Results obtained during γ -rays irradiation at 1 kGy/h dose rate for two different samples of F-MMF_1: *sample A* (a) and *sample B* (b). The grey dashes indicate an error of $\pm 0.2^\circ\text{C}$.

Brief discussion on the differential temperature induced attenuation (ΔTIA)

We also calculate the differential attenuation ($-\Delta\alpha_{\text{fit}}$) during the thermal treatment at 80°C of the 6°MGy γ -ray irradiated fiber PSC-MMF_1 during several days. These RDTS measurements have been discussed in section 6.2. Figure 7.9 shows the time evolution of this differential attenuation due to only the thermal treatment (ΔTIA). It is acquired directly by the RDTS measurement and obtained by the difference between the $-\Delta\alpha_{\text{fit}}$ evaluated at every instant and that one calculated on the measurement recorded at 30°C (i.e. our reference).

In section 6.2 (Figure 6.5) we discussed the ΔTIA obtained by the spectral measurement performed on the PSC-MMF_1 sample irradiated at 10°MGy during the thermal treatment at 80°C . Comparing the ΔTIA obtained, in the same experimental condition, through these two different techniques we observe that, during the thermal treatment, the differential attenuation evolves similarly. However, the achieved ΔTIA value at every instant differs between the two acquisition techniques; the difference being supposed to be related to the different TID deposited on the fiber used during the two experiments (6°MGy for the RDTS measurement and 10°MGy for the spectral attenuation one).

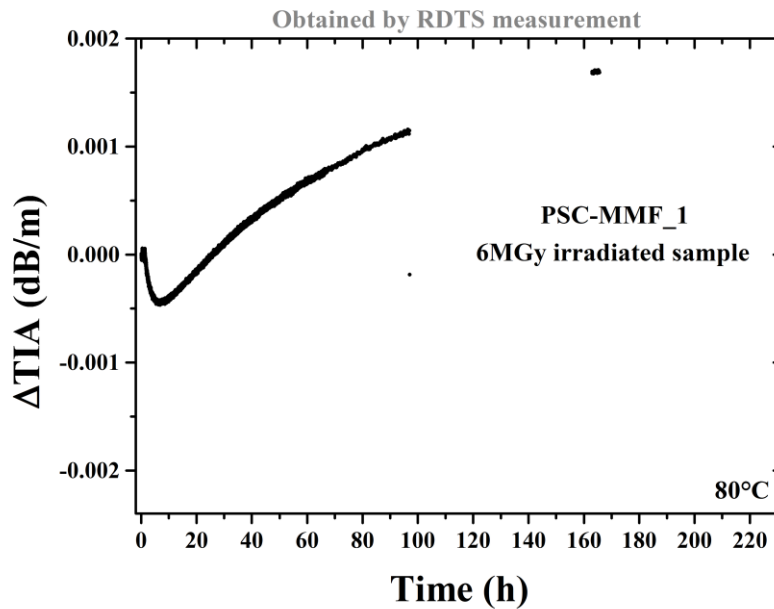


Figure 7.9. Differential temperature induced attenuation evolution as a function of time acquired by RDTS measurements for the 6^oMGy irradiated sample of fiber PSC-MMF_1 kept at 80 °C.

7.4 Conclusion

In the previous chapters we showed that the SE-RDTS response is strongly affected by γ -rays and or combined radiations and H₂ exposure so adapting the characteristics of the used fiber for the sensing we can limit its degradation. However the error on the temperature measurement can be only reduced and not suppressed with the commercially-available optical fibers. The additional hardening procedure reported in this chapter aims to correct this error due to the differential attenuation induced by gamma radiation and/or hydrogen presence. The current version of our correction technique allows today to limit the temperature error to $\sim 2^\circ$ C for sample irradiated at TID of 10 MGy, but this technique can only be applied under the following conditions: 1) Δ -IA uniform and 2) temperature constant along the sensing fiber. Moreover, in harsh environment, during an irradiation run at a constant dose rate of 1 kGy/h (up to ~ 160 kGy/h), using our technique on the radiation

resistant fiber (F-MMF_1) it is possible to avoid the Δ RIA effect on single-ended DTS sensor performances and achieved only ± 0.2 °C of temperature measurement error.

This procedure is the first step to correct the error observed on the SE-RDTS response in view of the integration of this technology in Cigéo. However, obtaining such performances in environments associated with non-homogeneous irradiation and/or temperature values along the fiber sensing length are required and are not covered by the today's proposed methodology.

Finally, through the *in-situ* measurements performed both under gamma irradiation and during the thermal treatment of irradiated fiber samples, we confirm once again that the SE-RDTS temperature error detected along the sensing fiber is mainly caused by the differential attenuation values between the two Raman Stokes and anti-Stokes signals.

Chapter 8

BOTDA sensing in gamma-ray and H₂ presence: Results

This chapter focuses on the study of the γ -ray radiation effects on the Brillouin distributed temperature and strain sensor performances when the sole fiber is exposed to γ -rays. In order to characterize the sensor behavior at a dose rate representative of the Cigéo application, the radiation tolerances of sensors using various classes of optical fibers are investigated through both *ex-situ* and *in-situ* measurements.

8.1 Introduction

As formerly discussed in Chapter 3 it is known that γ -rays lead to two macroscopic phenomena affecting the response of sensors exploiting the Brillouin scattering phenomena: *i*) the Radiation induced attenuation (RIA) and *ii*) the Brillouin frequency shift (BFS) [58], [59], [60].

- i*) RIA degrades the optical sensor performances by limiting the sensing distance range.
- ii*) BFS is due to the change of the Brillouin scattering properties modifying the central Brillouin frequency or its dependence on temperature and strain.

Previous studies (reported in Chapter 3), performed by *Phéron et al.* in our laboratory [59], [60], have shown that these radiation induced effects are dependent on the fiber composition. *Phéron et al.* reported the analysis of the radiation induced effects on the sensor performances using pure-silica and Ge-doped (with different Ge concentrations) optical fibers. Both in this work and in the *Phéron's* one two types of experiments are conducted: *ex-situ* and *in-situ*. The *ex-situ* measurements are performed at controlled RT after the γ -irradiation some weeks or months after the end of irradiation. It means that the remaining defects and changes in the fiber properties can be considered as stable at the RT conditions. The nominal total ionizing doses deposited in the fibers for these *ex-situ* tests are 1, 3, 6, 10 MGy (SiO₂). Instead, the *in-situ* tests are done during the γ -ray exposure at a dose rate of 1 kGy/h during several days. The test conditions of our work are close to the one of *Phéron's* study: same ⁶⁰Co sources and similar dose rate and TID, the results presented in this chapter extend the range of optical fibers and environmental constraints.

The *in-situ* tests conducted by *Phéron et al.* monitor the BOTDA response under γ -rays for 80 h (to reach ~80 kGy TID). They evaluated the device response under γ -rays when different levels of external stress are applied to the fiber coil reaching strained sample up to 150 g.

Instead, in our *in-situ* investigation the BOTDA signal is acquired for 160 h from the irradiation run start in order to reach a cumulated dose of 160 kGy deposited on the sensing fiber. Moreover, all the fibers have been coiled with higher levels of stress (up to 349 g) except the pure-silica-core one (PSC-SMF_2).

The *Phéron's* investigations reveal the pure-silica core fiber as a very promising candidate for temperature monitoring in high dose radiation environments (up to 10 MGy). Indeed, *ex-situ* tests show limited value of RIA (~50 dB/km at 10 MGy and radiation induced Brillouin Frequency Shift (RI-BFS) of ~2 MHz leading to a radiation induced temperature error below 2 °C for this fiber [59], [60] and at the highest investigated TID. Moreover, the *in situ* tests at lower doses show minor changes in the BOTDA sensor response when its sensing part (pure-silica core fiber) is irradiated at 1 kGy/h up to 90 kGy.

Our investigation aims to complete and confirm this previous study through both *ex-situ* and *in-situ* measurements using different classes of Ge-doped and pure-silica-core fibers. In particular, the experiments were carried out on 6 types of single-mode fibers: Ge-SMF_50g,

Ge-SMF_110g, Ge-SMF_270g, PSC-SMF_1, PSC-SMF_2 and PSC-SMF_3. Their main characteristics being reported in section 4.1. Moreover, the dependence of the Brillouin central frequency on the drawing tension applied during the fabrication of Ge-doped fibers is investigated as a function of the irradiation dose.

Finally, for the PSC-SMF_1 we examine in depth all constraints of the Cigéo application requiring the use of BOTDA systems in an environment (waste storage cells) where the temperature can change between 25 °C and 90 °C and both γ -ray dose rates and the H₂ release can evolve with time and then highly degrade the optical fiber properties or impact the device response. Therefore, we evaluate the sensor response both undergoing to a constant temperature of 80 °C after γ -rays exposure as well as a function of combined *ex-situ* γ -ray radiation and hydrogen loading effects. Moreover, the evolution response during the H₂ desorption from the core of the sensing fiber is also investigated.

In order to evaluate the impact of the RIA phenomena on the device performances the experiments are supported by attenuation measurements performed at the operation wavelength of our BOTDA setup: 1550 nm.

8.2 RI-BFS

In order to correctly evaluate the BOTDA response under γ -rays it is mandatory to discriminate between the different contributions to the observed BFS. As known, three different factors can induce a shift in the Brillouin central frequency (BF or ν_B) of a fiber: application of a stress to the fiber, a change in the fiber temperature, its exposure to γ -rays or to H₂ atmosphere. During our tests to avoid the stress contribution, the samples of each fiber were realized with the same controlled strain conditions (see Chapter 4). Similarly, when possible (*ex-situ* tests) the measurements are performed at a well-known and constant temperature (RT) in order to avoid the temperature contribution and to highlight on the sole part of the RI-BFS.

Nevertheless, during our *in-situ* measurements the temperature within the irradiation zone evolves between 23 °C and 26 °C. Ergo, in order to eliminate temperature related errors on

the RI-BFS evaluation, the sensor measurements have been corrected for these limited temperature changes that were monitored by two thermocouples.

The RI-BFS, $\Delta\nu_{B_{rad}}$, is therefore calculated as:

$$\Delta\nu_{B_{rad}} = \Delta\nu_B - C_T\Delta T \quad 8.1$$

where $\Delta\nu_B$ is the acquired Brillouin frequency peak shift, ΔT is the temperature variation during the measurement and C_T is the temperature coefficient obtained for the pristine fiber (as explained in section 4.2.2.1). Indeed, it was also checked that this temperature coefficient does not change with irradiation for the TID < 0.2 MGy [59], [60].

As mentioned in Chapter 4, the results presented hereafter were obtained by averaging several successive measurements carried out under the same experimental conditions.

8.3 Germanium doped fibers

This section reports the results obtained from the *ex-situ* and *in-situ* session concerning the BFS measurements using 3 different Ge-doped fibers: Ge-SMF_50g, Ge-SMF_110g, Ge-SMF_270g as the sensing elements. The three investigated samples have been designed from the same Modified Chemical Vapor Deposition (MCVD) preform but differently drawn at various tensions of: 50 g, 110 g and 270 g, respectively. Changing the drawing tension could affect the residual internal stress radial distribution within the fiber and then its Brillouin response.

8.3.1

Ex-situ measurements

This paragraph deals with the permanent effects induced by γ -rays (*ex-situ* tests) on the previously defined Ge-doped fibers after cumulated TIDs of: 1, 3, 6 and 10 MGy.

Radiation-Induced Attenuation

Figure 8.1 reports the RIA dose dependence at 1550 nm measured at RT for all investigated samples. While the RIA grows with the TID, it reaches ~ 0.13 dB/m at 10 MGy. Moreover, the induced attenuation appears independent on the drawing tension and this behavior is

reported in Figure 8.1. For all Ge-doped fibers we estimate at 10 MGy a maximum sensing range of 76 m.

As expected from [121], [122] the RIA dose-dependence can be described by the following power-law function:

$$a = c \cdot D^f \quad 0 < f < 1 \quad 8.2$$

where D is the TID and f and c are two experimental parameters. Whereas f is supposed to be independent on the dose rate \dot{D} , c is given by $c = K \left(\frac{dD}{dt}\right)^b$ where b and K are two constants. The obtained parameters for the Ge-SMF_50g are: $c = (0.070 \pm 0.006) \frac{dB}{m} MGy^{-f}$ and $f = (0.30 \pm 0.05)$.

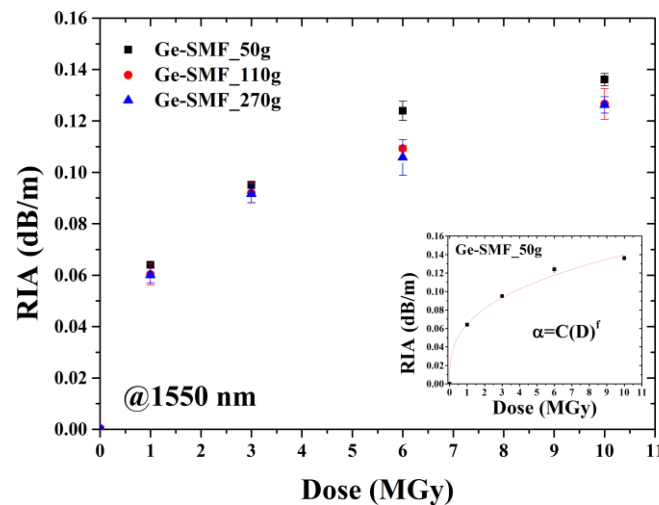


Figure 8.1. RIA evolution at 1550 nm as a function of the TID (1, 3, 6 and 10 MGy) measured in the Ge-SMF_50g (black squares), Ge-SMF_110g (red circles) and Ge-SMF_270g (blue triangles). The inset reports a sub linear fit describing the RIA as a function of the dose (D) for Ge-SMF_50g. Measurements performed at $\sim 25^\circ\text{C}$. The confidence level is on the order of two standard deviations (95%).

The RIA phenomenon causes a reduction of the Brillouin peak amplitude and its normalized evolution as a function of deposited dose is reported in Figure 8.2.

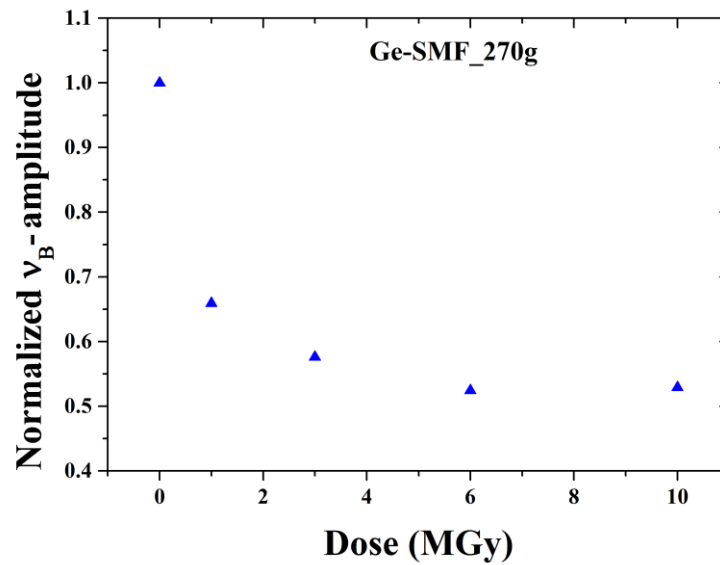


Figure 8.2. Normalized amplitude of the Brillouin central frequency peak as a function of the dose obtained for the Ge-SMF_270g.

Brillouin frequency changes due to the γ -radiation

Table 8.1 summarizes the Brillouin central frequencies measured at 40°C in the pristine samples for the three tested Ge-doped fibers. As expected from literature [123], obtained results show that the fibers drawn with the larger tension have the smaller v_B values.

TABLE 8.1. MEASURED BRILLOUIN CENTRAL FREQUENCY OF THREE TESTED GE-FIBERS

GE-DOPED FIBERS			
DRAWING TENSION (g)	50	110	270
v_B (MHz)	10344.2±0.2	10318.8±0.2	10231.0±0.6

The confidence level is on the order of a two standard deviation (95%).

In Figure 8.3, the dose dependences of the radiation induced Brillouin frequency shifts (RI-BFS) are reported for the three tested Ge-doped optical fibers. Although the fibers present different RI-BFS at lower TID (≤ 3 MGy), their evolutions tend to the same limit of about 10 MHz at 10 MGy.

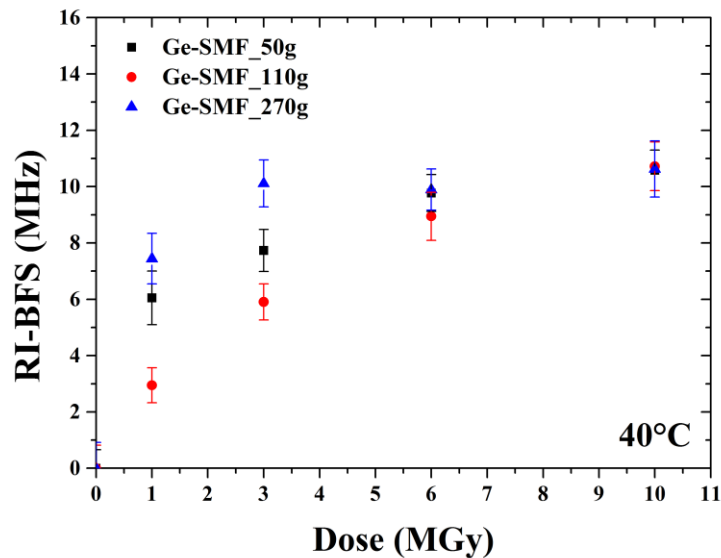


Figure 8.3. Dependence of the RI-BFS on the TID (1, 3, 6 and 10 MGy) for the Ge-SMF_50g (black squares), Ge-SMF_110g (red circles) and Ge-SMF_270g (blue triangles). The confidence level is of the order of two standard deviations (95%).

The v_B dependence as a function of the TID is investigated for all the studied fibers and illustrated in Figure 8.4. As expected [59], [60], both pristine and γ -irradiated samples, show linear dependence of the Brillouin frequency with the drawing tension. In order to evaluate if radiation impacts this property, we calculate through a weighted linear fit, the drawing tension dependence coefficient, C_{Dr} for all samples. Obtained values, reported in Table 8.2, are close, within an error of $\pm 3\%$. Therefore, the v_B -dependence on the drawing tension is unaffected by radiations up to 10 MGy cumulated dose.

TABLE 8.2. DRAWING TENSION DEPENDENCE COEFFICIENT

GE-DOPED FIBERS					
DOSE (MGY)	0	1	3	6	10
C_{Dr} (MHz/100 g)	-52.8	-51.6	-51.3	-52.8	-53.7

The confidence level is of the order of a two standard deviation (95%).

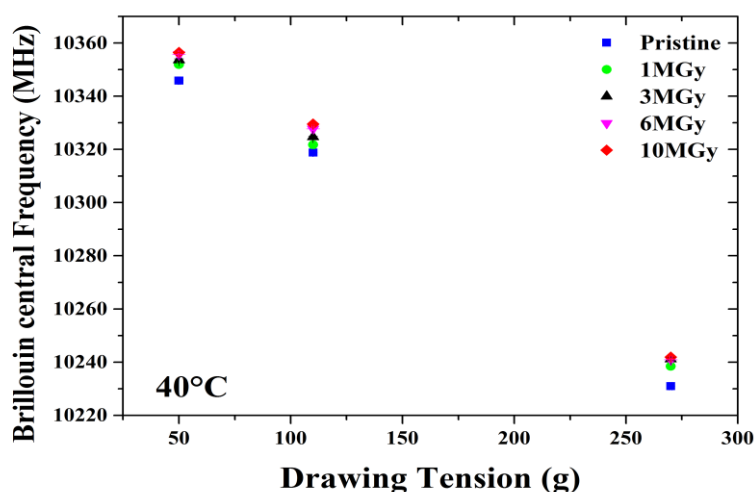


Figure 8.4. Brillouin central frequency as a function of the drawing tension measured on the Ge-doped samples: pristine (blue squares) and γ -ray irradiated at 1 (green circles), 3 (black triangles), 6 (pink triangles), 10 MGy (red rhombi). The confidence level is on the order of two standard deviations (95%).

Temperature and strain coefficient changes with TID

Figure 8.5 a reports typical measurements of the Brillouin central frequency dependence on the temperature (range $30^{\circ}\text{C} \div 80^{\circ}\text{C}$) observed for the 3 pristine samples: Ge-SMF_50g, Ge-SMF_110g and Ge-SMF_270g. In all samples the expected linear dependence of ν_B to design a temperature sensor is highlighted [26], [124]. From these results we calculate the C_T values for each pristine sample and are reported in the inset of Figure 8.5 a. The evolution of the temperature coefficients as a function of the dose is reported in Figure 8.5 b. This study was performed using the same previous procedure applied on the similar samples γ -irradiated at 1, 3, 6 and 10 MGy. As a conclusion, C_T values can be considered as constant within 3% error (grey dashed lines in Figure 8.5 b) as well as affected by neither the considered drawing tensions nor the considered TID range.

The BFS dependence on the applied strain is illustrated in Figure 8.6 for the three Ge-doped fibers before and after their irradiation at MGy dose levels. Figure 8.6 a exhibits the expected linear increase of the BFS with the applied strain on all samples and its strain dependency slightly differs between pristine and γ -irradiated samples.

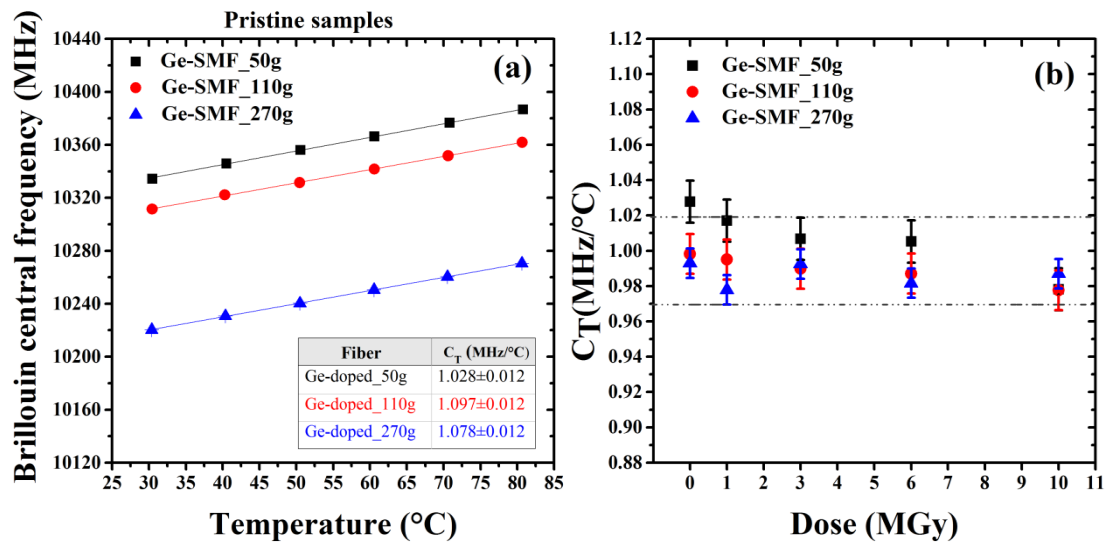


Figure 8.5. Brillouin central frequency evolution as a function of the temperature for the 3 pristine Ge-doped fibers (a) and C_T values evolution as a function of the TID (b): Ge-SMF_50g (black squares), Ge-SMF_110g (red circles) and Ge-SMF_270g (blue triangles). The inset sums up the extracted C_T values. In (b) the grey dashed lines delimit a $\pm 3\%$ variation. The confidence level is on the order of a two standard deviation (95%).

In particular, for the Ge-SMF_50g and the Ge-SMF_110g, shown in Figure 8.6 a and b respectively, the BFS at high strain values is larger in the 10 MGy irradiated sample than in the pristine one. Differently, the Ge-SMF_270g results of Figure 8.6 c show an opposite behavior in which the BFS of the irradiated samples are smaller than that of the pristine fiber. In order to quantify this BFS variation with the TID, C_{ϵ} of each tested sample was acquired through a linear fit. Its TID evolution is reported in Figure 8.7 and shows different behaviors as a function of the drawing tensions. Indeed, as discussed in advance for the previous Figure 8.6, in Figure 8.7 both the 10 MGy γ -irradiated Ge-SMF_50g and Ge-SMF_110g show higher C_{ϵ} values than the respective pristine samples. Whereas the fiber drawn with the highest tension (270 g) shows a reverse evolution with the TID, indeed the C_{ϵ} estimation obtained for the 2 γ -irradiated Ge-SMF_270g samples (at 3 and 10 MGy) is lower than that not irradiated. The C_{ϵ} values are scattered within a variation of $\pm 10\%$, highlighted by the grey dashed lines in Figure 8.7. However, this variation could be also due to an error induced by the used strain setup.

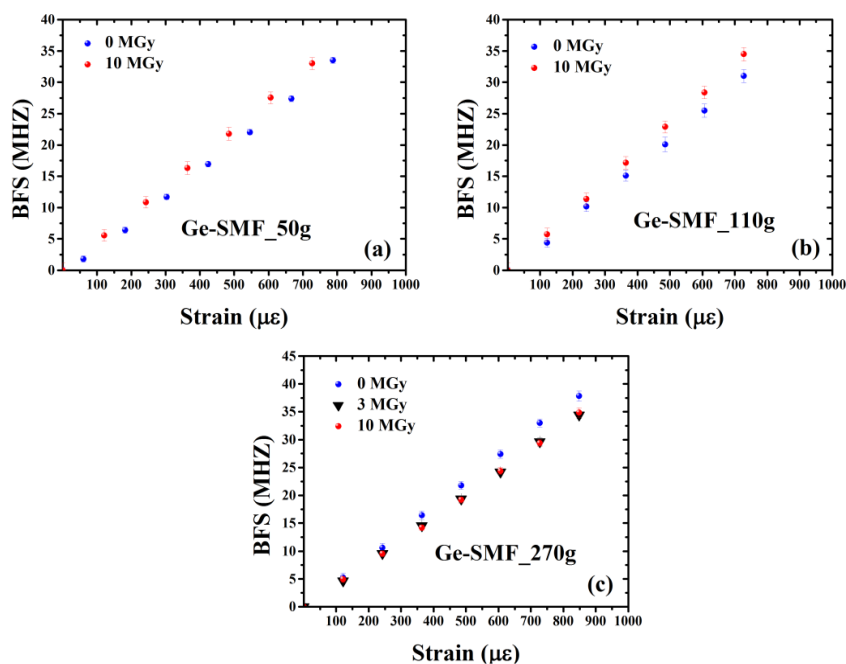


Figure 8.6. Brillouin frequency shift (BFS) evolution as a function of the applied strain for the 3 Ge-doped fibers: Ge-SMF_50g (a), Ge-SMF_110g (b) and Ge-SMF_270g (c) as well as for a γ -irradiation at 10 MGy. An additional 3 MGy irradiated sample was tested for the Ge-SMF_270g. The confidence level is on the order of a two standard deviation (95%).

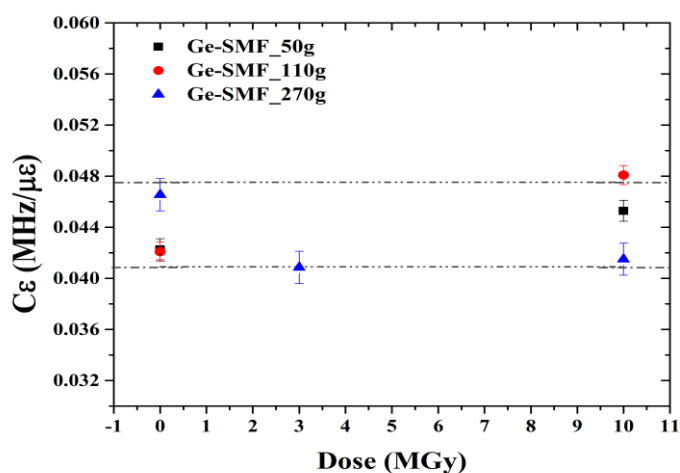


Figure 8.7. C_ϵ values as a function of the TID: Ge-SMF_50g (black squares), Ge-SMF_110g (pink circles) and Ge-SMF_270g (blue triangles). The grey dashed lines delimit a $\pm 10\%$ variation. The confidence level is of the order of a two standard deviation (95%).

In-situ measurements

Whereas in our previous paragraph 8.3.1 we investigated the radiation influence on the BOTDA performances at MGy dose levels, this section focuses on the sensor response when its sensing fiber is exposed to steady state γ -rays at 1 kGy/h dose rate. Moreover, the γ -radiation *in-situ* effects variations on the Ge-doped fiber were evaluated for the different fiber drawing tensions. All measurements were performed at the irradiation room temperature ($23^{\circ}\text{C} \div 26^{\circ}\text{C}$).

Transient RIA

Figure 8.8 reports the RIA time evolution acquired at 1550 nm during γ -rays (transient RIA) and monitored for about 7 days to reach TID of ~ 160 kGy. The measurements were carried out on the three optical fibers: Ge-SMF_50g, Ge-SMF_110g and Ge-SMF_270g. All samples under test show transient RIA values increasing with the dose as well as with the same kinetic at least up to ~ 70 kGy. After this value only the Ge-SMF_50g signal is detected (due to instrumental limit). The γ -ray effect on the fiber transient RIA seems to be independent on its drawing tension.

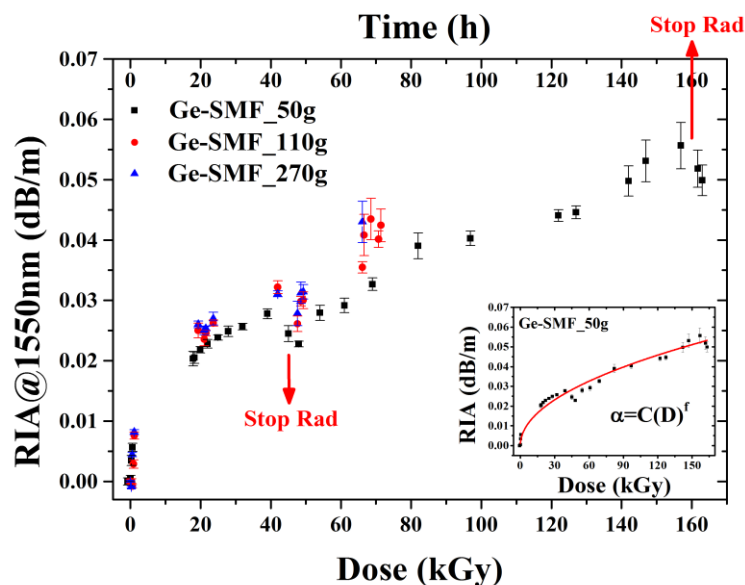


Figure 8.8. Transient RIA evolution at 1550 nm during ~ 4 days under γ -rays at 1 kGy/h dose rate for Ge-SMF_50g (black squares), Ge-SMF_110g (red circles) and Ge-SMF_270g (blue triangles). The inset reports a sub linear fit describing the RIA time/dose evolution for Ge-SMF_50g. Measurements performed around 25°C . The confidence level is on the order of 2 standard deviations (95%).

Moreover, for the Ge-SMF_50g we observe that the transient RIA increases with the dose reaching ~ 0.05 dB/m at 160 kGy TID. As reported in Chapter 4 after 42 h of irradiation, the source was switched off for few hours as indicated by the red arrow in Figure 8.8.

As for the *ex-situ* RIA results, we describe the dose-dependence through the power-law and the corresponding parameter values are reported in Table 8.3 for these fibers. Using this dose evolution parameter we extrapolated the RIA level at 10 MGy to be around 0.4 dB/m, higher compared to that obtained by the *ex-situ* measurement (~ 0.13 dB/m) at the same TID. This difference can be explained by the *in situ* tests where both stable and unstable defects are involved whereas mostly the stable ones contribute to the RIA measured during *ex situ* tests.

TABLE 8.3. DOSE DEPENDENCE FIT PARAMETERS. *IN-SITU* MEASUREMENT ON GE-DOPED FIBERS.

GE-DOPED FIBERS			
DRAWING TENSION (g)	50	110	270
$c \left(\frac{dB}{m} \cdot MGy^{-f} \right)$	$(0.47 \pm 0.10) \cdot 10^{-2}$	$(0.53 \pm 0.10) \cdot 10^{-2}$	$(0.59 \pm 0.13) \cdot 10^{-2}$
f	0.48 \pm 0.2	0.48 \pm 0.5	0.47 \pm 0.5

The fit doesn't take into account the measurements performed when the source is switched off.

Brillouin frequency changes under γ -rays

The Brillouin central frequency of the Ge-SMF_50g, Ge-SMF_110g and Ge-SMF_270g during the γ -ray exposure at 1 kGy/h was monitored for 160 h. As described in Chapter 4, each sample was 70 m long and coiled with a 10 cm diameter with 4 different applied external strain levels along the sensing lines: 20 g, 131 g, 240 g, and 349 g. Figure 8.9 reports two measurements of ν_B along the Ge-SMF_50g sensing fiber length: *i*) the *reference measurement* defined as the first result acquired before the irradiation start *ii*) the last measurement, recorded at the end of the irradiation run after 159 h. It has been corrected for the temperature evolution with respect to the reference⁹, as explained in section 8.2, and so highlights the radiation induced Brillouin Frequency shift (RI-BFS) at 159 kGy. Both measurements provide a clear evidence for the different frequency steps due to the applied

⁹ Since no change was observed as a function of the TID for the temperature coefficient (see Figure 8.5 b), the measurement was corrected for the temperature with respect to the reference sample using the C_T obtained for the pristine fiber.

strain levels along the fiber length. Moreover, no significant changes are observed between the reference *measurement* and that one at 159 h.

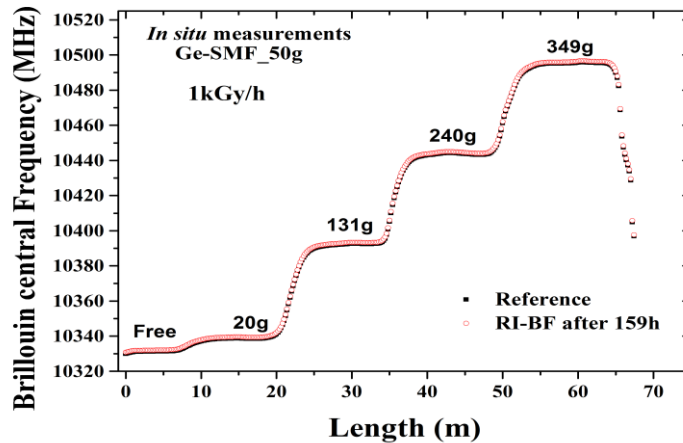


Figure 8.9. Brillouin central frequency evolution all along the studied Ge-SMF_50g samples: the *reference measurement* (black circles) and the irradiated at 159 kGy dose. This last one was corrected for the temperature change with respect to the reference.

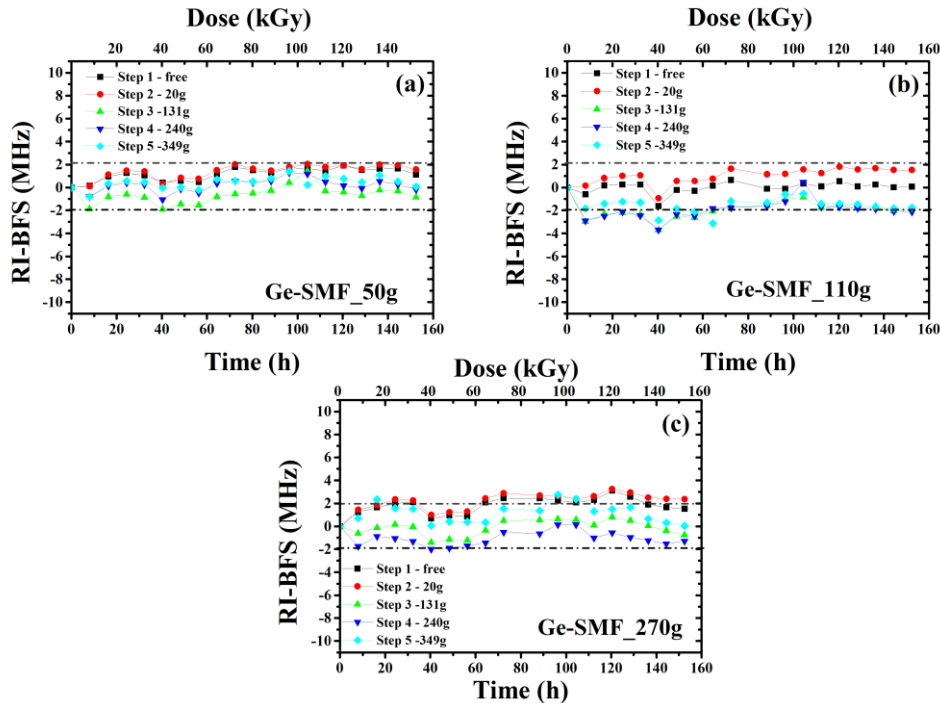


Figure 8.10. Radiation induced Brillouin frequency shift (RI-BFS) as a function of the irradiation time for the various fiber parts with different applied strain levels: Results for Ge-SMF_50g (a), Ge-SMF_110g (b) and Ge-SMF_270g (c). The black dashed lines delimit a variation of 2 MHz.

Figure 8.10 reports the RI-BFS time/dose evolution of each applied strain level for the Ge-SMF_50g (a), Ge-SMF_110g (b) and Ge-SMF_270g (c). All strain steps show the same behavior with the dose exposure, the small shifts (~ 2 MHz) with respect to the reference, observed for each step, are attributed to systematic errors of our experimental setup.

Discussion

8.3.3 We evaluated the γ -ray effects on the performances of the BOTDA using a Ge-doped fiber as sensing element. In particular, for the first time, these radiation induced effects were investigated using fibers manufactured from the same preform, but drawn using different tensions: 50 g, 110 g and 270 g. The analysis highlights diverse important results:

i) **The Brillouin central frequency changes with the drawing tensions.** In particular, this frequency decreases for larger drawing tension. This result agrees with the literature. Indeed, *Zou et al.* [123], [125] reported a study on a Ge-doped fiber (8 mol. % of Ge and $3.5 \mu\text{m}$ of core radius) characterized by different drawing tensions (43 g, 143 g and 193 g) and they observed a v_B decreases when increasing the tension. Both our and Zou studies show that the drawing tension dependence of v_B is linear and its dependence coefficients, C_{Dr} , found in both studies are close to each other ($-42.0 \text{ MHz} / 100 \text{ g}$ in [123]). However, our study is extended to irradiation influence so to the TID dependence with investigated doses up to 10 MGy. Radiation does not impact the observed linearity of v_B with the drawing tension and C_{Dr} remains constant within an error of 3 %.

ii) **Both the *ex-situ* and the *in-situ* measurements show that the RIA dose dependence is independent on the drawing tension.** The three fibers RIA growths kinetics follows the power law dependence reported in literature [121], [122]. This Ge-doped fiber exhibits RIA value of $\sim 0.13 \text{ dB/m}$ at 10 MGy and can be considered much radiation resistant than the standard SMF28 with a RIA level of $\sim 0.25 \text{ dB/m}$ at the same 10 MGy cumulated dose [59], [60]. However, regarding the different application constraints and the instrument optical budget (10 dB), **the RIA values of such fiber is not suitable as sensing element for the considered radioactive wastes disposal cells monitoring.**

iii) *Ex-situ* BFS measurements: although the radiation effects on the fiber transmission are not influenced by the drawing, **we observe for the 3 fibers drawn with different tensions different RI-BFS behaviors as a function of the TID.** Indeed, the v_B shift due to

the γ -rays differs in the three OFs at lower TID (1 MGy and 3 MGy), reaching the saturation with the same RI-BFS value at the highest 10 MGy dose. Concerning the dose evolution of the temperature coefficient C_T of each fiber, our result agrees with the literature [59], [60]. The C_T remains constant within an error of $\sim 3\%$ regardless the drawing tension. Instead, concerning the strain coefficient C_ε our results show a variation of this parameter a function of the TID within $\sim 10\%$.

However, the RI-BFS of ~ 10 MHz obtained at 10 MGy leads a temperature error of $\sim 10^\circ\text{C}$ and therefore makes this fiber not suitable to operate in high dose (>10 MGy) radiation environment of the Cigéo application.

iv) ***In-situ* measurements: the BOTDA response under γ -rays exposure shows no “transient” error in the temperature estimation during low dose rate (1 kGy/h) exposures up to doses of 160 kGy.**

8.4 PSC-doped fiber

This section investigates the γ -radiation exposure effects on the BOTDA performances using different types of pure-silica-core fibers as sensing elements: PSC-SMF_1, PSC-SMF_2 and PSC-SMF_3. The PSC-SMF_1 is the same pure-silica core fiber investigated in the *Phéron*'s work, named F/SiO₂ (see Chapter 3). The sensor response using PSC-SMF_1 in presence of combined γ -rays and H₂ constraints is also investigated.

8.4.1

***Ex-situ* measurement**

This paragraph reports the investigations of γ -ray and combined γ -ray and H₂ loading *ex-situ* impact on the BOTDA performances using pure-silica-core fibers: PSC-SMF_1 and PSC-SMF_2. The radiation effects are evaluated at several TID values up to 10 MGy.

Radiation-Induced Attenuation

Figure 8.11 shows the RIA dose dependence at 1550 nm measured at RT for the two OFs: PSC-SMF_1 and PSC-SMF_2.

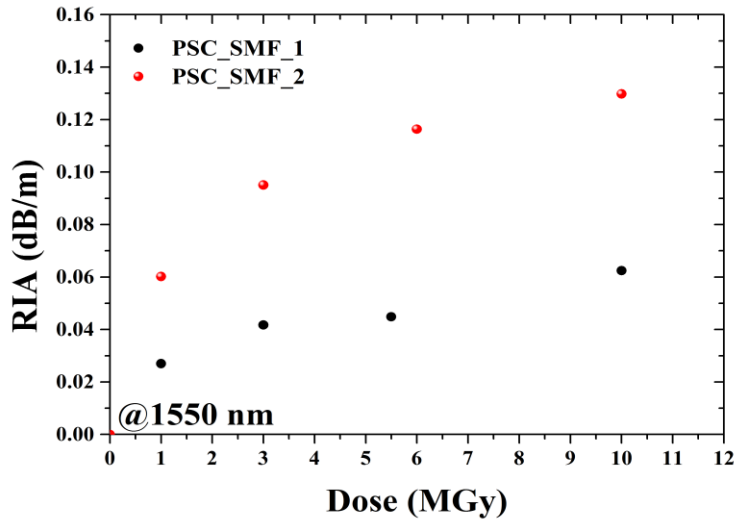


Figure 8.11. RIA evolution at 1550 nm as a function of the TID in PSC-SMF_1 (black circles) and PSC-SMF_2 (red spheres). The measurements are performed at RT ($\sim 25^\circ\text{C}$). The confidence level is on the order of two standard deviations (95%).

Both fibers show RIA values growing with the TID, but the PSC-SMF_1 RIA at 1550 nm is meaningfully lower than for the PSC-SMF_2. Indeed, whereas the PSC-SMF_2 shows a RIA of ~ 0.13 dB/m at 10 MGy, the PSC-SMF_1 RIA value reached a saturation value of ~ 0.06 dB/m at the same dose. We estimate at 10 MGy a maximum sensing range of 76 m and 200 m for PSC-SMF_2 and PSC-SMF_1, respectively.

As for the Ge-doped fiber (section 8.3.1), we can describe the RIA dose dependence through the power-law of Equation 8.2. The parameters obtained for the two fibers are reported in Table 8.4.

TABLE 8.4. DOSE DEPENDENCE FIT PARAMETERS. *EX-SITU* MEASUREMENTS ON PSC-FIBERS

GE-DOPED FIBERS		
DRAWING TENSION (g)	PSC-SMF_1	PSC-SMF_2
$c \left(\frac{\text{dB}}{\text{m}} \cdot \text{MGy}^{-f} \right)$	0.03 ± 0.02	0.072 ± 0.002
f	0.22 ± 0.04	0.26 ± 0.02

It is worth noting that the PSC-SMF_2 is described by the same RIA power law than the Ge-doped fiber discussed in section 8.3.1. This topic will be discussed later in section 8.4.3.

Brillouin frequency and temperature coefficient changes induced by radiation

In Figure 8.12, the dose dependence of the radiation induced Brillouin frequency shift (RI-BFS) is reported for the two tested PSC-OFs. The fibers present different RI-BFSs: for the PSC-SMF_1 it shows a slight increase with increasing the TID up to ~ 2 MHz at 10 MGy while for the PSC-SMF_2 it evolves forward higher values with the TID increase, reaching about 4 MHz at 10 MGy.

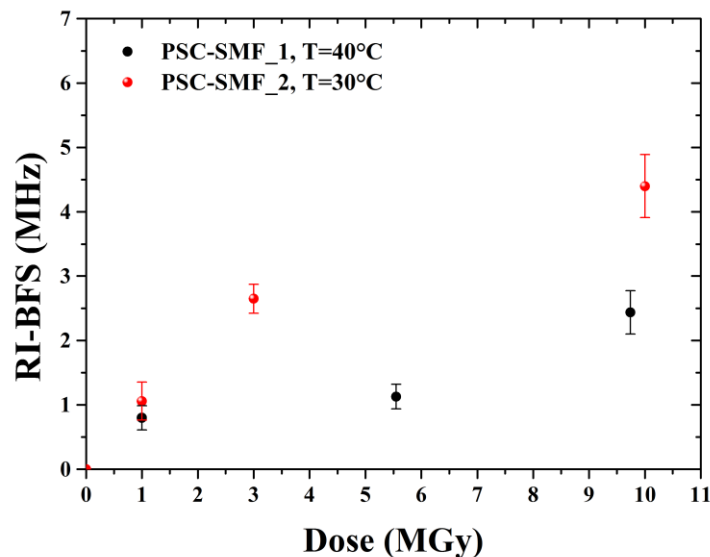


Figure 8.12. Dependence of the RI-BFS on the TID for the PSC-SMF_1 (black circles) and the PSC-SMF_2 (red spheres). The measurements were performed at two different T: 40°C for the PSC-SMF_1 and 30°C for the PSC-SMF_2. The confidence level is on the order of two standard deviations (95%).

The BFS dependence on the temperature performed on PSC-SMF_2 from 30°C up to 300°C was studied. Also in this case we observe a linear dependence of ν_B versus the temperature for all samples (as-drawn, irradiated) and the corresponding C_T values are reported in the Figure 8.13. As expected [59], [60], no real change with TID is observed for the temperature coefficient of PSC-SMF_2, indeed its value remains constant within an error of 4% (highlighted by the grey dashed lines in Figure 8.13). Similar C_T measurements were carried

out on a pristine sample of the same fiber with only a polyimide coating and no change in the temperature coefficient was observed.

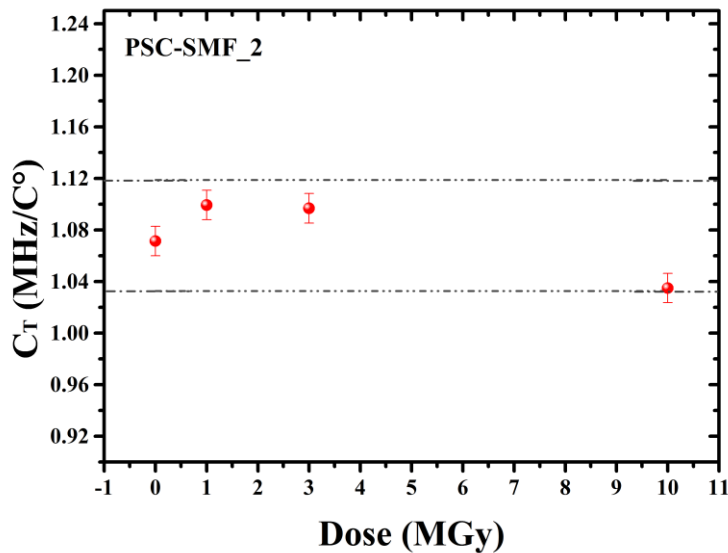


Figure 8.13. C_T values evolution versus the TID in PSC-SMF_2 fiber. The C_T parameters are acquired in the range $30^\circ\text{C} \div 300^\circ\text{C}$. The grey dashed lines delimit a 4 % error. The confidence level is on the order of a two standard deviations (95%).

Concerning the PSC-SMF_1, only the temperature coefficient of the pristine sample was evaluated $C_T = (1.197 \pm 0.013)$ and its value is comparable with the Pheron's study [59], [60]. The dose-dependence of the temperature coefficient is not investigated in this work. However, we assume that its value does not change with the TID as shown in [59], [60], where the C_T stays constant within a 2 % error.

BOTDA performances degradation induced by combined H_2 and γ -rays exposures

In the previous paragraph, the evaluation of the vulnerability of the BOTDA performances as a function of the dose was investigated for two PSC-fibers. This section reports the *ex-situ* tests aiming to evaluate the combined γ -rays exposures and hydrogen loading effects on the sensor response. The investigation was carried out on the PSC-SMF_1. In particular, regarding the hydrogen influence, we considered two different situations: while one sample was H_2 -loaded just before the irradiation run, the second one was also H_2 -loaded and kept at

RT for two months before the irradiation session. Consequently, the differences between the two samples is quite clear as the first one will have the entire H₂ content during the irradiation, the second will have enough time to out-diffuse.

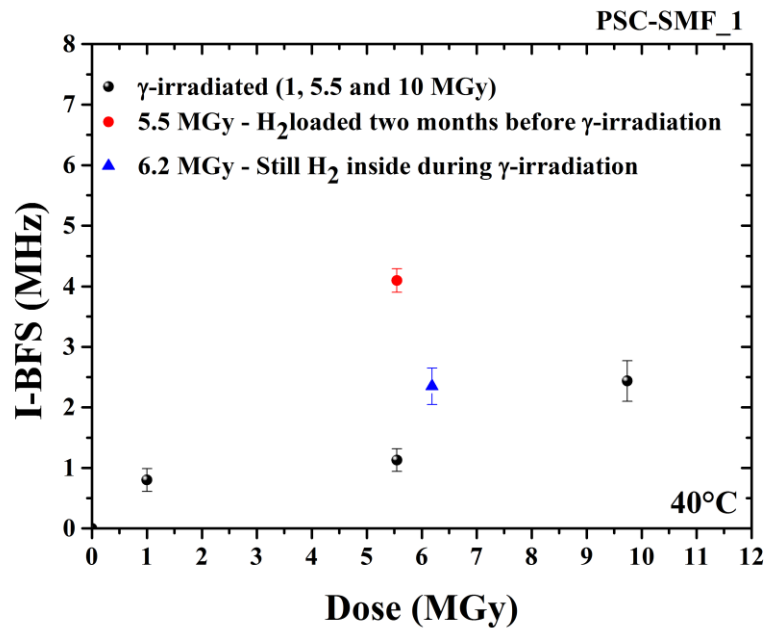


Figure 8.14. I-BFS measured on PSC-SMF₁ as a function of the treatments. Results of only γ -irradiated at (black spheres), γ -irradiated with H₂ inside (blue triangle) and γ -irradiated two months after the H₂-loading (red circle) samples are shown. The confidence level is on the order of two standard deviations (95%). Test performed at 40°C.

TABLE 8.5. IA AND I-BFS VALUES OF PSC-SMF₁

*TREATMENT	IA@1550 nm (dB/m)	I-BFS (MHz)
5.5 MGy	0.045±0.002	1.12±0.19
5.5 MGy TWO MONTHS AFTER THE H ₂ -LOADING	0.079±0.008	4.10±0.19
6.2 MGy WITH STILL H ₂ INSIDE	0.050±0.004	2.3±0.3

The IA test are performed at RT and the BFS at 40°C.

*The TID slightly differs from the nominal one because of the different fiber location with respect to the γ -ray source.

Table 8.5 shows the induced attenuation, IA, at 1550 nm and the I-BFS values measured on three different samples irradiated with the same nominal dose of 6 MGy: the only γ -irradiated

one, the sample γ -irradiated with H₂ inside and that one γ -irradiated two months after H₂-loading. Moreover, the BFS as a function of the treatments (dose and combined γ -radiation/H₂ loading) is depicted in Figure 8.14.

For the γ -irradiated with H₂ inside the sample the induced attenuation at 1550 nm is comparable with that one detected in the only irradiated fiber (~ 0.05 dB/m), whereas it results higher for the γ -irradiated 2 months after the H₂ pre-treatment samples. Instead, the BFS measured for the both irradiated and H₂-treated samples is higher with respect to the only irradiated sample. In particular, the samples irradiated 2 months after the H₂-loading shows the worst response of all tested samples with ~ 4 MHz of BFS.

***In-situ* measurements**

8.4.2

This section is aimed to study the BOTDA response when its sensing fiber is exposed to different environment constraints: *i)* steady state γ -rays at 1 kGy/h dose rate and *ii)* H₂ presence inside the fiber core.

Brillouin frequency changes during the γ -ray exposure

The tests were carried out on 3 pure-silica-core fibers: PSC-SMF_1, PSC-SMF_2 and PSC-SMF_3. All measurements were performed at the irradiation room temperature ($23^\circ\text{C} \div 26^\circ\text{C}$). The reference is considered at the beginning of the irradiation run.

The Brillouin central frequency of the three OFs is monitored during 160 h of γ -ray exposures with 1 kGy/h dose rate. As reported in Chapter 4, each investigated fiber is ~ 100 m long, coiled with different applied strain levels along its sensing line. The PSC_SMF_1 is looped in 10 cm diameter with 7 applied stress steps from 20 g to 184 g. The PSC_SMF_2 is 100 m long coiled in 8 cm diameter and is kept free from stress. Finally, the PSC-SMF_3 is 70 m long, coiled in 10 cm diameter with 4 different applied strain levels, from 20 g to 349 g. For this last OF the RIA values measured at the TIDs of 1 MGy and 3 MGy are (0.052 ± 0.003) dB/m and (0.072 ± 0.004) dB/m, respectively and its C_T (measurements range $20^\circ\text{C} \div 80^\circ\text{C}$) is (1.3 ± 0.04) MHz/ $^\circ\text{C}$.

Figure 8.15 shows for the PSC-SMF_1 (a) and PSC-SMF_3 (b) the RI-BFS time evolution for fibers submitted to each applied strain level (calculated using Equation 8.1). In Figure 8.15 a, for the PSC-SMF_1, the fiber shows the same behavior with the dose exposure independently of the strain applied, the small observed shifts (~ 1.5 MHz) with respect to the reference, are attributed to systematic errors of our experimental setup. Concerning the PSC-SMF_3 of Figure 8.15 b, a shift toward the smaller frequencies with respect to the reference measurement is observed. This shift fluctuates around 2.5 MHz with respect to its mean value, ~ -3 MHz.

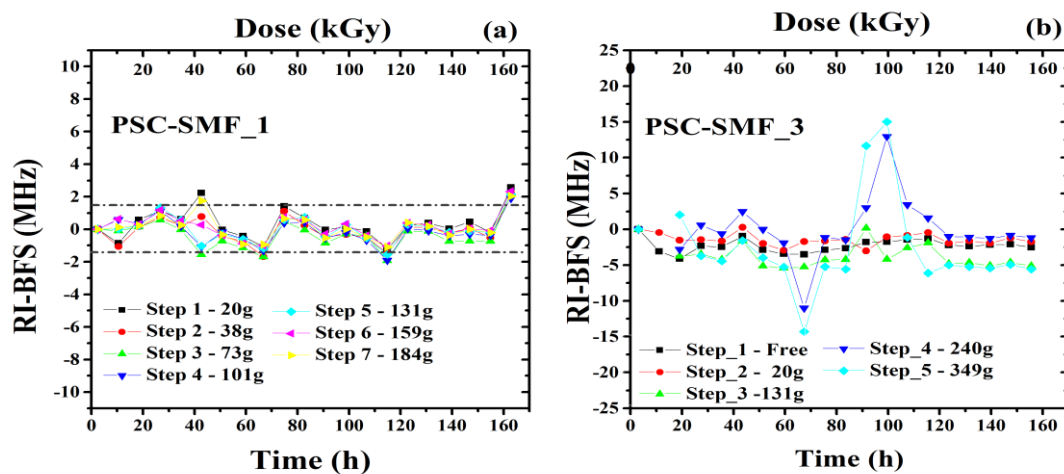


Figure 8.15. Radiation induced Brillouin frequency shift (RI-BFS) as a function of the irradiation time for the various parts of fibers submitted to different applied strain levels. Results concern PSC-SMF_1 (a) and PSC-SMF_3 (b) fibers. In (a) the black dashed lines delimit a variation of 1.5 MHz.

Figure 8.16 a reports the evolution of the peak amplitude during γ -ray exposure of the PSC-SMF_2 fiber. Although the irradiation run was carried out for 160 h, the signal was no more exploitable after ~ 80 h due to a too small signal-to-noise ratio. We perform the analysis up to ~ 53 h of irradiation. After this time, the amplitude value is reduced by more than 90%. Figure 8.16 b reports the RI-BFS as a function of the fiber length for this specific irradiation conditions (53 h). A RI-BFS toward lower frequencies is observed during the γ -ray exposure at 1 kGy/h up to 53 h; its value remains almost constant along the fiber and is equal to (-1.8 ± 0.4) MHz.

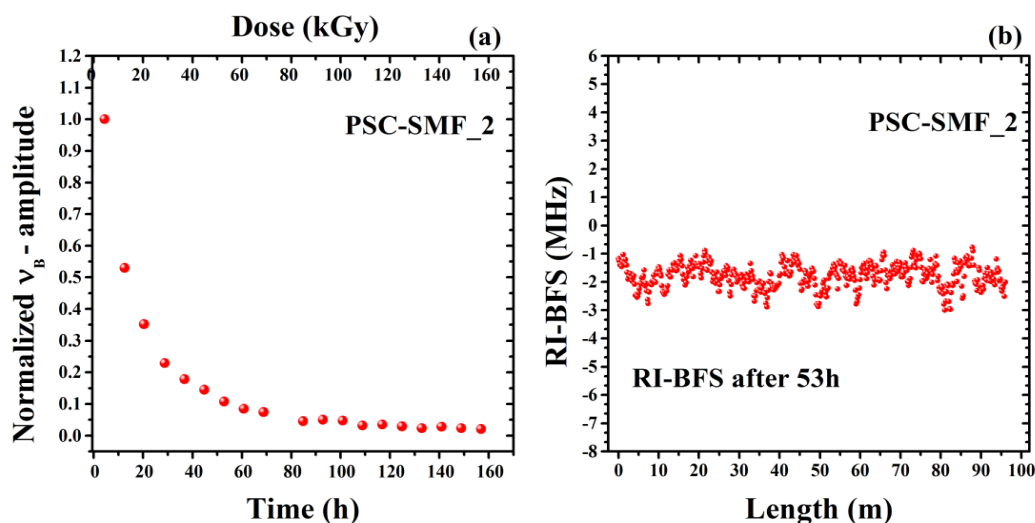


Figure 8.16. Normalized Brillouin signal amplitude response versus the irradiation time (a). RI-BFS as a function of the PSC-SMF_2 fiber length after 53 kGy (b).

Brillouin frequency changes due to the H_2 presence inside the fiber

The influence of hydrogen presence on BFS is conducted on PSC-SMF_1. The OF was soaked in H_2 vessel at 80 °C and 202 bars for 62 hours (H_2 session 1). The fiber is then removed from the H_2 tank and the effect of the natural hydrogen desorption on the BOTDA response is followed leaving the treated samples at room temperature (RT) for ~ 7 days. Moreover, the desorption measurements are supported by attenuation measurements at the operating wavelength of our setup, 1550 nm.

Figure 8.17 reports both the hydrogen induced attenuation (HIA at 1550 nm) (a) and the hydrogen induced BFS (HI-BFS) evolution (b) recorded during the desorption process (~ 7 days). Both HIA and HI-BFS exponentially decrease with the elapsed time and so with the H_2 outgassing. The BOTDA response is strongly influenced by the hydrogen presence inside the OF. During the first hours of desorption, the BOTDA response is very noisy due to the high losses at the operating wavelength of 1550 nm. However, for the first exploitable

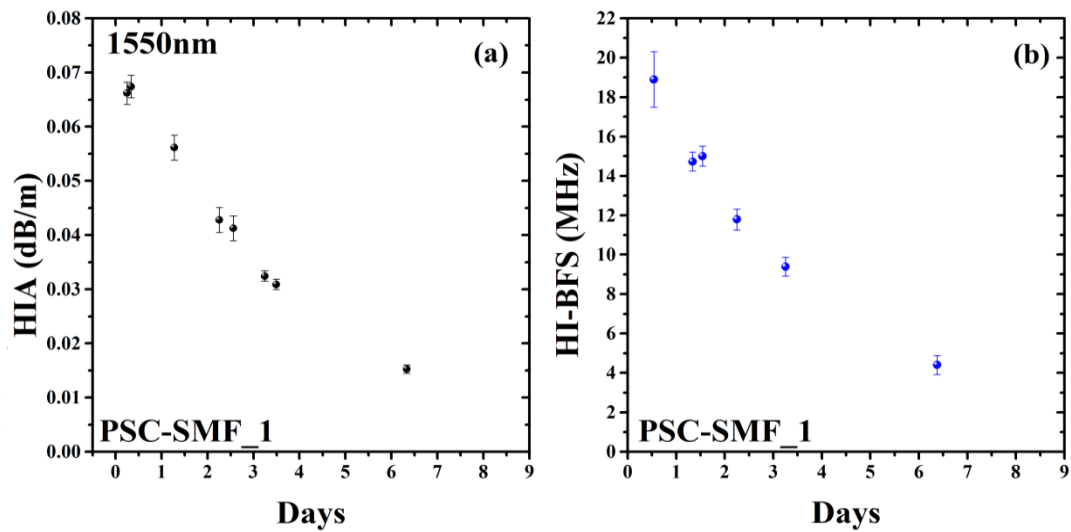


Figure 8.17. Hydrogen induced-attenuation at 1550 nm (a) and HI-BFS (b) as a function of the H₂ desorption time in PSC-SMF_1 for ~ 7 days. The H₂ is left to desorb naturally at RT. The confidence level is on the order of two standard deviations (95%).

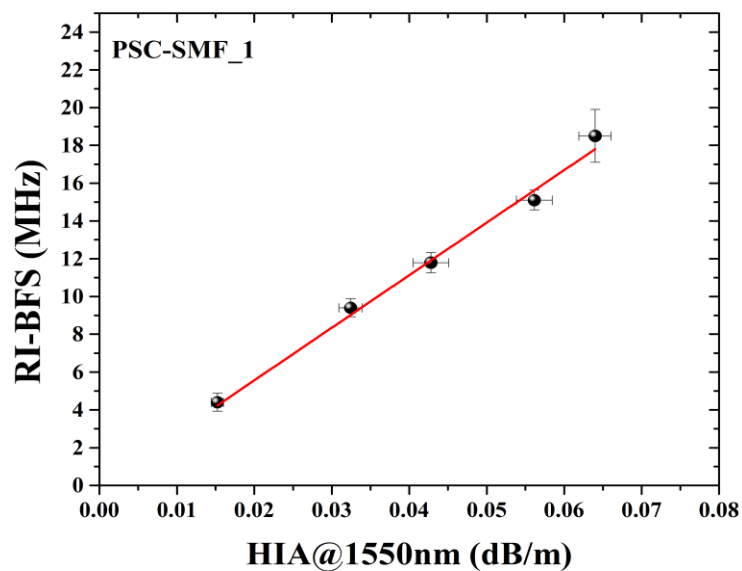


Figure 8.18. HI-BFS as a function of the HIA measured at 1550 nm. The red line indicates the linear fit $y=Ax$, where $A=(278\pm 5)$ MHz*(dB/m)⁻¹. The confidence level is on the order of two standard deviations (95%).

measurement, performed after ~13 h of outgassing when the H₂ concentration level is still high inside the fiber, we observed a BFS of ~ 20 MHz. As both HIA and HI-BFS follow

similar time tendencies, we plot the HI-BFS as a function of the HIA for possible correlation (Figure 8.18). The HI-BFS behavior is linear with the HIA and can be described from the equation $y=Ax$, where $A=(278\pm 5) \text{ MHz} \cdot (\text{dB/m})^{-1}$.

Discussion

8.4.3 γ -ray effects on the BOTDA performances are pointed out using 3 different PSC-fibers as sensing element. The radiation and/or H_2 exposure effects were also investigated via the sensor response using the PSC-SMF_1. The analysis highlights diverse important results:

- i) **The *ex-situ* evaluation of γ -radiation induced changes highlights no correlation between the RIA and the RI-BFS, as expected [59].** The PSC-SMF_1 shows the smallest RIA and RI-BFS values over the investigated dose range and in literature [58], [59]. Indeed, at the same TID of 10 MGy, the PSC-SMF_1 presents only a 2 MHz shift, corresponding to a T error of $\sim 1.7^\circ\text{C}$, whereas the PSC-SMF_2 exhibits a shift of about 4 MHz, i.e. $\sim 3.8^\circ\text{C}$ error. Moreover, although the PSC-SMF_2 has a limited RI-BFS, its RIA values at high TID are too large to fulfill the Cigéo requirements. In fact, the obtained value of $\sim 0.12 \text{ dB/m}$ exceeds the optical budget of the equipment (10 dB) for 100 m sample length. Surprisingly its RIA follows the same power law dose-evolution of the Ge-doped fiber discussed in section 8.3.1. Generally, the pure-silica core fiber is expected to exhibit lower RIA values than Ge-doped fibers [91], [92], as it is observed for example in the case of the PSC_SMF_1 fiber. Furthermore, the temperature coefficients of both fibers remain unaffected over the tested TID range (as previously shown for PSC_SMF_1 by Phéron [59], [60]). In particular, for the first time the unchanged C_T dose-dependence was evaluated estimating the BFS as a function of the temperature from RT up to 300°C . This is an important result for the employment of this sensor in radiation environment characterized by temperatures exceeding 80°C , the maximum temperature for acrylate-coated fibers. Finally, we conclude that using PSC_SMF_1 fiber as sensing element leads to small T error ($\leq 1.7^\circ\text{C}$) at high TID (up to 10 MGy).
- ii) **The *ex-situ* evaluation of the PSC-SMF_1 exposed to combined H_2 and γ -rays shows modifications of both the fiber transmission and its Brillouin response.** Indeed, the RIA value acquired when the fiber is H_2 -loaded during the irradiation at 6 MGy is comparable to that one measured in the only 6 MGy irradiated sample, whereas the sample

hydrogenated two months before the γ -irradiation at the same TID shows higher value compared to the only irradiated one (with no H₂). However, in both cases the measured RIA seems acceptable for the application (< 80 dB/km). The RI-BFS are high in both H₂ loaded-samples than in 6 MGy irradiated non-treated fiber: we estimate a T error of only ~ 2 °C when H₂ is inside the fiber during the γ -ray exposure, 3.3 °C when H₂ is already outgassed and 1.1 °C when no H₂ loading is performed and irradiated at the same TID. The fiber degradation due to H₂ presence can be avoided by using a carbon coated fiber, as discussed in Chapter 4 and in [61].

iii) **The *in-situ* evaluation of γ -ray induced changes in BOTDA response shows different results for the 3 different fibers: PSC-SMF_1, PSC-SMF_2 and PSC-SMF_3.**

The RI-BFS observed during *in situ* measurements on PSC_SMF_2 and PSC-SMF_3 corresponds to radiation induced errors on the temperature evaluation of ~ 1.5 °C and ~ 2.3 °C, respectively. Moreover, the PSC-SMF_2 signal-to-noise (SNR) ratio limited even before the γ -rays exposure quickly degrades with dose during the irradiation run due to high “transient RIA” leading to the total loss of signal after 80 hours. Therefore, this fiber appears not suitable for our application. Finally, the PSC_SMF_1 fiber shows the best response among the three studied ones. Our results highlight no changes of the Brillouin frequency due to the γ -rays even for the highest applied strain level (up to 181 g). Thus, this fiber is a promising candidate for nuclear waste temperature monitoring at low doses ≤ 0.2 MGy.

iv) The *in-situ* investigation of H₂ induced changes on the BOTDA response shows that the HI-BFS exponentially decays with time or with the hydrogen outgassing. In particular, the HI-BFS and the HIA at 1550 nm have the same desorption evolution. In fact, the HI-BFS changes linearly as a function of the HIA at 1550 nm. We note that the optical absorption in this region is linked to the vibration H₂ overtone silica-lattice vibration combination [68], [83], [126], [127]. Therefore, the BFS seems to change linearly with the H₂ content inside the fiber, as observed by Lesoille et al. in [61] for a Ge-doped fiber. Thus, all in all, the employment of PSC_SMF_1 as BOTDA sensing element seems auspicious to build a hydrogen sensor based on Brillouin scattering.

8.5 Thermal treatment

In the previous section we identified the PSC-SMF_1 fiber as a promising candidate for its employment in the harsh conditions of Cigéo project. In particular, its RI-BFS saturates at low values (~ 3 MHz) even at high TIDs. This behavior leads *Phéron et al.* to conclude that a pre-irradiation treatment of such fiber could be favorable for the temperature monitoring in radiation environment. In order to characterize the potential of this fiber to act as a temperature sensor, we evaluate its response after γ -ray exposure when submitted to a constant temperature of 80°C . As previously discussed, this study is done since inside the waste storage cells the temperature can change between 25°C and 90°C .

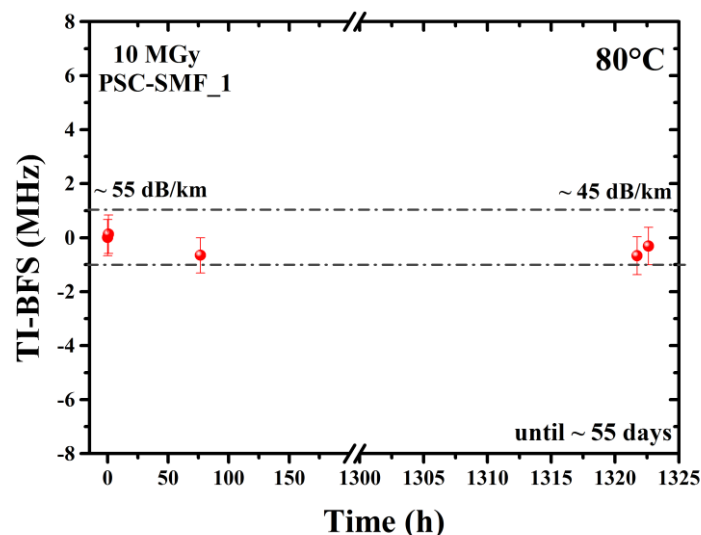


Figure 8.19. TI-BFS of the 10 MGy γ -irradiated PSC-SMF_1 as a function of the thermal treatment time (80°C for ~ 55 days). The black dashed lines delimit a variation of ± 1 MGy and the confidence level is on the order of one standard deviation (95%).

Figure 8.19 reports the results of the thermal treatment of the 10 MGy γ -irradiated PSC-SMF_1 kept during ~ 55 days at $\sim 80^\circ\text{C}$. The fiber attenuation was monitored at the beginning and the end of the thermal treatment. An improvement in the OF transmission at 1550 nm is observed after 55 days due to the thermal bleaching of the radiation induced attenuation. Indeed, we measure RIA of ~ 55 dB/km at the beginning of the treatment and of ~ 45 dB/km after 55 days at 80°C . In particular, the figure shows no variations of the BFS

induced by the 80°C treatment; the observed fluctuations ($\sigma \sim 0.4$ MHz) are within the measurement error.

Therefore, although the thermal treatment at 80°C of the 10 MGy pre-irradiated PSC-MMF_1 fiber ameliorates its transmission, its Brillouin central frequency remains unchanged.

The sensor response, using the PSC-MMF_1, exposed to γ -radiation results therefore reliable in environment characterized by temperature changes up to 80°C.

8.6 Conclusion

The study concerning the vulnerability of the BOTDA using different classes of sensing optical fibers exposed to several harsh constraints such as γ -rays and/or hydrogen has been presented in this chapter. Both *ex-situ* characterizations using fiber samples previously exposed to γ -rays or/and hydrogen and *in-situ* tests on fibers undergone to continuous exposure to γ -radiation or containing various H₂-concentrations (from zero to nearly fully-loaded) have been performed. We have shown that the performances of our system are affected both by RIA and/or HIA that limits the operating sensing range and RI-BFS and/or HI-BFS, which causes temperature measurement errors. In particular, we show that for high TIDs the amplitude of the BFS depends on the fiber composition and is limited in PSC-OFs compared to Ge-doped ones. Moreover, the temperature and strain coefficients are unaffected by radiations even at the high considered dose of 10 MGy. During the steady state γ -ray exposure at 1 kGy/h, no “transient RI-BFS” is observed for both the Ge-doped and the PSC_SMF_1 fibers. Moreover, the radiation induced BFS is not influenced neither by the drawing tension applied during the fiber manufacturing nor by the different applied strain levels along the sensing fiber. Nevertheless, as the RIA phenomenon strongly depends on the fiber composition and its manufacturing process, this parameter is a key driving one to control. Thus, the RIA evaluation should be considered for the fiber-based systems in order to minimizing the sensor vulnerability to the targeted harsh conditions. In addition, the RI-BFS is not influenced by the temperature. Our studies report very positive result for the integration of BOTDA system in the radioactive waste repository: among the different tested optical

fibers, the RIA as well as BFS evaluations suggest the PSC-SMF_1 fiber as the most promising candidate for the development of radiation-hardened Brillouin sensor.

Furthermore, the H₂ presence strongly affects the Brillouin response, to the extent that it could even be employed as hydrogen sensor. However, the hydrogen influence on the BF can be overcome using suitable coatings, such as carbon one, which avoid the H₂ diffusion inside the fiber for Cigéo specifications.

Chapter 9

Conclusion and Future developments

In this PhD Thesis we have reported an experimental study on the γ -ray and hydrogen presence impacts on Brillouin- and Raman-based optical fiber sensors. The vulnerability of their performances has been evaluated in view of their integration in the future French deep geological repository for radioactive wastes.

The results highlight both radiation and hydrogen loading degrade the optical fiber transmission properties thus limiting the sensing range of the sensors. However, the hydrogen induced attenuation (HIA) can be prevented by using hermetic coating such as carbon one that acts as a molecular hydrogen diffusion barrier. However, further tests are mandatory to evaluate the hydrogen diffusion resistance proprieties of the carbon coating during the irradiation at the Cigéo target dose rate. The radiation induced attenuation, RIA, is of a major importance parameter and plays a key role which must be carefully evaluated in selecting the appropriate sensing element for the each sensor.

The radiation induced effects on the Brillouin sensor performances are highlighted through the RIA as well as the Brillouin central frequency shift (BFS) that leads to errors in temperature or strain estimation. However, if the sensing element is appropriately chosen in order to reduce these induced effects, so the sensor fulfills the Cigéo requirements. The radiation tolerant PSC-SMF_1 is a suitable candidate as sensing fiber for our Brillouin system used to monitor both HLW disposal cells and ILW-LL disposal cells of 400 m long, as shown in Table 9.1

Table 9.1. BOTDA performance using PSC-SMF_1 with 10 dB optical budget

Fiber	HLW disposal cell		ILW-LL disposal cell	
	Maximum sensing range at 10 MGy	Temperature error at 10 MGy	Maximum sensing range at 1 MGy	Temperature error at 1 MGy
PSC-SMF_1	200m	~2°C	400m	~1°C, within the Cigéo required accuracy

The pre-irradiation treatment of the PSC-SMF_1 could be promising to further reduce or even cancel out the temperature error observed at high TID. However, in order to license this sensor for monitoring Cigéo environment, additional *in-situ* tests done up to the high total ionizing dose values (~8 MGy) are mandatory.

The Raman sensor performances are also strongly affected by radiation through both the RIA and the differential RIA, which lead to false temperature estimation with an error that increases with the sensing fiber distance. It has been shown that the RIA levels of the F-MMF_1 are acceptable so this fiber is an appropriate candidate to its employment as sensing element for our Raman system in order to monitor both HLW disposal cells and ILW-LL disposal cells of 500 m long, as shown in Table 9.2

Table 9.2. RDTS performances using F-MMF_1 with 5 dB of optical budget

Fiber	HLW disposal cell		ILW-LL disposal cell
	Maximum sensing range at 10 MGy	Temperature error at 10 MGy	Maximum sensing range at 1 MGy
F-MMF_1	430 m	10°C at 100 m	520m

However, although during the irradiation exposures at 1 kGy/h dose rate up to 0.16 MGy the pre-irradiation at high TID of F-MMF_1 can reduce the temperature error (due to the Δ RIA) keeping it constant (≤ 2 °C), at high TID larger error, up to 10°C at 10 MGy. If the temperature and the differential attenuation are constant all along the fiber length, the measurement can be corrected limiting the error over 100 m to only 2°C (at 10 MGy).

Therefore, these results show that the single ended Raman-based sensor performances do not satisfy the Cigéo requirements. For this reason we propose two possible alternative solutions.

The first one is the **employment in the HLW disposal cells of the Raman sensor in dual ended configuration (DE-RDTS) employing the F-MMF_1 as sensing element**, which shows promising performances at high total ionizing dose, as elucidated by Table 9.2 and Figure 9.1. For more clarity, we reported in Figure 9.1 the distributed temperature measurements detected by the RDTS arranged in two different configurations: single ended (red line) and dual ended (black line). Several irradiated samples of the same pure silica core fiber are spliced to each other on the same measurement line and kept at different stable temperatures, monitored by thermocouples, as shown in the graph. Whereas, as expected, the system in single ended configuration detects false values of temperature along the fiber length, using the dual ended arrangement the temperature read-out along the sensing line results compatible with that detected by the thermocouples.

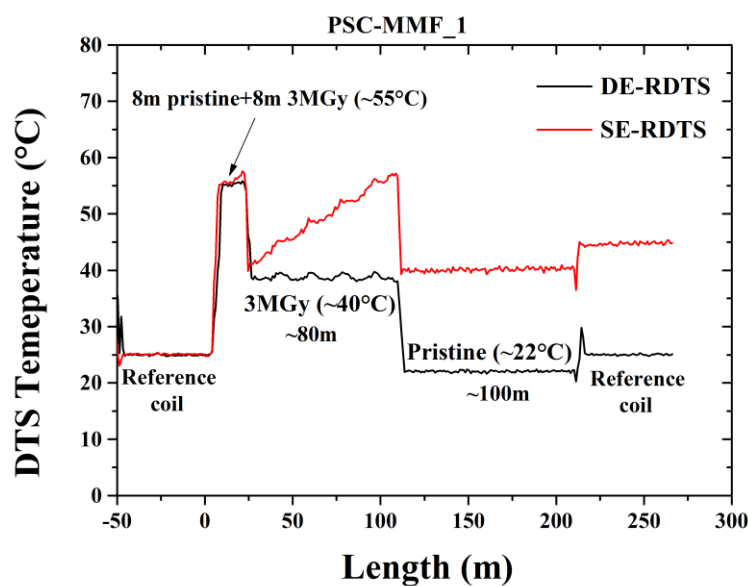


Figure 9.1. Distributed Temperature measurements detected by the RDTS using both single ended (red line) and double ended (black line) arrangements. Measurement performed on commercial PSC-MMF_1 in which both TID and temperature are not uniform along the sensing length. The temperature values in the bracket indicate the temperature measured by thermocouples. The reference coil is located inside the detection unit itself ($\sim 25^{\circ}\text{C}$).

The second solution is still under investigation in our laboratory. It involves an **original kind of Raman based sensor technology** [128], [129] which works using SMFs as sensing

elements. This system overcomes the issue associated with the $\Delta\alpha$ influence without renouncing to the single-ended interrogation configuration. For the first time we perform an evaluation of such interrogator scheme performance under radiations. Our system is indicated as **Radiation-Hardened-by-Designed Raman Distributed Temperature Sensor (RHD-RDTS)**. In the RHD-DTS two infrared excitation laser sources (~ 1550 nm and ~ 1625 nm) are employed: the wavelength of the backscattered Stokes component due to the first excitation source coincides with the wavelength of the second excitation; vice versa, the wavelength of the backscattered anti-Stokes component due to the second excitation source coincides with the wavelength of the first excitation. The overall result is that the powers of the Stokes and anti-Stokes components are automatically corrected for the radiation induced losses along the OF sensor. Some preliminary experimental results performed with a prototype of this system are shown in Figure 9.2 [130].

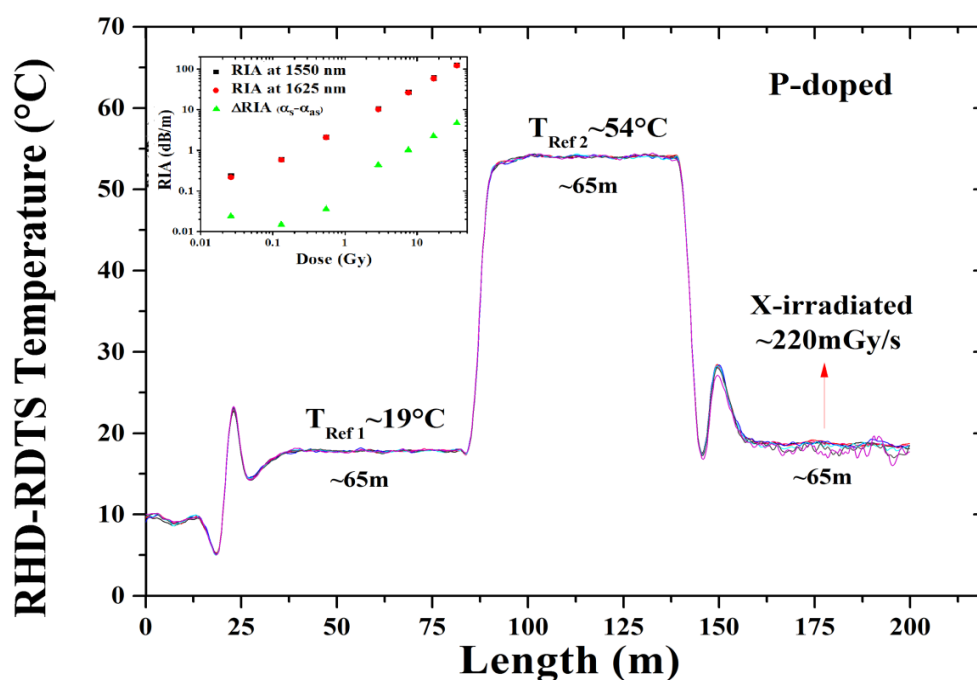


Figure 9.2. Distributed temperature measurements detected by the RHD-DTS employing a P-doped sensing fiber during X-rays exposure at dose rate of ~ 220 mGy/s. The reference temperatures were detected by two thermocouples. The inset shows the RIA at 1550 and 1625 nm and the related ΔRIA measured during the X-irradiation run.

In order to highlight the performances of the RHD-DTS and certify its employment in radiation environments, the test is carried on a phosphorous-doped fiber that is a very

radiation sensitive. Figure 9.2 shows the RHD-DTS temperature measurement performed during X-rays exposure at 220 mGy/s dose rate up to ~50 Gy TID: it results reliable up to radiation induced optical losses of ~0.12 dB/m and differential attenuation of $\sim 5 \cdot 10^{-3}$ dB/m.

However, in order to fulfil the Cigéo requirements, further tests will be done using this system in combination with a radiation resistant fiber during γ -rays exposed at the target total ionizing doses and dose rates of the application.

Consequently, both DE-RDTS using the F-MMF_1 and the RHD-RDTS employing the PSC-SMF_1 seem promising for the disposal cells monitoring at Cigéo. Particularly, by coupling Raman and Brillouin sensors (using the PSC-SMF_1), it will be possible to obtain discriminated spatially-resolved cartographies of the temperature and strain along a two fiber pathways. This is a very positive result for the integration of such sensors in nuclear facilities such as the envisaged French deep geological repository of radioactive wastes.

List of publications and communications

International peer reviewed journals:

1. **C. Cangialosi**, S. Girard, M. Cannas, A. Boukenter, E. Marin, S. Agnello, S. Delepine-Lesoille, C. Marcandella, P. Paillet, and Y. Ouerdane., “On-line Characterization of Gamma Radiation Effects on Single-Ended Raman Based Distributed Fiber Optic Sensor”, IEEE Transactions on Nuclear Science, accepted for publication, 2016.
2. S. Girard, D. Di Francesca, A. Boukenter, T. Robin, E. Marin, A. Ladaci, I. Reghioua, A. Morana, S. Rizzolo, **C. Cangialosi**, I. Planes, J-Y. Michalon, C. Marcandella, P. Paillet, M. Gaillardin, M. Raine, N. Richard, B. Cadier, and Y. Ouerdane, “On-site Regeneration Technique for Hole-Assisted Optical Fibers Used In Nuclear Facilities”, IEEE Trans. Nucl. Sci., vol. 62 (6), 2941-2947, Dec 2015.
3. L. Vaccaro, M. Cannas, **C. Cangialosi**, L. Spallino, and F. Gelardi, “Visible luminescence peculiar to sintered silica nanoparticles: spectral and decay properties”, J. Lumin., vol. 166, no. LUMIN-D-15-00331, 123-129, October 2015.
4. **C. Cangialosi**, S. Girard, A. Boukenter, M. Cannas, S. Delepine-Lesoille, J. Bertrand, P. Paillet, and Y. Ouerdane, “Effects of radiation and hydrogen-loading on the performances of Raman distributed temperature fiber sensors”, J. Lightwave Technol., vol. 33 (12), 2015.
5. **C. Cangialosi**, Y. Ouerdane, S. Girard, A. Boukenter, S. Delepine-Lesoille, J. Bertrand, C. Marcandella, P. Paillet, M. Cannas, “Development of a Temperature Distributed Monitoring System Based On Raman Scattering in Harsh Environment”, IEEE Trans. Nucl. Sci., vol. 61 (6), 3315–3322, Dec. 2014.

List of international conferences:

D. Di Francesca, S. Girard, I. Planes, A. Cebollada, A. Alessi, I. Reghioua, **C. Cangialosi**, A. Ladaci, S. Rizzolo, V. Lecoeuche, A. Boukenter, A. Champavère, Y. Ouerdane, “Radiation Hardened Architecture of a Single-Ended Raman-based Distributed Temperature Sensor”, 2016 IEEE Nuclear and Space Radiation Effects Conference”, (NSREC), Portland, Oregon, USA, July 2016.

C. Cangialosi, S. Girard, A. Boukenter, E. Marin, M. Cannas, S. Delepine-Lesoille, C. Marcandella, P. Paillet, Y. Ouerdane “Steady State γ -ray radiation effects on Brillouin fiber sensors”, 24rd International Conference on Optical Fiber Sensors, (OFS24), Curitiba, Brasil, September 28 – October 2, 2015, Poster Contribution.

C. Cangialosi, Y. Ouerdane, S. Girard, A. Boukenter, S. Delepine-Lesoille, J. Bertrand, C. Marcandella, P. Paillet, M. Cannas, “Raman based Distributed Fiber Optic Temperature Sensors for Structural Health Monitoring under Radiations Environment”, Conference on Radiation Effects on Components and Systems”, (RADECS), Moscow, Russian, September 14-18, 2014, Poster Contribution.

S. Girard, A. Boukenter, T. Robin, E. Marin, A. Ladaci, I. Reghioua, A. Morana, D. Di Francesca, S. Rizzolo, **C. Cangialosi**, I. Planes, C. Marcandella, P. Paillet, M. Gaillardin, M. Raine, N. Richard, B. Cadier, and Y. Ouerdane, “On-site Regeneration Technique for Hole-Assisted Optical Fibers Used In Nuclear Facilities”, 2015 IEEE Nuclear and Space Radiation Effects Conference, (NSREC), Boston, USA, July 2015, Oral Contribution.

C. Cangialosi, Y. Ouerdane, S. Girard, A. Boukenter, S. Delepine-Lesoille, J. Bertrand, C. Marcandella, P. Paillet, M. Cannas, “Development of a Temperature Distributed Monitoring System Based On Raman Scattering in Harsh Environment, 2014 IEEE Nuclear and Space Radiation Effects Conference”, (NSREC-RADECS), Paris, France, July 2014, Oral Contribution.

C. Cangialosi, Y. Ouerdane, S. Girard, A. Boukenter, M. Cannas, S. Delepine-Lesoille, J. Bertrand, P. Paillet, “Hydrogen and radiation induced effects on performances of Raman

fiber-based temperature sensors”, 23rd International Conference on Optical Fiber Sensors, (OFS23), Santander, Cantabria, Spain, June 2014, Poster Contribution.

L. Vaccaro, C. **Cangialosi**, L. Spallino, M. Cannas, F.M. Gelardi, R. Boscaino,. “Luminescence properties induced by sintering of silica nanoparticles SiO₂” 10th Symposium SiO₂ - Advanced Dielectrics and Related Devices, Cagliari, Italy, Juin 2014, Poster Contribution.

L. Vaccaro, C. **Cangialosi**, L. Spallino, M. Cannas, F.M. Gelardi, R. Boscaino, “Luminescent defects induced by sintering of silica nanoparticles”, E-MRS Fall Meeting Warsaw, 16-20 September 2013, Poster Contribution.

References

- [1] IAEA, "Monitoring and Surveillance of Radioactive Waste Disposal Facilities," *Series No. SSG-31*, 22 May 2014..
- [2] "ANDRA-Cigeo Project," [Online]. Available: <https://www.andra.fr/download/andra-international-en/document/editions/504va.pdf>.
- [3] IRSN, "Radioactive waste management," [Online]. Available: http://www.irsn.fr/EN/publications/thematic/Documents/irsn_booklet_radioactive_waste.pdf.
- [4] Loi n°2006-739 (2006). Loi de programme n° 2006-739 du 28 juin 2006 relative à la gestion.
- [5] S. Buschaert, S. Lesoille, J. Bertrand, S. Mayer and P. Landais, "Developing the tools for geologic repository monitoring - Andra's monitoring R&D Program - 12045," in *WM2012 Conference*, Phoenix, Arizona, USA, 2012.
- [6] "ANDRA Site," [Online]. Available: www.andra.fr.
- [7] Guide de sûreté relatif au stockage définitif des déchets radioactifs en formation géologique profonde, France, 2008.
- [8] S. Delephine-Lesoille, J. Bertrand, S. Buschaert, A. Boukenter, Y. Ouerdane, S. Girard, L. Lablonde and X. Pheron, "Durcissement des capteurs à fibre optique fondés sur la rétrodiffusion Brillouin," *I2M*, vol. 1, pp. 1-5, 2012.
- [9] S. Delephine-Lesoille, X. Pheron, J. Bertrand, G. Pillorget, G. Hermand, R. Farhoud, Y. Ouerdane, A. Boukenter, S. Girard, L. Lablonde, D. Sporea and V. Lanticq, "Industrial

-
- qualification process for optical fibers distributed strain and temperature sensing in nuclear waste repositories," *J. Sensor*, vol. 2012, p. Article ID 369375, 2012.
- [10] MoDeRn, "Monitoring Developments for Safety Repository Operation and Staged Closure," [Online]. Available: <http://modern-fp7.eu/publications/project-reports/index.html>.
- [11] J. Dakin, "Distributed optical-fibre sensors for the measurement of pressure, strain and temperature," in *in Proc. SPIE 1797, Distributed and Multiplexed Fiber Optic Sensors II*, Boston, MA, USA, 1993.
- [12] A. Ukil, H. Braendle and P. Krippner, "Distributed Temperature Sensing: Review of technology and application," *IEEE Sens. J.*, vol. 12, no. 5, pp. 885-892, 2012.
- [13] L. Palmieri and L. Schenato, "Distributed Optical Fiber Sensing Based on Rayleigh Scattering," *TOOPTSJ*, vol. 7, pp. 104-127, 2013.
- [14] X. Bao and L. Chen, "Recent progress in Brillouin scattering based fiber sensor," *Sensors*, vol. 11, pp. 4152-4187, 2011.
- [15] C. A. Galindez-Jamiroy and J. M. Lopez-Higuera, "Brillouin Distributed Fiber Sensors: An Overview and Applications," *J. Sensors*, vol. 2012, p. 17, 2012.
- [16] R. Boyd, "Spontaneous light scattering and acousto-optics," in *Nonlinear Optics*, Academic press 4th Ed. New York, USA, 2008.
- [17] X. Bao and L. Chen, "Recent progress in distributed fiber optic sensors," *Sensors*, vol. 12, no. 7, pp. 8601-8639, 2012.
- [18] R. Feynman, "Volume II. Mainly electromagnetism and matter," in *The Feynman Lectures on Physics*, Addison–Wesley, 1964.
- [19] S. Foaleng Mafang, "Distributed Brillouin sensing with sub-meter spatial resolution: modeling and processing," École Polytechnique Fédérale de Lausanne, Lausanne, 2011.
- [20] M. Niklés, "La diffusion Brillouin dans les fibres optique: étude et application aux

- capteurs distribués," PhD thesis, Ecole polytechnique fédérale de Lausanne, Switzerland, 1997.
- [21] A. Rogers, "Distributed optical-fibre sensors for the measurement of pressure, strain and temperature," *Phys Rep*, vol. 169, p. 99–143, 1988.
- [22] M. Niklès, L. Thévenaz and P. Robert, "Brillouin gain spectrum characterization in single-mode optical fibers," *J. Lightwave Technol.*, vol. 15, no. 10, pp. 1842-1851, 1997.
- [23] A. Kobayakov, M. Sauer and D. Chowdhury, "Stimulated Brillouin scattering in optical fibers," *Adv. Opt. Photonics*, vol. 2, pp. 1-59, 2009.
- [24] V. Lecoecueche, D. J. Webb, C. N. Pannell and D. A. Jackson, "Transient response in high-resolution Brillouin-based distributed sensing using probe pulse shorter than the acoustic relaxation time," *Opt. Lett.*, vol. 25, no. 3, pp. 156-158, 2000.
- [25] X. Bao, A. Brown, M. DeMerchant and J. Smith, "Characterization of the Brillouin-loss spectrum of single-mode fibers by use of very short (<10ns) pulses," *Opt. Lett.*, vol. 24, no. 8, pp. 510-512, 1999.
- [26] T. Horiguchi, K. Shimizu, T. Kurashima and M. Tateda, "Development of a distributed sensing technique using Brillouin scattering," *J. Lightwave Technol.*, vol. 13, no. 7, pp. 1296-1302, 1995.
- [27] A. Fellay, L. Thévenaz, M. Facchini, M. Niklès and P. Robert, "Distributed sensing using stimulated Brillouin scattering: Towards ultimate resolution," in *Proc. 12th Opt. Fiber Sensors OSA Tech.*, vol. 16, pp. 324- 327, 1997.
- [28] N. Nakamoto, in *Infrared and Raman spectra of inorganic and coordination compounds*, J. Wiley and Sons, Inc., 1997.
- [29] . D. C. Harris and M. D. Bertolucci, in *The physics of amorphous solids*, New York, Oxford University Press, 1978.
- [30] G. Vaccaro, "Structural modification process in bulk and nano-sized amorphous SiO₂ system," PhD thesis, Università degli studi di Palermo, Palermo - Italy, 2011.

-
- [31] M. A. Farahani and T. Gogolla, "Spontaneous Raman Scattering in Optical Fibers with Modulated Probe length for Distributed Temperature Raman Remote Sensing," *J. Lightw. Technol.*, vol. 17, no. 8, pp. 1379-1391, 1999.
- [32] R. H. Stolen and E. P. Ippen, "Raman gain in glass optical waveguides," *Appl. Phys. Letters*, vol. 22, pp. 276-278, 1973.
- [33] P. R. Stoddart, P. J. Cadusch, J. B. Pearce, D. Vukovic, C. R. Nagarajah and D. J. Booth, "Fiber optic distributed temperature sensor with an integrated background correction function," *Meas Sci Technol.*, vol. 16, no. 6, pp. 1299-1304, 2005.
- [34] D. Hwang, D. Yoon, I. Know, D. Seo and Y. Chung, "Novel auto-correction method in a fiber optic distributed-temperature sensor using reflected anti-Stokes Raman scattering," *Opt. Express*, vol. 18, no. 10, pp. 9747-9753, 2010.
- [35] B. Soller, D. Gifford, M. Wolfe and M. Froggatt, "High resolution optical frequency domain reflectometry for characterization of components and assemblies," *Opt. Express*, vol. 13, no. 2, pp. 666-674, 2005.
- [36] S. Rizzolo, A. Boukenter, E. Marin, M. Cannas, J. Perisse, S. Bauer, J.-R. Mace, Y. Ouerdane and S. Girard, "Vulnerability of OFDR-based distributed sensors to high gamma-ray doses," *Opt. Express*, vol. 23, no. 15, pp. 18997-19009, 2015.
- [37] T. Horiguchi, T. Kurashima and M. Tateda, "Tensile strain dependence of Brillouin frequency shift in silica optical fibers," *IEEE Photon. Technol. Lett.*, vol. 1, no. 5, pp. 107-108, 1989.
- [38] B. Culshaw and A. Kersey, "Fiber-Optic Sensing: A Historical Perspective," *J. Lightw. Technol.*, vol. 26, no. 9, pp. 1064-1078, 2008.
- [39] M. Barnoski and S. Jensen, "Fiber waveguides: a novel technique for investigating attenuation characteristics," *Appl. Opt.*, vol. 5, no. 9, pp. 2012-2015, 1976.
- [40] K. Shimizu, T. Horiguchi, T. Koyamada and T. Kurashima, "Coherent Self-Heterodyne Brillouin OTDR for Measurement of Brillouin Frequency Shift Distribution in Optical Fibers," *J. Lightw. Technol.*, vol. 12, no. 5, pp. 730-736, 1994.

-
- [41] T. Kurashima, M. Tateda, T. Horiguchi and Y. Koyamada, "Performance Improvement of a Combined OTDR for Distributed Strain and Loss Measurement by Randomizing the Reference Light Polarization State.," *IEEE Photon. Technol. Lett.*, 1997.
- [42] D. Garus, T. Gogolla, K. Krebber and F. Schliep, "Brillouin optical-fiber frequency domain analysis for distributed temperature and strain measurements.," *J. Lighthwave Technol.*, vol. 15, no. 4, pp. 654-662, 1997.
- [43] J. Toccafondo, T. Nannipieri, A. Signorini, E. Guillermain, J. Kuhnenn, M. Brugger and F. Di Pasquale, "Raman distributed temperature measurement at CERN high energy accelerator mixed field radiation test facility (CHARM)," *Proc. SPIE, 24th International Conference on Optical Fibre Sensors*, vol. 9634, no. 20, pp. 2182-2185, 2015.
- [44] N. Van de Giesen, S. C. Steele-Dunne, J. Jansen, O. Hoes, M. B. Hausner, S. Tyler and J. Selker, "Double-Ended Calibration of fiber-Optic Raman Spectra Distributed Temperature Sensing Data," *Sensors*, vol. 12, no. 5, pp. 5471-5485, 2012.
- [45] F. Jensen, E. Takada, M. Nakazawa, T. Kakuta and S. Yamamoto, "Distributed Raman temperature measurement system for monitoring of nuclear power plant coolant loops," *Proc. SPIE*, vol. 2895, pp. 132-143, 1996.
- [46] M. A. Soto, A. Signorini, T. Nannipieri, S. Faralli, G. Bolognini and F. Di Pasquale, "Distributed optical fiber temperature sensor using only anti-Stokes Raman scattering light in a loop configuration," in *Proc. of SPIE - 21st International Conference on Optical Fiber Sensors*, Vols. 7753, 77539U-1, 2011.
- [47] A. Fernandez Fernandez, P. Rodeghiero, B. Brichard, F. Berghmans, A. H. Hartog, P. Hughes, K. Williams and A. P. Leach, "Radiation-tolerant Raman Distributed Temperature monitoring system for large nuclear infrastructures," *IEEE Trans. Nucl. Sci.*, vol. 52, no. 6, pp. 50-58, Dec. 2005.
- [48] D. Zhou, W. Li and X. Bao, "Distibuted temperature and strain discrimination with stimulated Brillouin scattering and Rayleigh backscatter in an optical fiber," *Sensors*, vol. 13, pp. 1835-1845, 2013.

-
- [49] M. Alahbabi, Y. Cho and T. Newson, "Simultaneous temperature and strain measurement with combined spontaneous Raman and Brillouin scattering," *Opt. Lett.*, vol. 30, pp. 1276-1278, 2005.
- [50] OZ_Optics. [Online]. Available: <http://www.ozoptics.com/>.
- [51] Sensornet. [Online]. Available: <http://www.sensornet.co.uk/>.
- [52] "Luna Technology," [Online]. Available: <http://lunainc.com/>.
- [53] S. Girard, J. Kuhnenn, A. Gusarov, B. Brichard, M. Van Uffelen, Y. Ouerdane, A. Boukanter and C. Marcandella, "Radiation Effects on Silica-Based Optical Fibers: Recent Advances and Future Challenges," *IEEE Trans. Nucl. Sci.*, vol. 60, no. 3, 2013.
- [54] S. Girard, "Analyse de la reponse des fibres optiques soumises à divers environnements radiatifs," PhD thesis, Université Jean Monnet de Saint Etienne, Saint Etienne - France, 2003.
- [55] A. Sang, M. Froggatt, D. Gifford, S. Kreger and B. Dickerson, "One Centimeter Spatial Resolution Temperature Measurements in a Nuclear Reactor Using Rayleigh Scatter in Optical Fiber," *IEEE Sensors J.*, vol. 8, no. 7, pp. 1375-1380, 2008.
- [56] A. Faustov, A. Gussarov, A. Wuilpart, A. A. Fotiadi, L. B. Liokumovich, O. I. Kotov and I. Zolotovskiy, "Distributed optical fibre temperature measurements in a low dose rate radiation environment based on Rayleigh backscattering," in *Proc. SPIE 8439, Optical Sensing and Detection II*, 2012.
- [57] S. Rizzolo, E. Marin, A. Boukenter, Y. Ouerdane, M. Cannas, J. Périssette, S. Bauer, J. R. Macé, C. Marcandella, F. Paillet and S. Girard, "Radiation Hardened Optical Frequency Domain Reflectometry Distributed Temperature Fiber-Based Sensors," *IEEE Trans. Nucl. Sci.*, vol. 62, no. 6, pp. 2988 - 2994, 2015.
- [58] D. Alasia, A. F. Fernandez, L. Abrardi, B. Brichard and L. Thévenaz, "The effects of gamma-radiation on the properties of Brillouin scattering in standard Ge-doped optical fibres," *Meas. Sci. and Technol.*, vol. 17, no. 5, p. 1091–1094, 2006.
- [59] X. Pheron, S. Girard, A. Boukenter, B. Brichard, S. Delephine-Lesoille, J. Bertrand and

- Y. Ouerdane, "High gamma ray dose radiation effects on the performance of Brillouin scattering based optical fiber sensors," *Opt. Express*, vol. 20, no. 24, pp. 26978-26985, 2012.
- [60] X. Pheron, "Durabilité des capteurs à fibres optiques sous environnement Gamma," Thèse de doctorat de l'Université Jean Monnet de Saint Etienne, Saint Etienne - France , 2013.
- [61] S. Delepine-Lesoille, J. Bertrand, L. Lablond and X. Pheron, "Distributed Hydrogen Sensing With Brillouin Scattering in Optical Fibers," *IEEE Photon. Technol. Lett.*, vol. 24, no. 17, pp. 1475-1477, 2012.
- [62] F. Jensen , E. Takada , M. Nakazawa, T. Kakuta and S. Yamamoto, "Consequences of radiation effects on pure-silica-scattering-based temperature measurements," *Trans. Nucl. Sci.*, vol. 45, no. 1, pp. 50-58, Feb. 1998.
- [63] E. Takada, A. Kimura, F. B. H. Jensen and M. Nakazawa, "Correction Techniques of Radiation Induced Errors for Raman Distributed Temperature Sensor and Experiment at the Experimental Fast Reactor: JOYO," *JNST*, vol. 35, no. 8, pp. 547-553, 1998.
- [64] A. Kimura, E. Takada, K. Fujita, M. Nakazawa, H. Takahashi and S. Ichige, "Application of a Raman distributed temperature sensor to the experimental fast reactor JOYO with correction techniques," *Meas. Sci. Technol*, vol. 12, no. 7, p. 966–973, 2001.
- [65] J. Toccafondo, "Distributed Optical Fiber Radiation and Temperature Sensing at High Energy Accelerators and Experiments," PhD Thesis of the Scuola Superiore Sant'Anna and the CERN, Pisa - Italy, 2014-2015.
- [66] "JEOL," [Online]. Available: <http://www.jeol.co.jp/en/products/detail/JSM-7100F.html>.
- [67] Aztec, "User Manual," [Online]. Available: <https://engineering.temple.edu/sites/engineering/files/Oxford%20EDS%20AZtec%20User%20Manual.pdf>.

-
- [68] J. Stone, "Interactions of Hydrogen and Deuterium with Silica Optical Fiber: A Review," *J. Lightw. Technol.*, vol. 5, no. 5, pp. 712-733, May 1987.
- [69] P. J. Lemaire and E. A. Lindholm, "Hermetic optical fibers: carbon coated fibers," in *Specialty Optical Fibers Handbook*, New York Academic, 2007, p. 453–490.
- [70] COST, "Guideline for Use of Fibre Optic Sensor," 2009. [Online]. Available: <http://infoscience.epfl.ch/record/143489/files/COST299%20Guideline%20FOS.pdf>.
- [71] "Picolog," [Online]. Available: <https://www.picotech.com/>.
- [72] P. Chelliah, K. Murgesan, S. Samvel, B. R. Chelamchala, J. Tammana, M. Nagarajan and B. Raj, "Looped back fiber mode for reduction of false alarm in leak detection using distributed optical fiber sensor," *Appl. Opt.*, vol. 49, no. 20, pp. 3869-3874, 2010.
- [73] T. Landolsi, L. Zou and O. Sezerman, "Utility applications of fiber optic Distributed Strain and Temperature Sensor," [Online]. Available: http://www.ozoptics.com/ALLNEW_PDF/APN0017.pdf.
- [74] JDSU. [Online]. Available: www.jdsu.com.
- [75] EXFO. [Online]. Available: <http://www.exfo.com/>.
- [76] A. Morana, "Gamma-rays and neutrons effects on optical fibers Bragg grating for temperature sensors," PhD thesis, Université Jean Monnet de Saint Etienne and Università degli studi di Palermo, Saint Etienne, 2013.
- [77] F. Messina, "Role of hydrogen on the generation and decay of point defects in amorphous silica exposed to UV laser radiation," PhD thesis, Università degli studi di Palermo, Palermo - Italy, 2007.
- [78] G. Origlio, "Properties and Radiation Response of Optical Fibers: Role of Dopants," PhD thesis, Université de Saint Etienne and Università degli studi di Palermo, Saint Etienne - Francia, 2010.
- [79] *Bruker EMX user Manual*.
- [80] C. P. Poole, in *Electron Spin Resonance*, John Wiley and Sons Inc., New York, 1967.

- [81] G. Buscarino, "Experimental investigation on the microscopic structure of intrinsic paramagnetic point defects in amorphous silicon dioxide," PhD thesis, Università degli studi di Palermo, Palermo - Italy, 2006.
- [82] iXBlue. [Online]. Available: <https://www.ixblue.com/>.
- [83] K. Mochizuki, M. Namihira, M. Kuwazura and Y. Iwamoto, "Behaviour of hydrogen molecules adsorbed on silica in optical fibers," *J. Quantum Electron*, vol. 20, no. 7, pp. 694-697, 1984.
- [84] A. Fernandez Fernandez, H. Ooms, B. Brichard, F. Berghmans, A. Hermanne and H. Thienpont, Test facilities at SCK·CEN for radiation tolerance assessment: from space applications to fusion environments, 2001.
- [85] L. Berger, M. Raboin and J. Corbiere, "IAEA-The IRMA irradiation facility," [Online]. Available: https://inis.iaea.org/search/search.aspx?orig_q=RN:42088821.
- [86] F. L. Galeener, "Planar Rings in Glasses," *Solid State Commun*, vol. 44, pp. 1037-1040, 1982.
- [87] A. Pasquarello and R. Car, "Identification of Raman Defect Lines as Signatures of Ring Structures in Vitreous Silica," *Phys. Rev. Lett.*, vol. 80, no. 23, pp. 5145-5147, 1998.
- [88] A. Alessi, S. Girard, C. Marcandella, M. Cannas, A. Boukenter and Y. Ouerdane, "Micro-Raman investigation of X or γ irradiated Ge doped fibers," *Nucl. Instr. Meth. Phys. Res. Sect. B*, vol. 269, no. 12, pp. 1346-1349, 2011.
- [89] M. Leon, L. Giacomazzi, S. Girard, N. Richard, P. Martin, L. Martin-Samos and A. Ibarra, "Neutron Irradiation Effects on the Structural Properties of KU1, KS-4V and I301 Silica Glasses," *IEEE Trans. on Nucl. Sci.*, vol. 61, no. 4, pp. 1522-1530, 2014.
- [90] D. L. Griscom, " γ -ray induced optical attenuation in Ge-doped silica fiber image guides," *J. Appl. Phys.*, vol. 78, no. 11, pp. 6696-6704, 1995.
- [91] S. Girard, J. Keurinck, A. Boukenter, J.-P. Meunier, Y. Ouerdane, B. Azais, P. Charre and M. Vié, "Gamma-rays and pulsed X-ray radiation responses of nitrogen-,

-
- germanium-doped and pure silica core optical fibers," *Nucl. Instr. Meth. Phys. Res. Sect. B*, vol. 215, no. 1, pp. 187-195, 2004..
- [92] E. Regnier, I. Flammer, S. Girard, F. Gooijer, F. Achten and G. Kuyt, "Low-dose radiation-induced attenuation at infrared wavelengths for p-doped, ge-doped and pure silica-core optical fibres," *IEEE Trans. Nucl. Sci.*, vol. 54, no. 4, p. 2115–2119, 2007.
- [93] C. M. Hartwig, "Raman scattering from hydrogen and deuterium dissolved in Silica as a function of pressure," *J. Appl. Phys.*, vol. 47, pp. 956-959, 1976.
- [94] M. Fox and S. J. Stannard Powell, "Attenuation changes in optical fibers due to hydrogen," *Electron. Lett.*, vol. 9, no. 22, pp. 115-124, 1983.
- [95] P. J. Lemaire, "Reliability of optical fibers exposed to hydrogen: prediction of long-term loss increases," *Opt. Eng.*, vol. 30, no. 6, pp. 780-788, 1991.
- [96] P. L. Swart and A. A. Chtcherbakov, "Study of Hydrogen Diffusion in Boron/Germanium Codoped Optical Fiber," *J. Lightwave Technol.*, vol. 20, no. 11, pp. 1933-1941, 2002.
- [97] C. M. Hartwig and J. Vitko, "Raman spectroscopy of molecular hydrogen and deuterium dissolved in vitreous silica," *Phys. Rev. B*, vol. 18, no. 7, pp. 3006 -3014, 1978.
- [98] B. Schmidt, F. Holtz and J. Bény, "Incorporation of H₂ in vitreous silica, qualitative and quantitative determination from Raman and infrared," *J. Non-Cryst. Solids*, vol. 240, pp. 91-103, 1998.
- [99] D. L. Griscom and M. Mizuguchi, "Determination of the visible range optical absorption spectrum of peroxy radicals in gamma irradiated fused silica," *J. Non-Cryst. Solids*, vol. 239, pp. 66-77, 1998.
- [100] M. Cannas, L. Vaccaro and B. Bozoit, "Spectroscopic parameters related to non bridging oxygen hole center in amorphous-SiO₂," *J. Non-Cryst. Solids*, vol. 352, pp. 203-208, 2006.
- [101] A. Morana, M. Cannas, S. Girard, A. Boukenter, L. Vaccaro, , J. Perisse, J. Perisse, J.

- R. Mace, Y. Ouerdane and R. Boscaino, "Origin of the visible absorption in radiation-resistant optical fibers," *Opt. Mater. Express*, vol. 3, no. 10, p. 1769–1776, 2013.
- [102] D. L. Griscom, E. J. Friebele and G. H. J. Siegel, *Solid State Commun*, vol. 15, no. 3, p. 479–483, 1974.
- [103] J. Vitko, "ESR studies of hydrogen hyperfine spectra in irradiated vitreous silica," *J. Appl. Phys.*, vol. 49, no. 11, p. 5530, 1978.
- [104] K. Kajihara, M. Hirano, L. Skuja and H. Hosono, "Role of interstitial voids in oxides on formation and stabilization of reactive radicals: interstitial H₂O radicals in F-laser-irradiated amorphous SiO₂," *J. Am. Chem. Soc.*, vol. 128, pp. 5371-5374, 2006.
- [105] D. L. Griscom, "Diffusion of radiolytic molecular hydrogen as a mechanism for the post-irradiation buildup of interface states in SiO₂-on-Si structures," *J. Appl. Phys.*, vol. 58, no. 7, p. 2524, 1985.
- [106] K. Kajihara, L. Skuja, M. Hirano and H. Hosono, "Diffusion and reactions of hydrogen in F₂-laser-irradiated SiO₂ glass," *Phys. Rev. Lett.*, vol. 89, no. 13, p. 135507, 2002.
- [107] F. Messina and M. Cannas, "Character of the Reaction between Molecular Hydrogen and a Silicon Dangling Bond in Amorphous SiO₂," *J. Phys. Chem. C*, vol. 111, no. 18, p. 6663–6667, 2007.
- [108] G. Origlio, S. Girard, M. Cannas, Y. Ouerdane, R. Boscaino and A. Boukenter, "Paramagnetic germanium-related centers induced by energetic radiation in optical fibers and preforms," *J. Non-Cryst. Solids*, vol. 355, no. 18-21, p. 1054–1056, 2009.
- [109] S. Girard, N. Richard, Y. Ouerdane, G. Origlio, A. Boukenter, L. Martin-Samos, P. Paillet, J.-P. Meunier, J. Baggio, M. Cannas and R. Boscaino, "Radiation Effects on Silica-Based Preforms and Optical Fibers-II: Coupling Ab initio Simulations and Experiments," *IEEE Trans. Nucl. Sci.*, vol. 55, no. 6, pp. 3508-3514, 2008.
- [110] N. Richard, S. Girard, L. Martin-Samos, A. Boukenter, Y. Ouerdane and J.-P. Meunier, "A first principles study of neutral and charged oxygen vacancies in pure and Ge-doped amorphous silica," *Nucl. Instr. Meth. Phys. Res, NIMB*, vol. 266, no. 12-13, pp. 2719-

2722, 2008.

- [111] S. Girard, J. Baggio and J. Bisutti, "14-MeV Neutron, gamma ray and Pulsed X-Ray Radiation-Induced Effects on Multimode Silica-Based Optical Fibers," *IEEE Trans. Nucl. Sci.*, vol. 53, no. 6, 2006.
- [112] G. Origlio, F. Messina, S. Girard, M. Cannas, A. Boukanter and Y. Ouerdane, "Spectroscopic studies of the origin of radiation-induced degradation in phosphorus-doped optical fibers and preforms," *J. Appl. Phys.*, vol. 108, no. 123103, pp. 1-7, 2010.
- [113] A. Alessi, "Germanium point defects induced by irradiation in Ge-doped silica," PhD thesis, Università degli studi di Palermo, Italy, 2010.
- [114] J. Bisutti, "Etude de la transmission du signal sous irradiation transitoire dans les fibres optiques," PhD thesis, Université de Saint Etienne, France, 2010.
- [115] D. L. Griscom, E. J. Friebele and K. J. Long, "Fundamental defect centers in glass: ESR and optical spectroscopic studies of irradiated P-doped silica glass and optical fibers," *J. Appl. Phys.*, vol. 54, no. 7, 1983.
- [116] B. Brichard, A. L. Tomashuk, V. A. Bogatyriov, A. N. Klyamkin, S. Girard and F. Berghmans, "Reduction of the radiation-induced absorption in hydrogenated pure silica core fibres irradiated in situ with gamma rays," *J. Non-Cryst. Solids*, vol. 353, p. 466–472, 2007.
- [117] J. E. Shelby, "Reaction of hydrogen with hydroxyl-free vitreous silica," *J. Appl. Phys.*, vol. 51, pp. 2589 -2593, 1980.
- [118] F. Messina and M. Cannas, "Photochemical generation of E' centres from Si-H in amorphous SiO₂ under pulsed ultraviolet laser irradiation," *J. Phys Condens Matter*, vol. 18, pp. 9967-9963, 2006.
- [119] J. Kuhnenn, S. K. Höffgen and U. Weinand, "Quality assurance for irradiation tests of optical fibers: Uncertainty and reproducibility," *IEEE Trans. Nucl. Sci.*, vol. 56, no. 4, p. 2160–2166, 2009.
- [120] S. Theriault, "Radiation effects on COTS laser-optimized graded-index multimode

- fibers exposed to intense gamma radiation fields," *in Proc. SPIE*, vol. 6343, p. 63431Q, 2006.
- [121] D. L. Griscom, M. E. Gingerich and E. J. Fribele, "Radiation-induced defects in glasses: Origin of power-law dependence of concentration on dose," *Phys. Rev. Lett.*, vol. 71, no. 7, p. 1019, 1993.
- [122] M. Van Uffelen, "Modélisation de Systèmz d'acquisition et de transmission à fibres optique destinés à fonctionner en environnement nucleare," Université de Paris-Sud U.F.R Scientifique D'Orsay, Paris, 2001.
- [123] W. Zou, Z. He, A. D. Yablon and K. Hotate, "Dependence of Brillouin Frequency Shift in Optical Fibers on Draw-Induced Residual Elastic and Inelastic Strain," *IEEE Photon. Technol. Lett.*, vol. 19, no. 18, pp. 1389-1391, 2007.
- [124] T. Kurashima, T. Horiguchi and M. Tateda, "Distributed temperature sensing using stimulated Brillouin scattering in optical silica fibers," *Opt. Lett.*, vol. 15, no. 18, pp. 1038-1040, 1990.
- [125] W. Zou, Z. He and K. Hotate, "Investigation of Strain- and Temperature- Dependences of Brillouin Frequency Shift in GeO₂-Doped Optical Fibers," *J. Lightwave Technol.*, vol. 26, no. 13, pp. 1854-2008, 2008.
- [126] S. Kobayashi, N. Shibata and T. Izawa, "Characteristics of optical fibers in infrared wavelength region," *Rev. Elec. Cmmun. Lab.*, vol. 26, pp. 453-467, 1978.
- [127] K. J. Balers, Cooper, D.M. ; Rush, J.D., . D. M. Cooper and J. D. Rush, "Increased attenuation in optical fibres caused by diffusion of molecular hydrogen at room temperature," *Electron. Lett.*, vol. 19, no. 22, pp. 917-919, 1983.
- [128] G. Bibby. Patent US patent US4859065, 1989..
- [129] K. Suh and C. Lee, "Auto-correction method for differential attenuation in a fiber-optic distributed-temperature sensor," *Opt. Lett.*, vol. 33, no. 16, pp. 1845-1847, 2008.
- [130] D. Di Francesca, S. Girard, I. Planes, A. Cebollada, A. Alessi, I. Reghioua, C. Cangialosi, A. Ladaci, S. Rizzolo, V. Lecoeuche, A. Boukenter, A. Champavère and Y.

- Ouerdane, "Radiation Hardened Architecture of a Single-Ended Raman-based Distributed Temperature Sensor," *Abstract - IEEE Nuclear and Space Radiation Effects Conference, submitted, 2016* .
- [131] K. Kishida, Y. Yamauchi and A. Guzik, "Study of optical fiber strain temperature sensitivities using hybrid Brillouin-Rayleigh system," *Photonic Sensor*, vol. 4, no. 1, pp. 1-11, 2014.
- [132] D. Di Francesca, "Role of dopants, interstitial O₂ and temperature in the effects of irradiation on silica-based optical fibers," PhD thesis, Université Jean Monnet de Saint Etienne and Università degli studi di Palermo, Saint Etienne - France, 2015.
- [133] "<http://www.horiba.com>," [Online].
- [134] J. Stone and G. E. Walrafen, "Overtone vibrations of OH groups in fused silica optical fibers," *J. Chem. Phys.*, vol. 76, no. 4, pp. 1712-1722, 1982.
- [135] G. P. Agrawal, in *Fiber-Optic Communication Systems*, Wiley Interscience, 2002.